Republic of Türkiye's 100th Anniversary.
We are stronger together, our beloved
Turkish Nation.

PROCEEDINGS OF THE 6TH PAK-TÜRK CONFERENCE ON EMERGING TECHNOLOGIES IN THE FIELD OF SCIENCES AND ENGINEERING

May 4 – 6, 2023

Karabük University

Science Faculty, Physics Department

Karabük, Türkiye

2007
KARABÜK
ÜNİVERSİTESİ

6th PAK-TÜRK
International Conference On
Emerging Technologies In The Field Of Sciences And Engineering

PREFACE

The Pak-Türk conference series is a technical event that focuses on the advances in new technologies in engineering sciences, nuclear astrophysics, renewable energy resources, optical engineering, computer science, and electrical engineering.

The purpose of this conference series is to provide a platform for researchers, academicians, and practitioners to make them familiar with recent advances in various fields of engineering and sciences. The organization committee accepts a wide range of papers to encourage young and experienced researchers to present their work and the possibility of initiating mutual collaboration with internationally renowned researchers and experts in the relevant industries. The conference format comprises multiple sessions and the selected works in these sessions are based on substantial and novel research.

The series of events was initiated in 2018 by Ghulam Ishaq Khan Institute of Engineering Science and Technology (GIKI) which organized the "First International Pak-Türk Workshop on Emerging Technologies in the Field of Sciences and Engineering" held on 9th May of 2018 at Barber's Building in their campus.

Later events in the series are listed as:

- ✓ 2nd PAK-TÜRK International Conference (GIKI, Pakistan)
  (Face-To-Face) (March 11 – 13, 2019)
- ✓ 3rd PAK-TÜRK International Conference (GIKI, Pakistan)
  (Online Presentations – COVID restrictions) (June 9 – 10, 2020)
- ✓ 4th PAK-TÜRK International Conference (GIKI, Pakistan)
  (Online Presentations – COVID restrictions) (November 3 – 4, 2021)
- ✓ 5th PAK-TÜRK International Conference
  (University of Wah, Pakistan) (Online + Face-To-Face) (December 1 – 2, 2022)

We were wishing that **6th PAK-TÜRK** conference would be a face-to-face event in which we could enjoy international collaborations between our Pakistani and Turkish researchers in a direct and more accessible way. And for the first time, it would be organized in our home, Türkiye. However, on **February 6 - 2023**, Türkiye hit and affected by a massive earthquake.

As shattered by the devastating images of the quake and tried to manage the aftermath, it was now impossible to organize this event in a way that we could manage accommodations, travel problems, and other issues related to having some or all participants required to be in the same physical location. Therefore, we decided to conduct **6th** of the series as an online event starting on May 4, 2023, and ending on May 6, 2023. **Collected fees were directed to AFAD as an aid for the survivors of the earthquake.**

Hosted and organized by the Physics Department of the University of Karabük, the conference was comprised of a series of online presentations contributed by researchers from different countries. **5** renowned researchers across Pakistan and Türkiye were invited to give talks on various subjects that can give directions to future scientific studies. **46** speakers from **8** different countries presented their works (**51** speeches in total). The countries represented by their respective fellow researchers were ***Türkiye, Pakistan, Philippines, Ukraine, Libya, Morocco, Iraq, and Azerbaijan***. There were also participants from ***Brazil, Portugal, and France*** who had a chance of watching and listening to presentations, asking some important questions on the possible future directions of presented works and igniting useful discussions. In total, the number of participants was **127** attending from across **11** different countries.

The event was conducted with the aim of honouring the **100th anniversary of the foundation of the Turkish Republic**, and we believe, we achieved that. The topics of the meeting were more diverse compared to the previously held ones, but we managed to keep the integrity of the series intact. The quality of the works presented was evident. Respected researchers around the world appreciated our sincere efforts and praised useful discussions among peers that made the event even more delightful. Our hope is that this meeting will have a positive impact on future collaborations among participants and guide our young Turkish researchers to the right path in their respective scientific studies.

Thanks to **Mustafa Kemal ATATÜRK** and his reforms, we achieved significant advances in science in the first century of our republic’s history. We wish a brighter future for our beloved country and its young researchers.

Neclaçakmak

Prof. Dr. Necla ÇAKMAK
Chief of PAK-TÜRK 2023 Conference

ACKNOWLEDGEMENTS

First of all, we would like to thank all participants for their important contributions. Sounded and well-researched works presented in these meetings will encourage future participants to have even more quality in their respective works. The organizers of this conference make every effort to keep conference fees as low as possible to facilitate the attendance of young researchers. These efforts were relatively successful, and a lot of new young faces could be seen at the conference.

We also thank the chairs of each session, who successfully managed to let each presentation start and finish on time. Thanks to their patience and persistence in keeping track of time, we could have enough time for question-answer sessions that were really necessary to ignite useful discussions along the lines of relevant topics. They also helped young presenters when they needed some encouragement during their presentations, and they kindly handled some difficulties that are inherent in any online meeting.

The organizing committee also wishes to acknowledge the assistance and encouragement that we have received from our organizations, and the many other individuals, who helped prepare this event. In some stages of preparations, there were really only a handful of people who could sacrifice their time and they did it without asking for favours. We are also very grateful to the reviewers, whose very consistent reviewing of abstracts was of great help in improving the quality of many papers.

I am particularly thankful to the Jameel-Un NABI, a highly respected contributor and initiator of PAK-TÜRK conference series. As the current director of WAH University, his decision to have his university support many young students and academicians financially, just to be able to register and present their work at this conference, was an invaluable contribution to this event. He and his co-worker’s presence greatly contributed to the friendly atmosphere we had here.

Finally, we would like to note that this year is the 100th anniversary of the foundation of the Turkish Republic. 100 years ago, Mustafa Kemal ATATÜRK and his fellow fighters fought for independence of this country with great resolve. Therefore, we like to see this event as a commemoration of their efforts on saving our beloved nation and leading us to create a modern Turkish state. The following quotation united us in the past and will always guide us to the future:

“My moral heritage is science and reason. Anyone willing to appropriate my ideas for themselves after me will be my moral inheritors, provided they would approve the guidance of science and reason on this axis”.

Mustafa Kemal ATATÜRK

Neclaçakmak

Prof. Dr. Necla ÇAKMAK
Chief of PAK-TÜRK 2023 Conference

COMMITTEES

Honorary Board

Prof. Dr. Refik POLAT (Rector, Karabük University, Türkiye)

Prof. Dr. Ayşe NALLI (Dean, Science Faculty, Karabük University, Karabük, Türkiye)

Chief of PAK-TÜRK 2023 Conference

Prof. Dr. Necla ÇAKMAK (Karabük University, Physics Department, Karabük, Türkiye)

Scientific Committee

Aamir Hanif (Wah University, Department of Electrical Engineering, Wah, Pakistan)
Adnan Tariq (Wah University, Department of Mechanical Engineering, Wah, Pakistan)
Anam Javeed (Wah University, Department of Management Sciences, Wah, Pakistan)
Ayşe Nallı (Karabük University, Department of Mathematics, Karabük, Türkiye)
Elif Çepni (Karabük University, Department of Business, Karabük, Türkiye)
Faisal Nawaz (Wah University, Department of Chemistry, Wah, Pakistan)
Fariha K. Vardag (Quaid-i-Azam University, İslamabad, Pakistan)
Halil Demir (Karabük Un., Department of Manufacturing Engineering, Karabük, Türkiye)
Hakan Kutucu (Karabük University, Department of Software Engineering, Karabük, Türkiye)
Hamiyet Şahin Kol (Karabük Un., Department of Environmental Eng., Karabük, Türkiye)
Hayrettin Ahlatçı (Karabük Un., Dep. of Metallurgy and Materials Eng., Karabük, Türkiye)
Inayatullah Khan (University of Eng & Technology, Vice Chancellor, Taxila, Pakistan)
İzzet Açar (Karabük University, Department of Forest Industrial Eng, Karabük, Türkiye)
Jameel-Un Nabi (Wah University, Vice Chancellor, Wah, Pakistan)
Javid Shabbir (Wah University, Department of Statistics, Wah, Pakistan)
Kamil Arslan (Karabük University, Department of Mechanical Eng., Karabük, Türkiye)
Khasan S. Karimov (GIK Institute of Engineering Science and Technology, Pakistan)
Mahmut Böyükata (Kırıkkale University, Department of Physics, Kırıkkale, Türkiye)
Malik Muneeb Abid (Wah University, Department of Civil Engineering, Wah, Pakistan)
Matiullah Shah (Wah University, Department of Physics, Wah, Pakistan)
Muhammad Sharif (University of Lahore, Department of Math & Statistics, Lahore, Pakistan)
Mustafa Yaşar (Karabük Un., Department of Industrial Design Eng., Karabük, Türkiye)
Mücahit Coşkun (Karabük University, Department of Geography, Karabük, Türkiye)
Necmi Serkan Tezel (Karabük Un., Department of Electrical Engineering, Karabük, Türkiye)

Nihal Büyükçizmeci (Selçuk University, Department of Physcis, Konya, Türkiye)
Oğuz Fındık (Karabük University, Department of Computer Engineering, Karabük, Türkiye)
Qazi Mahmood Ul Hassan (Wah University, Department of Mathematics, Wah, Pakistan)
Raif Bayır (Karabük University, Department of Mechatronic Engineering, Karabük, Türkiye)
Serkan Akkoyun (Sivas Cumhuriyet University, Department of Physics, Sivas, Türkiye)
Shaukat Ali (Wah University, Department of Mechatronics Engineering, Wah, Pakistan)
Syed Waqas Hassan (Wah University, Department of Biosciences, Wah, Pakistan)
Şaban Uysal (Karabük University, Department of Chemistry, Karabük, Türkiye)
Şenol Gürsoy (Karabük University, Department of Civil Engineering, Karabük, Türkiye)
Tuncay Bayram (Karadeniz Techical University, Department of Physics, Trabzon, Türkiye)
Tülay Ekemen (Karabük University, Department of Civil Engineering, Karabük, Türkiye)
Uzma Ghazanfar (Wah University, Department of Physics, Wah, Pakistan)
Wazir Zada Khan (Wah University, Department of Computer Science, Wah, Pakistan)
Zahid Halim (GIK Institute of Engineering Science and Technology, Pakistan)
Zulfiqar Ahmad (Wah University, Wah Engineering Collage, Wah, Pakistan)

Organizing Committee – (Karabük University)

Ahmet Mustafa Erer (Physics Department)
Çağlar Emre Karababa (Mathematics Department)
Güldane Ateşoğlu (Metallurgy and Materials Engineering Department)
Hakan Kutucu (Software Engineering Department)
Hüseyin Yıldırım (Physics Department)
Merve Nur Baran (Mathematics Department)
Necla Çakmak (**Chief**, Physics Department)
Nurettin Eltuğral (Medicine Engineering Department)
Özlem Öztürk Mızrak (Mathematics Department)
Sedef Şişmanoğlu (Chemistry Department)
Savaş Ağduk (Physics Department)
Ulvi Kanbur (Physics Department)
Yasin Kanbur (Chemistry Department)

INVITED SPEAKERS

Ayben KARASU UYSAL

(KTO Karatay University, Department of Electrical & Electronic Engineering, Konya, Türkiye)

Recent Results from the ALICE Experiment

Fariha K. VARDAG

(Quaid-i-Azam University, Department of High Energy Physics & Cosmology, İslamabad, Pakistan)

Supergravity Hybrid Inflation and Gravitino Dark Matter

Jameel-Un NABI

(University of Wah, Vice Chancellor, Wah, Pakistan)

Investigations On Effects of Pairing Gaps on Charge-Changing Transitions

Serkan AKKOYUN

(Sivas Cumhuriyet University, Department of Physics, Sivas, Türkiye)

Artificial Intelligence Supported B(E2) Values Determination and An Online Calculation Tool

Zahid HALIM

(GIK Institute of Engineering Science and Technology, Department of Computer Sciences and Engineering, Khyber Pakhtunkhwa, Pakistan)

AI-Based Early Identification of an Accident and Profiling Utilizing Driver Dependent Vehicle Driving Features: A Scheme for Critical Infrastructure Protection

TOPICS

- ✓ Nuclear Astrophysics
- ✓ Internet of Things
- ✓ Computer Science
- ✓ Electrical Engineering
- ✓ Electronics
- ✓ Biotechnology
- ✓ Mechanical Engineering
- ✓ Statistics
- ✓ Microbiology
- ✓ Civil Engineering
- ✓ Chemistry & Chemical Engineering
- ✓ Material Science
- ✓ Manufacturing Engineering
- ✓ Data Science
- ✓ Mathematics
- ✓ Physical Sciences
- ✓ Welding Technologies
- ✓ Physical Geography
- ✓ Forest Industrial Engineering
- ✓ Energy Systems Engineering
- ✓ Management Sciences

CONTACT

Address: Karabük University, Science Faculty, Head of Physics Department, TR-78050 Karabük / Türkiye

Phone: +90 370 418 91 89

E-mail: pakturk2023@karabuk.edu.tr

Website: https://pakturk2023.karabuk.edu.tr/en

SCIENTIFIC PROGRAMME

May 4, 2023 Thursday

Morning Session 08.00 – 10.10 **Time Zone Istanbul (GMT+3)**
Chair: Necla Çakmak (Karabük Un., Karabük, Türkiye)

08.00 – 08.30 Opening Remarks

08.30 – 08.55 **Jameel-Un Nabi** (University of Wah, Wah Cantt, Pakistan)
Investigations on effects of pairing gaps on charge-changing transitions

08.55 – 09.10 **Tuncay Bayram** (Karadeniz Technical Un., Trabzon, Türkiye)
An Approach for Estimation of β-delayed Neutron Emission Probability

09.10 – 09.25 **Javeria Amin** (University of Wah, Wah Cantt, Pakistan)
Semantic Segmentation of Brain Tumor and Classification based on Quantum Neural Network

09.25 – 09.40 **Javid Shabbir** (University of Wah, Wah Cantt, Pakistan)
Estimation of Sensitive Proportion Based on Kuk's Randomized Response Model Using the Auxiliary Data

09.40 – 09.55 **Abdullah Kepçeoğlu** (Koç University, Istanbul, Türkiye)
The Role of Ion Properties in Reflection System Design for Time-of-Flight Mass Spectrometry: A SIMION Simulation-Based Investigation

09.55 – 10.10 **Abdullah Kepçeoğlu** (Koç University, Istanbul, Türkiye)
Electrospin biotin- and streptavidin-coated quartz crystal microbalance surfaces: characterization and mass sensing performance using Open QCM

10.10 – 10.30 COFFEE BREAK

Morning Session 10.30 – 12.00 **Time Zone Istanbul (GMT+3)**
Chair: Nihal Büyükçizmeci (Selçuk Un., Konya, Türkiye)

10.30 – 10.45 **Aamra Urooj** (University of Wah, Wah Cantt, Pakistan)
Analysis of Analytical Approximate Solutions of Relaxation Oscillation Differential Equation of Fractional Order

10.45 – 11.00 **Kashaf Tehreem** (University of Wah, Wah Cantt, Pakistan)
Techno-Economic Evaluation of Bio-Ethylene Production from Zea-Mays (Biorefinery as a sustainable solution for the utilization of waste)

11.00 – 11.15 **Lina Majeed Hayder Al-Haideri** (Baghdad Un., Baghdad, Iraq)
Obtaining the adsorption surfaces of some radioactive materials by DFT calculations

11.15 – 11.30 **Attaullah Sial** (University of Wah, Wah Cantt, Pakistan)
Advance Exponential Expansion Method via Modified Kawahara Equation in Mathematical Physics

11.30 – 11.45 **Ayesha Bibi** (University of Wah, Wah Cantt, Pakistan)
Effective Energy Management System and Bill Calculation using PLC and SCADA

11.45 – 12.00 **Amna Ali A. Mohamed** (Tripoli Machine Learning TechniquesUn., Tripoli, Libya)
A Hybrid machine learning techniques with Deep Neural Network Model for Colon Cancer Diagnosis

12.00 – 13.00 LUNCH BREAK

Afternoon Session 13.00 – 14.55 Time Zone Istanbul (GMT+3)
Chair: Savaş Ağduk (Karabük Un., Karabük, Türkiye)

13.00 – 13.25 **Zahid Halim** (GIKI, Khyber Pakhtunkhwa, Pakistan)
AI-Based Early Identification of an Accident and Profiling Utilizing Driver Dependent Vehicle Driving Features: A Scheme for Critical Infrastructure Protection

13.25 – 13.40 **Bushra Shakoor** (University of Wah, Wah Cantt, Pakistan)
Synthesis, Spectral Study and Comparative Pharmacological Assessment of Silver (I) Complexes Based on Electron Donor Ligands

13.40 – 13.55 **Fazeel Ahmad** (University of Wah, Wah Cantt, Pakistan)
Effect of optimized cycle of concentration on cooling tower for water conservation: A case study for cement plant (Pakistan)

13.55 – 14.10 **Seyran Ibrahimov** (Karabük University, Karabük, Türkiye)
On a Pillai-type Problem Associated with Lucas Numbers

14.10 – 14.25 **Ahmet Öztürk** (Karabük University, Karabük, Türkiye)
Modeling of Average Temperature Values in Türkiye for 2050 and 2096

14.25 – 14.40 **Ahmet Öztürk** (Karabük University, Karabük, Türkiye)
Assessment of Annual Average Drought Conditions in Türkiye Based on Surface Soil Moisture, Soil Moisture Anomaly, and Soil Moisture Profile Parameters

14.40 – 14.55 **Hakan Öcal** (Bartın University, Bartın, Türkiye)
Comparison of Baseline Unet and Depthwise Separable Unet models on Slices Left Atrium Segmentation from MRI

May 5, 2023 Friday

Morning Session 08.00 – 10.00 Time Zone Istanbul (GMT+3)
Chair: Necla Çakmak (Karabük Un., Karabük, Türkiye)

08.00 – 08.25 **Serkan Akkoyun** (Sivas Cumhuriyet University, Sivas, Türkiye)
Artificial Intelligence Supported B(E2) Values Determination and An Online Calculation Tool

08.25 – 08.40 **Huseyngulu Quliyev** (National Aviation Academy, Baku, Azerbaijan)
Investigation of the level structures of Giant and Pygmy dipole excitations

08.40 – 08.55 **Javad Rahebi** (Istanbul Topkapi Un., Istanbul, Türkiye)
A blockchain based to intrusion detection system in Software-defined networking

08.55 – 09.10 **Khalid Agayr** (Polytechnic University, Ben Guerir, Morocco)
Sulfuric Acid Recovery from Phosphate Waste Using Electro-Membrane Technology

09.10 – 09.25 **Bilal Karaduman** (Istanbul Ticaret Un., Istanbul, Türkiye)
Effect of Microcracks on Solar Module Efficiency

09.25 – 09.40 **Bilal Karaduman** (Istanbul Ticaret Un., Istanbul, Türkiye)
Prevention Methods of Microcracks on Solar Module

09.40 – 09.55 **Arzu Cevdetoğlu** (Mosi Textile R&D Center, Izmir, Türkiye)
A Review on Computer Aided Manufacturing Systems Used in the Apparel Industry

10.00 – 10.30 COFFEE BREAK

Morning Session 10.30 – 12.00 Time Zone Istanbul (GMT+3)
Chair: Khalid Hadi Mahdi Aal-Shabeeb (Karabük Un., Karabük, Türkiye)

10.30 – 10.55 **Ayben Karasu Uysal** (KTO Karatay University, Konya, Türkiye)
Recent Results from the ALICE Experiment

10.55 – 11.10 **Irum Jamil** (University of Wah, Wah Cantt, Pakistan)
A Facile Multicomponent Synthesis and antibacterial activity of Spiro Nitrogen Heterocycles

11.10 – 11.25 **Nihal Büyükçizmeci** (Selçuk Un., Konya, Türkiye)
Quality control of radiation dose estimation by using treatment plans on 3d phantom

11.25 – 11.40 **Madiha Rashid** (University of Wah, Wah Cantt, Pakistan)
Assessment of Prevalence of Hypertension-Related Heart Diseases Among Diabetic Patients

11.40 – 11.55 **Moin Khan** (University of Wah, Wah Cantt, Pakistan)
Numerical Modeling for Stresses Analysis in Single Lap Joints for Aerospace Applications

12.00 – 13.00 LUNCH BREAK

Afternoon Session 13.00 – 14.45 Time Zone Istanbul (GMT+3)
Chair: Necla Çakmak (Karabük Un., Karabük, Türkiye)

13.00 – 13.15 **Volodymyr V. Tkach** (Chernivtsi National Un., Chernivtsi, Ukraine)
The theoretical description for sucralose and perillartine CoO(OH)-assisted electrochemical determination in beverages

13.15 – 13.30 **Volodymyr V. Tkach** (Chernivtsi National Un., Chernivtsi, Ukraine)
The mathematical modeling for galvanostatic heavy metal removal from wastewater by a green conducting polymer, based on three poisonous mushrooms

13.30 – 13.45 **Masoud Giyathaddin Obaid** (Karabük Un., Karabük, Türkiye)
Impact of Aluminum Addition on The Melting Point and Wettability of The Sn-2Ag-0.5Cu-1In Solder Alloy System

13.45 – 14.00 **Serkan Oguz** (Karabük Un., Karabük, Türkiye)
Effect of Melting Temperature on Wettability of (96.5-x)Sn-2Ag-0.5Cu-1Bi-xAl Solder Alloy Systems

14.00 – 14.15 **Zeenat Haq** (University of Wah, Wah Cantt, Pakistan)
Physicochemical properties of Anthozoan Fluorescent proteins: an in-silico analysis for biotechnology applications

14.15 – 14.30 **Yavuz Ekincioğlu** (Bayburt University, Bayburt, Türkiye)
Structural and Electronic Characterization of m-Fluoroaniline and m-Iodineaniline: A Density Functional Theory study

14.30 – 14.45 **M. Waqas Mustafa** (University of Wah, Wah Cantt, Pakistan)
Comparative Structural and Thermal Analysis of Aluminum Alloys Piston using FEA

May 6, 2023 Saturday

Morning Session 09.00 – 10.30 **Time Zone Istanbul (GMT+3)**
Chair: Necla Çakmak (Karabük Un., Karabük, Türkiye)

09.00 – 09.25 **Fariha K. Vardag** (Quaid-i-Azam University, Islamabad, Pakistan)
Supergravity hybrid inflation and gravitino dark matter

09.25 – 09.40 **Sajjad Saeed Ali Ali** (Selçuk Un., Konya, Türkiye)
Use of Alkylbromide-derived Calix[4]arene segments in Inhibition of Hemoglobin Pseudo-Peroxidase Activity in Patients with Thalassemia

09.40 – 09.55 **Ramadan Ahmed Ali Agoub** (Tripoli Un., Tripoli, Libya)
Optimum Modeling In Terms Of Energy Efficiency In Pv/T Solar Systems By Using New Advanced Jellyfish Algorithm

09.55 – 10.10 **Yusof-den Jamasali** (Mindanao State Un., Marawi City, Philippines)
Simulation of air pollutant dispersion around Afşin Elbistan – A Thermal Power
Plant, Türkiye using Gaussian Plume Model in Freemat

10.10 – 10.15 **Yusof-den Jamasali** (Mindanao State Un., Marawi City, Philippines)
Radiological Assessment of Seyitömer Thermal Power Plant in Kütahya, Türkiye using RESRAD-ONSITE Code 7.2

10.15 – 10.30 **Samet Nohutçu** (Karabük Un., Karabük, Türkiye)
Improving The Mechanical Properties of Force TIG Welded Ti6Al4V Titanium Alloy by Post Weld Heat Treatment

10.30 – 11.00 COFFEE BREAK

Morning Session 11.00 – 12.00 Time Zone Istanbul (GMT+3)
Chair: Hüseyin Yıldırım (Karabük Un., Karabük, Türkiye)

11.00 – 11.15 **Jalaleddin Mohamed** (Karabük Un., Karabük, Türkiye)
An Approach to Alzheimer Disease Classification Based on The Artificial Neural Network

11.15 -11.30 **Hifza Azam** (University of Wah, Wah Cantt, Pakistan)
Design and development of voice and gesture controlled smart wheelchair for specially abled persons using dc motors

11.30 – 11.45 **Anes Hayder** (Karadeniz Technical Un., Trabzon, Türkiye)
The Collimator Optimization for ^{133}Xe and ^{201}Tl Isotopes on the Simulation SPECT Imaging Model

11.45 – 12.00 **Şevki Şentürk** (Karadeniz Technical Un., Trabzon, Türkiye)
Investigation of production cross-sections of ^{73}Se radioisotope via proton indicated reaction channels

12.00 – 13.00 LUNCH BREAK

Afternoon Session 13.00 – 14.00 Time Zone Istanbul (GMT+3)
Chair: Ahmet Mustafa Erer (Karabük Un., Karabük, Türkiye)

13.00 – 13.15 **Najm Abdullah Saleh Saleh** (Karabük Un., Karabük, Türkiye)
U1F Transition Properties for K-44 Isotope by pn-QRPA

13.15 – 13.30 **Mehmet Dağ** (Karabük Un., Karabük, Türkiye)
Gamow-Teller Transition Properties for Tc-100 Isotope by Pyatov Method

13.30 – 13.45 **Khalid H. Mahdi Aal-Shabeeb** (Karabük Un., Karabük, Türkiye)
Comparing the concentration of radon in the old and new residential houses in Karabük city/Türkiye using the passive method

14.00 – 14.30 Closing Remarks

FULLTEXTS

Modeling of Average Temperature Values in Turkey for 2050 and 2096

Ahmet ÖZTÜRK[1*], Mücahit COŞKUN[1], Ferhat TOPRAK[1], Enes TAŞOĞLU[1], and Onur CANBULAT [1]

[1]*Karabük University, Department of Geography, Karabük, Türkiye*

*Corresponding author's e-mail address: ahmetozturk2371@gmail.com

ORCID Numbers: 0000-0002-4074-0201 (Ahmet Öztürk), 0000-0002-7881-6742 (Mücahit Coşkun), 0000-0001-5452-5855 (Ferhat Toprak), 0000-0002-6365-6926 (Enes Taşoğlu), 0000-0000-0000-00000000-0002-9269-4219 (Onur Canbulat)

Abstract— The climate system resulting from the mutual interaction of natural environments exhibits variations due to natural events, such as changes in orbit and axial inclination, precession movement, and major volcanic eruptions. The increasing industrial activities and population size over the last century have given rise to the notion that human factors also influence these changes, leading to a growing body of research in this area. The Rio Conference, Kyoto Protocol, and Paris Agreement represent significant international efforts in the fight against climate change. Unfortunately, reports indicate that the Mediterranean basin, including Turkey, is expected to experience serious impacts from climate change. This research aims to reveal the possible changes in average temperatures in Turkey in the coming years due to climate change. The analyses were carried out using the Google Earth Engine operating system based on the socio-economic (stage 1) greenhouse gas emission scenario of the Coupled Model Intercomparison Project 6 (CMIP6), derived from the General Circulation Model (GCM). The "NASA Earth Exchange Global Daily Downscaled Climate Projections" forms the data source of the research. As a result of the analyses, it is predicted that the average temperature of 13.1°C measured for the Turkish territory in 2022 will be 15°C in 2050 and 17.7°C in 2096. The increase in the amount of temperature will be 1.9°C during the period 2022-2050 and 2.7°C during the period 2050-2096. This indicates that the trend of increasing average temperatures will continue to strengthen. When it is considered that the lowest average temperatures during the 2022-2096 period will rise from approximately 2°C to 6°C and the highest average temperatures will rise from 21°C to 26°C, the model results predict a strong warming trend that spreads over large areas in Turkey. When the model outputs are examined regionally, the Southeastern Anatolia Region, the Mediterranean coasts, and the southwestern Aegean are the areas where the temperature increase will be experienced the most. The areas where low temperatures are observed in the Eastern Anatolia Region will rapidly decrease until 2096. The average temperatures seen on the southern coasts today will likely occur on the Aegean coast in 2050 and even on the Black Sea coast in 2096. The North Anatolian Mountain Range, the Taurus Mountains, and the rugged terrains in the Eastern Anatolia Region are also among the areas that will be heavily affected by the warming trend. In the Central Anatolia Region, it is estimated that the annual average temperatures, which are approximately 11.5-13.5°C in 2022, will rise to the range of 14-16°C in 2050 and 16.5-18.5°C in 2096. Changes in climate parameters are notable as a consequence of both natural and anthropogenic influences. Prolonged heat waves and increases in tropical days are indicative of rising temperature averages. Depending on the drought conditions, agricultural production, drinking water quantity, and human health are likely to be negatively affected by this increasing trend. In addition, forests will become more susceptible to both natural and anthropogenic fires. Considering all of these outcomes, combating and adapting to global climate change should be carefully carried out, and investments in measures should be made in areas that are expected to be more affected by drought, particularly.

Keywords— *Global climate change, Temperature increase, CMIP6, Google Earth Engine, Turkey*

INTRODUCTION

The global climate has been in a continuous state of change from geological periods of the past up to the present day. The climate system resulting from the mutual interaction of natural environments shows variations due to natural events such as changes in orbit and axial inclination, precession movement, and major volcanic eruptions. The increasing industrial activities and population size over the last century have given rise to the idea that human factors are also effective in these changes, and research has focused intensively on this issue [1, 2]. The Rio Conference, Kyoto Protocol, and Paris Agreement are important steps taken by the international community in the fight against climate change [3, 4]. Reports predict that the Mediterranean basin, including Turkey, will be seriously affected by climate change [5, 6]. This research aims to reveal the possible changes in average temperatures in Turkey in the coming years due to climate change.

MATERIALS AND METHODS

The analyses were carried out using the Google Earth Engine operating system based on the socio-economic (stage 1) greenhouse gas emission scenario of the Coupled Model Intercomparison Project 6 (CMIP6), derived from the General Circulation Model (GCM). The "NASA Earth Exchange Global Daily Downscaled Climate Projections" forms the data source of the research.

RESULTS AND DISCUSSIONS

As a result of the analyses, it is predicted that the average temperature of 13.1°C measured for the Turkish territory in 2022 (Fig. 1) will be 15°C in 2050 (Fig. 2) and 17.7°C in 2096 (Fig. 3). The increase in the amount of temperature will be 1.9°C during the period 2022-2050 and 2.7°C during the period 2050-2096. This indicates that the trend of increasing average temperatures will continue to strengthen. When it is considered that the lowest average temperatures during the 2022-2096 period will rise from approximately 2°C to 6°C and the highest average temperatures will rise from 21°C to 26°C, the model results predict a strong warming trend that spreads over large areas in Turkey.

When the model outputs are examined regionally, the Southeastern Anatolia Region, the Mediterranean coasts, and the southwestern Aegean are the areas where the temperature increase will be experienced the most. The areas where low temperatures are observed in the Eastern Anatolia Region will rapidly decrease until 2096. The average temperatures seen on the southern coasts today will likely occur on the Aegean coast in 2050 and even on the Black Sea coast in 2096. The North Anatolian Mountain Range, the Taurus Mountains, and the rugged terrains in the Eastern Anatolia Region are also among the areas that will be heavily affected by the warming trend. In the Central Anatolia Region, it is estimated that the annual average temperatures, which are approximately 11.5-13.5°C in 2022, will rise to the range of 14-16°C in 2050 and 16.5-18.5°C in 2096.

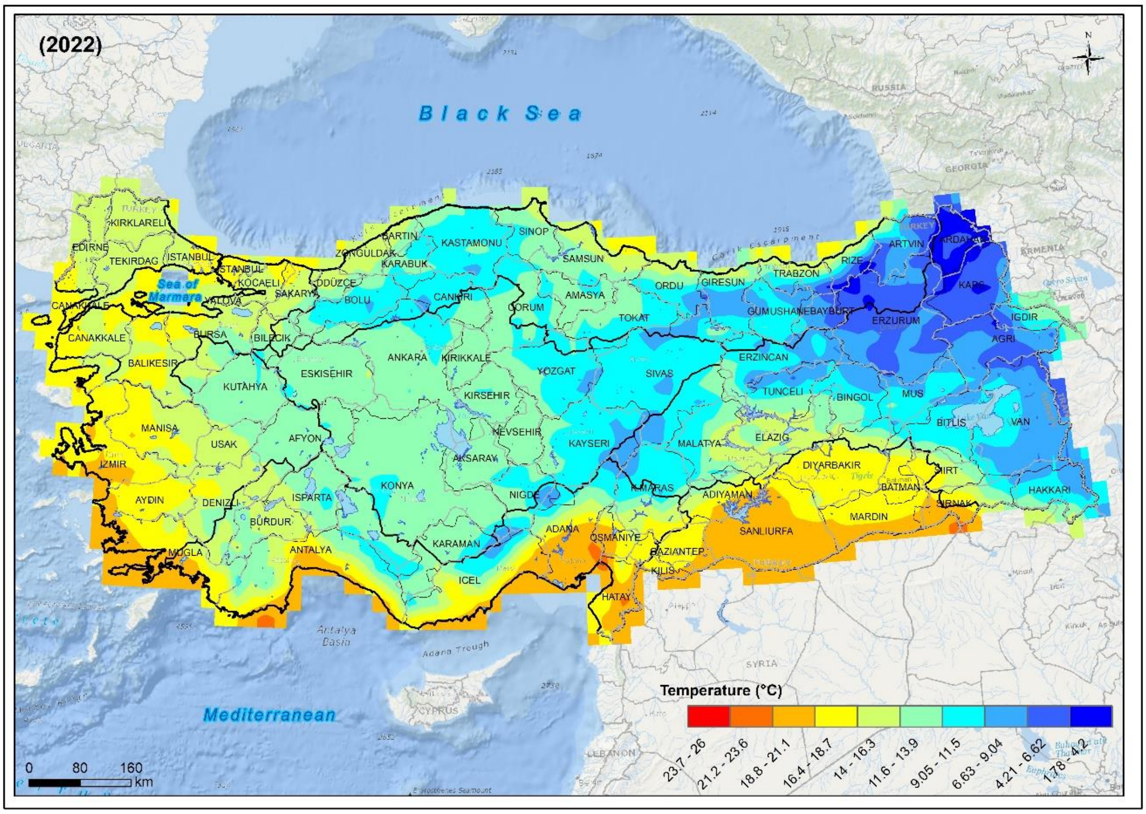

Figure 1. 2022 Temperature Averages Model Output

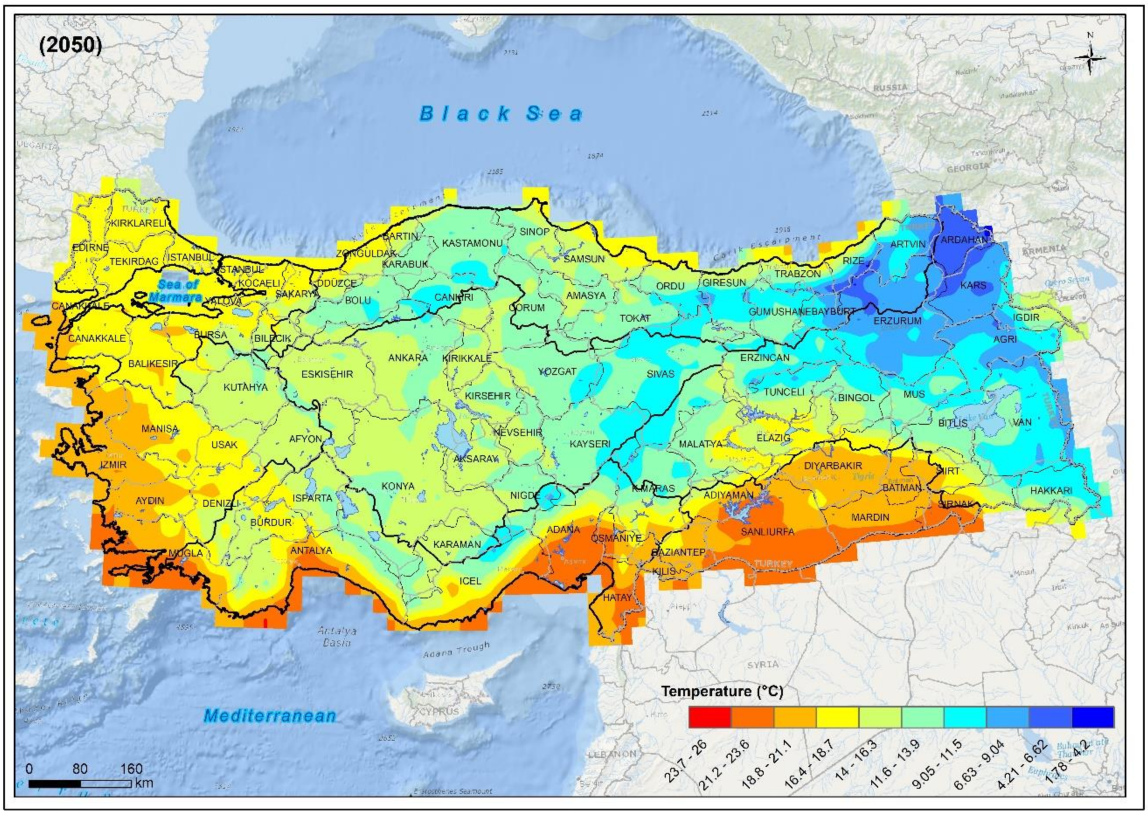

Figure 2. 2050 Temperature Averages Model Output

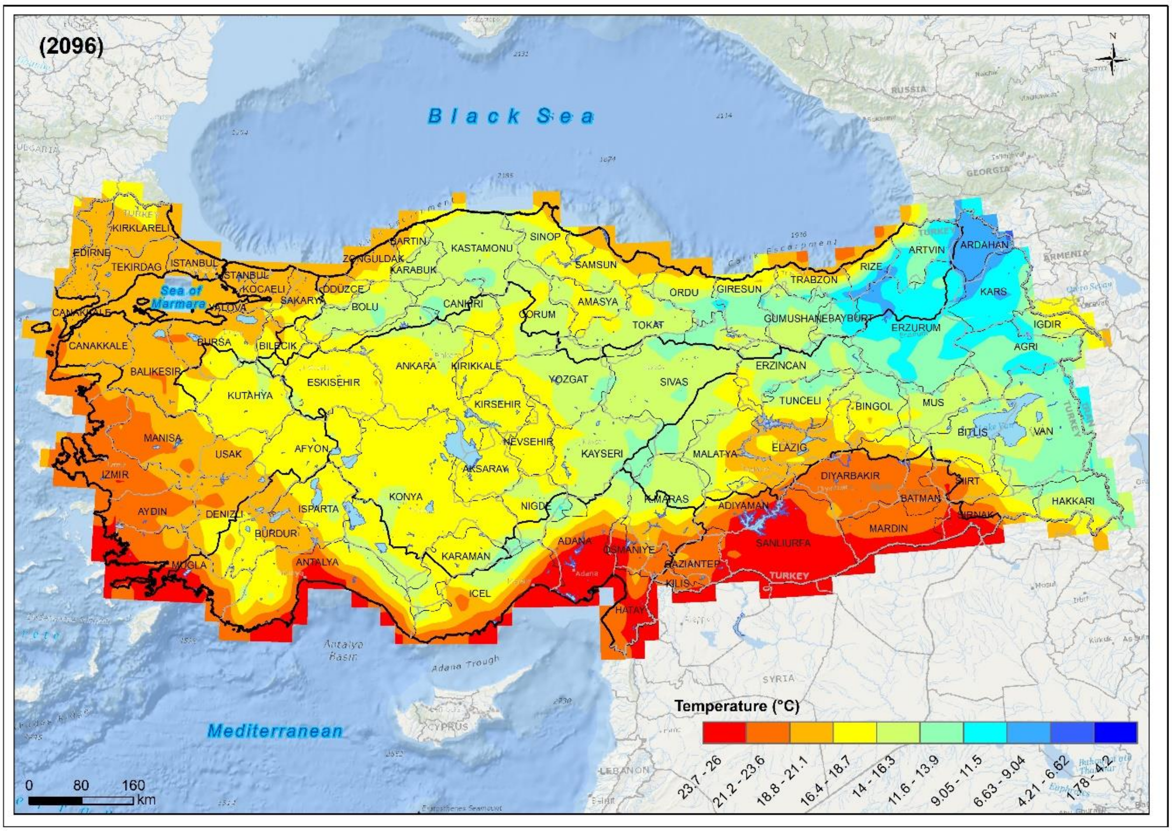

***Figure 3**. 2096 Temperature Averages Model Output*

CONCLUSION

Changes in climate parameters, such as temperature, precipitation, and extreme weather events, have been observed in recent decades as a result of both natural and anthropogenic factors. Natural factors, such as volcanic activity and solar radiation, have influenced the Earth's climate throughout history. However, the current rate of change in climate parameters is unprecedented and is largely attributed to human activities such as the burning of fossil fuels and deforestation. The increase in temperature averages is a particularly noteworthy climate change trend, as evidenced by the occurrence of prolonged heat waves and an increase in tropical days. These trends are expected to continue in the coming years and are likely to have significant impacts on a variety of sectors, including agriculture, public health, and water resources. For example, drought conditions associated with rising temperatures can lead to reduced agricultural productivity, lower water availability, and increased risk of heat-related illness. In addition to these direct impacts, climate change can also lead to increased risks of wildfires, particularly in forested areas. Both natural and human-caused fires can result in loss of biodiversity, damage to infrastructure, and threats to human lives and livelihoods. As such, combating and adapting to climate change should be a key priority for policymakers, as well as for communities and individuals. To address the impacts of climate change, measures must be taken to mitigate greenhouse gas emissions and increase resilience to changing climate conditions. Investments in areas expected to be most affected by drought, such as water management systems and agricultural practices, are particularly important in this regard. Additionally, efforts to reduce deforestation and restore degraded landscapes can help to enhance carbon sequestration, reduce greenhouse gas emissions, and enhance ecosystem resilience. Overall, a coordinated and sustained effort is necessary to address the impacts of climate change and build a more sustainable future.

REFERENCES

[1] S. T. Fakana, ‘Causes of Climate Change: Review Article’, *Glob. J. Sci. Front. Res. Environ. Earth Sci.*, vol. 20, no. 2, pp. 7–12, 2020.

[2] D. I. Stern and R. K. Kaufmann, ‘Anthropogenic and natural causes of climate change’, *Clim. Change*, vol. 122, no. 1, pp. 257–269, 2014, doi: 10.1007/s10584-013-1007-x.

[3] D. Klein, M. P. Carazo, M. Doelle, J. Bulmer, and A. Higham, *The Paris Agreement on climate change: Analysis and commentary*. 2017.

[4] D. Bodansky, ‘The History of the Global Climate Change Regime’, *Int. Relations Glob. Clim. Chang.*, vol. 23, no. 23, p. 505, 2001.

[5] F. Giorgi and P. Lionello, ‘Climate change projections for the Mediterranean region’, *Glob. Planet. Change*, vol. 63, no. 2, pp. 90–104, 2008, doi: https://doi.org/10.1016/j.gloplacha.2007.09.005.

[6] P. Lionello, F. Abrantes, M. Gacic, S. Planton, R. Trigo, and U. Ulbrich, ‘The climate of the Mediterranean region: research progress and climate change impacts’, *Reg. Environ. Chang.*, vol. 14, no. 5, pp. 1679–1684, 2014, doi: 10.1007/s10113-014-0666-0.

Assessment of Annual Average Drought Conditions in Turkey Based on Surface Soil Moisture, Soil Moisture Anomaly, and Soil Moisture Profile Parameters

Ahmet ÖZTÜRK[1*], Mücahit COŞKUN[1], Onur CANBULAT [1], Enes TAŞOĞLU[1], Ferhat TOPRAK[1]

[1]*Karabük University, Department of Geography, Karabük, Türkiye*

*Corresponding author e-mail address: ahmetozturk2371@gmail.com

ORCID Numbers: 0000-0002-4074-0201 (Ahmet Öztürk), 0000-0002-7881-6742 (Mücahit Coşkun), 0000-0000-0000-00000000-0002-9269-4219 (Onur Canbulat), 0000-0002-6365-6926 (Enes Taşoğlu), 0000-0001-5452-5855 (Ferhat Toprak)

Abstract— The term "soil moisture" refers to the water held in the soil by the molecular attraction force. The water accumulated in the soil through the effects of adhesion and cohesion is lost through evaporation, transpiration, and percolation. Changes in soil moisture are crucial for plant growth and agricultural production. Monitoring soil moisture is essential in detecting drought conditions, along with other important parameters such as plant health. The purpose of this study is to evaluate the regional parameters of surface soil moisture, soil moisture anomaly, and soil moisture profile in the Turkish terrain between 2015 and 2023 and to reveal trends under drought conditions. The analyses were conducted using the Google Earth Engine cloud computing platform and mapped using ArcMap 10.4. The data source for the study was the "NASA-USDA Enhanced SMAP Global Soil Moisture Data" catalog available in the Google Earth Engine data library. Regional mean values were determined for all three parameters (surface soil moisture, soil moisture anomaly, and soil moisture profile), and the resulting maps were overlaid to identify the riskiest areas. Furthermore, trends in drought conditions have been identified by comparing surface soil moisture and soil moisture anomaly analyses from the first and last years in the data source, which have data integrity, namely the years 2016-2021. As a result of the research, it was observed that surface soil moisture had the lowest values, especially in the Central Anatolia and Southeastern Anatolia regions, based on the eight-year average values. The eastern part of the Küre Mountains in the Black Sea Region, the Iğdır region in Eastern Anatolia, the Ergene and Southern Marmara Regions in the Marmara Region, the Western Taurus and Hatay regions in the Mediterranean Region, and the southeastern region of the Aegean region are areas where the values are lowest. The eight-year average anomaly values for soil moisture are strongly negative in Southeast and Eastern Anatolia regions, indicating maximum drought conditions. Other areas where negative anomalies are common include the Western Black Sea Region, Western Taurus, Çukurova, and the Hatay region. The coastal Aegean region, the Sakarya region, the west of the Ergene Plain, and the north and south of the Central Black Sea region have positive anomaly values. According to the soil moisture profile data expressed as a percentage, the driest regions in Turkey are the Central Anatolia Region, the southern part of Southeast Anatolia, the Western Taurus, Southeastern Aegean, Malatya, Elazığ, Hatay, and the Iğdır region. The highest soil moisture profile values are observed on the Black Sea coast, especially in the Eastern Black Sea. The risk analysis, which was created by combining the results of all three parameters, reveals that the entire Southeast Anatolia Region, the lower parts of the Central Anatolia Region, the Western Taurus, Çukurova, and Hatay in the Mediterranean Region, the southeastern region of the Aegean Region, the eastern part of the Western Black Sea Region, the south of the Central Black Sea Region, the eastern and southern parts of Van Lake in Eastern Anatolia Region, and the Malatya-Elazığ-Iğdır region are the areas that experience the most severe drought in Turkey. When the surface soil moisture and soil moisture anomaly values of 2016 and 2021 are compared, it is noteworthy that there is a transition towards drier conditions throughout the country. Surface soil moisture values are decreasing throughout Turkey, especially in the Southeast and Eastern Anatolia regions. The Eastern Anatolia Region, which had the highest positive anomaly values (moist) in 2016, along with the high-altitude regions of the Eastern Black Sea and the Western Black Sea, now exhibit the highest negative (extremely dry) anomaly values in 2021. These areas have rapidly become drier over time. Considering that drought is a slowly developing and highly impactful natural disaster that is difficult to recover from, it needs to be continuously monitored. Soil moisture properties are the most accurate data sources that reflect drought. According to the analyses based on the eight-year average values, the severity of drought is increasing and persisting in Turkish lands. The regions with the driest climates in Turkey are the Central and Southeast Anatolian regions, the Western Taurus Mountains, the eastern part of the Western Black Sea, the Southeast Aegean, and the areas around Hatay-Iğdır-Malatya and Elazığ. Planning agricultural policies according to the changing conditions and effective management of water resources are among the measures that need to be taken now to mitigate the effects of the increasingly inevitable dry periods in the coming years.

Keywords*— *Soil Moisture, Soil Moisture Anomaly, Soil Moisture Profile, Drought Conditions, Google Earth Engine, Turkey.

INTRODUCTION

"Soil moisture" refers to the water held in the soil through molecular attraction force. The water retained in soil by the force of molecular attraction, resulting from adhesion and cohesion, is released through various processes including evaporation, transpiration, and percolation. [1]. Changes in soil moisture play a vital role in facilitating the growth of plants and ensuring successful agricultural production [2–5]. Monitoring soil moisture is a critical activity for detecting drought conditions and assessing plant health, among other essential parameters [6]. This study aims to assess the surface soil moisture, soil moisture anomaly, and soil moisture profile in the Turkish terrain from 2015 to 2023 and identify patterns during drought conditions at a regional level.

MATERIALS AND METHODS

The study utilized the Google Earth Engine cloud computing platform to conduct analyses and ArcMap 10.4 to map the results. The "NASA-USDA Enhanced SMAP Global Soil Moisture Data" catalog available in the Google Earth Engine data library served as the data source. Regional mean values were calculated for the three parameters of interest (surface soil moisture, soil moisture anomaly, and soil moisture profile) and the resulting maps were overlaid to identify areas of highest risk. Trends in drought conditions were identified by comparing the surface soil moisture and soil moisture anomaly analyses from the years 2016-2021, which were selected for their data integrity as the first and last years in the data source.

RESULTS AND DISCUSSIONS

Based on the eight-year average values, the study found that surface soil moisture has the lowest values in the Central Anatolia and Southeast Anatolia regions. The eastern part of the Küre Mountains in the Black Sea Region, the Iğdır region in Eastern Anatolia, the Ergene and Southern Marmara Regions in the Marmara Region, the Western Taurus and Hatay regions in the Mediterranean Region, and the southeastern region of the Aegean region are areas where the values are lowest (Fig. 1). The Southeast and Eastern Anatolia regions show a strong negative trend in the eight-year average anomaly values for soil moisture, which suggests that the areas are experiencing extreme drought conditions. Other areas where negative anomalies are common include the Western Black Sea Region, Western Taurus, Çukurova, and the Hatay region. The coastal Aegean region, the Sakarya region, the west of the Ergene Plain, and the north and south of the Central Black Sea region have positive anomaly values (Fig.1). According to the soil moisture profile data expressed as a percentage, the driest regions in Turkey are the Central Anatolia Region, the southern part of Southeast Anatolia, the Western Taurus, Southeastern Aegean, Malatya, Elazığ, Hatay, and the Iğdır region. The highest soil moisture profile values are observed on the Black Sea coast, especially in the Eastern Black Sea (Fig. 1). The risk analysis, which was created by combining the results of all three parameters, reveals that the entire Southeast Anatolia Region of the lower parts of the Central Anatolia Region, the Western Taurus, Çukurova, and Hatay in the Mediterranean Region, the southeastern region of the Aegean Region, the eastern part of the Western Black Sea Region, the south of the Central Black Sea Region, the eastern and southern parts of Van Lake in

Eastern Anatolia Region, and the Malatya-Elazığ-Iğdır region are the areas that experience the most severe drought in Turkey (Fig. 1). When the surface soil moisture and soil moisture anomaly values of 2016 and 2021 are compared, it is noteworthy that there is a transition towards drier conditions throughout the country.

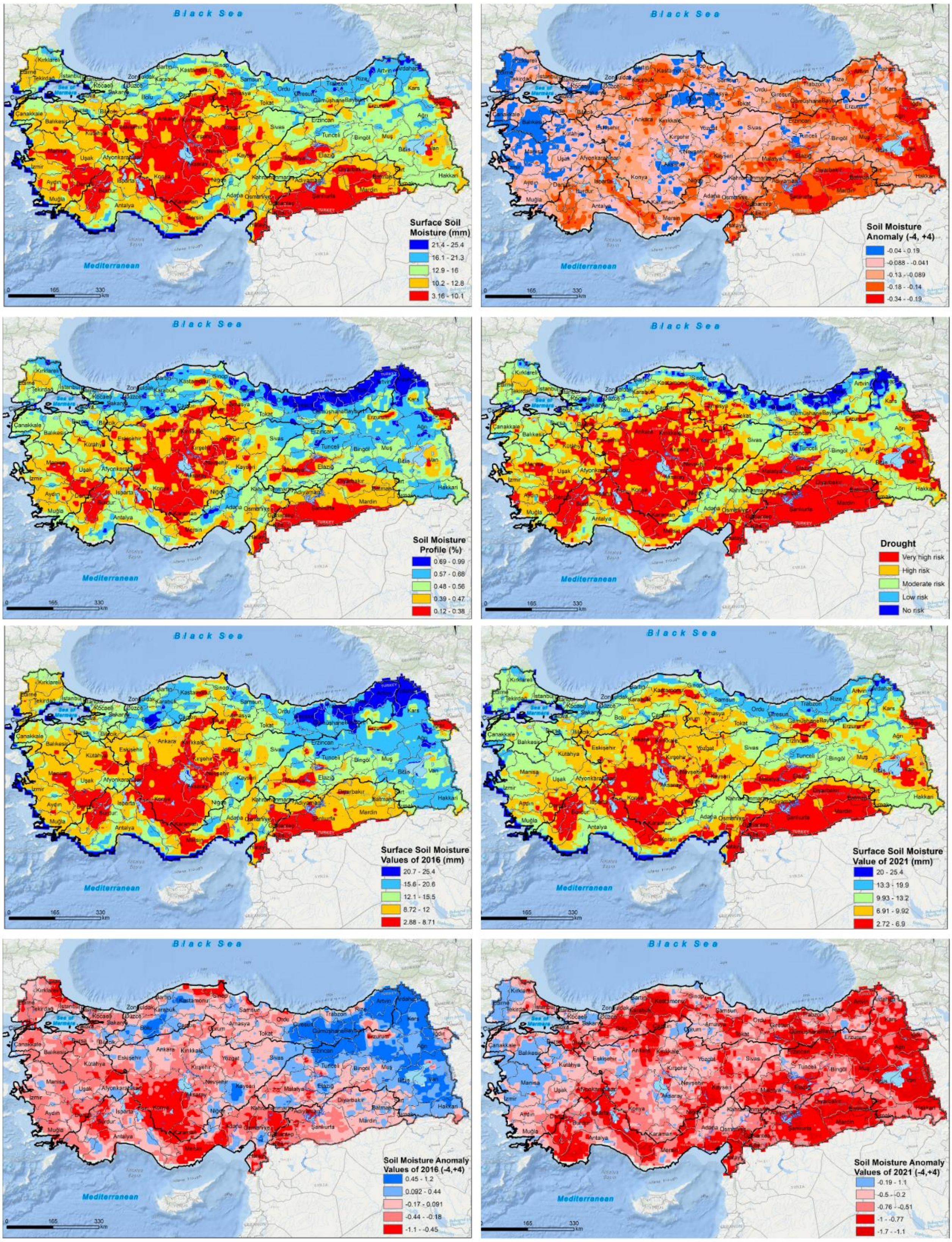

Figure 1. Avg. Surface Soil Moisture, Avg. Soil Moisture Anomaly, Avg. Soil Moisture Profile, Drought Risk Map Created by Combining Maps of Parameters, 2016- 2021 Annual Avg. Surface Soil Moisture, and 2016- 2021 Annual Avg. Soil Moisture Anomaly Maps

Surface soil moisture values are decreasing throughout Turkey, especially in the Southeast and Eastern Anatolia regions. The Eastern Anatolia Region, which had the highest positive anomaly values (moist) in 2016, along with the high-altitude regions of the Eastern Black Sea and the Western Black Sea, now exhibit the highest negative (extremely dry) anomaly values in 2021. These areas have rapidly become drier over time (Fig. 1-2).

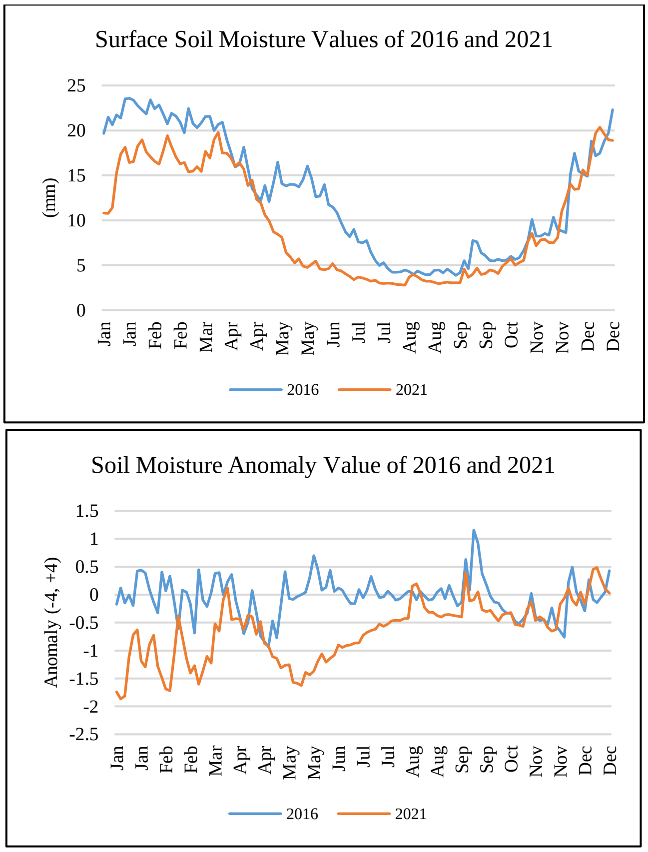

Figure 2. Surface Soil Moisture and Soil Moisture Anomaly Time-series in Turkey for 2016 and 2021

CONCLUSION

Continuous monitoring is essential for drought as it is a natural disaster that develops slowly and has significant impacts that are difficult to compensate for during its occurrence. Soil moisture characteristics are one of the data sources that allow for the most accurate monitoring of drought. The analysis based on the eight-year average values indicates that the severity of drought is increasing and continuing in Turkish territory. The Central and Southeastern Anatolia Regions, Western Taurus, the eastern part of the Western Black Sea, Southeastern Aegean, Hatay-Iğdır-Malatya, and Elazığ are the aridest areas in Turkey. Developing agricultural policies in line with changing conditions, increasing and planning irrigation facilities, and effectively managing water resources are among the necessary measures that must be taken now to prepare for the drought periods that are already becoming an undeniable reality in the future.

REFERENCES

[1] W. J. Rawls, D. L. Brakensiek, and K. E. Saxtonn, ‘Estimation of Soil Water Properties’, *Trans. ASAE*, vol. 25, no. 5, pp. 1316–1320, 1982, doi: https://doi.org/10.13031/2013.33720.

[2] F. J. Veihmeyer and A. H. Hendrickson, ‘Soil moisture in relation to plant growth’, *Annu. Rev. Plant Physiol.*, vol. 1, no. 1, pp. 285–304, 1950.

[3] Y. Wang, D. Kou, M. Muneer, G. J. Fang, and D. R. Su, ‘The Effects of Irrigation Regimes on Soil Moisture Dynamics, Yield and Quality Of Lucerne Under Subsurface Drip Irrigation’, *Appl. Ecol. Environ. Res.*, vol. 18, no. 3, pp. 4179–4194, 2020, doi: 10.15666/aeer/1803_41794194.

[4] T. Singh and D. S. Malik, ‘Effect of water stress at three growth stages on the yield and water-use efficiency of dwarf wheat’, *Irrig. Sci.*, vol. 4, no. 4, pp. 239–245, 1983, doi: 10.1007/BF00389646.

[5] T. Oweis and A. Hachum, ‘Water harvesting and supplemental irrigation for improved water productivity of dry farming systems in West Asia and North Africa’, *Agric. Water Manag.*, vol. 80, no. 1, pp. 57–73, 2006, doi: https://doi.org/10.1016/j.agwat.2005.07.004.

[6] B. Kashyap and R. Kumar, ‘Sensing Methodologies in Agriculture for Soil Moisture and Nutrient Monitoring’, *IEEE Access*, vol. 9, pp. 14095–14121, 2021, doi: 10.1109/ACCESS.2021.3052478.

On a Pillai-type Problem Associated with Lucas Numbers

Seyran Ibrahimov [1*], Ayşe Nallı [2]

[1,2]*Karabuk University, Department of Mathematics, Türkiye*

* Corresponding author's e-mail address: aysenalli@karabuk.edu.tr

ORCID Numbers: 0000-0002-3664-6781 (Seyran.Ibrahimov), 0000-0002-0489-3649 (Ayşe.Nallı)

Abstract— Let $(L_k)_{k\geq 1}$ be the Lucas sequence defined by the recurrence relation $L_1 = 1, L_2 = 3$ and $L_k = L_{k-1} + L_{k-2}$ for all $k \geq 3$. In this paper, we find all positive integer solutions to the Pillai-type equation $3^x - L_n 2^y = 1$ using the properties of Lucas numbers.

Keywords— *Lucas numbers, Pillai equation*

INTRODUCTION

Diophantine equations are one of the oldest and essential topics in number theory. One of the reasons this topic is interesting is that there is no general algorithm for solving equations. Therefore, it is possible to solve only particular-class Diophantine equations by existing methods. It is not surprising that some old and important problems on this subject are still not fully resolved. One of these equations is the following equation proposed by Pillai in 1936 [1, 2].

$$m^x - n^y = c \qquad (1)$$

Pillai conjectured that equation (1) has a finite number of positive integer solutions (m, n, x, y), with $x \geq 2$ and $y \geq 2$. Mihailescu solved this problem in the case of $c = 1$, called the Catalan conjecture [3]. In addition, Herschfeld had studied a special case of this problem with $(m, n) = (2,3)$ before Pillai [4-5]. During this period, various variants of this equation have been explored by different authors. Recently, Pillai-type problems involving recurrence number sequences have been investigated [6-12].

PRELIMINARIES

We now give some useful Lemmas that will be our key tools to prove our result.

Lemma 1. [13] Let $k \geq 0$. Then

$$L_{4k} \equiv 2\ (mod\ 5), L_{4k+1} \equiv 1\ (mod\ 5),$$

and

$$L_{4k+2} \equiv 3\ (mod\ 5)\ , L_{4k+3} \equiv 4\ (mod\ 5).$$

Lemma 2. Let t, u, l, k be some positive integers then:

1) $3^{2t-1} - 1 = 2A_t$ 5) $3^{8t-4} - 1 = 16F_t$

2) $3^{2t-1}+1=4B_t$
3) $3^{2t}+1=2C_t$
4) $3^{8t-2}-1=8D_t$
6) $3^{8t-6}-1=8R_t$
7) $3^{8t}-1=32I_t$, for all $t=2k-1$
8) $3^{8t}-1=2^{l+4}L_t$, for all $t=u\cdot 2^{l-1}$

where A_t, B_t, C_t, D_t, F_t, R_t, I_t, L_t are odd numbers that change according to the value of t.

Proof.

1) $3^{2t-1}-1=(3-1)(3^{2t-2}+3^{2t-3}+\cdots+3+1)=2A_t$

3) $3^{2t}+1=3\cdot 3^{2t-1}+1=3\cdot(2A_t+1)+1=6A_t+4=2(3A_t+2)=2C_t$

4) $3^{8t-4}-1=(\ 3^{2t-1}-1)(3^{2t-1}+1)(3^{4t-2}+1)=$

$$=(\ 3^{2t-1}-1)(3^{2t-1}+1)((\ 3^{2t-1}-1)(3^{2t-1}+1)+2)=8A_tB_t(8A_tB_t+2)=16F_t$$

8) $3^{2^{l+3}}-1=(3-1)(3+1)(3^2+1)\cdot\ldots\cdot\left(3^{2^{l+2}}+1\right)$

If we use part 3), we get that

$$(3-1)(3+1)(3^2+1)\cdot\ldots\cdot\left(3^{2^{l+2}}+1\right)=2\cdot 4\cdot 2^{l+2}L_t=2^{l+5}L_t.$$

We can prove the other parts of Lemma in the same way.

From Lemma 2 we obtain the following important result.

Result 3. If $3^t-1\equiv 0\ (mod\ 2^l)$ and $l\geq 3$ then

$$t_{min}=2^{l-2} \text{ and } t=u\cdot 2^{l-2}, u\geq 1.$$

Using induction method we can prove that the following lemma.

Lemma 4. If $l\geq 4$ and $u\geq 1$. Then:

$$3^{u\cdot 2^{l-2}}-1\equiv 0\ (mod\ 5)$$

MAIN RESULT

Theorem 5. The only positive integer solutions of the following equation (2) are

$$(x,y,n)=\{(1,1,1),(2,3,1),(2,1,3)\}$$

$$3^x-L_n2^y=1 \qquad (2)$$

Proof. From Lemmas 1, 4 and Result 3 we get that there are no solutions to equation (2) when $y \geq 4$. Therefore we have to investigate the cases $y = 1$, $y = 2$, and $y = 3$.

1) If we take $y = 1$ in equation (2) we obtain following equation

$$L_n = \frac{3^x - 1}{2} \tag{3}$$

2) If we take $y = 2$ in equation (2) we get $L_n = \frac{3^x-1}{4}$. Let $x = 2k$ then we have

$$L_n = \frac{9^k - 1}{4} \tag{4}$$

If $x = 2k + 1$, then we have $4L_n = 3^{2k+1} - 1$ which is not possible.

3) If we take $y = 3$ and in equation (2) we obtain $L_n = \frac{3^x-1}{8}$. Let $x = 2k$ then we get

$$L_n = \frac{9^k - 1}{8} \tag{5}$$

If $\mathrm{x} = 2\mathrm{k} + 1$, then we have $8\mathrm{L}_\mathrm{n} = 3^{2\mathrm{k}+1} - 1$ which is not possible.

Furthermore, from the theorem proved by Erduvan, Keskin, and Şiar in [12], we get that equations (4) has no solution, and the solutions of equation (3) and equation (5) are $(x, n) = \{(1,1), (2,3)\}$ and $(k, n) = (1,1)$ respectively. Then we obtain the only solutions to equation (2) are $(x, y, n) = \{(1,1,1), (2,3,1), (2,1,3)\}$.

ACKNOWLEDGMENT We would like to thank Prof. Carlos A. Gomez for carefully reading our paper and giving valuable suggestions.

REFERENCES

[1] Pillai, S.S. On ax - by = c. J. Indian Math. Soc. (N.S.) 2, pp. 119–122, 1936.
[2] Pillai, S.S. A correction to the paper on ax - by = c. J. Indian Math. Soc. (N.S.) 2, p. 215, 1937.
[3] Mihailescu, P. Primary cyclotomic units and proof of Catalan’s conjecture. J. Reine Angew. Math. (Crelles J.) 572, pp. 167–195, 2006.
[4] Herschfeld, A.: The equation 2x - 3y = d. Bull. Am. Math. Soc. 41, p. 631, 1935.
[5] Herschfeld, A.: The equation 2x - 3y = d. Bull. Am. Math. Soc. 42, pp. 231–234, 1936.
[6] Ddamulira, M., Luca, F., Rakotomalala, M.: On a problem of Pillai with Fibonacci numbers and powers of 2. Proc. Indian Acad. Sci. Math. Sci. 127(3), pp. 411–421, 2017.
[7] Ddamulira, M., Gómez-Ruiz, C.A., Luca, F.: On a problem of Pillai with k-generalized Fibonacci numbers and powers of 2. Monatsh. Math. 187(4), pp. 635–664, 2018.
[8] Bravo, J.J., Luca, F., Yazán, K., On Pillai’s problem with Tribonacci numbers and power of 2. Bull. Korean Math. Soc. 54, pp. 1069–1080, 2017.
[9] Chim, K.C., Pink, I., Ziegler, V., On a variant of Pillai’s problem. Int. J. Number Theory 13, pp. 1711–1727, 2017.

[10] García, A.C., Hernández, S., Pillai's problem with Padovan numbers and powers of two. Revista Colombiana de Matemáticas 53, pp. 1–14, 2019.
[11] Hernane,M., Luca,F., Salah Eddine,R., Togbé,A. On Pillai's problem with Pell numbers and powers of 2, Hardy-Ramanujan Journal, 41, pp. 22–31, 2018.
[12] Erduvan, F., Keskin, R., Şiar, Z., Repdigits base b as products of two Lucas numbers Quaestiones Mathematicae, 44(10), pp. 1283-1293, 2021.
[13] T. Koshy, Fibonacci and Lucas Numbers with Applications, Toronto, New York, NY, USA, 2001.

6th Pak – Türk International Conference on Emerging Technologies in the field of Sciences and Engineering, May 4 – 6, 2023, Karabük University, Karabük, Türkiye

Comparison of Baseline Unet and Depthwise Separable Unet models on Slices Left Atrium Segmentation from MRI

Hakan Öcal[1*]

[1]*Department of Computer Engineering, Faculty of Engineering, Architecture, and Design, Bartin University, Bartin, Turkey*

* Corresponding author's e-mail address: hocal@bartin.edu.tr

ORCID Numbers: 0000-0002-8061-8059 (Hakan.Öcal)

Abstract**—** Accurate and precise segmentation of the left atrial node is crucial in early diagnosing and treating atrial fibrillation. Segmentation of 3D images obtained by Magnetic Resonance Imaging with the naked eye is time-consuming and challenging. Therefore, the use of deep learning-based segmentation methods, which are popular today, comes to the fore. Many deep-learning models have been proposed in the literature for the segmentation of medical images. Baseline Unet and Depthwise Separable Unet models, among the best segmentation architectures presented in this study, were analyzed comparatively. The architectures were trained and tested with the same parameters in the Left Atrium Segmentation Challenge 2013 (LASC'13) Magnetic Resonance Imaging (MRI) dataset. As a result of the analysis, Depth-wise, Separable Unet obtained a Dice score of 92.5, while the Baseline Unet architecture obtained a Dice score of 95.5. The obtained scores show that when a trade-off is made, Depthwise, Separable Unet can achieve good results with three times fewer parameters than Basic Unet.

Keywords**—***Baseline Unet, Depthwise Separable Unet, Left Atrium Segmentation*

INTRODUCTION

Atrial fibrillation (AF) is one of the most common cardiac arrhythmias that can cause permanent damage to the heart and body [1]. AF, particularly permanent AF, is driven by complex substrates widely distributed in both atrial compartments [2]. Recurrent atrial attacks cause various defacto effects, such as dilatation, myofiber changes, and fibrosis in the atrium structure [1,3]. For this reason, it is essential to segment the system of the atrium in patients with AF and to have detailed information [4]. Sensitive and accurate segmentation of left atrium images obtained from MRI will provide many advantages for precise diagnosis and treatment of the atrium. Recently, techniques with deep learning architecture have achieved many successes in segmentation [5]. In this study, Baseline Unet and Depthwise Separable Unet architectures, which are the most used in segmentation, were analyzed comparatively on the LASC'13 dataset.

RELATED WORKS

In recent years, deep learning-based architectures based on large datasets have become increasingly important [6,7, 8,9]. In addition, great strides have been made in deep learning-based LA segmentation [4,6,7,10,11,12,13]. Yu et al. trained a self-ensembling model of the uncertainty-aware for semi-supervised learning [14]. Li et al. [15] proposed an Unet with hierarchical aggregation and attention module to more precisely position the ROI in LA. Liu et al. [16] and Borra et al. [17] proposed a deep segmentation network using a modified Unet network to segment the LA. Yang et al. [18] used Fast Repeat CNN(RCNN) for precise and accurate segmentation of LA and accurate focus on ROI. Puybareau et al. [19] adopted a transfer learning model using VGG-Net as the backbone for the segmentation of LA. Bian et al. [20] used ResNet modified with spatial pyramid pooling for the segmentation of LA.

PREPARING THE DATASET AND THE DEEP LEARNING ARCHITECTURES

For experimental studies, the data set was passed through various preprocessing stages. In addition, the architectures were cross validated by five times, and the ideal structures were adopted for experimental studies.

A. *LASC'13 Dataset*

Random scaling and elastic transformation methods were used to prepare the data set. Seventeen cases that make up the training dataset are divided into train and 4 cases validation datasets. Two-dimensional slices of the data sets were obtained and converted to Numpy matrices. In addition, random rotation was applied to the data at +-45 degrees angles. Datasets are fed into deep learning architectures in 256x256x1 dimensions.

B. *Architectures*

Deep learning architectures analyzed comparatively shown in Fig. 1 and Fig. 2. ADAM was used as the optimizer in the proposed architectures [21]. The Bilinear Upsampling method was used in the upsampling phase in both architectures. 3x3 convolutional blocks are used in both architectures' encoder and decoder stages. In addition, 2x2 Maximum pooling is used to make feature extraction more efficient. In the Depthwise Sparable Unet architecture, a 3x3 kernel was used in the Depthwise stage, and a 1x1 kernel was used in the pointwise setting. In addition, ReLU was used as the activation function.

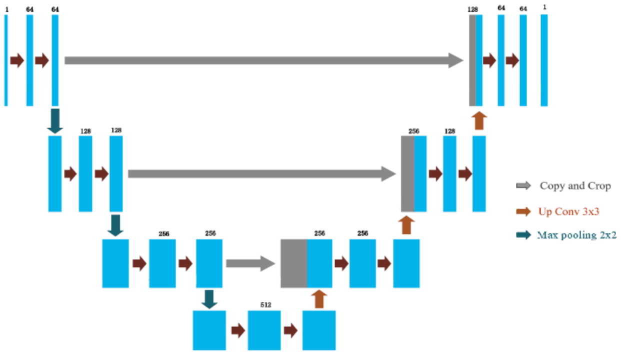

Fig.1. Baseline Unet Architecture

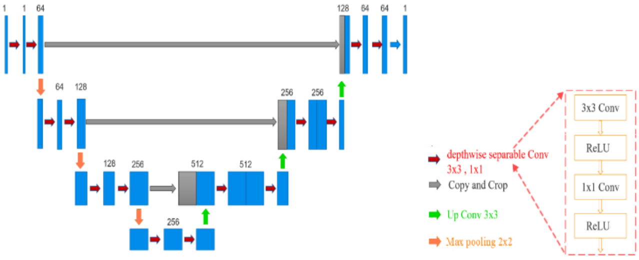

Fig.2. Depthwise Separable Unet Architecture

C. *Loss Function*

In the proposed architecture, the Dice Loss loss function, which achieved very successful results in segmentation, was used to calculate the cost. Dice Loss is obtained by subtracting the Dice Similarity coefficient (DSC) from 1. The mathematical expression of the DSC and Dice Loss loss function is shown in Eq. 1. and Eq. 2., respectively. In all mathematical expressions in the article, TP=True represents positive, TN=True negative, FP=False positive, and FN=False negative.

$$DSC = \frac{2*TP}{2*TP+FP+FN} \quad (1)$$

$$Dice\ Loss = 1 - DSC \quad (2)$$

D. *Performance metric*

The Accuracy(ACCUR) precision metric, whose mathematical model is given in Eq. 3., was used to score the training and testing performances of the analyzed architectures.

$$ACCUR = \frac{TN+TP}{TN+TP+FN+FP} \quad (3)$$

EXPERIMENTAL RESULTS AND DISCUSSION

Fig. 3. and Fig. 4. show Baseline Unet's training accuracy and training loss values for 100 epochs graphically. As can be seen from the figures, Baseline Unet has consistently reduced its Dice loss in LA segmentation.

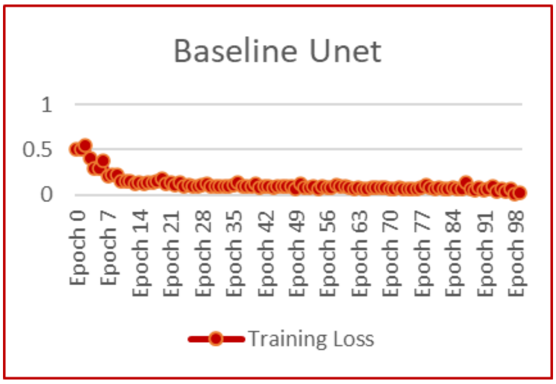

Fig. 3. Baseline Unet Training Loss on LA segmentation

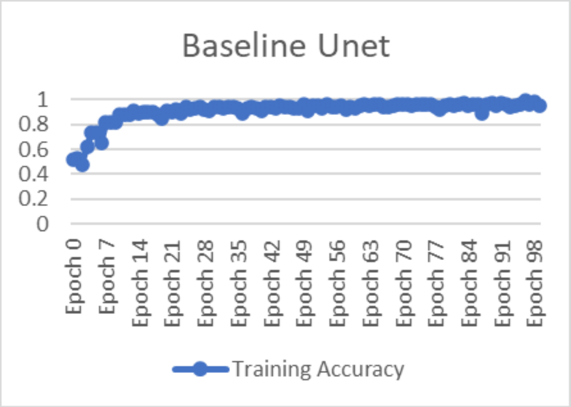

Fig. 4. Baseline Unet Training Accuracy on LA segmentation

Figures 5 and 6. show Depthwise Separable Unet's training accuracy and loss values for 100 epochs graphically. As can be seen from the figures, Depthwise Sparable Unet had more difficulty in reducing Dice loss than Baseline Unet in LA segmentation.

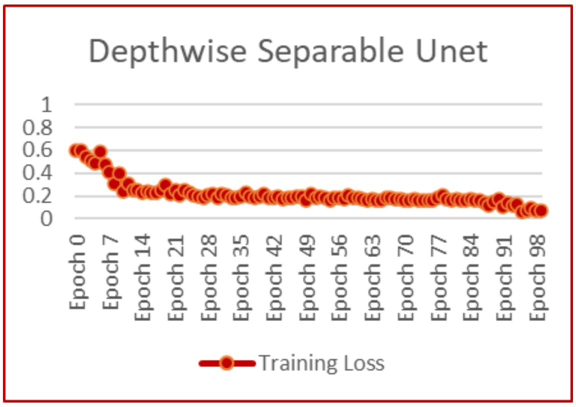

Fig. 5. Depthwise Separable Unet Training Loss on LA segmentation

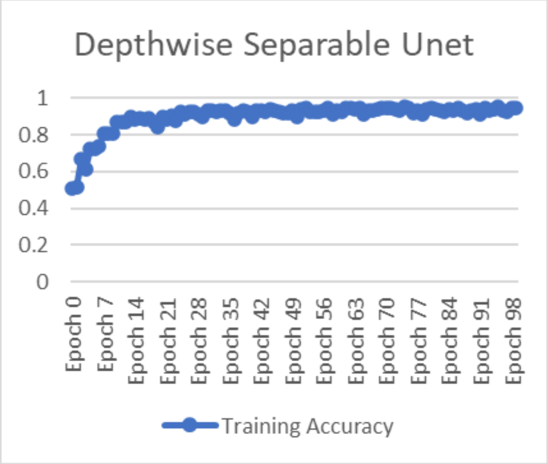

Fig. 6. Depthwise Separable Unet Training Accuracy on LA segmentation

Baseline Unet and Depthwise Sparable Unet architectures were analyzed as 50, 100, and 150 epochs as seen in Table 1. At 100 epochs, both architectures achieved the best performances. At 150 epochs, however, the loss started to rise again. As a result of the experimental studies, Mini batch-size=8 and learning rate=1e - 4 were selected. As can be seen from the training and validation scores, Baseline Unet achieved 3 points higher validation sensitivity values. Also, Depthwise Separable Unet had a hard time reducing Dice loss. But Depthwise Separable Unet consists of 455 thousand parameters, while Baseline Unet consists of 1.365 million parameters. The difference of 3 points between the two models is a high figure for a trade-off.

Table 1. Comparative Analyzes of The Two Architectures

Architectures	***Methods***	***Training Accuracy***	***Validation Accuracy***	***Epoch***
Baseline Unet	Slice-based MRI	0.97	0.936	50
Depthwise Separable Unet	Slice-based MRI	0.932	0.902	
Baseline Unet	Slice-based MRI	**0.99**	**0.955**	**100**

Architectures	***Methods***	***Training Accuracy***	***Validation Accuracy***	***Epoch***
Depthwise Separable Unet	Slice-based MRI	**0.967**	**0.935**	
Baseline Unet	Slice-based MRI	0.965	0.928	150
Depthwise Separable Unet	Slice-based MRI	0.927	0.90	

The segmentation images of the proposed model obtained in the LASC'13 test set are shown in Fig. 7 and Fig. 8.. As seen from the images, the Baseline Unet architecture has achieved more successful segmentation results.

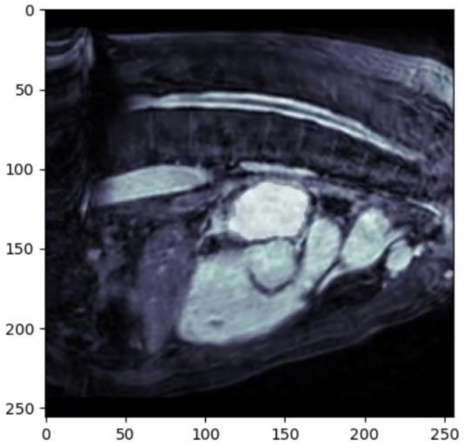

Fig. 7. Baseline Unet LA Segmentation Test Result

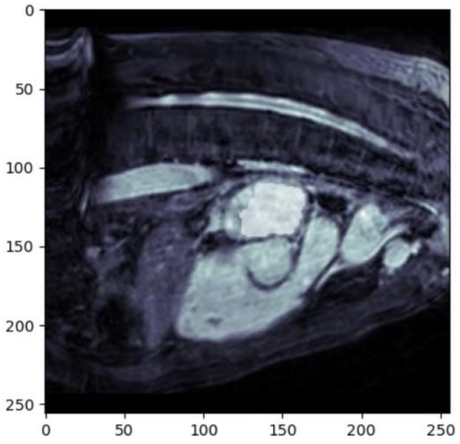

Fig. 8. Depthwise Separable Unet LA Segmentation Test Result

CONCLUSION

In this study, Baseline Unet and Depthwise Separable Unet architectures were analyzed comparatively on the LASC'13 dataset. As a result of the analysis, Baseline Unet architecture achieved higher performance results. Depthwise Separable Unet architecture may be one-third of the Baseline Unet architecture in terms of parameters used, but there is a difference of 3 pounds. This situation shows that Baseline Unet architecture has a very practical place compared to the architectures used in the literature.

REFERENCES

[1] S. M. Narayan, M. Rodrigo, C. A. Kowalewski, F. Shenasa, G. L. Meckler, M. N. Vishwanathan, et al., "Ablation of focal impulses and rotational sources: What can be learned from differing procedural outcomes?", Current Cardiovascular Risk Reports, 11(9), 27. https://doi.org/10.1007/s12170-017-0552-7. (2017).

[2] B. J. Hansen, J. Zhao, V. V. Fedorov, "Fibrosis and atrial fibrillation: computerized and optical mapping: A view into the human atria at submillimeter resolution", JACC: Clinical Electrophysiology, 3(6), 531–546. https://doi.org/10.1016/ j.jacep.2017.05.002. (2017).

[3] B. H. Smaill, J. Zhao, M. L. Trew, "Three-dimensional impulse propagation in myocardium." Circulation Research", 112(5), 834–848. https://doi.org/10.1161/ CIRCRESAHA.111.300157.

[4] Z. Xiong, V.V. Fedorov, X. Fu, E. Cheng, R. Macleod, J. Zhao, "Fully automatic left atrium segmentation from late gadolinium enhanced magnetic resonance imaging using a dual fully convolutional neural network", IEEE Transactions on Medical Imaging, 38(2), 515–524. https://doi.org/10.1109/ TMI.2018.2866845.(2018).

[5] O. Bernard, A. Lalande, C. Zotti et al. "Deep learning techniques for automatic MRI cardiac multi-structures segmentation and diagnosis: Is the problem solved?", IEEE Trans. Med. Imaging, 37 (11) (2018), pp. 2514-2525, 10.1109/TMI.2018.2837502.

[6] H. Zhang, W. Zhang, W. Shen, N. Li, Y. Chen, S. Li, et al., "Automatic segmentation of the cardiac MR images based on nested fully convolutional dense network with dilated convolution", Biomedical Signal Processing and Control, 68, Article 102684. https://doi.org/10.1016/j.bspc.2021.102684.(2021).

[7] X. Zhang, M. Noga, D. G. Martin, K. Punithakumar, "Fully automated left atrium segmentation from anatomical cine long-axis MRI sequences using deep convolutional neural network with unscented Kalman filter", Medical Image Analysis, 68. https://doi.org/10.1016/j.media.2020.101916. (2021).

[8] W. Shen, W. Xu, Z. Sun, H. Zhang, J. Ma, X. Ma, et al., "Automatic segmentation of the femur and tibia bones from X-ray images based on pure dilated residual U-Net. Inverse Problems and Imaging", 15(6), 1333–1346. https://doi.org/ 10.3934/ipi.2020057. (2020).

[9] W. Wang, Y. Wang, Y. Wu, S. Li, B. Chen, "Quantification of full left ventricular metrics via deep regression learning with contour-guidance", IEEE Access, 7, 47918–47928. https://doi.org/10.1109/ACCESS.2019.2907564. (2019).

[10] Q. Xia, Y. Yao, Z. Hu, A. Hao, "Automatic 3D atrial segmentation from GE-MRIs using volumetric fully convolutional networks, in International workshop on statistical atlases and computational models of the heart", Granada, Spain, 11395, 211–220. https://doi.org/10.1007/978-3-030-12029-0_23. (2018).

[11] C. Chen, W. Bai, D. Rueckert, "Multi-task learning for left atrial segmentation on GE-MRI, Statistical Atlases and Computational Models of the Heart", Granada, Spain, 11395, 292–301. https://doi.org/10.1007/978-3-030-12029-0_32. (2018).

[12] L. Li, X. Weng, J. A. Schnabel, X. Zhuang, "Joint left atrial segmentation and scar quantification based on a DNN with spatial encoding and shape attention, Medical Image Computing and Computer Assisted Intervention (MICCAI)", Lima, Peru, 12264, 118-127. https://doi.org/10.1007/978-3-030-59719- 1_12. (2020).

[13] L. Li, F. Wu, G. Yang, L. Xu, T. Wong, R. Mohiaddin et al., "Atrial scar quantification via multi-scale CNN in the graph-cuts framework. Medical Image Analysis", 60. https://doi.org/10.1016/j.media.2019.101595. (2020).

[14] L. Yu, S. Wang, X. Li, W. C. Fu, P. A. Heng, "Uncertainty-aware selfensembling model for semi-supervised 3D left atrium segmentation, Medical image computing and computer assisted intervention (MICCAI)", Shenzhen, China, 11765, 605- 613. https://doi.org/10.1007/978-3-030-32245-8_67. (2019).

[15] C. Li, Q. Tong, X. Liao, W. Si, Y. Sun, Q. Wang, P. A. Heng, "Attention based hierarchical aggregation network for 3D left atrial segmentation Int. Workshop Statistical Atlases and Computational Models of the Heart", Springer (2018), pp. 255-264, 10.1007/978-3-030-12029-0_28.

[16] Y. Liu, Y.Dai, C. Yan, K. Wang, "Deep learning based method for left atrial segmentation in GE-MRI Int. Workshop Statistical Atlases and Computational Models of the Heart", Springer (2018), pp. 311-318, 10.1007/978-3-030-12029-0_34.

[17] D. Borra, A. Masci, L. Esposito, A. Andalò, C. Fabbri, C. Cors, "A semantic-wise convolutional neural network approach for 3-D left atrium segmentation from late gadolinium enhanced magnetic resonance imaging", Int. Workshop Statistical Atlases and Computational Models of the Heart, Springer (2018), pp. 329-338, 10.1007/978-3-030-12029-0_36.

[18] X. Yang, N. Wang, Y. Wang, X. Wang, R. Nezafat, D. Ni, P. A. Heng, "Combating uncertainty with novel losses for automatic left atrium segmentation Int. Workshop Statistical Atlases and Computational Models of the Heart", Springer (2018), pp. 246-254, 10.48550/arXiv.1812.05807.

[19] É. Puybareau, Z. Zhao, Y. Khoudli, E. Carlinet, Y. Xu, J. Lacotte, T. Géraud, "Left atrial segmentation in a few seconds using fully convolutional network and transfer learning", Int. Workshop Statistical Atlases and Computational Models of the Heart, Springer (2018), pp. 339-347, 10.1007/978-3-030-12029-0_37.

[20] C. Bian, X. Yang, J. Ma, S. Zheng, Y. A. Liu, R. Nezafat, P. A. Heng, Y. Zheng, "Pyramid network with online hard example mining for accurate left atrium segmentation", Int. Workshop Statistical Atlases and Computational Models of the Heart, Springer (2018), pp. 237-245, 10.1007/978-3-030-12029-0_26.

[21] J. Ba, D. P. Kingma, "Adam: a method for stochastic optimization", in: International Conference on Learning Representations (ICLR), pp.1–11. 2015.

A Facile Multicomponent Synthesis and antibacterial activity of Spiro Nitrogen Heterocycles

Irum Jamil[1*], Faisal Nawaz[1]

[1]*Department of Chemistry, University of Wah, Wah Cantt, 47040, Pakistan*

[*]Corresponding author e-mail: irum.jamil@uow.edu.pk

ORCID Numbers: 0000-0002-8908-1171 (Irum Jamil), 0000-0002-8445-6683 (Faisal Nawaz)

***Abstract* -** Over the last few years, multicomponent reactions (MCRs) have gained great interest and were used to synthesize complex molecules and are highly functionalized in a single synthetic operation. MCRs are considered an inventive strategy in organic chemistry. Therefore, multicomponent reactions are part of sustainable chemistry and constitute a novel way of ideal organic synthesis. Complex structures are rapidly obtained from very simple substrates involving simple synthetic operations and safe processes in the environment. Many heterocyclic compounds are distinguished as active products pharmaceutically and are gaining consistent attention in the development of new active multifunctional drugs derivatives. Heterocyclic molecules have various clinical applications and play an active role as antitumor, antibacterial, anti-inflammatory, antiviral, and antifungal agents. Current study deals with the synthesis of Spiro Nitrogen Heterocycles using ninhydrin, o-phenylenediamine, L-proline and alpha-beta unsaturated derivatives in the presence of ethanol as solvent under reflux for 6 hours to afford the corresponding spiro indenoquinoxaline derivatives characterized through spectral analysis. High yields, simple procedure, easy workup, short reaction times are the advantages of this green methodology. The synthesized compounds were evaluated for biological activity and were found to have very good anti-bacterial activity.

Key Words: *Heterocyclic compounds, Multicomponent Reaction, Antibacterial.*

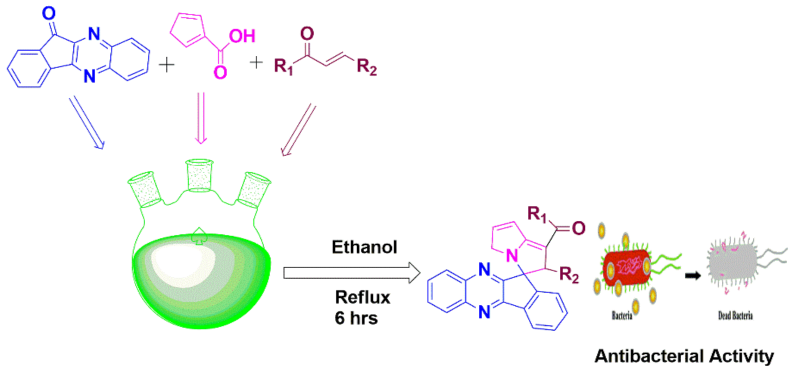

Figure 1. Graphical Representation of 3-Component Reaction via Spiro Indenoquinoxaline Pyrrolizin Methanone.

INTRODUCTION

Multicomponent reactions (MCRs) are one-pot, convergent chemical processes that use more than two starting components and retain a substantial amount of each starting element in the final product. This cutting-edge method has emerged as an effective, affordable, and environmentally friendly alternative to the traditional sequential multi-step synthesis of a variety of physiologically active pharmacophores [1]. Due to the production of several non-hydrogen atom bonds during a single synthetic transformation, MCRs have an extremely high bond-forming index (BFI), One of the distinguishing characteristics of MCRs is their rapid and empirically straightforward chemical reactions, which promote diversity-oriented synthesis (DOS) and complexity of the desired end products [2]. The production of large libraries of synthetic molecules for structure-activity relationship (SAR) investigations of drug-like compounds, a crucial component of research in the domains connected to pharmaceuticals and agrochemical [3].

Green Chemistry established the multicomponent reaction as viable method for chemists in the design, synthesis, and future development of genuinely sustainable manufacture of medicines, catalysts, or innovative materials, and food additives **(Figure 2)** [4].In order to achieve the synthesis of medicinally significant heterocyclic pharmacophores, multicomponent reactions provide a variety of environmentally friendly green reaction conditions, such as solvent and catalyst free using iodine as a catalyst for MCR using recyclable organo-catalysts synthesising imidazoles via MCR and using ionic liquids as recyclable organocatalys [5].

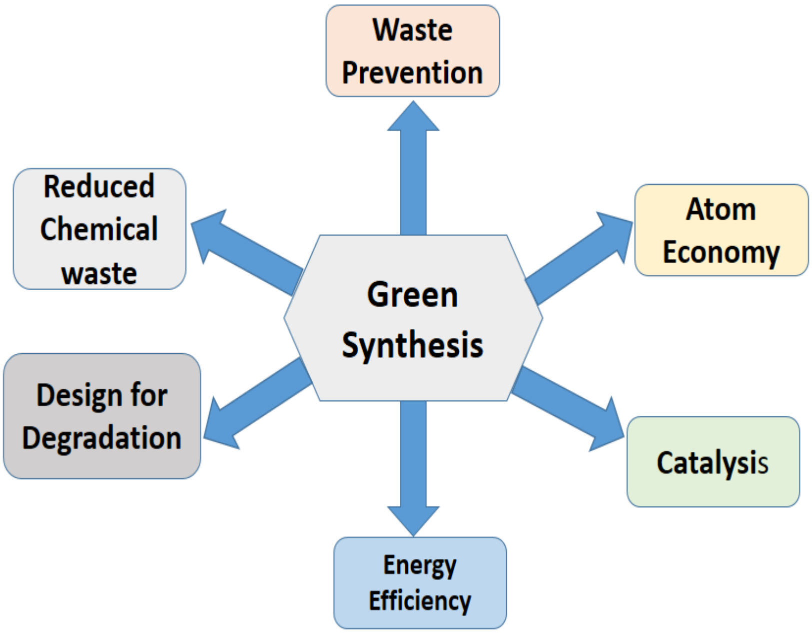

Figure 2. Different Advantages of Green Synthesis.

Since over 150 years ago, MCRs have been used in a wide range of applications and are mostly named reactions. With a variety of commercial products available on the market, MCRs have demonstrated their broad usefulness in the field of chemistry [6]. One atom is shared by two rings in spiranes or spiro compounds. Spiro-compounds are a significant class of naturally occurring chemicals with distinct biological characteristics [7]. One of the most crucial components of many naturally occurring, physiologically active substances, and medicinal molecules, are spiro molecules [8]. Due to these advantageous characteristics, scientists have given considerable consideration to developing a variety of effective synthesis techniques for this family of molecules [9]. Derivatives of indenoquinoxalines are significant families of heterocycles that include nitrogen and serve as helpful intermediates in the synthesis of organic compounds [10]. Intermolecular cycloaddition reactions of azomethine ylides have been extensively explored in recent years, and these reactions go forward with remarkable regioselectivity [11]. Consequently, with increased interest in these intricate heterocycles and a commitment to continuing our study on 1,3-dipolar cycloaddition of azomethine ylide generated from 1,2-phenylenediamine, ninhydrin and L-proline with alpha-beta unsaturated dipolarophiles [12].

EXPERIMENT

A mixture containing 11H-indeno [1, 2-b] quinoxaline 11-one (2.5 mmol), 3-(4-bromophenyl)-1-phenylprop-2-en-1-one (IJC 005) (2.5mmol) and L-proline (2.5mmol) were refluxed in ethanol for 6 hrs. Filtered, dried and recrystallized to get pure product.

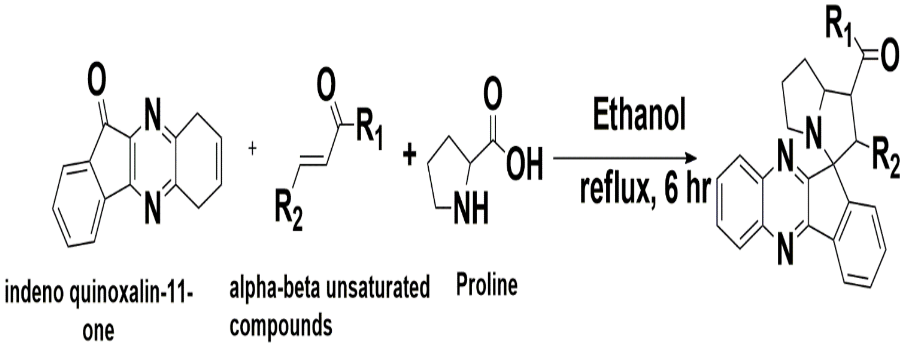

Figure 3. Schematic representation of Spiro Indenoquinoxaline Pyrrolizin

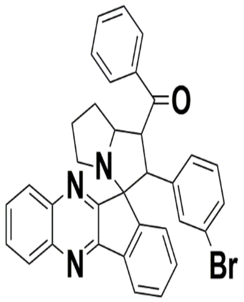

(2'-(3-bromophenyl)-1',2',5',6',7',7a'-hexahydrospiro[indeno[1,2-*b*]quinoxaline-11,3'-pyrrolizin]-1'-yl)(phenyl)methanone

Figure 4. Synthesized Compound Via Multicomponent Reaction

RESULT and DISCUSSION

The synthesized compound is Pale Yellow solid with 82% yield. IR spectra: C- N- 3325 cm-^{1}, C-H aromatic 3060 cm^{-1},C-H bend 757 cm^{-1}, C=O 1675 cm^{-1}, C-O 983 cm^{-1}, C=N 1564 cm$^{-1,}$ C-N 1247 cm^{-1}, C=C aromatic 1510 cm^{-1}, C-H stretch of CH3 2965 cm^{-1}, C-H bend of 1247 cm^{-1}. UV spectral analysis showed that almost all derivatives showed three absorption peaks in the range of 240nm, 341nm and 360nm. Mostly quinoxalines show absorption in this range. Synthesized derivatives showed great biologically activity.

Table 1. Biological Activity of Synthesized compound against *E.coli.*

		Escherichia Coli	
Compound	**1mg/ml**	**10mg/ml**	**20mg/ml**
Compound 1	5	8	10
Amoxicilin	8	9	10

From above results it was proven that the synthesized compound have great antibacterial potential.

CONCLUSION

Spiro-indenoquinoxaline analogues were synthesized using synthesized derivatives of alpha beta unsaturated compound. Ethanol has proven to be a suitable solvent for all the reactions pertaining to better yield and shorter reaction time.

ACKNOWLEDGEMENT.

Authors are grateful to university of Wah, Wah Cantt for Providing Lab facilities.

REFERENCES

[1] Patil, P. (2012). *From isocyanide based multicomponent reactions to heterocyclic synthesis* (Doctoral dissertation).

[2] Malinakova, H. C. (2019). Multicomponent Reaction Sequences Using Palladacyclic Complexes. In *Palladacycles* (pp. 263-295). Elsevier.

[3] Tamimi, M., Heravi, M. M., Mirzaei, M., Zadsirjan, V., Lotfian, N., & Eshtiagh-Hosseini, H. (2019). Ag3 [PMo12O40]: An efficient and green catalyst for the synthesis of highly functionalized pyran-annulated heterocycles via multicomponent reaction. *Applied Organometallic Chemistry*, *33*(9), e5043.

[4] Estevez, V., Villacampa, M., & Menendez, J. C. (2010). Multicomponent reactions for the synthesis of pyrroles. *Chemical Society Reviews*, *39*(11), 4402-4421.

[5] Zadmard, R., Akbarzadeh, A., & Jalali, M. R. (2019). Highly functionalized calix [4] arenes via multicomponent reactions: synthesis and recognition properties. *RSC advances*, *9*(34), 19596-19605.

[6] Zarganes-Tzitzikas, T., Chandgude, A. L., & Dömling, A. (2015). Multicomponent reactions, union of MCRs and beyond. *The Chemical Record*, *15*(5), 981-996.

[7] Zhu, J., & Bienaymé, H. (Eds.). (2006). *Multicomponent reactions*. John Wiley & Sons.

[8] Abdelraheem, E. M., Shaabani, S., & Dömling, A. (2018). Macrocycles: MCR synthesis and applications in drug discovery. *Drug Discovery Today: Technologies*, *29*, 11-17.

[9] Kouznetsov, V. V., & Galvis, C. E. P. (2018). Strecker reaction and α-amino nitriles: recent advances in their chemistry, synthesis, and biological properties. *Tetrahedron*, *74*(8), 773-810.

[10] Ramesh, S., Sivakumar, K., Panja, C., Arunachalam, P. N., & Lalitha, A. (2010). Water-Mediated Strecker Reaction: An Efficient and Environmentally Friendly Approach for the Synthesis of α-Aminonitriles via a Three-Component Condensation. *Synthetic Communications®*, *40*(23), 3544-3551.

[11] Debache, A., Ghalem, W., Boulcina, R., Belfaitah, A., Rhouati, S., & Carboni, B. (2009). An efficient one-step synthesis of 1, 4-dihydropyridines via a triphenylphosphine-catalyzed three-component Hantzsch reaction under mild conditions. *Tetrahedron Letters*, *50*(37), 5248-5250.

[12] Allochio Filho, J. F., Lemos, B. C., de Souza, A. S., Pinheiro, S., & Greco, S. J. (2017). Multicomponent Mannich reactions: General aspects, methodologies and applications. *Tetrahedron*, *73*(50), 6977-7004.

Synthesis, Spectral Study and Comparative Pharmacological Assessment of Silver(I) Complexes Based on Electron Donor Ligands

Bushra Shakoor[1*], Faiza Asghar[1] and Faisal Nawaz[1]

[1] *University of Wah, Quaid Avenue, Wah Cantt 47040, Punjab, Pakistan*

* Corresponding author e-mail address: bushra.shakoor@uow.edu.pk

ORCID Numbers: 0000-0002-6704-6981 (Bushra1.Shakoor1), 0000-0001-5197-8218 (Faiza2.Asghar2), 0000-0002-8445-6683 (Faisal3.Nawaz3)

Abstract—An important reagent in the synthesis of numerous heterocyclic compounds is an O and S-containing compound that is thiourea is employed as a source of sulphides. The presence of O and S donor atoms open up a wide range of bonding options, enabling them to function as versatile ligands, and makes it possible for them to form stable complexes. In order to synthesize effective antibacterial and antifungal compounds, this research sought to prepare transition metal complexes of acyl derivatives with oxygen and sulphur donor atoms. The interaction between isothiocyanate and substituted amine produced a S donor ligand. These monodentate ligands' metal complexes were synthesized through a reaction between the metal salt and the ligands. Silver based thioureas such as: 1-(3,4-dichlorobenzoyl)-3-(4-fluorophenyl) and 1-(3,4-dibromobenzoyl)-3-(4-nitrophenyl) thioureas show a wide spectrum of biological applications. Acyl derivatives and its complexes were structurally analyzed by Fourier transform infrared spectroscopy and elemental analysis. Biological activities were analyzed by preparing various culture media.

Keywords—*Acyl derivative, FT-IR, elemental analysis, antibacterial activity, antifungal activity*

INTRODUCTION

Since a very long time [1, 2], thiourea derivatives have been used as organocatalysts and as starting precursors in numerous chemical compounds with important therapeutic applications [3]. A survey of the literature finds numerous studies describing the synthesis and characterization of metal complexes stabilized by thiourea derivatives, particularly Zn, Cd, and Hg [4-6]. These metals have an abundance of electrons, and their complexes exhibit exceptional non-linear optical characteristics [7-9]. Unsymmetrical thiourea compounds also have beneficial biological properties as antifungal and antibacterial agents [10]. Group 12 metals are soft among metal ions, and compounds made from thiourea derivatives should be thermally stable. Ag and its compounds are known for antibacterial and antifungal properties [11-16]. The metal is active at low concentrations that is its greatest advantage over other medicinally relevant metals [17-18]. High concentration of a metal is toxic to the living organisms as it happens by the displacement of essential metal atoms from their original binding sites.

To lower the time factor, newer methodologies exploit improved selectivity of metal-organic complexes (for example, the silver-thiourea approach) as a one-step procedure [19-20]. One reason some metals, including copper, are necessary components of biological systems is because of their redox characteristics [21]. Generally speaking, non-essential metals bind to sulfur-containing groups and oxygen sites more readily than do essential metals. Some of its compounds showed excellent antibacterial potentials [22]. Here, we have synthesized the 1-(3,4-dichlorobenzoyl)-3-(4-fluorophenyl) and 1-(3,4-dibromobenzoyl)-3-(4-nitrophenyl) thioureas and reported their structures. Their complexes with Ag(I) in 1:2 ratios have also been prepared.

METHODOLOGY

Specific Temperature conditions were used to conduct experiment. 3,4-dichlorobenzoyl chloride, 4-nitroaniline, 3,4-dibromobenzoyl chloride, 4-fluoroaniline, Potassium thiocyanate, Acetone, Methanol and silver acetate was purchased from Sigma-Aldrich / Merck and was used as purchased. Kofler melting point apparatus for temperature determination, BRUKER FT-IR Spectrophotometer for FT-IR analysis and for percentage calculations of different elements in the prepared compounds elemental analysis was done.

A. General protocol to prepare thiourea ligand (L)

(0.010 mol) solution of benzoyl chloride was mixed in the solution of (0.010 mol) KSCN in dry acetone. Resulted mixture was stirred for 2 hours. After that, (0.010 mol) solution of aniline was mixed in the above solution and continued stirring for next 48 hours. Formed product was filtered and dried. General protocol to prepare such ligands has been shown in figure 1 and substitutions to prepare thiourea ligands has been given in table1.

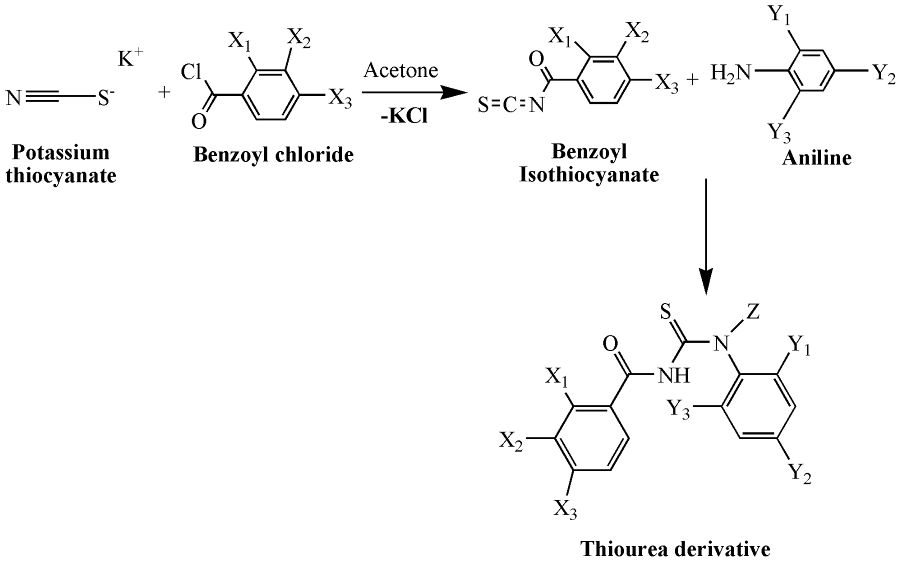

Fig. 1.General protocol to prepare thiourea ligands.

TABLE I. SUBSTITUTIONS TO PREPARE THIOUREA LIGANDS (L_1-L_2)

LIGAND CODE	**X_1**	**X_2**	**X_3**	**Y_1**	**Y_2**	**Y_3**	**Z**
(GENERAL)	H	H	H	H	H	H	H
L_1	H	Cl	Cl	H	F	H	H
L_2	H	Br	Br	H	NO_2	H	H

B. Synthesis of 1-(3,4-dichlorobenzoyl)-3-(4-fluorophenyl) thiourea (L_1)

Quantities used were (0.02 molar, 2 g) dried potassium thiocyanate, (80 mL) anhydrous acetone, (0.02 mol, 4.18 g) 3,4-dichlorobenzoyl chloride, (0.02 mol, 2.22 g) 4-fluoroaniline, Yield (%) 71; Color Mustard; m.p 170 ^{0}C; FT-IR (powder, cm^{-1}): 3166 (N-H), 2822 (C-H$_{aromatic}$), 2754 (C-H$_{aliphatic}$), 1650 (C=O), 1485 (C=C), 1282 (C=S), Elemental Anal. Calcd (%) for $C_{14}H_9Cl_2FN_2OS$: C, 48.99; H, 2.64; N, 8.16; S, 9.34. Found (%): C, 49.12; H, 2.51; N, 8.20; S, 9.43.

C. Synthesis of 1-(3,4-dibromobenzoyl)-3-(4-nitrophenyl) thiourea (L_2)

Quantities used were (0.02 molar, 2 g) dried potassium thiocyanate, (80 mL) anhydrous acetone, (0.02 mol, 5.96 g) 3,4-dibromobenzoyl chloride, (0.02 mol, 2.76 g) 4-nitroaniline, Yield (%) 74; Color Grape; m.p 104 ^{0}C; FT-IR (powder, cm^{-1}): 3383 (N-H), 3131 (C-H$_{\text{aromatic}}$), 3016 (C-H$_{\text{aliphatic}}$), 1652 (C=O), 1494 (C=C), 1284 (C=S), Elemental Anal. Calcd (%) for $C_{14}H_9Br_2N_3O_3S$: C, 36.62; H, 1.98; N, 9.15; S, 6.98. Found (%): C, 36.51; H, 2.13; N, 9.20; S, 7.06.

D. General protocol to prepare thiourea metal complex

(0.001 mol) metal salt solution in methanol was added dropwise into the solution of corresponding acyl thiourea (0.002 mol) dissolved in 30 mL methanol in 1:2 ratios at approx 50-60 ^{0}C. The resulting solution was stirred for 24 hours. Formed product was filtered, dried and recrystallized.

E. Synthesis of Bis(1-(3,4-dichlorobenzoyl)-3-(4-fluorophenyl) thioureato) Ag(I) (C_1)

Quantities used were (0.002 mol, 0.686 g) 1-(3,4-dichlorobenzoyl)-3-(4-fluorophenyl) thiourea, (0.0013 mol, 0.167 g) silver acetate, (40 mL) methanol, Yield (%) 75; Color Brown; m.p 231 ^{0}C; FT-IR (powder, cm^{-1}): 3143 (N-H), 2801 (C-H$_{\text{aromatic}}$), 2747 (C-H$_{\text{aliphatic}}$), 1642 (C=O), 1479 (C=C), 1271 (C=S), Elemental Anal. Calcd (%) for $C_{28}H_{18}AgCl_4F_2N_4O_2S_2$: C, 42.34; H, 2.28; Ag, 13.58; N, 7.05; S, 8.07. Found (%): C, 42.15; H, 2.11; Ag, 13.62; N, 7.10; S, 8.03.

F. Synthesis of Bis(1-(3,4-dibromobenzoyl)-3-(4-nitrophenyl) thioureato) Ag(I) (C_2)

Quantities used were (0.002 mol, 0.918 g) 1-(3,4-dibromobenzoyl)-3-(4-nitrophenyl) thiourea, (0.001 mol, 0.167 g) silver acetate, (40 mL) methanol, Yield (%) 69; Color Orange; m.p 136 ^{0}C; FT-IR (powder, cm^{-1}): 3093 (N-H), 3126 (C-H$_{\text{aromatic}}$), 2998 (C-H$_{\text{aliphatic}}$), 1645 (C=O), 1487 (C=C), 1269 (C=S), Elemental Anal. Calcd (%) for $C_{28}H_{18}AgBr_4N_6O_6S_2$: C, 32.77; H, 1.77; Ag, 10.51; N, 8.19; S, 6.25. Found (%): C, 32.80; H, 1.75; Ag, 10.47; N, 8.23; S, 6.19.

BIOLOGICAL ACTIVITY

A. *Antifungal Activity*

Prepared thiourea ligands and its metal complexes were applied on different fungicides like *Aspergillus fumigates*, and *Aspergillus flavus* to check their fungicidal activity. To check activity test sample (2 mg) of each was dissolved in $(CH_3)_2SO$ separately. To prepare culture media sabouraud dextrose agar (6 g) was mixed in distilled H_2O (80 mL) with 5.6 pH value. 10 mL of above solution was taken in test tube plugged with cotton kept in autoclave at 121 ^{0}C for 20 minutes. Then tubes were cooled and 70 µL solution of test sample was added in it. Tubes were placed in oblique position for coagulation. Slants of test tubes were set for each fungal strain. Tubes containing solidified medium with test sample was injected with 5 mm width diameter of inoculumns resulted from 7 days old culture media. To test each sample, one test tube was setup used as a +ve control. Slants having no test sample was used as a –ve control. Tubes were refluxed at 28 ^{0}C for 7 days and linear length was measured for determining fungus reproduction. With reference to control inhibition of fungal growth was calculated.

Following formula was used to calculate fungal growth inhibition:

$$\text{Fungal growth inhibition} = \frac{\text{Linear growth in test(cm)}}{\text{Linear growth in control (cm)}} \text{ X } 100$$

B. *Antibacterial Activity*

Prepared thiourea ligands and its metal complexes were applied on different bacterial strains like *Enterobacter aerogenes*, *Salmonella typhimurium*, and *Micrococcus luteus*. Initially bacterial strains were cultured in nutrient for 18 hours and standardized to 0.5 McFarland turbidity scale. 2.3 g nutrient agar (MERCK) in 100 mL distilled H_2O was dissolved at 7 pH value to prepare medium, placed in autoclave and down its temperature to 45 ^{0}C and then sowed. 75 mL seeded nutrient medium was used to prepare triplicates and allowed to solidify. To bore wells into agar sterile cork borer having diameter 6 mm was used. Test sample (100 µL) was injected into wells at room temperature and kept for 2 hours at 37 ^{0}C. After plates incubation zone's diameter was determined and observed effects was compared with +ve control (penicillin). % Inhibition of test sample was calculated relative to +ve control by following formula.

Relative % inhibition of test compound = 100-(x-y) (z-y)

X= total area of inhibition of test sample   Z= total area of inhibition of solvent

RESULT AND DISCUSSION

Chloro group of acid halide is substituted by thiocyanate group of KSCN. The thiocyanate rearranges itself resulting in the formation of isothiocyanates. H^+ from aniline shifted to N of isothiocyanates forming respective thiourea.

A. *Solubility data of thioureas and Ag complexes*

Solubility of each ligand and its complex was checked in different solvents as presented in table 2. Prepared compounds are soluble in polar solvents but insoluble in non-polar solvents.

TABLE II. SOLUBILITY DATA OF THIOUREAS AND METAL COMPLEXES IN DIFFERENT SOLVENTS

CODE	Methane	Benzene	Diethyl ether	Dichloro methane	Tetrahydrofuran	n-hexane
L_1	Soluble	Insoluble	Insoluble	Soluble	Soluble	Insoluble
L_2	Soluble	Insoluble	Insoluble	Soluble	Soluble	Insoluble
C_1	Soluble	Insoluble	Insoluble	Soluble	Soluble	Insoluble
C_2	Soluble	Insoluble	Insoluble	Soluble	Soluble	Insoluble

B. *Physical data of thioureas and Ag complexes*

Physical data such as molecular mass, melting point, colour and percentage yield of all the prepared compounds were calculated and determined as given in table 3.

TABLE III. PHYSICAL DATA OF THIOUREAS AND METAL COMPLEXES

CODE	Formula	Mol. mass (g/mol)	M.P (^{0}C)	Color	Yield (%)
L_1	$C_{14}H_9Cl_2FN_2OS$	343	170	Mustard	71
L_2	$C_{14}H_9Br_2N_3O_3S$	459	104	Grape	74
C_1	$C_{28}H_{18}AgCl_4F_2N_4O_2S_2$	794	231	Brown	75
C_2	$C_{28}H_{18}AgBr_4N_6O_6S_2$	1026	136	Orange	69

CHARACTERIZATION TECHNIQUES

Synthesized thiourea ligands and silver complexes were characterized by Elemental analysis, and FT-IR spectroscopy.

A. *Elemental Analysis*

Calculated values of C, H, N, S, and Ag were very close to obtained values that confirms the completion and formation of desired product as shown in table 4 for ligands and table 5 for metal complexes. Results obtained also verify1:2 ratios metal ligands coordination in complexes (C).

TABLE IV. ELEMENTAL ANALYSIS DATA OF LIGANDS (L_1-L_2)

LIGANDS (L_1-L_2)	**Calculated Values (%)**				**Observed Values (%)**			
	C	**H**	**N**	**S**	**C**	**H**	**N**	**S**
$C_{14}H_9Cl_2FN_2OS$	48.99	2.64	8.16	9.34	49.12	2.51	8.20	9.43
$C_{14}H_9Br_2N_3O_3S$	36.62	1.98	9.15	6.98	36.51	2.13	9.20	7.06

TABLE V. ELEMENTAL ANALYSIS DATA OF THIOUREA COMPLEXES (C_1-C_2)

COMPLEXES (C_1-C_2)	**Calculated Values (%)**					**Observed Values (%)**				
	C	**N**	**S**	**Ag**	**H**	**C**	**N**	**S**	**Ag**	**H**
$C_{28}H_{18}AgCl_4F_2N_4O_2S_2$	42.34	7.05	8.07	13.58	2.28	42.15	7.10	8.03	13.62	2.11
$C_{28}H_{18}AgBr_4N_6O_6S_2$	32.77	8.19	6.25	10.51	1.77	32.80	8.23	6.19	10.47	1.75

B. *FT-IR Spectroscopic Study*

FT-IR spectrum was analyzed between 4000-400 cm^{-1}. Frequencies (stretching and bending) of certain bonds observed in prepared thiourea ligands and its silver complexes are presented in the table 6.

C. *FT-IR result of thiourea ligands and Silver complexes*

TABLE VI. FT-IR RESULT OF THIOUREA LIGANDS AND SILVER COMPLEXES

CODE	**N-H PEAK**	**C-H (AROMATIC)**	**C-H (ALIPHATIC)**	**C=O**	**C=C**	**C=S**
L_1	3166	2822	2754	1650	1485	1282
L_2	3383	3131	3016	1652	1494	1284
C_1	3143	2801	2747	1642	1479	1271
C_2	3093	3126	2998	1645	1487	1269

Different peaks such as N-H, C=O and C=S of thioureas were compared with their silver complexes. FT-IR spectrum of ligand 1 and 2 show N-H peak appear at 3160 cm^{-1} and 3387 cm^{-1} respectively. For C=O peaks appear between 1645-1655 cm^{-1} and for C=S peaks appear between 1278-1286 cm^{-1}. Thiourea is monodentate ligand so coordinates with silver ion *via* sulfur atom and because of these complexation of sulfur of thiourea with metal cation certain peaks will shift that indicates formation of thiourea complex. The C=O peak in complexes shifts to lower value due to weak interaction of oxygen with Ag^+ and results in stability. The C=S peak in complex also shifts to lower value that indicates complexation of thiourea with silver ion *via* sulfur atom. The peak shift confirms the synthesis of complex. For thioureas N-H peak appears between 3166-3383 cm^{-1}, C=O peaks appear between 1650-1652 cm^{-1} and C=S appears between 1282-1284 cm^{-1}. However, for complexes N-H peaks appear between 3137-

3085 cm^{-1}, C=O peaks appear between 1638-1650 cm^{-1} and C=S peaks appear between 1265-1275 cm^{-1}.

BIOLOGICAL SCREENING

Thiourea ligands and their Ag(I) complexes were compared for their biological activity. In order to do this, penicillin was used as +ve and $(CH_3)_2SO$ as –ve control. Values lies from medium to good activity for each strains. Comparison shows that presence of metal enhances the antimicrobial activity of complexes as compared to ligands. Upon complexation polarity of metal centre decreases and lipophilicity of metal centre increases results the penetration of complexes into lipid bilayer membrane of microorganisms. The results showed that 1-(3,4-dibromobenzoyl)-3-(4-nitrophenyl) thiourea Ag(I) complex has efficient antibacterial activity due to the presence electron donating bromide groups that increases the lipophilicity of metal centre and hence enhances its antimicrobial activity. Results of antibacterial and antifungal activity are presented in table 7 and 8 respectively.

TABLE VII. ANTIBACTERIAL DATA OF SYNTHESIZED COMPOUNDS AND STANDARD DRUG

CODE	***Salmonella Typhimurium***	***Micrococcus Luteus***	***Enterobacter Aerogenes***
L_1	12.9 ± 0.33[a]	11.5 ± 0.58	08.3 ± 0.60
L_2	16.3 ± 0.33	18.1 ± 0.33	15.2 ± 0.63
C_1	15.1 ± 0.58	13.6 ± 0.58	11.8 ± 0.33
C_2	18.7 ± 0.33	20.1 ± 0.60	15.8 ± 0.63
PC	26.3 ± 0.33	27.3 ± 0.33	20.3 ± 0.67

PC= Penicillin (1mg/mL) Penicillin (Terbinafine) was used as standard drug for +ve control and DMSO was used for -ve control.

[a] Zone of inhibition = mm

TABLE VIII. ANTIFUNGAL DATA OF SYNTHESIZED COMPOUNDS AND STANDARD DRUG

CODE	***Aspergillus Fumigates***		***Aspergillus Flavus***	
L_1	5.70 ± 0.03[a]	38[b]	5.03 ± 0.09	42
L_2	5.32 ± 0.33	45	4.32 ± 0.33	49
C_1	4.31 ± 0.70	47	4.21 ± 0.09	52
C_2	4.49 ± 0.57	53	2.90 ± 0.07	60
TERBINAFINE	0.89 ±0.03	92	0.83 ±0.01	92

As standard drug Terbinafine was used as +ve and DMSO as -ve control.

[a] Fungal growth = mm

[b] Zone of inhibition = %

CONCLUSION

Two new 1-(3,4-dichlorobenzoyl)-3-(4-fluorophenyl) and 1-(3,4-dibromobenzoyl)-3-(4-nitrophenyl) thiourea ligands and their Ag(I) complexes have been prepared during this research. The ligand and its complexes were then characterized by FT-IR. The ligands and complexes are in good yield and stable in air. In these complexes benzoyl thiourea acts as monodentate ligand coordinating with silver metal *via* S atom and exhibit linear geometry of silver. Biocidal activities were investigated which indicate complexes show greater activity than that of their organic ligands.

ACKNOWLEDGEMENT

All praise is to Allah (S.W.T), we thank Him, beg His assistance, and beg His pardon. I want to sincerely thank my supervisor, Dr. Faiza Asghar, for her great advice and patience throughout this research work. I couldn't have successfully completed my dissertation without her assistance.

REFERENCES

[1] P. R. Schreiner, “Metal-free organocatalysis through explicit hydrogen bonding interactions,” Chem soc. Rev. vol. 32(5), pp. 289-296, June 2003.

[2] I. T. Raheem, and E. N. Jacobsen, “Highly enantioselective aza-baylisehillman reactions catalyzed by chiral thiourea derivatives,” Adv. Synth. Catal. vol. 347(11-13), pp. 1701-1708, October 2005.

[3] C. H. Perry, Q. H. Charles, F. L. Richard, R. M. James, O. W. Leland, and P. W. Jeffery, “An efficient acylation/base-catalyzed cyclization of thioureas affords N, N_0-disubstituted thiobarbituric acids,” Tetrahedron Lett. vol. 42(9), pp. 1607-1610, February 2001.

[4] G. Marcotrigiano, “Preparation, infrared, Raman and NMR spectra of N, N_0–Diethylthiourea complexes with zinc (II), cadmium (II) and mercury (II) halides,” Z. Anorg. Allg. Chem. vol. 422(1), pp. 80-88, April 1976.

[5] J. M. Alia, H. G. M. Edwards, and M. D. Stoey, “A systematic FT-Raman spectroscopic study of twelve bis-thiourea complexes, A (tu) 2B2 (A1/4 Zn, Cd, Hg; B1/4 C1, Br, I, SCN),” Spectrochim. Acta Mol. Biomol. Spectrosc. vol. 55(12), pp. 2423-2435, October 1999.

[6] A. A. Isab, and M. 1. Wazeer, “Complexation of Zn (II), Cd (II) and Hg (II) with thiourea and selenourea: a 1H, 13C, 15N, 77Se and 113Cd solution and solid-state NMR study,” J. Coord. Chem. vol. 58(6), pp. 529-537, October 2005.

[7] M. P. Mohamed, P. Javaprakash, and M. L. Caroline, “Growth and characterization of chloro bis thiourea mercury (II) chloride (CBTMC) grown by slow evaporation technique for nonlinear optical applications, in: Recent Trends in Materials Science and Applications,” Springer. pp. 521-534, May 2017.

[8] G. T. C. Sabari, S. Dhanukskodi, D. Mangalaraj, and J. Phillip, “Synthesis growth and characterization of bisthiourea zinc bromide for optical limiting applications,” Curr. Appl. Phys. vol. 11(3), pp. 838-843, May 2011.

[9] T. S. Girisum, and S. Dhanukskodi, “Tuning the dielectric properties of thiourea analog crystals for efficient nonlinear optical applications,” Mater. Res. Bull. vol. 45(1), pp. 88-91, January 2010.

[10] S. M. Jambi, “Cd (II), Hg (II) and Pt (II) complexes of 1-ethy1-3-(4- methylthiazol2-yl) thiourea: synthesis, X-ray crystal structure, DFT studies, antimicrobial and antioxidant applications,” J. Mol. Liq. vol. 262, pp. 237-247, January 2018.

[11] D. S. Mohamed, R. M. Abd El-Baky, T. Sandle, S. A. Mandour, and E. F. Ahmed, “Antimicrobial activity of silver-treated bacteria against other multi-drug resistant pathogens in their environment,” Antibiotics. vol. 9(4), pp.181-194, April 2020.

[12] S. Chen, G. Wu, and H. Zeng, “Preparation of high antimicrobial activity thiourea Chitosan-Ag+ complex,” Carbohydrate Polymers. vol. 60(1), pp. 33-38, April 2005.

[13] S. Medici, M. Peana, G. Crisponi, V. M. Nurchi, J. I. Lachowicz, M. Remelli, and M. A. Zoroddu, “Silver coordination compounds: A new horizon in medicine,” Coord. Chem. Rev. vol. 327-328, pp. 349-359, November 2016.

[14] H. J. Klasen, “A historical review of the use of silver in the treatment of burns. II. Renewed interest for silver,” Elsevier. vol. 26, pp. 131-138, March 2016.

[15] M. I. Azocar, G. Gomez, P. Levin, M. Paez, H. Munoz, and N. Dinamarca, “Review: Antibacterial behaviour of carboxylate silver(I) complexes,” J. Coord. Chem. vol. 67, pp. 3840-3853, October 2014.

[16] Seerat-ur-Rehman, M. A. Choudhary, S. Ahmad, M. Aslam, M. Saleem, M. F. Tahir, and A.

A. Isab, “Synthesis, crystal structure and antimicrobial activities of a dinuclear silver(I) complex of bis(diphenylphosphano)methane and thiourea,” Zeitschrift Fur Naturforschung B. vol. 76, pp. 745-750, September 2019.

[17] R. Chhabra, J. Pleysier, and A. Cremers, “The measurement of the cation exchange capacity and exchangeable cations in soils: a new method,” Proc. Int. Clay Conf. pp. 439-449, May 1975.

[18] R. Dohrmann, “Cation exchange capacity methodology II: A modified silver-thiourea method,” Applied Clay Science. vol. 34(1-4), pp. 38-46, October 2006.

[19] M. M. Eatock, A. Schatzlein, and S. B. Kaye, “Tumour vasculature as a target for anticancer therapy,” Elsevier. vol. 26, pp. 191-204, June 2000.

[20] W. K. Hsien, F. C. Su, C. W. Chin, R. C. Dar, and H. L. Jau, “Serum and tissue trace elements in patience with breast cancer in Taiwan,” Biol. Trace Elem. Res. vol. 89(1), pp. 1-11, October 2002.

[21] J. M. Ehud, G. S. Joseph, and C. Mordechai, “Copper and Zinc in normal and malignant tissues,” Cancer. vol. 52, pp. 868-872, September 1983.

[22] F. U. Rahman, M. Bibi, A. A. Altaf, M. N. Tahir, F. Ullah, Zia-Ur-Rehamn, and E. Khan, “Zn, Cd and Hg complexes with unsymmetric thiourea derivatives; synthesis, free radical scavenging and enzyme inhibition essay,” Journal of Molecular Structure. vol. 1211(5), pp. 1-33, July 2020.

Quality control of radiation dose estimation by using treatment plans on three dimensional phantom

Nihal Büyükçizmeci[1*] and Kevser Sözen[2]

[1]*Department of Physics, Science of Faculty, Selcuk University, Konya, Türkiye.*
[2]*The Graduate School of Selcuk University, Institute of Science, 42130, Konya, Türkiye.*

* Corresponding author e-mail address: nihal@selcuk.edu.tr, kevser07@gmail.com

ORCID Numbers: 0000-0002-6030-9574 (Nihal,Büyükçizmeci), 0009-0005-9561-4674 (Kevser Sözen)

Abstract**—** Nowadays, CyberKnife® radiosurgery systems are commonly used in treatment plan. Herein, we have investigated this application by comparing the irradiation of all metastases at once and the protocols of irradiation of metastases separately in multiple brain metastases. We have used new the three-dimensional (3d) head phantom; multiple brain metastases were determined over the spaces where the luminescence (OSL) dosimeters with BeO were placed. Computed tomography (CT) images of the head phantom were taken, tumors and 3 critical organs were drawn (contouring) on the image. In the treatment planning system, the dose was written, and irradiation plans were created to be done separately with a single irradiation. As a conclusion, a single plan was more reliable in terms of duration.

Keywords**—** *Cyberknife System, Multiple brain metastases, Treatment time*

INTRODUCTION

Treating brain cancer, including primary and metastatic brain tumours, is one of the most challenging areas in oncology. One of the difficulties encountered is the anatomical localization of the tumour, and the other is the presence of multidrug resistance. Brain metastases, due to differences in drug sensitivity between primary and metastatic tumours, often exhibit a weak response to chemotherapy [1]. Therefore, whole-brain radiation therapy (WBRT) has been commonly used as the primary treatment for brain metastases, which involve the spread of cancer from other parts of the body to the brain. With advancements in surgical techniques, radiosurgical treatments, and systemic therapies, multidisciplinary and multimodality approaches are increasingly being utilized in the management of brain metastases [2]. In recent years, stereotactic radiosurgery (SRS) has become a standard treatment option for patients with a limited number of brain metastases and has shown effectiveness in cases with four or more brain metastases [3]. Ongoing research aims to determine the most effective approach for using CyberKnife® in the treatment of multiple brain metastases. The purpose of this study is to compare the outcomes of individually fractionated and single-session treatment radiation plans for multiple brain metastases using the CyberKnife® device in terms of duration of care.

MATERIAL METHODS

The CyberKnife® system (Accuray Inc., Sunnyvale, Calif., USA), developed at Stanford in the 1990s, consists of a 6 MV linear accelerator mounted on an industrial robot (Kuka, Augsburg, Germany), without a flattening filter. The patient bed can be either conventional or robotic. In the treatment room, there is a ceiling-mounted X-ray imaging system with two cameras directed obliquely towards amorphous silicon detectors integrated into the floor. This imaging system allows for near real-time determination of the patient's position using live images and is used to correct patient motion during treatment. Thus, active image guidance is performed during the delivery of treatment. Typically, the system performs imaging every 3-5 beams or every 20-60 seconds depending on the patient's condition [4, 5].

In this study, the comparison of treatment durations for individually fractionated and single-session radiation of multiple brain metastases is conducted using the CyberKnife® treatment device (Figure 1). A 128-slice GE Revolution Evo Model CT scanner located at Medicana International Ankara Hospital was used to obtain computed tomography (CT) scans with a newly produced thermoplastic mask placed on a phantom (Figure 2a and 2b). The acquired CT data was then transferred to the multi-plan treatment planning system. Contouring of each metastasis and critical organ was performed. Treatment plans were created using 6 MV photon beams with a 10 mm collimator, delivering a dose of 100 cGy to the target. The tumor locations in the phantom consisting of 20 slices are as follows: Tumor 1 at the 4th slice, Tumor 2 at the 6th slice, Tumor 3 and Tumor 4 at the 7th slice, Tumor 5 at the 8th slice, and Tumor 6 at the 15th slice. Dose Volume Histogram (DVH) graph of the 2rd metastasis tumor in a single treatment plan is demonstrated in Figure 3.

Figure 1. CyberKnife® Device

Figure 2. a) Phantom produced by a 3D printer b) Placing a thermoplastic mask on the phantom produced by a 3D printer.

	VOI, Objective
1	TOPLAM, OMI
2	TOPLAM, OCO

Dose Calculation
Algorithm: Ray-Tracing
Resolution: High
Uncertainty %: 0

Patient
HU1 Fantom Selcuk Tez
HU1
Plan
TOPLAM_1Gy
06 Feb 2022, 04:58:38 PM
Rx
76%, 100.00 cGy

Selected DVH: Tumor 2

Nodes	123	Total MU	3191.81
Beams	520	Min MU	1.00
Max Dose (cGy)	131.58	Max MU	35.79

Estimated Treatment Time Per Fraction (minutes) 70

	Name	Min (cGy)	Mean (cGy)	Max (cGy)	CI	nCI	HI	Coverage (%)
🟨	TOPLAM	86.96	114.83	131.58	1.21	1.26	1.32	95.84
🟥	Tumor 1	92.09	115.47	130.64	6.97	7.10	1.32	98.19
🟪	Tumor 2	91.25	114.98	129.79	6.41	6.68	1.32	95.93
🟪	Tumor 3	90.71	115.40	131.48	7.59	7.82	1.32	97.08
🟦	Tumor 4	92.48	114.58	130.74	7.40	7.81	1.32	94.80
🟦	Tumor 5	90.60	115.25	131.58	8.15	8.47	1.32	96.33
🟦	Tumor 6	86.96	113.37	129.50	7.26	7.82	1.32	92.87
🟦	Critical 1	3.25	7.14	16.14	n/a	n/a	n/a	n/a
⬜	Critical 2	16.30	26.69	32.27	n/a	n/a	n/a	n/a
🟪	Critical 3	19.12	42.43	101.60	n/a	n/a	n/a	n/a
🟩	Skin	0.87	8.92	131.58	n/a	n/a	n/a	n/a

X:275 Y:300 Z:221 Value:1111

Figure 3. DVH graph of the 2rd metastasis tumor in a single treatment plan (obtained from the Multiplan treatment planning system).

Table 1. Total duration comparisons of single and separately made plans.

Plan Name	Approximate Treatment Time (min.)
Tumor-1	18 minute
Tumor-2	20 minute
Tumor-3	19 minute
Tumor-4	16 minute
Tumor-5	18 minute
Tumor-6	19 minute
One Plan	70 minute
Individual plan total	110 minute

In our study, the durations for planning 6 brain metastases in the head phantom were calculated by the Multiplan treatment planning system and presented in Table 1. While separate treatment plans were created for each tumor, the irradiation time ranged from 16 to 20 minutes. The average total irradiation time was 110 minutes. In contrast, when a single treatment plan was used, the average irradiation time was 70 minutes. The comparison of average durations revealed that separate planning required an additional 40 minutes of irradiation time compared to a single plan.

RESULTS

The choice of treatment approach depends on various factors such as tumor characteristics, patient preferences (condition), and the overall clinical context. In our study, the use of a single plan for irradiating multiple brain metastases was considered more advantageous in terms of treatment duration compared to separate planning. The ability to complete the treatment in a shorter time allows the patient to return to normal life more quickly. However, it should be taken into consideration that separate irradiation may result in less exposure of healthy tissues.

ACKNOWLEDGEMENT

The authors thank Dr. Hasan Uysal, Dr. Kaan Oysul (Ankara Medicana Hospital), Mehmet Fazıl Enkavi, Eng. İsmail Burak Korkut (PHYSMART Medical) for their collaboration. This research was supported by the Selçuk University, Research project BAP (21111004).

REFERENCES

[1] Regina, A., et al., Multidrug resistance in brain tumors: Roles of the blood–brain barrier. Cancer Metastasis Rev., 2001. **20**: p. 13-25.

[2] Chung, C., M. Tsao, and S. Lutz, Conventional radiation therapy for brain metastases. Journal of Radiation Oncology, 2012. **1**(3): p. 211-219.

[3] Hartgerink, D., et al., LINAC based stereotactic radiosurgery for multiple brain metastases: guidance for clinical implementation. Acta Oncol, 2019. **58**(9): p. 1275-1282.

[4] Dieterich, S.G., I.C., The CyberKnife in Clinical Use: Current Roles, Future Expectations. Radiation Oncology, 2011. **43**: p. 181-194.

[5] Kilby, W., Dooley, J. R., Kuduvalli, G., Sayeh, S., and Maurer C.R.Jr., The CyberKnife®Robotic Radiosurgery System in 2010. Technology in Cancer Research and Treatment, 2010.

Gamow-Teller Transition Properties for Tc-100 Isotope by Pyatov Method

Mehmet Dağ[1,2*], Necla Çakmak[2]

[1]*Karabük University, Department of Medical Services and Techniques, Vocational School of Health Services, Karabük, Türkiye*
[2]*Karabük University, Faculty of Sciences, Department of Physics, Karabük, Türkiye*

*Corresponding author e-mail address: *mehmetdag@karabuk.edu.tr*

ORCID Numbers: 0000-0002-0074-307X (Mehmet Dağ), 0000-0001-5989-6663 (Necla Çakmak)

Abstract**—**Nuclear beta decay includes properties of the weak, strong, and electromagnetic forces and has provided more information about these fundamental building blocks of the nucleus than any other nuclear process [1]. Due to the L orbital angular momentum carried by the beta (β) particle and the neutrino, β decay is classified as allowed (L=0), first forbidden (L=1). The selection rules for allowable beta decay are total angular momentum change, ±1 and no parity change between initial (decaying) and final (populated) states [2]. The Gamow-Teller (GT) transition is one of the nuclear weak processes of the spin-isospin (στ) type. Spin-isospin excitations in nuclei, especially Gamow-Teller (GT) excitations, are important for the investigation of nuclear structure [3]. Gamow–Teller transitions are important in many astrophysical processes: they govern, for example, electron capture during the core collapse of supernovae [4]. The β^- logft value of ^{100}Tc to the ground state of Ru-100 is known from the half-life and decay branch to the ground state [5]. In this study, Gamow-Teller transition properties of Tc-100 nuclei were investigated by Pyatov method within the scope of proton-neutron Quasiparticle Random Phase Approximation (pn-QRPA) formalism. Our calculations were based on the Woods-Saxon (WS) potential. The obtained logft value was compared with the data in the literature and discussed.

Keywords**—** *Beta decay, Gamow-Teller transition, pn-QRPA, Pyatov Method, Woods-Saxon potential*

INTRODUCTION

The weak interaction is one of the four fundamental forces found in nature. It plays an important role in many astrophysical processes such as strong, electromagnetic, and gravitational forces. During the final evolution of a massive star, electron capture, and beta decay occur as Fermi and Gamow-Teller (GT) transition [6]. Beta decay can be defined as a nuclear decay process in which the mass number (A) of the nucleus remains the same and the atomic number (Z) changes. Beta decay studies provided insight into the fundamental properties of nuclear structure and helped researchers better understand the interactions between nucleons and the structure of the nucleus [7]. The Gamow-Teller (GT) transition is one of the most prominent nuclear weak transitions of the spin isospin (**στ**) type. Transitions of GT with $\Delta J^{\pi} = 1^{+}$ are mediated by a single operator $\sigma\tau$, so it has no orbital angular momentum transfer ($\Delta L = 0$) and spin-isospin flip type ($\Delta S = 0 \; and \; \Delta T = 0$). Therefore, $GT \pm$ transitions are of $T_z = \pm 1$ type, where T_z is the third component of isospin T given by T = (N-Z)/2 [8]. This state is a pure Gamow-Teller type transition that takes place and is allowed between nuclear states characterized by spin and parity $(1^{+}) \rightarrow (0^{+})$. In this article, we investigate the properties of beta decay of ^{100}Tc by considering new theoretical and experimental results.

THEORETICAL FORMALISM

In this study, the supersymmetry property of the terms is restored using the Pyatov method by including the coupling interaction in the nuclear part of the total Hamiltonian. Restoration is done in quasi-particle space. The schematic model Hamiltonian does not include the term h_0 for GT excitations in quasi-particle notation, considered in the following form:

$$H_{SM} = H_{sqp} + h_{ph} + h_{pp} \tag{1}$$

where H_{sqp} is the single quasi-particle (sqp) Hamiltonian, h_{ph} and h_{pp} are GT-acting interactions in particle-hole (ph) and particle-particle (pp) channels, respectively. The effective interaction constants in the ph and pp channels are fixed from the experimental value of the GTR energy and the β-decay log ft values between the low energy states of the parent and daughter nuclei. The supersymmetry property of the matching part in the total Hamiltonian was restored according to the Pyatov method. Certain terms invariant with the GT operator were subtracted from the total Hamiltonian, and the commutativity of the remainder, which was disrupted by the shell model mean-area approximation, was restored by adding an effective interaction term h_0 as follows [9-10]:

$$\left[H_{SM} - \left(h_{ph} + h_{pp}\right) - (V_1 + V_C + V_{Is} + h_0, G^{\pm}_{1\mu})\right] = 0 \tag{2}$$

or

$$\left[H_{sqp} - V_1 - V_C - V_{Is} + h_0, G^{\pm}_{1\mu})\right] = 0 \tag{3}$$

where V_1, V_C, and V_{ls} are the isovector, Coulomb, and spin-orbit terms of the shell model potential, respectively. According to the quasiboson approximation, the GT operator in quasiparticle space is given as:

$$G^{-}_{1\mu} = \sum_{np} [\bar{b}_{np} C^{\dagger}_{np}(\mu) + (-1)^{1+\mu} b_{np} C_{np}(-\mu)], \tag{4}$$

$$G^{\dagger}_{1\mu} = [G^{-}_{1\mu}]^{\dagger} \tag{5}$$

where $G^{\dagger}_{np}(\mu)$ and $C_{np}(\mu)$ are the quasiboson creation and annihilation operators. The total Hamiltonian of the system with respect to PM is given as:

$$H_{PM} = H_{sqp} + h_{ph} + h_{pp} + h_0. \tag{6}$$

The $\beta^{\pm}$ reduced matrix elements are given by

$$B^{(\pm)}_{GT}(w_i) = \sum_{\mu} \left|M^{i}_{\beta\pm}(0^+ \to 1^+_i)\right|^2. \tag{7}$$

The $\beta^{\pm}$ transition strengths ($S^{\pm}$) must fulfill the Ikeda sum rule (ISR).

$$S^{\pm} = \sum_{i} B^{(\pm)}_{GT}(w_i) \tag{8}$$

$$ISR = S^{(-)} - S^{(+)} \cong 3(N - Z). \tag{9}$$

The ft values for Gamow-Teller transitions are as follows:

$$(ft)_{\beta^{\mp}} = \frac{D}{\left(\frac{g_A}{g_V}\right)^2 4\pi B_{GT}\left(I_i \rightarrow I_f, \beta^{\mp}\right)} \tag{10}$$

RESULTS AND DISCUSSION

The GT strength distribution for the Tc-100 nucleus was calculated beta-decay direction. The β-decay log*ft* value was also estimated using the pn-QRPA theory. Our calculation is done without the quenching factor. For open-shell nuclei, the pair correlation function was chosen as $C_n = C_p = 12/\sqrt{A}$. Restoration of the supersymmetry property of the pairing interaction is physically important [11]. The energies were calculated from the ground state of the daughter nuclei in the calculations. The basis used in the calculations included all neutron-proton transitions that change the radial quantum number n by Δn = 0, 1, 2, 3. The reliability of our foundation was tested by calculating the Ikeda sum rule (ISR). Table 1 and Table 2 show a comparison of our calculated values of ISR with the theoretically predicted values. Figure 1 shows the decay of Tc-100. The 1^+ excited states in the low-energy region are composed of proton–neutron quasiparticle transitions with $\Delta_n = 0$, and these transitions are weakly collectivized. The 1^+ excited state with the biggest B_{GT} value in the spectrum is accepted as the GTR state. The obtained results in both methods were compared with each other and with the corresponding experimental data. The β^- transition logft values calculated by Pyatov and schematic methods were found close to the experimental values.

$${}^{100}_{43}Tc \longrightarrow {}^{100}_{44}Ru + e^- + \bar{\nu}$$

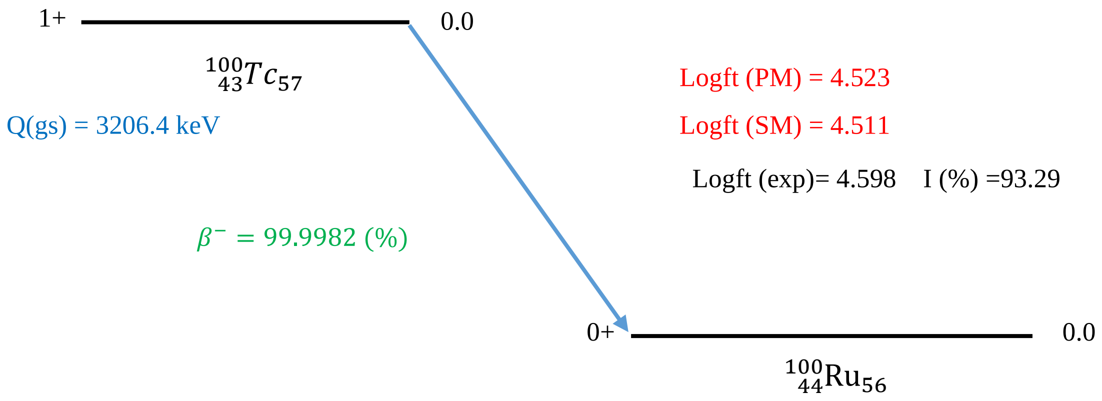

Figure 1. The Tc-100 decay scheme from taken NUDAT [12].

Table 1. Logft values for Tc-100 nucleus.

Nucleus	*Logft (exp.)*	*Logft (PM)*	*Logft (SM)*
Tc-100	4.598	4.523	4.511

Table 2. ISR values for Tc-100 nucleus.

Nucleus	*ISR (theoretical)*	*ISR (PM)*	*ISR (SM)*

Tc-100	42	41.891	41.788

REFERENCES

[1] Chou, W. T., Warburton, E. K., & Brown, B. A. (1993). Gamow-Teller beta-decay rates for A≤18 nuclei. Physical Review C, 47(1), 163.

[2] Berry, T. A., Podolyak, Z., Carroll, R. J., Lică, R., Grawe, H., Timofeyuk, N. K., and De Witte, H. (2019). Investigation of the Δn= 0 selection rule in Gamow-Teller transitions: The β-decay of 207Hg. Physics Letters B, 793, 271-275.

[3] Garrett, J. D. (1980). Book Review: Table of isotopes. CM Lederer and VS Shirley, ed.,(Wiley-Interscience, New York, 1978; xx-1523-A64 pp). Nuclear Physics A, 342(3), 528-529.

[4] Hinke, C. B., Böhmer, M., Boutachkov, P., Faestermann, T., Geissel, H., Gerl, J., ... & Strmeň, P. (2012). Superallowed Gamow–Teller decay of the doubly magic nucleus 100Sn. Nature, 486(7403), 341-345.

[5] Garcia, A., Chan, Y. D., da Cruz, M. T. F., Larimer, R. M., Lesko, K. T., Norman, E. B., ... & Hindi, M. M. (1993). Electron-capture decay of Tc 100 and the double-β decay of Mo 100. Physical Review C, 47(6), 2910.

[6] Langanje, K. & Martinez-Pinedo, G. (2003). Nuclear weak-interaction processes in stars. Reviews Of Modern Physics, 75: 819.

[7] Li, H. & Ren, Z. (2014). Shell model calculations for the allowed Gamow-Teller β-decays of light nuclei, Science China Physics. Mechanics & Astronomy, 57: 1005–1012.

[8] Obaid, S. M. & Tawfeek, H. M. (2020). Gamow-Teller strengths of some sd-shell nuclei in the shell model framework. Revista Mexicana de Fisica, 66 (3): 330–335.

[9] Pyatov, N.I. & Salamov, D.I. (1977). Conservation laws and collective excitations in nuclei. Nukleonika, 22: 127-141.

[10] Cakmak, N., Unlu, S., & Selam, C. (2010). Gamow-Teller 1^+ states in $^{112\text{-}124}$Sb isotopes. Pramana journal of physics, 75:649-663.

[11] Duygu, Ş., Çakmak, N. (2016). Beta decay rates for $^{50,\ 52}$Fe isotopes by Pyatov-Salamov method. Cumhuriyet Üniversitesi Fen Edebiyat Fakültesi Fen Bilimleri Dergisi, 37, 38-41.

[12] National Nuclear Data Center (2023, April 29). https://www.nndc.bnl.gov/nudat3/getdecayscheme.jsp?nucleus=100MO&dsid=100tc%20ec%20decay%20(15.65%20s)&unc=nds

U1F Transition Properties for K-44 Isotope by pn-QRPA

Najm Abdullah Saleh Saleh[1*], Mehmet Dağ[1,2], Necla Çakmak[1]

[1]*Karabük University, Faculty of Sciences, Department of Physics, Karabük, Türkiye*
[2]*Karabük University, Department of Medical Services and Techniques, Vocational School of Health Services, Karabük, Türkiye*

* Corresponding author e-mail address: najmabdola2014@gmail.com
ORCID Numbers: 0000-0001-6118-3582 (Najm Abdullah Saleh Saleh), 0000-0002-0074-307X (Mehmet Dağ), 0000-0001-5989-6663 (Necla Çakmak)

Abstract – *T*he aim of this work is to present an analysis of the $\mathbf{2^-} \rightarrow \mathbf{0^+}$ $\boldsymbol{\beta}$-transition from K-44 by Pyatov Method (PM) within the formalism of proton-neutron Quasiparticle Random Phase Approximation (pn-QRPA). The ground states of K-44 ($\boldsymbol{J^\pi} = \mathbf{2^-}$) populate the ground states of Ca-44 with $\boldsymbol{J^\pi} = \mathbf{0^-}$, through unique first forbidden β-decay with logft = $\mathbf{9.474 \pm 0.005}$ and $\mathbf{9.61 \pm 0.68}$, respectively [1]. The theoretical basis consists of the proton-neutron half-particle random phase approximation (pn-QRPA) in the particle-hole (ph) channel. Transition probabilities based on Woods-Saxon potential were calculated. As a result of the calculations, the unique first forbidden β-decay logft values were found to be in better agreement with the experimental data.

Keywords — *Beta decay, U1F transition, pn-QRPA, Pyatov Method, Woods-Saxon potential*

INTRODUCTION

Beta decay can be further categorized based on the **J** (angular momentum) and **S** (total spin) of the emitted radiation. The conservation of momentum, including total angular momentum, orbital angular momentum, and spin angular momentum, is a crucial requirement for β-decay. This process involves quantum-level transitions to distinct states of nuclear angular momentum (J) or spin (S), which are commonly referred to as Fermi and Gamow-Teller transitions. The forthcoming section will cover the topic at hand. The decay classification of a particle is determined as either allowed or forbidden based on whether its constituent element particles possess zero angular momentum (J=0) or not. The fewer common modes of decay are commonly known as double beta decay and bound-state decay.

Particles emitted through β-decay with a spin (S) value of S=0 and anti-parallel orientation are referred to as Fermi decay [8]. The decay process characterized by zero units of orbital angular momentum and parallel spin is commonly referred to as allowed Fermi decay. In the context of Fermi decay, it can be observed that there is an absence of nuclear spin when the difference in angular momentum quantum numbers, denoted as ΔJ and calculated as the absolute value of the difference between Ji and Jj, is equal to zero. The operator for the nuclear art in the non-relativistic limit of Fermi transitions is expressed as follows [2]:

$$U_{GT}=G_A \sum \sigma_\alpha \tau_{\alpha\pm} \qquad (1)$$

The Gamow-Teller transitions involve a weak axial vector coupling constant denoted as G_A, where $\boldsymbol{\sigma}$ represents the Pauli spin matrices, and the remaining terms carry their conventional meanings. β-decay transitions are a commonly observed form of decay among various other types. Another potential scenario to consider when examining β transitions involving conditions such as ΔJ>1 or opposite parities between initial and final states is the classification of such transitions as forbidden. In order to achieve parity transition, it is necessary for the e^- and ν be emitted with an odd orbital angular momentum of the nucleus. Decays that are forbidden with a limit of J=1 are commonly referred to as First-Forbidden (FF) decays. Fermi-type decays exhibit the characteristic of having electrons and neutrinos with spin orientations that are anti-parallel to each other (S=0), similar to allowed transitions. The selection rules for the First Forbidden decays are limited to ∆J values of 0, 1, and 2 [2]. While the mechanism underlying β-decay is well comprehended, generating a reasonable quantitative depiction of β-decay remains a formidable challenge. The resolution of the quantum many-body problem poses a persistent challenge across various fields of physics. The utilization of the proton-neutron quasiparticle random phase approximation (pn-QRPA) model, which was initially proposed by Halbleib and Sorensen [3], has yielded noteworthy advancements.

The pn-QRPA model can be utilized to facilitate the introduction of charge-changing transitions, such as $(A,Z)\longrightarrow(N\mp1,Z\pm1)$. The β-decay of nuclei, known as the unique first forbidden (U1F), is a topic of significant interest due to its reliance on a sole matrix element, namely $\langle\sigma,\ \tau_2^1\rangle$. The U1F decay strength in light nuclei exhibits an approximate theoretical strength of 102, as reported in reference [4]. Insufficient precision in measuring a limited number of cases has hindered the determination of a comprehensive pattern in heavier nuclei. The study conducted by [5,6] presents findings on two distorted nuclides that exhibit unexpectedly rapid U1F transitions. A recent analysis by Bosch et al. [7] examined the β-decay of 144pr. The investigation of the unique $0^-\rightarrow2^+$ and non-unique $0^-\rightarrow0^+$ β-transitions through experimental and theoretical means has revealed that the recent empirical findings can be accounted for without the inclusion of induced pseudo tensor terms. Nevertheless, the precision of these measurements has been insufficient to verify any conjectured value for the induced pseudoscalar constant. The study conducted by Homma and colleagues [10] on the β-decay properties of unique first-forbidden (U1F) and the microscopic calculations of allowed weak interaction rates using the pn-QRPA model [8,9], were carried out under terrestrial conditions, and have contributed significantly to the advancement of knowledge on the r-process. As demonstrated in reference [10], U1F transitions were found to make a greater contribution to the overall transition probability of nuclei that are near-stable and near-magic. As per Borzov's β-decay investigations [11], the exclusive utilization of the "allowed" β-decay approximation is insufficient in explaining the isotopic variation of the β-decay properties, particularly for the nuclei that traverse the closed N and Z shells.

The "forbidden transitions" play a significant role in determining the overall "half-life" for the nuclei that cross the closed shells, particularly for $N < 50$ in the 78Ni area. A recent study conducted a large-scale shell-model calculation of the half-lives of r-process waiting-point nuclei, which included first-forbidden contributions. This was documented in reference [12]. The purpose of this paper is to provide a detailed study of the $2^-\rightarrow0^+$ β-transition in K-44 nucleus. Through unique first forbidden β-decay, with logft = 9.474 ± 0.005 and 9.61 ± 0.68, the ground states of K-44 $J^\pi=2^-$, populate the ground states of Ca-44 $J^\pi=0^-$, [1]. The theoretical foundation is the particle-hole (ph) channel implementation of the proton-neutron half-particle random phase approximation (pn-QRPA). The Woods-Saxon potential was used to determine the probability of each transition. Compared to the experimental data, the calculated "unique first forbidden" -decay logft values are more in line with.

Formalism

The Hamiltonian responsible for providing the vibrational modes (U1F - rank 2) that are dependent on spin and isospin in odd-odd nuclei within the pn-QRPA(WS) model has been specified as follows:

$$\widehat{H}=\widehat{H}_{sqp}+\hat{h}_{ph} \tag{2}$$

the single quasi-particle (sqp) Hamiltonian of the system is given as follows

$$\widehat{H}_{sqp}=\sum_{j\tau}\varepsilon_{j_\tau}\alpha^{+}_{j_\tau m_\tau}\alpha_{j_\tau m_\tau} \tag{3}$$

The symbols ε_{j_τ} and $\alpha^{+}_{j_\tau}m_\tau\alpha_{j_\tau}m_\tau$ denote the nucleon single quantum particle energy and the operators for creating or annihilating quasi-particles, respectively. The $\hat{h}_{ph}$ represents the effective interaction of spin-isospin for U1F transition in the particle-hole (ph) channel. It is typically expressed as:

$$\hat{h}_{ph}=\frac{2x_2}{g_A}\sum_{j_p}\left\{b_{j_n j_{j_p} j_n}A^{+}_{j_p j_n}(\lambda\mu)+(-1)^{\lambda-\mu}\bar{b}_{j_p j_n}A_{j_p j_n}(\lambda-\mu)\right\}\times$$

$$\left\{b_{j_{\dot{p}}j_{\hat{n}}}A_{j_{\hat{p}}j_{\hat{n}}}(\lambda\mu)+(-1)^{\lambda-\mu}\bar{b}_{j_{\hat{p}}j_{\hat{n}}}A^{+}_{j_{\hat{p}}j_{\hat{n}}}(\lambda-\mu)\right\} \tag{4}$$

The symbol x_2 represents the effective interaction constant. The quasi-boson creation and annihilation operators, denoted $A^{+}_{j_p j_n}(\lambda\mu)$and $A_{j_{\hat{p}}j_{\hat{n}}}(\lambda\mu)$, respectively, are defined as follows.

$$A^{+}_{j_p j_n}(\lambda\mu)=\sqrt{\frac{2\lambda+1}{2j_p+1}}\sum_{m_p m_n}(-1)^{j_n-m_n}\left\langle j_n m_n\lambda\mu|j_p m_p\right\rangle\alpha^{+}_{j_p m_p}\alpha^{+}_{j_n}m_n \tag{5}$$

$$\left\{A^{+}_{j_p j_n}(\lambda\mu)\right\}^{\dagger}=A_{j_p j_n}(\lambda\mu) \tag{6}$$

The reduced matrix elements of the non-relativistic multipole operators, denoted as $b_{j_p j_n}$ and $\acute{b}_{j_p j_n}$, can be defined as follows:

$$b_{j_p j_n}=\left\langle j_p\left(l_p s_p\right)\|r_k\{Y_1(r_k)\sigma(k)\}_{2\mu}\|j_n(l_n s_n)\right\rangle V_{j_p}U_{j_p} \tag{7}$$

$$\acute{b}_{j_p j_n}=\left\langle j_p\left(l_p s_p\right)\|r_k\{Y_1(r_k)\sigma(k)\}_{2\mu}\|j_n(l_n s_n)\right\rangle V_{j_n}U_{j_n} \tag{8}$$

The standard BCS occupation amplitudes are denoted by U (jp) (U(jn) and V(jp) V(jn). Y_1denoted by Spherical Harmonic operator. In the pn-QRPA(WS) model, it is possible to linearize the Hamiltonian equation (1). Therefore, the process of charge exchange involving the transfer of two electrons can be represented as 2^+.The excitation of vibration modes in odd-odd nuclei is commonly attributed to phonon excitations and can be characterized by a specific set of parameters.

$$|\Psi_i\rangle=Q^{+}_{i}(\mu)|0\rangle=\sum_{j_p j_n}\left\{\psi^{i}_{j_p j_n}(\mu)A^{+}_{j_p j_n}(\lambda\mu)-\varphi^{i}_{j_p j_n}(\mu)A_{j_p j_n}(\lambda\mu)\right\}|0\rangle \tag{9}$$

The expression $Q_i^+(\mu)$ represents the creation operator for pn-QRPA phonons, while $|0\rangle$ denotes the phonon vacuum that corresponds to the even-even nucleus' ground state and executes the given operation. For all i, $Q_i(\mu)|0\rangle=0$. The quasi-boson amplitudes $\psi^i_{j_p}j_n(\mu)$ and $\varphi^i_{j_p}j_n(\mu)$, correspond to the forward and backward directions, respectively. The commutation relations are satisfied by the phonon operator.

$\left\langle 0\left|\left[Q_j(\mu),Q_j^+(\dot{\mu})\right]\right|0\right\rangle=\delta_{ij}\delta_{\mu\mu}$ and $\left\langle 0\left|\left[Q_j(\mu),Q_j(\dot{\mu})\right]\right|0\right\rangle=0$

The quasi-boson amplitudes $\psi^i_{j_pj_n}(\mu)$ and $\varphi^i_{j_pj_n}(\mu)$ satisfy the orthonormalization condition

$$\sum_{j_pj_n\mu\mu}\left\{\Psi^i_{j_pj_n}(\mu)\Psi^i_{j_pj_n}(\dot{\mu})-\varphi^i_{j_pj_n}(\mu)\varphi^i_{j_pj_n}(\dot{\mu})\right\}=\delta_{ii}\delta_{ii} \tag{10}$$

Solving equation of motion

$$\left[H,Q_i^+(\mu)\right]|0\rangle=\omega_iQ_i^+(\mu)|0\rangle \tag{11}$$

The variable ω_i denotes the 2-excitation energy in the ith odd-odd nucleus, measured from the ground state of the corresponding parent even-even nucleus. The equations for pn-QRPA(WS) are expressed in the following forms:

$$\sum_{j_pj_nj_p'j_n'\mu}\left\{\rho_{j_pj_nj_p'j_n'}\psi^i_{jpj_n}(\mu)-\eta_{j_pj_nj_p'j_n'}\varphi^i_{j_pj_n}(\mu)\right\}=\omega_i\psi^i_{jpj_n}(\mu) \tag{12}$$

$$\sum_{j_pj_nj_p'j_n'\mu}\left\{\eta_{j_pj_nj_p'j_n'}\psi^i_{j_pj_n}(\mu)-\rho_{j_pj_nj_p'j_n'}\varphi^i_{j_pj_n}(\mu)\right\}=\omega_i\varphi^i_{j_pj_n}(\mu) \tag{13}$$

Consequently, the matrices $\rho_{j_pj_nj_p'j_n'}$ and $\eta_{j_pj_nj_p'j_n'}$ correspond to the pn-QRPA(WS).

$$\rho j_pj_nj_p'j_n'=E_{j_pj_n}\delta_{j_nj_n'}\delta_{j_pj_p'}+2\chi_2\left\{b_{j_pj_n}b_{j_p'j_n'}+\bar{b}_{j_pj_nj_n}\bar{b}_{j'j_n'}\right\} \tag{14}$$

$$\eta_{j_pj_nj_p'j_n'}=-2\chi_2(-1)^{\lambda-\mu}\left\{b_{j_pj_n}\bar{b}_{j_p'j_n'}+b_{j_p'j_n'}\bar{b}_{j_pj_n}\right\} \tag{15}$$

The expression $E_{jpjn}=\varepsilon_{jn}+\varepsilon_{jp}$ represents the energy of a single particle. The excitation energies ω_i and amplitudes $\psi^i_{jpj_n}(\mu),\varphi^i_{j_pj_n}(\mu)$ can be obtained from equations (10), (11), and (12).

β-DECAY OPERATOR AND TRANSITIONS PROBABILITY IN THE PN-QRPA (WS) MODEL

The first forbidden β-Decay transitions can be defined in terms of multipole operator. For the transitions $2^-\rightarrow0^+$ these are

$$M^{U1F}_{\beta^{\Psi}}=M^{\mp}(J_A,K=1,\lambda=2,\mu)=g_A\sum_{k=1}^{A}t_{\pm}(k)r_k\{Y_1(r_k)\sigma(k)\}_{2\mu} \tag{16}$$

$M_{\beta^{\mp}}^{U1F}=M^{\mp}(J_A,K=1,\lambda=2,\mu)$ is the non-relativistic unique first forbidden β-Decay multipole operator. All symbols have their usual meanings. The transitions probability $B\left(I_i\rightarrow I_f\ \beta^{\mp}\right)$ is described by the reduced matrix element of the multipole operator equation. (16). Thus, we may write

$$B\left(I_i\rightarrow I_f,\beta^{\mp}\right)=\frac{1}{2I_i+1}\left|\left\langle I_f\middle\|M^{\mp}\left(j_A,k=1,\lambda=2\right)\middle\|\ I_i\right\rangle\right|^2 \qquad (17)$$

The reduce matrix elements $\left\langle 2_i^- \left\|M_{\beta^{\mp}}\right\| 0^+\right\rangle$within the framework of the pn-QRPA(WS) method are given as

$$\left\langle 2_i^-\middle|M_{\beta}\text{-}(\dot{\mu})\middle|0^+\right\rangle=\left\langle 0^+\middle|\left[Q_i(\mu),M_{\beta}\text{-}(\dot{\mu})\right]\middle|2\right\rangle=\sum_{j_pj_n}^{\delta_{\mu\mu}}\left\{b_{j_pj_n}\psi_{j_pj_n}^{i}(\mu)+\hat{b}_{j_pj_n}\varphi_{j_pj_n}^{i}(\mu)\right\}, \qquad (18)$$

$$\left\langle 2_i^-\middle|M_{\beta}(\dot{\mu})\middle|0^+\right\rangle=\left\langle 0^+\middle|\left[Q_i(\mu),M_{\beta}(\mu)\right]\middle|2\right\rangle=\sum_{j_pj_n}\delta_{\mu\mu}\left\{b_{j_pj_n}\psi_{j_pj_n}^{i}(\mu)+b_{j_pj_n}\varphi_{j_pj_n}^{i}(\mu)\right\}. \qquad (19)$$

Transitions with λ=n+1 are referred to as unique first forbidden transitions [21], and the ft values are expressed as

$$(ft)_{\beta^{\mp}}=\frac{D}{\left(g_A/g_V\right)^2 4\pi B\left(I_i\rightarrow I_f,\beta^{\mp}\right)}\frac{(2n+1)!!}{[(n+1)!]^2 n!} \qquad (20)$$

$$D=\frac{2\pi^3\hbar^3\ln 2}{g_V^2 m_e^5 c^4}=6250\text{sec}, \qquad \frac{g_A}{g_v}=-1.254$$

RESULTS AND CONCLUSION

The unique first forbidden U1F ($|\Delta J|=2$) transition by using the pn-QRPA model with the Woods-Saxon (WS) potential basis was considered in this work. In numerical calculation done by the FTN77 programme.

$${}_{19}^{44}K \longrightarrow {}_{20}^{44}Ca + e^- + \bar{\nu}$$

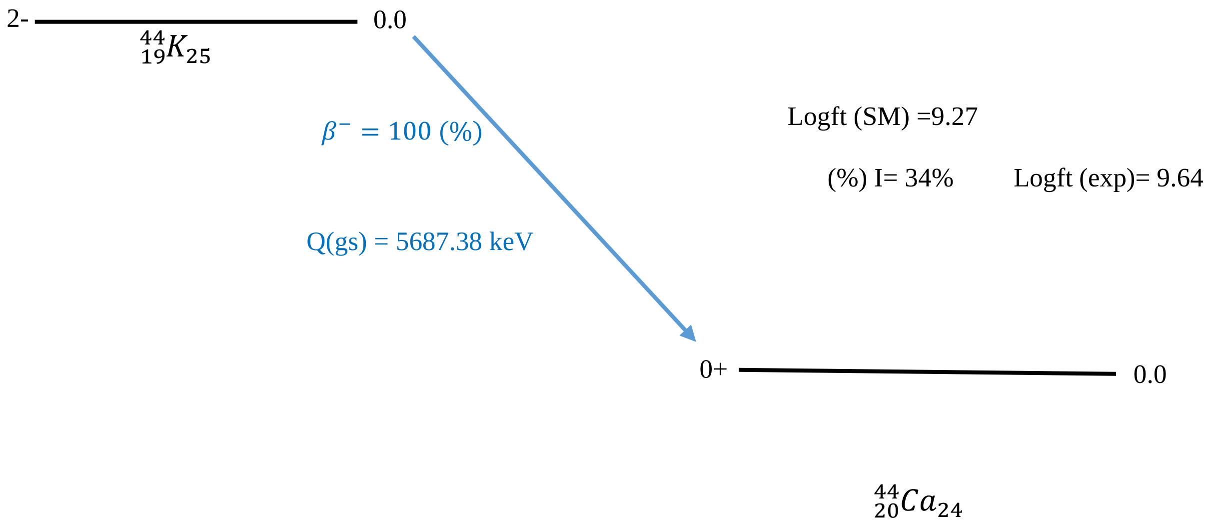

Figure 1. The ${}_{19}^{44}K$ decay scheme from taken NUDAT [13].

REFERENCES

[1] Rangachari, C., Steffen, W., Richter, A., Spamer, E., & Titze, O. (1984). Isovector M2 transitions in sup (42, 44) Ca and comparison with the analogous unique first-forbidden. beta. /Sup-/decays of sup (42, 44) K. Phys. Lett., B;(Netherlands), 135.

[2] K. S. Krane, Radioactive Decay, Introductory Nuclear Physics, New York: John Wiley and Sons, pp. 161, 1988.

[3] J. A. Halbleib and R. A. Sorensen, Gamow-Teller beta decay in heavy spherical nuclei and the unlike particle-hole RPA. Nucl. Phys. A, vol. 98, pp. 542, 1967.

[4] R. A. Meyer, In Problems of Vibrational Nuclei, edited by G. Alaga, V. Paar, and L. Sips (North-Holland, Amsterdam, 1975), Chap. 7.

[5] Y. A. Ellis, Nucl. Data Sheets 12, 533 (1974), and references cited therein.

[6] A. Artna-Cohen, Nucl. Data Sheets 16, 276 (1975).

[7] H.E. Bosch, M. Behar, M. C. Cambiaggio, G. Garcia Bermudez and L. Szybisz, Can. J. Phys. 51 (1973)
2260.

[8] Staudt, A., Bender, E., Muto, K., Klapdor-Kleingrothaus, H.V.: Second-generation microscopic predictions of beta-decay half-lives of neutron-rich nuclei. At. Data Nucl. Data Tables 44, 79 (1990).

[9] Klapdor, H.V., Metzinger, J., Oda, T., Beta-decay half-lives of neutron-rich nuclei. At. Data Nucl. Data Tables 31, 81 (1984).

[10] Homma, H., Bender, E., Hirsch, M., Muto, K., Klapdor-Kleingrothaus, H.V., Oda, T., Systematic study of nuclear β decay. Phys. Rev. C 54, 2972 (1996).

[11] Borzov, I.N., Beta-decay rates. Nucl. Phys. A 777, 645 (2006)].

[12] Zhi, Q., Caurier, E., Cuenca-García, J.J., Langanke, K., Martínez-Pinedo, G., Siega, K., Shell-model half-lives including first-forbidden contributions for r-process waiting point nuclei. Phys.Rev. C 87, 025803 (2013).

[13] National Nuclear Data Center (2023, April,28).
https://www.nndc.bnl.gov/nudat3/getdecayscheme.jsp?nucleus=44CA&dsid=44k%20bM%20decay%20(22.13%20m)&unc=nds

Effect of Microcracks on Solar Module Efficiency

Bilal Karaduman[1*], Vedat Tavas[2]

[1]*Electrical and Communication Engineering/Institute Of Science, Istanbul Ticaret University,Türkiye*
[2]*Electrical and Electronics Engineering/Engineering Faculty, Istanbul Ticaret University, Türkiye*

* Corresponding author e-mail address: bilal.karaduman@ht-saae.com

ORCID Numbers: 0009-0001-4886-4997 (Bilal.karaduman), 0000-0003-2945-9846 (Vedat.tavas)

Abstract— The popularity of solar energy has increased recently due to its clean and renewable nature and increasing energy demand. The solar module, which converts solar energy into electricity, is one of the main elements of the solar energy system. Micro cracking, one of the problems of solar modules regardless of cutting technologies, is a phenomenon that develops on the surface of solar modules when the solar module is exposed to mechanical stress or temperature fluctuations. Micro cracks can have a major negative impact on the conversion efficiency, power efficiency, and lifetime of solar modules. In this study, the effects of micro-cracks on solar module efficiency are described.

Keywords — *Micro crack, solar module, effect of micro crack, type of micro crack*

INTRODUCTION

The impact of a micro crack on a solar module's power production might differ based on several variables, including the crack's size and location, the solar cell technology employed, and the surrounding environment. In general, a solar module's power output may be reduced by a micro-crack on it. The severity of the crack and the electrical connection of the injured solar cell or cells determine how much power is lost 0. Micro cracks have the potential to produce concentrated regions of high resistance, which would restrict the passage of electrical current and limit the module's power output. Depending on the crack's severity, the power loss can be anything from a few percent to 50% or more. Micro cracks may not always have a substantial impact on a module's power production, especially if they are small and do not interfere with the electrical connections between the cells. It is crucial to keep in mind that micro-cracks may potentially result in long-term reliability problems, including heightened susceptibility to more cracking, degradation, and potential module failure.

MICRO-CRACK EFFECTS

Micro cracks on a solar module's surface can have several detrimental impacts 0, including:

A. Decrease in efficiency

Micro cracks can also reduce the efficiency of the solar module by causing the affected solar cells to operate at a lower level than the rest of the cells in the module. A solar module's capacity to convert sunlight into energy may be hampered by a crack, which can also result in a reduction in efficiency. The size and location of the crack will determine how much the efficiency is reduced. A break could let moisture enter the module, leading to short circuits and corrosion. Additionally, it may result in the module's cells becoming out of alignment, which can lower energy output. In addition, if the cracked cell is in the module's front glass, it might allow dirt, dust, and other particles to get inside and build up, which would further cut down on the quantity of sunlight that reaches the cells.

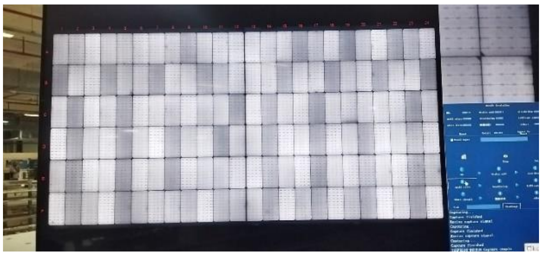

Fig. 1 Standard Module EL

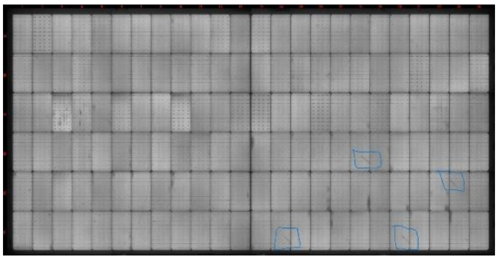

Fig. 2 Micro crack Module EL

The efficiency of a solar module is defined as the ratio of the output power to the input power (from the sun). If the power output of a module is reduced due to micro cracks [3], the efficiency of the module will also decrease. The amount of efficiency loss depends on the severity of the crack and the electrical connectivity of the affected solar cell(s). Any standard module given in Fig. 1 can supply nearly theory power, but some modules can have power lost with some problems. That power and efficiency loss generally depends on the micro cracked module in Fig. 1 we can see how can become a micro effect visual defect in module design [4].

Table 1. Power difference between cracked and standard module EL table

Module	CellEta	Cell Power	Theory Power	Voc(V)	ISc(A)	Vm(V)	Im(A)	PMax	LossEff
Fig. 4	23,2	7,69	553,68	49,7969	13,6928	40,412	13,701	553,683	0,0012%
Fig. 5	23,2	7,69	553,68	48,4046	13,8782	37,6118	13,8442	520,705	-6,33%

In general, the efficiency loss due to micro-cracks can range from a few percent to as much as 50% or more. The loss of efficiency in micro-cracked modules is given in Table 1. Standard modules can supply nearly theory power, but micro-cracked modules have nearly %6,33 efficiency loss.

B. Increased degradation

Micro cracks can lead to increased degradation of the solar module's performance over time, which can shorten its lifespan. Although micro-cracks are not noticed at the time of production, they may cause greater deterioration and power losses in the future. It is possible that some micro that are invisible and point-shaped in EL analyses during the production phase may progress with the effect of pressure and temperature, leading to larger fractures. The products assembled during the production phase may progress with the effect of pressure and temperature, as well as cause some problems. Fig. shows the increment of the micro-crack after a certain time, which should have a worse effect on yield.

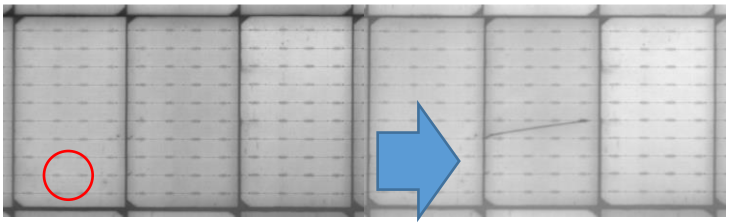

Fig. 3 In production time small micro-cracks and after production mounting micro-cracks

C. Reduction in output power

Micro cracks can cause a decrease in the output power of the solar module by reducing the amount of light that can be absorbed by the solar cells. Another effect of micro-crack is observed as excessive decreases in Pmax value. In Table 1, it is shown that the micro-cracked cell has less power generation than the normal cell. The reason for this is that as a result of the division of the resistance of the broken cell and the beam absorption surface, it cannot produce the desired voltage value and lower output power emerges [5].

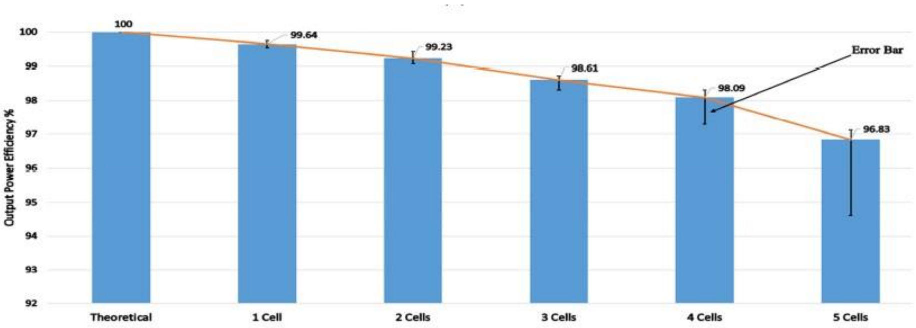

Fig. 4 Output power efficiency effect number of micro-cracks

In Figure 4, we can see that the series-connected micro-crack loses its output power effect, and also that the series-connected cell prevents a large amount of power output with conduction loss and increased resistance [9].

TYPE OF MICRO CRACK

Micro cracks caused by external forces, such as handling, installation, and shipping, can appear on the surface of a solar cell. Thermal strains brought on by temperature changes, hailstorms, and other meteorological conditions can also result in external micro-cracks [6]. These kinds of micro-cracks given in Figure 5 often develop on the surface of the solar cell's front surface, and they can reduce the quantity of sunlight that can be absorbed and converted into power, which can lower the efficiency of the module.

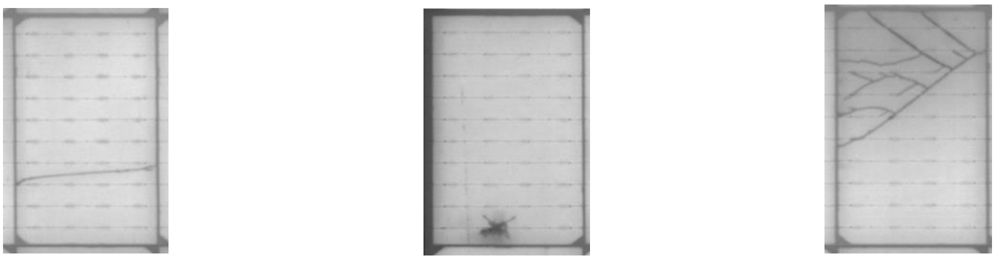

(a) (b) (c)

Fig 5. (a) Line Type Micro crack (b) Point Type Micro crack (c) Tree Type Micro crack,

Micro cracks that form internally in a solar cell are a result of manufacturing flaws such as imperfections in the crystal structure or stress from the growing process. Thermal pressures can also cause internal micro-cracks, which can develop over time and spread in Figure 5 (a). These kinds of micro-cracks might result in decreased efficiency by obstructing the flow of electrons through the solar cell; they are often found in the solar cell's bulk. In solar factory systems, we can see some type of micro crack with an electroluminescence machine [7]. In Figure 5 (b). An electric current running through a substance causes it to create light, a process known as electroluminescence. An electroluminescence machine, commonly referred to as an EL tester or an EL measurement system, is a tool used to gauge and analyse a material's electroluminescent characteristics [8]. An EL device typically includes a power source, a voltage/current source, and a detector or camera that can record the light the material emits. A voltage is applied to the sample material, which is sandwiched between two electrodes, creating an electric field. Light is produced as a result of the recombination of electrons with positively charged "holes" in materials as they go through them.

CONCLUSION

It is clearly seen that the use of high temperatures, which is a side effect of solving the problem of insufficient resources with high temperatures in the solar power generation process, causes micro-breaks. In this study, power and efficiency losses caused by microfractures and small micro-fractures may progress during assembly and cause larger power losses.

FUTURE WORKS

In our future studies, the methods created for these micro-fractures and the improvement of microfractures with these methods can be examined as well as different results can be compared.

ACKNOWLEDGMENT

This publication was produced from the master thesis of Bilal Karaduman in Istanbul Ticaret University Institute of Science, Electronics and Communication Engineering Program. Thanks to Istanbul Ticaret University employees for their support and HT-SAAE Solar Co. for their support in the necessary technical infrastructure and measurement environment.

REFERENCES

[1] G C. Olschok, M. Schmid, R. Haas, and G. Becker, “Inappropriate exposure to PV modules: description and effects of handling defaults”, Proceedings of the 28th European Photovoltaic Solar Energy Conference, Paris, France, 2013, pp. 3138 - 3141.

[2] Kontges M, Kunze I, Kajari-Schroder S, Breitenmoser X, Bjorneklett B, The risk of power loss in crystalline silicon based photovoltaic modules due to micro cracks, Sol. Energy Mater. Sol. Cells 95(4), 1131-1137 (2011) I. S. Jacobs and C. P. Bean, “Fine particles, thin films and exchange anisotropy,” in Magnetism, vol. III, G. T. Rado and H. Suhl, Eds. New York: Academic, 1963, pp. 271–350.

[3] Kontgers M., Kunze I., Kajari-Schroder S., and ET AL.: ‘Quantifying the risk of power loss in PV modules due to micro-cracks’. 25th European Photovoltaic Solar Energy Conf., Valencia, Spain, 2010 September, pp. 3745–3752

[4] Paggi, M., Corrado, M., & Rodriguez, M. A. (2013). A multi-physics and multi-scale numerical approach to microcracking and power-loss in photovoltaic modules. Composite Structures, 95, 630-638.

[5] J. Käsewieter, F. Haase, and M. Köntges, “Model of cracked Solar Cell Metallization leading to permanent Module Power Loss”, IEEE Journal of Photovoltaics, vol.6, no.1, pp. 28-33, Jan. 2016, DOI: 10.1109/JPHOTOV.2015.2487829.

[6] Kajari-Schroeder S, Kunze I, Koentges. Criticality of cracks in PV modules. Energy Procedia 2012; 27:658-63.

[7] Spataru S., Hacke P., Sera D., ET AL.: ‘Quantifying solar cell cracks in photovoltaic modules by electroluminescence imaging’, 2015 IEEE 42nd Photovoltaic Specialist Conf. (PVSC). IEEE, 2015 June, pp. 1–6

[8] Vs Khatri R, Agarwal S, Saha I, Singh SK, Kumar B. Study on long-term reliability of photo-voltaic modules and analysis of power degradation using accelerated aging tests and electroluminescence technique. Energy Procedia 2011; 8:396-01.

[9] Morlier, A., Haase, F., & Köntges, M. (2015). Impact of cracks in multi-crystalline silicon solar cells on PV module power—a simulation study based on field data. IEEE Journal of Photovoltaics, 5(6), 1735-1741.

6th Pak – Türk International Conference on Emerging Technologies in the field of Sciences and Engineering, May 4 – 6, 2023, Karabük University, Karabük, Türkiye

Prevention Methods of Microcracks on Solar Module

Bilal Karaduman[1*], Vedat Tavas[2]

[1]*Electrical and Communication Engineering/Institute Of Science, Istanbul Ticaret University, Türkiye*
[2]*Electrical and Electronics Engineering/Engineering Faculty, Istanbul Ticaret University, Turkiye*

* Corresponding author e-mail address: bilal.karaduman@ht-saae.com

ORCID Numbers: 0009-0001-4886-4997 (Bilal.karaduman), 0000-0003-2945-9846 (Vedat.tavas)

***Abstract*—**Solar energy has gained popularity in recent years due to its clean and renewable nature, as well as the increasing demand for energy. The solar module, which converts the sun's energy into electricity, is a crucial component of a solar energy system. However, micro-cracking is a common problem with solar modules, regardless of cutting technologies. Micro-cracking occurs on the surface of solar modules when they are exposed to mechanical stress or temperature fluctuations. These micro-cracks can significantly reduce the conversion efficiency, power output, and lifespan of the solar modules. This article aims to describe the effects of micro-cracks on solar module efficiency and propose methods to mitigate their consequences.

***Keywords* —** *Micro-crack, solar module, prevention methods*

INTRODUCTION

Micro-cracks on a solar module can significantly reduce its power output. The severity of the crack and how the damaged solar cell or batteries are electrically connected can determine the amount of power lost [1]. Micro-cracks can create areas of high resistance that concentrate and restrict the flow of electric current, ultimately limiting the module's power output. Depending on the severity of the crack, power loss can range from a few percent to 50% or more. Moreover, micro-cracks can lead to long-term reliability issues, including increased susceptibility to further cracking, deterioration, and potential module failure. Therefore, detecting any micro-cracks is crucial to maintaining the optimal performance and longevity of a solar module.

PREVENTING EXPERIMENTS

Effect of Different Temperatures on Micro-crack

Avoiding rapid temperature changes can prevent the solar modules from expanding and contracting, which can produce micro-cracks [2]. Micro-cracks may arise as a result of mechanical stress brought on by thermal stress within the solar cell. These tiny flaws can cause the solar cell's power output to drop and the layers of the cell to separate. Thermal stress can also alter a solar cell's electrical characteristics, which can lower the efficiency of the cell. For instance, high temperatures can cause charge carriers inside the solar cell to recombine more frequently, lowering the cell's total efficiency. Now we will use some different temperature effects on how many micro-cracks on the module. In solar production it is known in the solar module industry that soldering is done with infrared lamps. We can see that these heater lamps give temperature according to their percentage power and the effect of this temperature on the products produced. The temperature we determined in the production norms in our experiment operating procedures is 225±5 degrees Celsius showed in Fig.2. In Fig. 1 also we can see that high temperature soldering temperature.

Fig. 1 High temperature of soldering process

Fig. 2 Normal temperature of soldering process

Each experiment done with 10 modules with different rate micro-crack and results are given in Table 1. It has been seen in Table 2 that sudden temperature changes can cause micro cracks in soldering.

Table 1. Optimum Soldering temperatures and micro-crack rate

Test Number	Appling Temp 225±5	Number of micro	Soldering Time	Power Of Lamp
1	223,2	0	2400 ms	52%
2	224,9	0	2400 ms	52%
3	229,7	1	2400 ms	55%
4	226,3	0	2400 ms	53%
5	227,3	0	2400 ms	53%
6	229,2	0	2400 ms	54%
7	224,6	0	2400 ms	52%
8	230,0	1	2400 ms	55%
9	225,3	0	2400 ms	52%
10	226,2	0	2400 ms	53%

Table 2. High Soldering temperatures and micro-crack rate

Test Number	Appling Temp 245 ±5	Number Of Micro	Soldering Time	Power Of Lamp
1	243,6	1	2400 ms	58%
2	244,8	2	2400 ms	58%
3	249,8	3	2400 ms	61%
4	246,5	2	2400 ms	59%
5	245,9	1	2400 ms	59%
6	249,9	2	2400 ms	60%
7	244,5	1	2400 ms	58%
8	248,8	2	2400 ms	61%
9	243,9	1	2400 ms	58%
10	245,9	2	2400 ms	59%

In order to obtain more precise results, experiment was also made at high temperatures which results are given in Table 2. It was observed that high temperatures greatly increase the micro ratio and causes deterioration in the cell structure, point and line type fractures. It has been understood that high temperature has a great effect on the crack rate as well as disrupting the cell structure. In soldering process applying temperature must be 225±5 for a smoother and cleaner production. A solar module's efficiency can be greatly impacted by micro-cracks, which can reduce output power, efficiency, and speed up degradation over time [3]**Hata!**

Başvuru kaynağı bulunamadı.. These steps can be taken to minimize the occurrence of micro-cracks and increase the lifespan and efficiency of solar modules.

Using Thinner Cell

Using thinner solar cells will reduce the risk of micro-cracks because they are more flexible and resistant to mechanical stress. Since thinner solar cells have a more flexible structure, it is seen that they can be more resistant to mechanical stresses such as bending. However, it can be observed that micro-crack formed on the surface can spread more easily, and that they are less resistant after micro-crack than thicker cells. Thinner cells may be advantageous in preventing the development and spread of micro-crack in materials. This is because materials with thinner cells may have a more uniform distribution of stress, which may lessen the possibility of stress concentrations that could cause micro-cracking. Furthermore, thinner cells can offer a greater surface area for stress transfer, which can aid in more efficient stress dissipation and lessen the possibility of stress concentrations that could lead to micro-crack [4].**Hata! Başvuru kaynağı bulunamadı.** Additionally, by encouraging the development of smaller and more uniform grain structures, which can aid in preventing the formation and spread of micro-crack, thinner cells may increase the strength and durability of the material. It is crucial to remember that the benefits of thinner cells on micro-crack might vary depending on a number of variables, including the kind of material, the type of micro-crack, and the amount of stress or pressure placed on the material. Therefore, when maximizing for micro-crack resistance, it is crucial to carefully consider the design and material properties. We can check result of produced different thickness cell module.

Table 3. 0,175±5 cell thickness micro-crack

Test Number	Thickness	Number of micro	Soldering Time	Power Of Lamp
1	0,177	0	2400 ms	58%
2	0,176	0	2400 ms	58%
3	0,175	0	2400 ms	61%
4	0,178	0	2400 ms	59%
5	0,176	0	2400 ms	59%
6	0,175	0	2400 ms	60%
7	0,176	0	2400 ms	58%
8	0,177	0	2400 ms	61%
9	0,178	0	2400 ms	58%
10	0,179	1	2400 ms	59%

Table 4. 0,190±5 cell thickness micro-crack ratio

Test Number	Thickness	Number of micro	Soldering Time	Power Of Lamp
1	0,189	1	2400 ms	58%
2	0,188	0	2400 ms	58%
3	0,190	1	2400 ms	61%
4	0,191	1	2400 ms	59%
5	0,189	0	2400 ms	59%
6	0,190	1	2400 ms	60%
7	0,192	3	2400 ms	58%
8	0,190	0	2400 ms	61%
9	0,193	3	2400 ms	58%
10	0,191	2	2400 ms	59%

Thinner cell measurement Results are given in [3] where micro-crack ratio is less then %1, It is seen that thinner cells can potentially have an advantage in reducing the occurrence and propagation of micro-crack in materials. This is because thinner cells can provide a more uniform distribution of stress within the material, which can reduce the likelihood of stress concentrations that can lead to micro-cracking. Thick cell measurement Results are given in [4]. where micro-crack ratio is more then %8, 3, Thick cell micro crack is more than the thinner one. In thicker cells, we can see that the formation and propagation of micro-cracks in the materials is potentially increased. This is because thicker cells cannot withstand greater stress distribution within the material, increasing the likelihood of stress concentrations that can lead to micro-cracking [5]. Materials micro-cracks can be examined using a variety of mathematical models and methods. The Griffith criterion is one such model that offers a theoretical framework for comprehending how micro-cracks behave under stress.

$$G \geq Gc \qquad (1)$$

G is given by, where

$$G = \frac{E * gamma * a}{2} * (1 - nu\ 2)) \qquad (2)$$

According to the Griffith criterion given in equation (1), a crack will spread if its associated energy release rate (G) is greater than the critical value (Gc) needed for it to do so: where an is the crack length, In Eq2 is the Poisson's ratio, gamma is the surface energy per unit area, and E is the material's Young's modulus. Where an is the crack length, nu is the Poisson's ratio, gamma is the surface energy per unit area, and E is the material's Young's modulus. For a given material and micro-crack geometry, the critical energy release rate (Gc) necessary for crack propagation can be calculated experimentally. Depending on the unique properties of the material and the micro-crack, additional models and formulas may also be employed to study micro-cracks. The impact of micro-cracks on the performance of solar cells can be modelled using a variety of formulas. The Shockley- Queisser limit, a theoretical calculation of the maximum efficiency of a solar cell based on its material characteristics, is one widely used method. The modified Shockley-Queasier limit reduces the effective surface area of the cell that is available for absorbing sunlight in order to account for the influence of micro-cracks on the performance of the cell. The modified Shockley-Queisser limit can be calculated using the following formula:

$$\eta = \eta\ \mathrm{sqx}(1 - \alpha * \mathrm{f}) \qquad (3)$$

In Eq. 3 where the solar cell’s modified efficiency is, sq is the efficiency anticipated by the Shockley-Queisser limit (without micro-cracks) [6], is the percentage of the surface area of the cell that is covered by micro-cracks, and f is the decrease factor for the cell's efficiency brought on by the existence of micro-cracks. The specific model and assumptions made, the characteristics of the cell, and the micro-cracks may all affect the exact calculation for f. The modified Shockley-Queisser limit is a theoretical calculation [7].

CONCLUSION

It has been observed that the use of high temperatures during the solar production process, which is often employed to address insufficient resource problems, can lead to micro-crack in the cells. However, by reducing the temperature and optimizing the printing time, the rate of micro-cracks can be significantly reduced. Furthermore, the study also investigated the effect of cell thicknesses, which can vary from place to place during production. The results showed that thin cells are more resistant to thermal stress than thick cells, leading to reduced soldering resistance and a lower micro-crack rate. Using these optimized methods, a 15% decrease in cell breakage rates was achieved, resulting in minimized micro-crack rates during production.

ACKNOWLEDGEMENT

This publication was produced from the master thesis of Bilal Karaduman in Istanbul Ticaret University Institute of Science, Electronics and Communication Engineering Program. Thanks to Istanbul Ticaret University employees for their support and HT-SAAE Solar Co. for their support in the necessary technical infrastructure and measurement environment.

REFERENCES

[1] G C. Olschok, M. Schmid, R. Haas, and G. Becker, “Inappropriate exposure to PV modules: description and effects of handling defaults”,Proceedings of the 28th European Photovoltaic Solar Energy Conference, Paris, France, 2013, pp. 3138 - 3141.

[2] Eitner U, Kajari-Schroder S, Kontges M, Altenbach H, Thermal stress and strain of solar cells in photovoltaic modules, Advanced Structured Materials 15, 2011, p. 453-468. R. Nicole, “Title of paper with only first word capitalized,” J. Name Stand. Abbrev., in press.

[3] Van Mölken J.I., Yusufoğlu U.A., Safiei A., ET AL.: ‘Impact of micro-cracks on the degradation of solar cell performance based on two-diode model parameters’, Energy Procedia, 2012, 27, pp. 167–172

[4] J. H. Werner, S. W. Glunz, F. Haase, and R. Preu, "Effect of Cracks on the Performance of Multicrystalline Solar Cells," Progress in Photovoltaics: Research and Applications, vol. 14, no. 3, pp. 265-272, 2006

[5] Köntges, M., Kajari-Schröder, S., & Kunze, I. (2013). Crack statistic for wafer-based silicon solar cell modules in the field measured by UV fluorescence. IEEE Journal of Photovoltaics, 3(1), 95-101.

[6] X. Zhang, J. Wei, H. Huang, and B. Yan, "Modified Shockley-Queisser Efficiency Limit for Solar Cells with a Single or Multiple Microcracks," Journal of Applied Physics, vol. 123, no. 19, pp. 194503-1-194503-8, 2018

[7] W.Shockleyand, H.J.Queisser, J.Appl.Phys 32, 510 (1961).

Simulation of air pollutant dispersion around Afşin Elbistan-A Thermal Power Plant, Turkey using the Gaussian Plume Model in FreeMat

Yusof-den Jamasali[12*], Şeref Turhan[2], Aybaba Hançerlioğulları[2] and Aslı Kurnaz[2]

[2]*Kastamonu University, Kastamonu, Turkey*

[1]*Mindanao State University, Marawi City, Philippines*

* Corresponding author's e-mail address: yusof-den.jamasali@msumain.edu.ph

ORCID Numbers: 0000-0001-5259-9789 (Yusof-den Jamasli), 0000-0000-5303-3680 (Şeref Turhan), 0000-0000-1700-8480 (Aybaba Hançerlioğulları), 0000-0002-7910-3461 (Aslı Kurnaz)

Abstract**—** This study focuses on the simulation of air pollutant dispersion around Afşin Elbistan-A Thermal Power Plant (AEATPP), one of the largest power plants in Turkey. The dispersion of air pollutants was simulated in Freemat software using the Gaussian Plume Model. The model input data included effective stack height, mass rate of emission of the pollutant, wind speed and direction, and atmospheric stability. The simulations were performed for different meteorological conditions. The results showed that the highest concentration of pollutants occurred in the direction of prevailing winds. The study also examined the impact of the power plant on the surrounding environment and evaluated the effectiveness of potential mitigation strategies. Overall, the study provides valuable insights into the air quality impact of the AEATPP and can inform future policy decisions aimed at reducing emissions and improving air quality in the region.

Keywords**—** *Air Pollutants, Thermal Power Plant, Simulation, Gaussian Plume Model, Freemat*

INTRODUCTION

Air pollution is a pressing environmental issue that affects the health and well-being of millions of people around the world. One of the primary sources of air pollution is the combustion of fossil fuels, particularly in the production of electricity. Thermal power plants are among such kind of power plants that generates electricity by burning coal. They are known to emit pollutants such as carbon dioxide (CO_2), sulfur dioxide (SO_2), nitrogen oxides, and particulate matter into the atmosphere [1-3]. To assess the potential impact of these emissions, state agencies and local governments use dispersion models to predict the concentration of pollutants from plumes. There are several commercial software options available for dispersion modeling, such as AERMOD VIEW [4] and CALPUFF VIEW [5]. However, these software packages can be expensive and may not be accessible to all users. To address this issue, researchers have explored open-source alternatives such as FreeMat, which is a software package that enables rapid engineering and scientific prototyping and data processing, similar to Matlab. FreeMat can handle matrix operations and has relatively low hardware requirements. One commonly used model for the dispersion of gas is the Gaussian Plume Model, which is a simple and effective approach for simulating the spread of pollutants in the atmosphere. This model is based on the concept of turbulence and can be easily manipulated mathematically. This study aims to use the Gaussian Plume Model in FreeMat to simulate the dispersion of SO_2 pollutants from the plumes of the Afsin Elbistan-A Thermal Power Plant (AEATPP), which is one of the largest thermal power plants in Turkey. It is located in Kahramanmaraş province with a total power of 1360 MW [6], as shown in Figure 1. By utilizing open-source software and a commonly used dispersion model, this study provides a cost-effective and accessible approach to evaluating the potential impact of thermal power plant emissions on air quality.

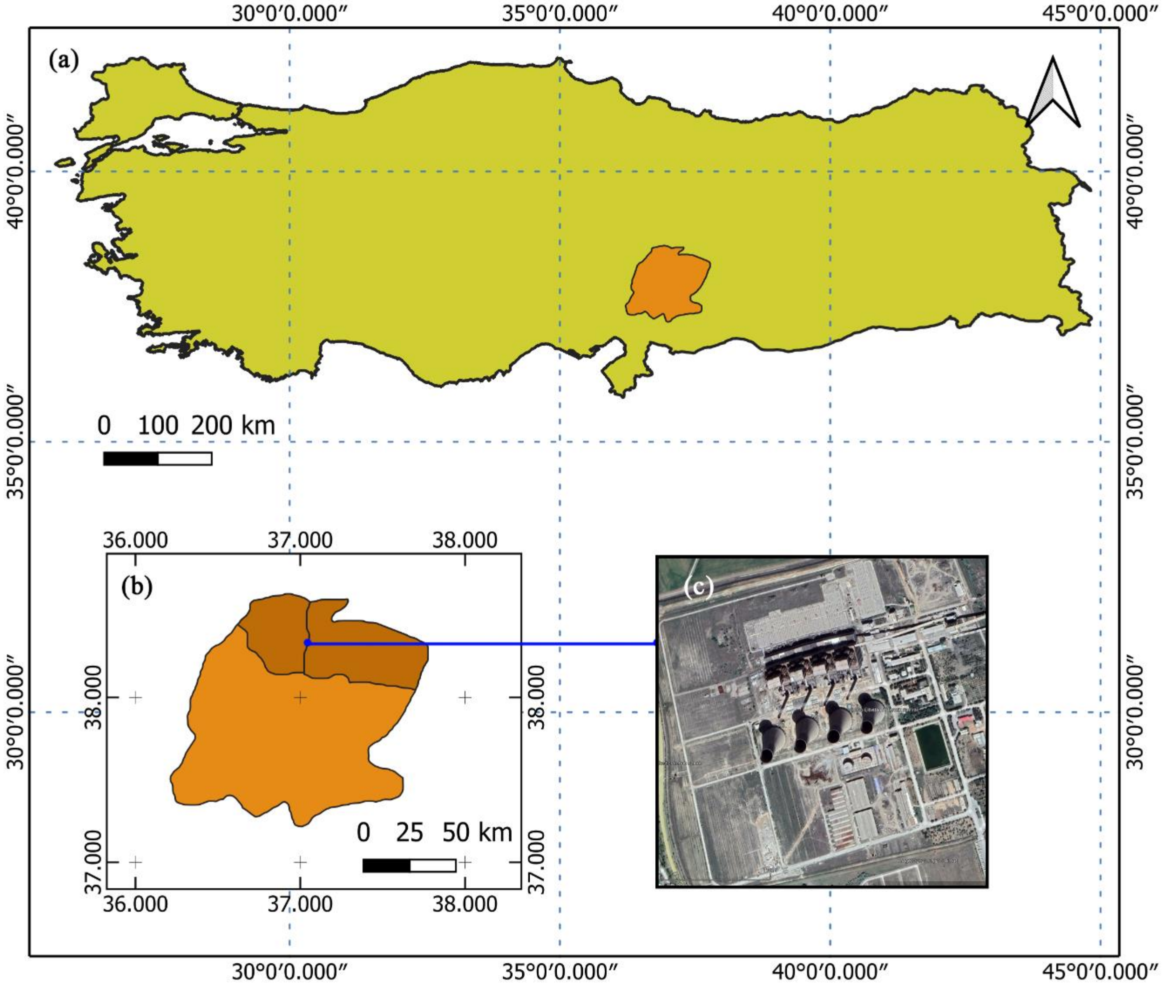

Fig.1. Map of (a) Turkey and (b) Kahramanmaraş province showing the location of (c) Afşin Elbistan-A Thermal Power Plant

METHODOLOGY

E. *Gaussian Plume Model*

The following are the assumptions in Gaussian Plume Model:

- The pollutant emissions are continuous.
- The pollutants are not reacting chemically in the atmosphere.
- At the wind direction the transport process is dominant to the turbulent dispersion.
- The aerosol diameter to be smaller than 20 μm for their residence time in the atmosphere to be larger than the time intervals which are studied.
- The atmosphere is a stationary condition concerning the meteorological parameters for the time interval of transport from the pollution source to the receptors.
- Crosswinds are minimal/negligible.
- Terrain is flat near the source.
- Plumes from different sources do not interact.
- Statistically normal distribution patterns are followed.

F. *Main Parameters*

The concentrations of pollutants occurring downwind is a function of effective stack height (H), mass rate of emission of the pollutant, wind speed and direction, and atmospheric stability. The equation for Ground Level Concentration of Air Pollutants in the Gaussian Plume Model is:

$$C = \frac{E}{\pi s_y s_z u}\left[exp\left[-\frac{1}{2}\left(\frac{y}{s_y}\right)^2\right]exp\left[-\frac{1}{2}\left(\frac{H}{s_z}\right)^2\right]\right] \qquad (1)$$

where E is emission rate pollutant (g/sec), u is wind speed (m/sec), s_y and s_z are standard deviations, y is the coordinate of a position perpendicular to the wind direction and H is effective stack height which is calculated using the following equation:

$$H = h + \Delta H \qquad (2)$$

$$\Delta H = \frac{v_s d}{u}\left[1.5 + \left(2.68 \times 10^{-2}(P)\left(\frac{T_s - T_a}{T_s}\right)d\right)\right] \qquad (3)$$

where h is the physical height (m), T_s is stack temperature (K), d is stack diameter (m), T_a is air temperature (K), u is wind speed (m/sec), and P is pressure (kPa). The specific input parameters in the present study are listed in Table 1. The values of wind velocity at AEATPP are based on EIA Report [6].

TABLE 1. SITE-SPECIFIC INPUT PARAMETERS [6]

Main Stack		Bruden stack	
Main stack height	145 m	Stack height	120 m
Main stack diameter	6.8 m	Stack diameter	3 m
Gas velocity	24 m/s	Gas velocity	15.8 m/s
SO_2	11000 kg/h	SO_2	500 kg/h
Stack temperature	483 K	Stack temperature	378 K

G. *FreeMat algorithm*

Since there are four stacks of AEATPP, all of these contribute to the ground concentration calculation. Stacks stand in a line with about 75 m distance apart. This line deviates by 14° from-West-to-East axis. For scenarios where the wind is coming from W, WNW, NW, NNW, N, NNE, NE, and ENE, the origin of the x-axis is placed at the main stack, at the west end of the line. Otherwise, the x-axis is placed at the fourth stack, at the east end of the line.

FreeMat code is written such that each scenario uses the appropriate values of the variables, i.e. employing the if loops. These appropriate values are based on the Table of Stability Classes mentioned in [7]. Then the ground concentration is calculated at each point in the region -5 km $\leq y \leq +5$ km,$0 \leq x \leq +2.06$ km, where the x-axis is parallel to the wind direction. This is done by employing for loops. All these values are saved into a matrix and a color map is then generated.

RESULTS AND DISCUSSIONS

The profile of ground concentration around AEATPP is shown in Figure 2. Wind velocity u is in m/s, maximum ground concentration C_{max} is in g/cm^3 and its location x is in km. The x-axis is oriented in the same direction as the wind velocity. Results show that the SO_2 pollutants are more dispersed in scenarios of greater wind speed. In these scenarios, the locations of maximum concentrations are farther from AEATPP. The farthest location of maximum concentration is at x = 2.06 km in the SW scenario with maximum concentrations 2.5 x10^{-3} g/cm^3. Conversely, the nearest is at x = 0.7 km in the NNE and S scenarios, with value 7.7 x10^{-3} g/cm^3.

CONCLUSION

The ground concentration profile of SO_2 pollutants around AEATPP has been successfully simulated in Freemat. SO_2 pollutants are more dispersed in scenarios of greater wind speed. Hence, the SW scenario has the smallest maximum concentration located farthest.

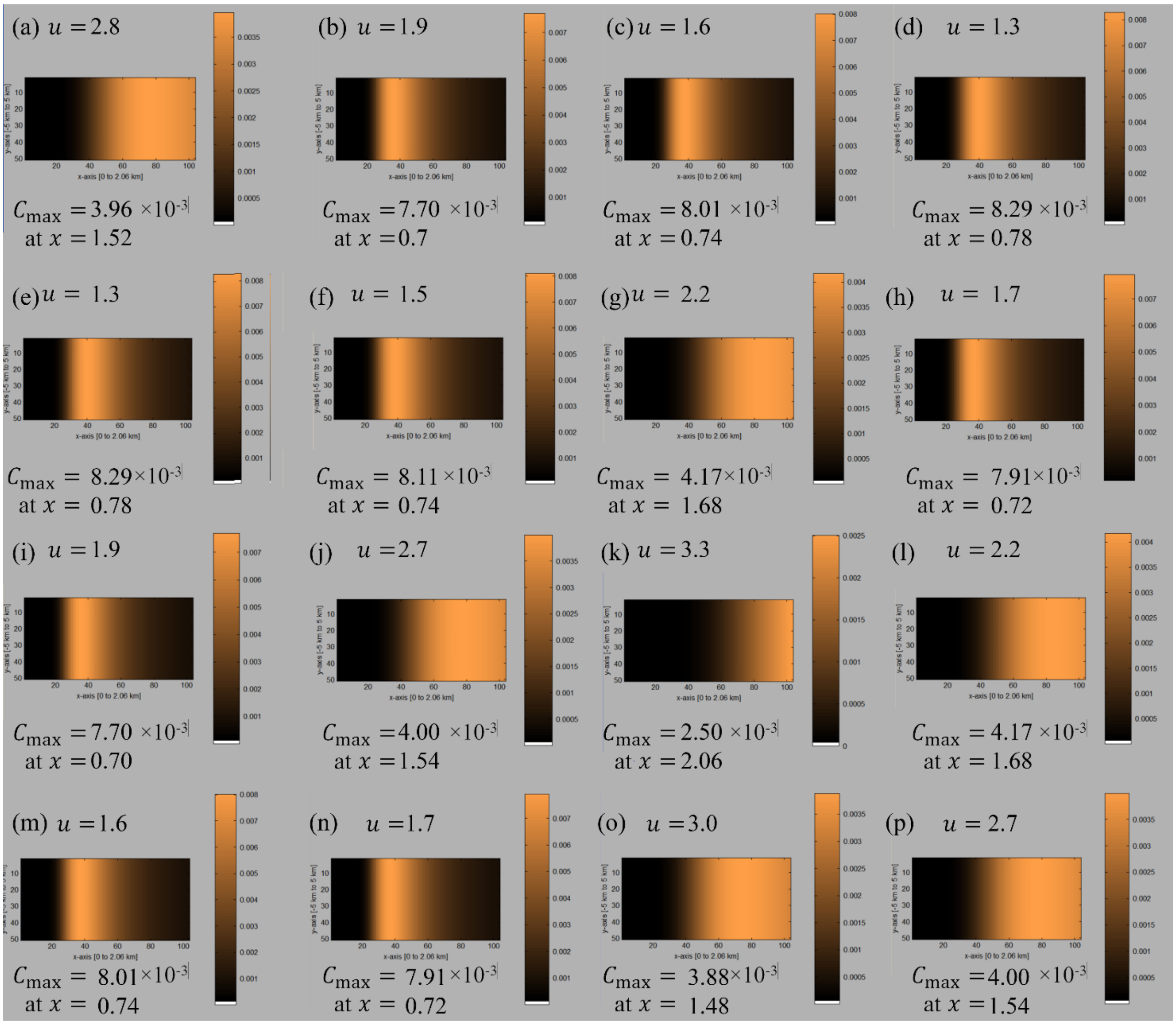

Fig. 2. Color map of ground concentration profile (with its corresponding color bar) around the AEATPP of scenario (a) N (b) NNE (c) NE (d) ENE (e) E (f) ESE (g) SE (h) SSE (i) S (j) SSW (k) SW (l) WSW (m) W (n) WNW (o) NW and (p) NNW.

REFERENCES

[1] S. A. Nihalani, Y. Mishra, and J. Juremalani, “Emission Control Technologies for Thermal Power Plants,” IOP Conf. Ser.: Mater. Sci. Eng., vol. 330, p. 012122, Mar. 2018, doi: 10.1088/1757-899X/330/1/012122.

[2] S. Nazari, O. Shahhoseini, A. Sohrabi-Kashani, S. Davari, R. Paydar, and Z. Delavar-Moghadam, “Experimental determination and analysis of CO2, SO2 and NOx emission factors in Iran’s thermal power plants,” Energy, vol. 35, no. 7, pp. 2992–2998, Jul. 2010, doi: 10.1016/j.energy.2010.03.035.

[3] Z. Ma et al., “Characteristics of NOx emission from Chinese coal-fired power plants equipped with new technologies,” Atmospheric Environment, vol. 131, pp. 164–170, Apr. 2016, doi: 10.1016/j.atmosenv.2016.02.006.

[4] https://www.weblakes.com/software/air-dispersion/aermod-view/

[5] https://www.weblakes.com/software/air-dispersion/calpuff-view/

[6] Y. Engineering Consultancy and Project Services Ltd. & International B.V. (2004) Afsin-Elbistan A Thermal Power Plant Rehabilitation and Construction of Flue Gas Desulphurization Unit Project (EIA Report) General Directorate of Electricity Generation Corporation Inc. https://documents1.worldbank.org/curated/zh/699451468174238273/pdf/E1307.pdf

[7] M. Lazaridis, First Principles of Meteorology and Air Pollution, vol. 19. in Environmental Pollution, vol. 19. Dordrecht: Springer Netherlands, 2011. doi: 10.1007/978-94-007-0162-5

Radiological Assessment of Seyitömer Thermal Power Plant in Kütahya, Turkey using RESRAD-ONSITE Code 7.2

Yusof-den Jamasali[12*], and Şeref Turhan[2]

[1]*Mindanao State University, Marawi City, Philippines*
[2]*Kastamonu University, Kastamonu, Turkey*

* Corresponding author's e-mail address: yusof-den.jamasali@msumain.edu.ph

ORCID Numbers: 0000-0001-5259-9789 (Yusof-den Jamasali), 0000-0000-5303-3680 (Şeref Turhan)

Abstract— The total dose rate of the contaminated Seyitömer Thermal Power Plant (TPP) site has been assessed using the RESRAD-onsite 7.2 code. The risk analysis simulation span over 1.0×10^3 years considering three cover scenarios of the contaminated site. The maximum total dose at Seyitömer TPP due to the ^{226}Ra, ^{232}Th, and ^{40}K radionuclides and their progenies is 1.436, 1.435, and 0.566 mSv y^{-1} at t = 1000 y for 0.5-m, 1.0-m and 2.0-m cover scenarios, respectively. Results also revealed that the total doses are less in thicker cover scenarios. Cancer risk data revealed that ^{232}Th is the major contributor to the risk in the scenarios considered.

Keywords— *RESRAD code, radiation dose, activity concentration, excess cancer risk*

INTRODUCTION

The energy demand has been increasing due to population growth and modernization. This has resulted in a rise in energy consumption from electricity generation, which is expected to continue based on projected scenarios [1]. Most countries currently rely more on nonrenewable sources despite environmental concerns than renewable sources [2]. Middle Eastern countries are major suppliers of fossil fuels, while Russia and Ukraine are known for nuclear energy [3]. Turkey has large domestic coal reserves, which are used to generate electricity and reduce dependence on imported energy sources [4]. There are 55 thermal power plants (TPP) in Turkey, including the Seyitömer Thermal Power Plant in Kütahya province [5]. The Seyitömer TPP is situated in the Tavşanlı region of Kütahya and is owned by the Çelikler Energy company. This power plant is the 32nd largest in Turkey and has an installed power of 600 MW, making it the biggest power plant in Kütahya. Additionally, it is the fifth-largest coal thermal power plant in Turkey [6]. Fly ash is a by-product of energy production at thermal power plants. Studies have shown that fly ashes from thermal power plants, as well as other significant industries, may contain naturally occurring radionuclides [7-10]. There are various tools [11-12] available for evaluating radiation levels at site contaminated with radionuclides, including a suite of programs called the RESRAD (RESidual RADioactivity) family of computer codes. These programs are suitable for assessing the level of radiation exposure in contaminated sites and buildings [13], both radiologically and chemically. RESRAD-ONSITE is a part of this family and is used to assess radiation exposure for individuals situated directly on contaminated soil [14]. In this study, the activity concentration of naturally occurring radionuclides at the Seyitömer TPP contaminated site for 1000 years has been simulated using RESRAD-onsite 7.2 code. Moreover, the total dose rate and excess cancer risk at the plant sites have been assessed as well.

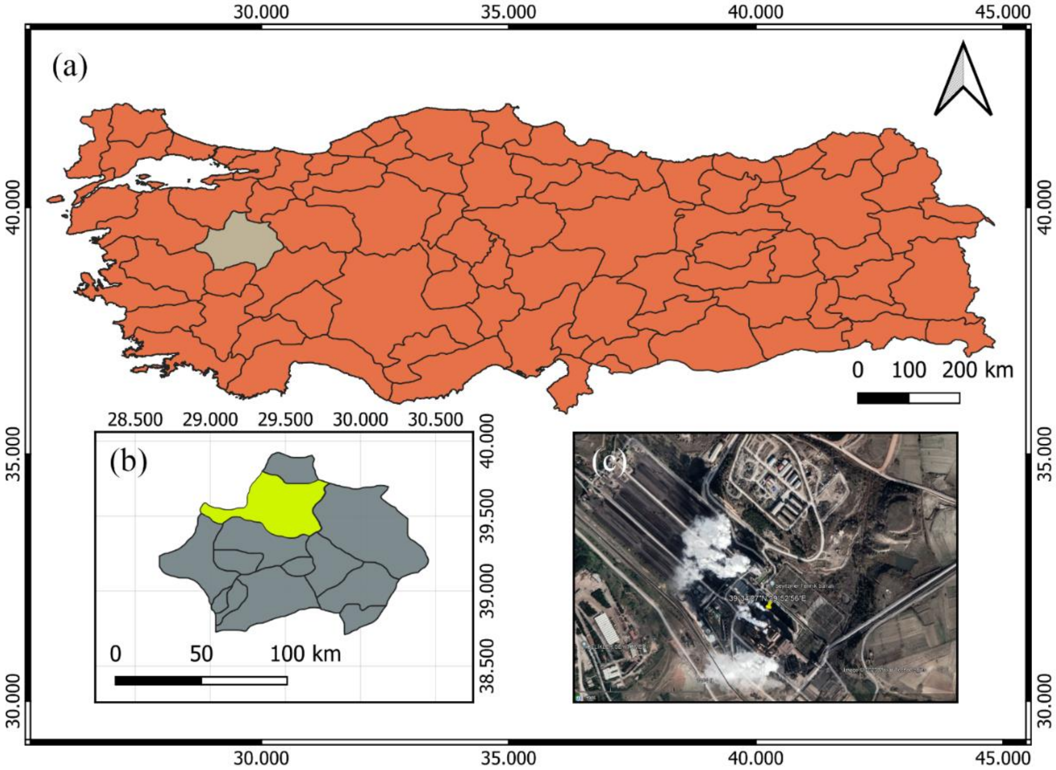

Fig. 1. Map of (a) Turkey (b) Kütahya province and (c) Seyitömer TPP

METHODOLOGY

H. *Collection and Measurement of samples*

A collection of thirty-seven fly ash samples were collected from Seyitömer TPP. The samples were dried in a temperature-controlled furnace at 110 °C for 4 h to remove moisture. After moisture removal, these samples were cooled in a moisture-free atmosphere. The samples were transferred to containers and weighed. Each container was hermetically sealed to prevent the escape of radon gas. Before counting each sample was stored for more than 4 weeks to allow ^{226}Ra and its short-lived decay products to reach the secular equilibrium.

Two high-resolution gamma-ray spectrometers with p-type coaxial HPGe detectors were used to determine the radiological characteristics of the samples. One of the HPGe detectors has a relative efficiency of 50% and an energy resolution of 1.8 keV at 1332.5 keV of ^{60}Co while the other detector has a relative efficiency of 110% and an energy resolution of 2.1 keV. These detectors were shielded to reduce background radiation. The absolute efficiency calibration of the gamma spectrometers was determined using a solid nuclide mixture of gamma reference materials sealed in standard Marinelli beakers with an active volume of 1000 ml, and average density of 1 g cm^{-3}, and IAEA reference materials RGU-1 (U-ore), RGTh-1 (Th-ore) and RGK-1 (K_2SO_4). Each sample was measured for an accumulating time between 10 and 24 h. Background measurements were taken under the same conditions as sample measurements and subtracted to get net counts for the sample.

İ. *Input Parameters*

Table 1 shows the input parameters used in the simulation in RESRAD-ONSITE.

TABLE 1. INPUT PARAMETERS

Parameters	**Site-Specific Data**		**Activity Concentrations**	
Area of the contaminated zone	82,130 m^2		Radionuclide	Average value

The thickness of the contaminated zone	2 m
Cover depth (scenarios)	0.5 m 1.00 m 2.00 m
The density of the contaminated zone	1.50 g/cm^3
Wind speed	3.48 m s^{-1}
Precipitation rate	1 m yr^{-1}
Well-pump intake depth	10 m
Indoor time factor	0.5
Outdoor time factor	0.25

^{226}Ra	150.43 Bq/kg
^{232}Th	96.34 Bq/kg
^{40}K	615.32 Bq/kg

RESULTS AND DISCUSSION

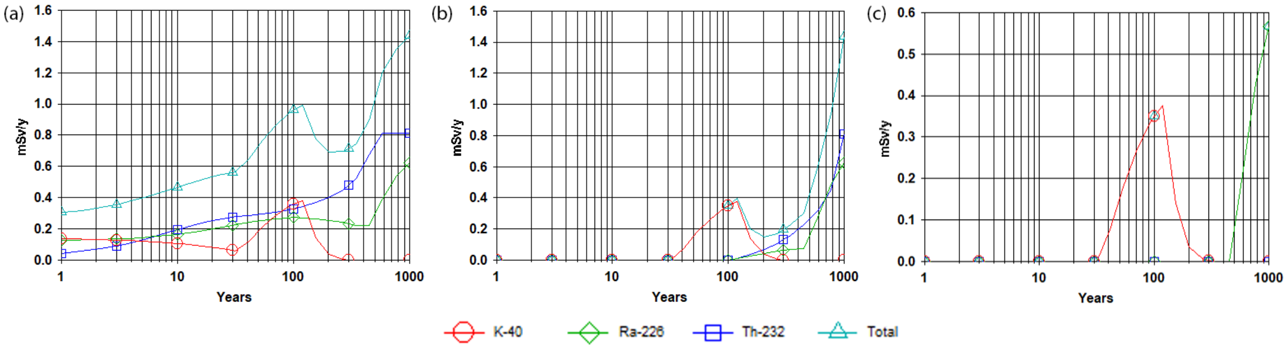

Fig.2. Summed total dose on contaminated site of Seyitömer Thermal Power Plant due to all nuclides and all pathways. (a) 0.5-m (b) 1.0-m (c) 2.0-m cover scenario.

Figure 2 shows the variation of dose due to ^{226}Ra, ^{232}Th, and ^{40}K for 1000 years at the contaminated site of Seyitömer TPP. The figure shows that the maximum total dose due to the above-mentioned radionuclides and their progenies is 1.436, 1.435, and 0.566 mSv y-1 at *t* = 1000 y for 0.5-m, 1.0-m and 2.0-m cover scenarios, respectively. The total dose contributions calculated with RESRAD-ONSITE for each radionuclide in 0.5-m cover scenario at t = 1000 y for the ground pathway were 0.62 mSv y-1 for ^{226}Ra, 0.812 mSv y-1 for ^{232}Th and 2.87 x 10^{-12} mSv y-1 for ^{40}K. In the 1.0-m cover scenario, the total dose contributions at t = 1000 y for the ground pathway were 0.62 mSv y-1 for ^{226}Ra, 0.81 mSv y-1 for ^{232}Th and 3.57 x10^{-12} mSv y-1 for ^{40}K. In the 2.0-m cover scenario, the total dose contributions at t = 1000 y for the ground pathway were 0.57 mSv y-1 for ^{226}Ra, 1.21x10^{-5} mSv y-1 for ^{232}Th and 3.48 x10^{-12} mSv y-1 for ^{40}K. Figure 3 shows the dose contributions from all nuclides summed and for all exposure pathways, in 0.5-m cover, 1.0-m, and 2.0-m cover scenarios at Seyitömer TPP. It can be seen that plant (water-independent) pathway is one major contributor to the dose with a peak of 0.66 mSv y-1 at t = 450 y in a 0.5-m cover scenario. The plant pathway has a peak of 0.44 mSv y-1 in 1.0-m cover scenarios at t = 766 y, while as in the 2.0-m cover scenario, there was none in the entire 1000 y time.

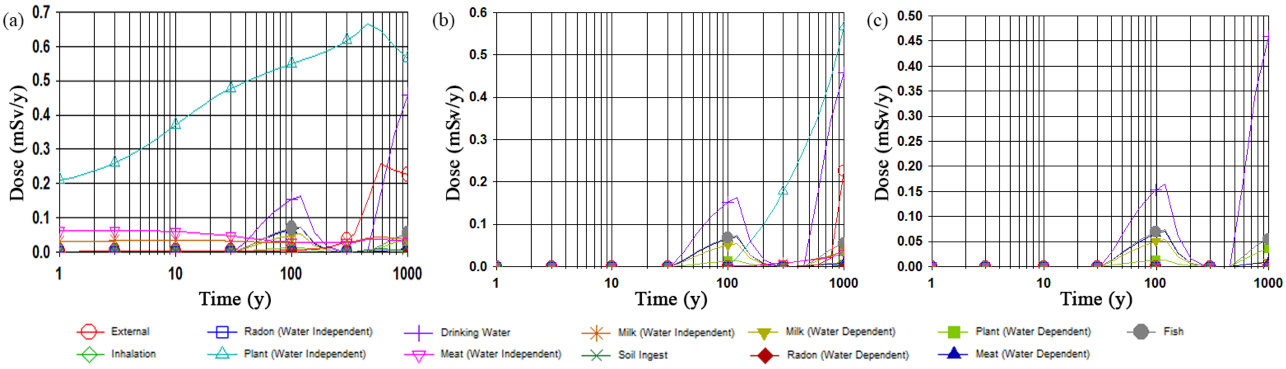

Fig. 2. Dose contributions on contaminated site of Seyitömer TPP from all nuclides summed and for all exposure pathways. (a) 0.5-m (b) 1.0-m (c) 2.0-m cover scenario.

Figure 4 shows the cancer risk of Seyitömer TPP assessed with RESRAD-ONSITE. These curves show that the risk following exposure to the various radionuclides increases from the first to the hundredth year. The risk tends to decrease until it reaches a minimum value. Cancer risk data revealed that ^{232}Th is the major contributor to the risk in the scenarios considered.

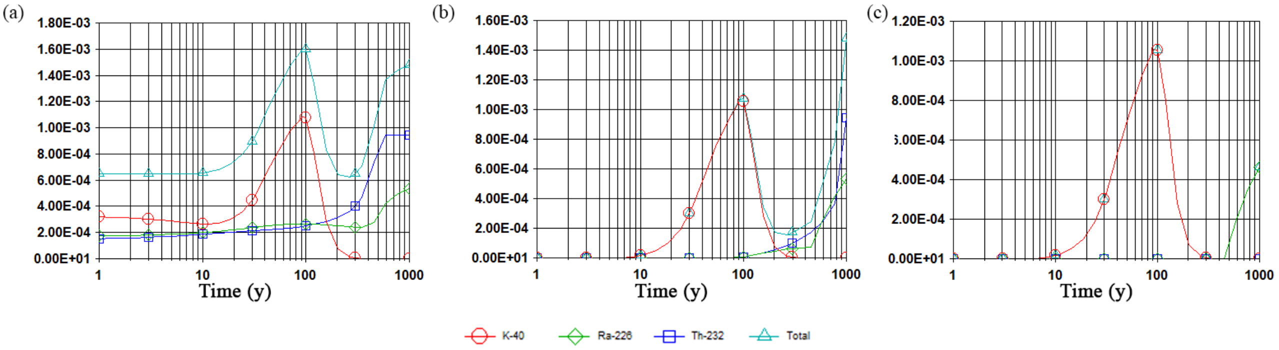

Fig. 3. Cancer risk at Seyitömer TPP and contributions from all nuclides. (a) 0.5-m (b) 1.0-m (c) 2.0-m cover scenario.

CONCLUSION

We evaluated the reduction of the total effective dose rate due to the exposure of radioactivity for long-term working workers at the Seyitömer TPP by considering the different thicknesses of cover scenarios. The maximum total dose at Seyitömer TPP due to the ^{226}Ra, ^{232}Th, and ^{40}K radionuclides and their progenies is 1.436, 1.435, and 0.566 mSv y-1 at t = 1000 y for 0.5-m, 1.0-m and 2.0-m cover scenario, respectively. Results also revealed that the total doses are less in thicker cover scenarios. Cancer risk data revealed that ^{232}Th is the major contributor to the risk in the scenarios considered.

REFERENCES

[1] Cozzi, L. & Gould, T. Arnish, J. (2022) World Energy Outlook 2022. International Energy Agency, IEA member and association countries.
[2] Güney, T. (2019). Renewable energy, non-renewable energy and sustainable development. Intl J of Sustainable Development & World Ecology DOI https://doi.org/10.1080/13504509.2019.1595214
[3] Droege, P. (Ed.). (2008). Urban energy transition: From fossil fuels to renewable power (1st ed). Elsevier. North South Wales, Australia
[4] Myllyvirta, L., Analist, B., & Farrow, A. (2022, April). "Future Air Quality and Health Impacts of the planned Afşin A power plant expansion". CREA. https://energyandcleanair.org/wp/wp-content/uploads/2022/04/Afsin-expansion_-Report.pdf
[5] Şirin, M. (2021, August 3). Türkiye'de kaç tane termik santral var? Tüm termik santrallerin isimleri! Haberler. https://www.haberler.com/haberler/turkiye-de-kac-tane-termik-santral-var-tum-14307220-haberi/

[6] https://web.archive.org/web/20150703071848/https://www.enerjiatlasi.com/komur/seyitomer-termik-santrali.html

[7] Pandit, G. G., Sahu, S. K., & Puranik, V. D. (2011). Natural radionuclides from coal fired thermal power plants – estimation of atmospheric release and inhalation risk. Radioprotection, DOI https://doi.org/10.1051/radiopro/20116982s

[8] Ademola, J. A., & Onyema, U. C. (2014). Assessment of Natural Radionuclides in Fly Ash Produced at Orji River Thermal Power Station, Nigeria and the Associated Radiological Impact. Natural Science, DOI https://doi.org/10.4236/ns.2014.610075

[9] Mahur, A. K., Kumar, R., Sengupta, D., & Prasad, R. (2008). Estimation of radon exhalation rate, natural radioactivity and radiation doses in fly ash samples from Durgapur thermal power plant, West Bengal, India. J Environmental Radioactivity DOI https://doi.org/10.1016/j.jenvrad.2008.03.010

[10] Mishra, M., Sahu, S. K., Mangaraj, P., & Beig, G. (2023). Assessment of hazardous radionuclide emission due to fly ash from fossil fuel combustion in industrial activities in India and its impact on public. J Environmental Management DOI https://doi.org/10.1016/j.jenvman.2022.116908

[11] Arnish, J. (2021) In: Greenspan E (ed) In Encyclopedia of Nuclear Energy. Elsevier. Tennessee, United States Birol, D. F. (n.d.). World Energy Outlook 2022.

[12] Liland, A. (2015) In: van Velzen L. V. (ed). Environmental Remediation and Restoration of Contaminated Nuclear and Norm Sites. Elsevier, Cambridge

[13] Yu, C. et al., (1999). Applications of RESRAD family of computer codes to sites contaminated with radioactive residues. https://www.researchgate.net/publication/236470286_Applications_of_RESRAD_family_of_computer_codes_to_sites_contaminated_with_radioactive_residues

[14] C. Yu et al., (2001) User's Manual for RESRAD Version 6. Argonne, Illinois 60439: Environmental Assessment Division; Argonne National Laboratory.

Effect of Melting Temperature on Wettability of (96.5-x)Sn-2Ag-0.5Cu-1Bi-xAl Solder Alloy Systems

Serkan OGUZ[1*], and Ahmet Mustafa ERER[2]

[1,2]*Faculty of Science Physics Department, Karabük University*

* Corresponding author e-mail address: soguz78@gmail.com

0000-0001-6315-8970 (Serkan OGUZ), ORCID Numbers: *0000-0003-4358-4010* (Ahmet Mustafa ERER)

Abstract**—** In this article, SACBi-xAl new quinary lead-free solder alloy was produced by adding Al at certain ratios (x=0.05, 0.1, 0.3, 0.5, and 0.6% wt.) to the previously produced SAC-1Bi quaternary lead-free solder alloy. The spreading properties and melting temperatures of SACBi-xAl solder alloy on Cu substrate in Ar gas atmosphere at 275, 300, and 325°C temperatures were investigated. It has been reported that the lowest melting temperature (212.5°C) and spreading angle (38.44°) belong to SACBi-0.1Al solder alloy. It has been reported that adding Al in microalloying improves the spreading by up to 0.1% and reduces the melting temperature. 0.1% wt. It has been observed that adding larger amounts of Al deteriorates the spreading properties and increases the melting temperatures.

Keywords—— *Al-added Lead-free Solder Alloy, wetting angle, SACBi-Al, sessile drop*

INTRODUCTION

Solder alloys are used in mechanical solder joints in the electrical and electronics industry [1]. Soldering alloy containing tin-lead (Sn-Pb) used in soldering and solder works is a widely used solder alloy because it is an ergonomic material regarding melting temperature and wetting properties [2]. However, its use has been restricted after Pb became a toxic substance for human and environmental health [3]. As an alternative to the Sn-Pb solder alloy, Pb-free solder alloys have been produced and developed [4]. Binary lead-free alloys Sn–Zn [5], Sn–Cu [6], Sn–Ag [7], and Sn–Bi [8]. Made on alloys such as ternary lead-free alloy Sn-Ag-Cu (SAC) [9], Sn-Zn-Ag [10], and Sn-Ag-Bi [11]. Among these lead-free solder alloys, environmentally friendly, eutectic, or near-eutectic SAC solders are preferred as an alternative [12]. The silver (Ag) content of the Sn-3Ag-0.5Cu (SAC305) alloy, which is currently widely used in soldering works, is reduced by 0.5%, by 1 and 2 weight, and by replacing it with bismuth (Bi) element, both cost and wetting properties are improved. The Sn-2Ag-0.5Cu-1Bi (SAC-1Bi) alloy gives the best results [13]. It has been reported that adding aluminum (Al) nanoparticles to Sn-based solder alloys improves the interfacial microspheres and melting temperatures [14]. To improve the wetting and mechanical properties of this alloy, the addition of aluminum (Al) is envisaged. This study produced a new quinary Sn-2Ag-0.5Cu-1Bi-xAl (SACBi-xAl) solder alloy by adding Al by weight (x=0.05, 0.1, 0.3, 0.5, and 0.6%) to the SAC-1Bi soldering alloy. Wetting properties and melting temperatures of these quinary lead-free solder alloys on copper (Cu) backing in argon (Ar) atmosphere at 275, 300, and 325°C temperatures were investigated. The behavior of Al-doped Sn-based solder alloys was investigated.

MATERIALS AND METHOD

SACBi-Al Pb-free solder alloy wettability was analyzed by the sessile drop method on a 99.85% pure electrolytic copper substrate. Lead-free solder alloys were dropped onto the copper substrate at predetermined temperatures (275, 300, and 325°C). The experiment was recorded for about 10 minutes at 5, 10, 15, 30, 60, 90, 120, 150, 300, and 600 seconds and by the "300 FPS" model video camera as soon as the drops fell on the Cu substrate. The contact angle between the solder/Cu substrate was measured with the "Corel Draw X5 software" with the help of the screenshots of the video in the specified seconds. The graphs of the wetting angle values measured at the end of the experiment were plotted using the "Sigma Plot 12" program. The chemical components and intermetallic layers (IMCs) that may occur on the interface between the solder alloy and the Cu substrate were investigated with the help of XRD analysis. The IMCs formed on the interface between the solder and the Cu substrate were examined with the help of SEM analysis. They observed one by one for three experimentally determined temperature values [15].

RESULTS AND DISCUSSIONS

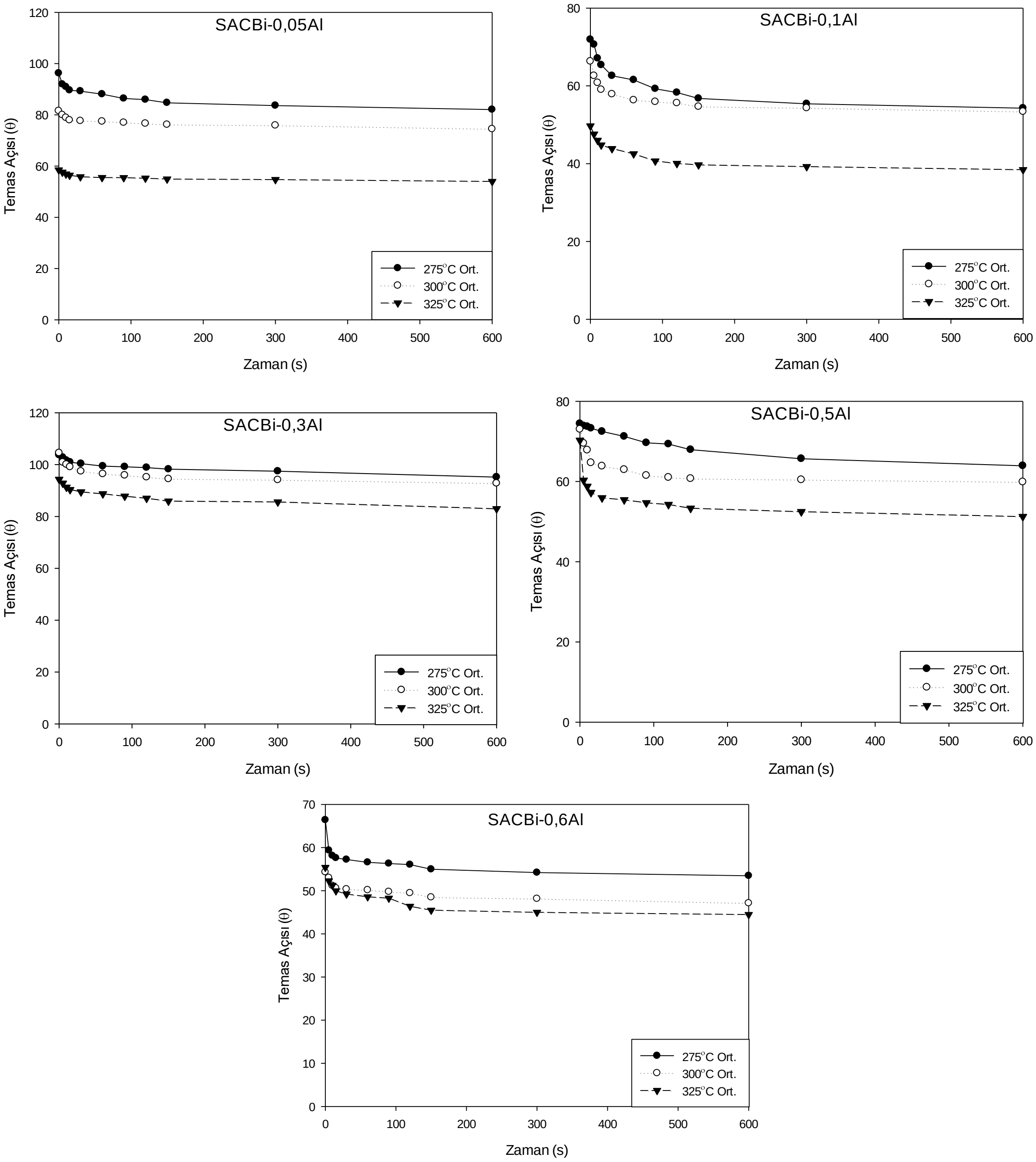

Fig. 1 Time-dependent wetting angle values of quinary lead-free solder alloy Sn-based SACBi-xAl at 275, 300, and 325°C.

When the graph of the wetting angle changes over time, it is seen that the angle values decrease parabolic and stabilize after the 60th second (Figure 1). When comparing temperatures of 275, 300, and 325℃, the contact angles corresponding to the temperature values decrease as the temperature rises. In addition, the tendency of the solder alloy to spread on the Cu substrate increases in proportion to the wetting angle value. The smaller the wetting angle values, the faster the spreading rate of the alloy. The contact angle measurement results of newly produced quintuple lead-free solder alloys at 275℃, 300℃, and 325℃ temperatures are graphed (Figure 1). It is degrees at 275℃, 82.05° for SACBi-0.05Al, 54.26° for SACBi-0.1Al, 91.21° for SACBi-0.3Al, 63.90° for SACBi-0.5Al and 53.46° for SACBi-0.6Al, respectively. It is degrees at 300℃, 74.45° for SACBi-0.05Al, 53.39° for SACBi-0.1Al, 89.37° for SACBi-0.3Al, 59.86° for SACBi-0.5Al and 47.11° for SACBi-0.6Al, respectively. It is degrees at 325℃, 53.98° for SACBi-0.05Al, 38.44° for SACBi-0.1Al, 76.12° for SACBi-0.3Al, 51.24° for SACBi-0.5Al and 44.46° for SACBi-0.6Al, respectively. It has been reported that the wetting angle value decreases as the temperature value increases for SACBi-xAl solder alloys. The lowest contact angle was reported as 38.44° for SACBi-0.1Al solder alloy.

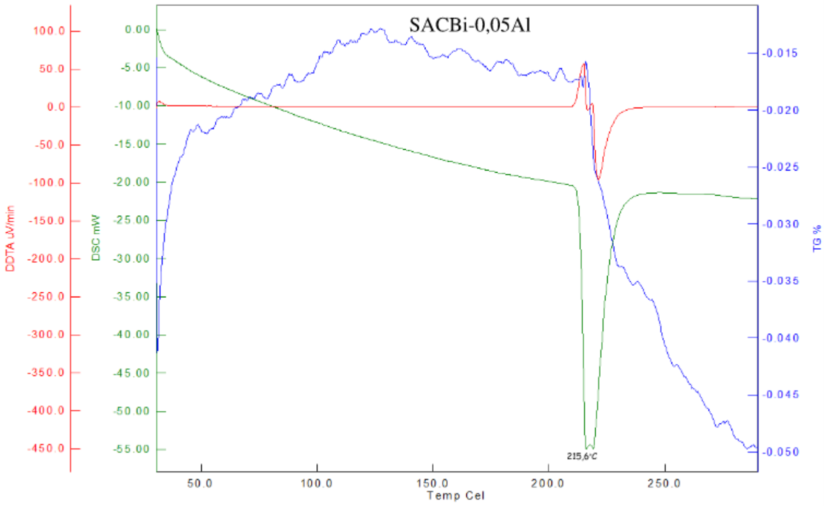

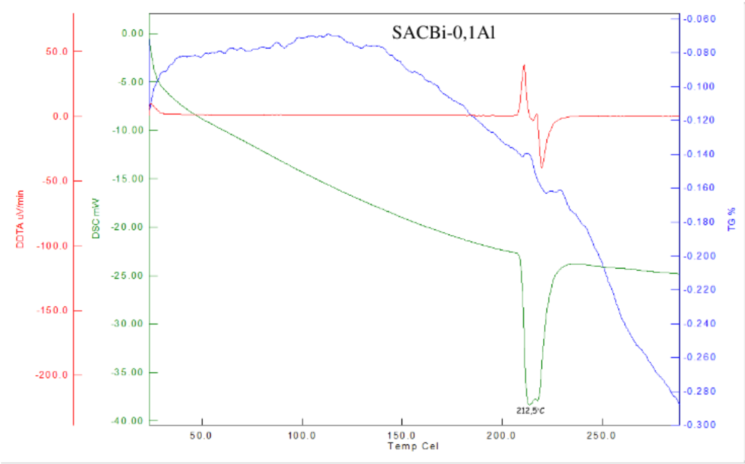

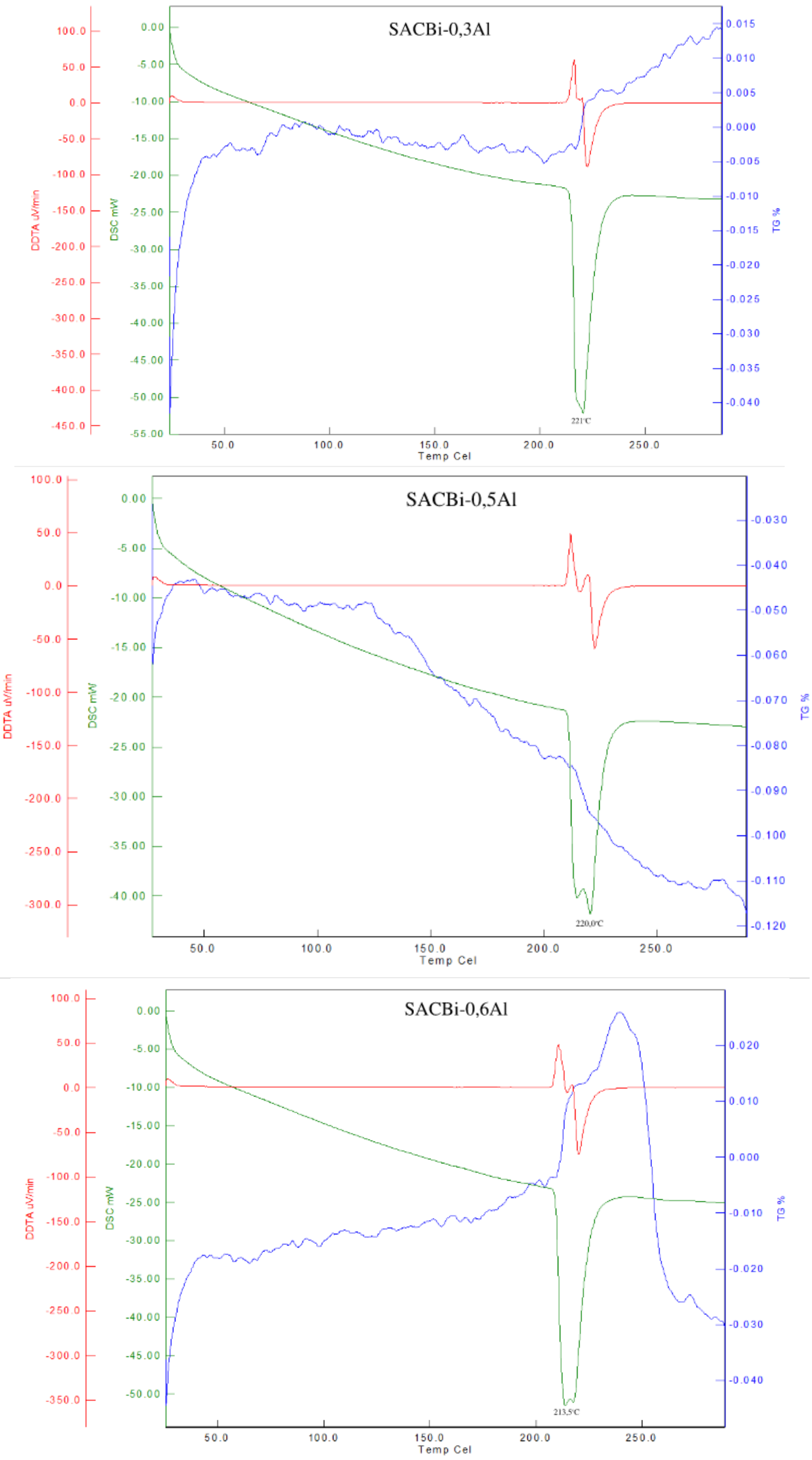

Fig. 2. DSC analysis of the quintuple lead-free solder alloys SACBi-xAl (x=0.05, 0.1, 0.3, 0.5 and 0.6).

The melting temperature of the SAC-1Bi solder alloy has been reported as 219°C [13]. With the addition of 0.05, 0.1, 0.3, 0.5, and 0.6% Al to the SAC-1Bi solder alloy, it is seen that the melting temperature decreases until the addition of 0.5% for micro alloyed solder alloys. The alloy’s melting temperature containing 0.5Al increases compared to the SAC-1Bi solder alloy. A decrease was achieved again with the 0.6Al solder alloy (Figure 2).

CONCLUSION

(96.5-x)Sn-2Ag-0.5Cu-1Bi-xAl (x = 0.05%, 0.1 0.3, 0.5 and 0.6) lead-free solder alloys in Argon (Ar) gas atmosphere The effects of Cu on wetting on the litter were investigated. In lead-free solder alloys with 0.05% and 0.1% addition, it is seen that the contact angle values decrease as the Al addition increases. It is seen that the solder alloy with the addition of 3%Al adversely affects the wetting. In 0.5% and 0.6% Al added alloys, a decrease was observed in the contact angle values again in terms of wetting properties. The lowest contact angle value was measured as 38.44° in SACBi-0.1Al alloy at a temperature of 325°C. The lowest melting temperature value was 212.5℃ for SACBi-0.1Al solder alloy. For the solder alloy containing 0.5 and 0.1Al, the melting temperature decreased as the Al addition increased. The melting temperature of the 0.3Al added solder alloy increased. The melting temperature has been reported to decrease as the Al content increases for 0.5 and 0.6 Al solder alloys. The lower the melting temperature, the lower the contact angle. At the same time, as the melting temperature increases, the wetting angle also increases. It is clearly seen that there is a correlation between the melting temperature and the contact angle.

ACKNOWLEDGEMENT

This work was supported by the Karabuk University Scientific Research Project (BAP). Within the scope of the Comprehensive Research Project, it was supported with the project number “KBÜBAP-21-KP-091”.

REFERENCES

[1] L. Yang, Y. Zhang, C. Du, J. Dai, and N. Zhang, “Effect of aluminum concentration on the microstructure and mechanical properties of Sn-Cu-Al solder alloy,” *Microelectronics Reliability*, vol. 55, no. 3–4, pp. 596–601, Feb. 2015, doi: 10.1016/j.microrel.2014.12.017.

[2] W. Yang *et al.*, “Effect of aluminum addition on the microstructure and properties of non-eutectic Sn-20Bi solder alloys,” *Materials*, vol. 12, no. 7, 2019, doi: 10.3390/ma12071194.

[3] D. Soares, C. Vilarinho, J. Barbosa, R. Silva, M. Pinho, and F. Castro, “Effect of the Bi content on the mechanical properties of a Sn-Zn-Al-Bi solder alloy.”

[4] X. Chen, M. Li, X. X. Ren, A. M. Hu, and D. L. Mao, “Effect of Small Additions of Alloying Elements on the Properties of Sn-Zn Eutectic Alloy.”

[5] M. F. Mohd Nazeri, M. Z. Yahaya, A. Gursel, F. Cheani, M. N. Masri, and A. A. Mohamad, “Corrosion characterization of Sn-Zn solder: a review,” *Soldering and Surface Mount Technology*, vol. 31, no. 1, pp. 52–67, Feb. 2019, doi: 10.1108/SSMT-05-2018-0013.

[6] M. Hasnine and M. J. Bozack, “Effects of Ga Additives on the Thermal and Wetting Performance of Sn-0.7Cu Solder,” *J Electron Mater*, vol. 48, no. 6, pp. 3970–3978, Apr. 2019, doi: 10.1007/S11664-019-07171-0/METRICS.

[7] H. Ma *et al.*, “Shielding effect of Ag3Sn on growth of intermetallic compounds in isothermal heating and cooling during multiple reflows,” *Journal of Materials Science: Materials in Electronics*, vol. 29, no. 6, pp. 4383–4390, Mar. 2018, doi: 10.1007/S10854-017-8428-7.

[8] N. Jiang *et al.*, “Influences of doping Ti nanoparticles on microstructure and properties of Sn58Bi solder,” *Journal of Materials Science: Materials in Electronics*, vol. 30, no. 19, pp. 17583–17590, Oct. 2019, doi: 10.1007/S10854-019-02107-0.

[9] B. Ali, M. F. M. Sabri, I. Jauhari, and N. L. Sukiman, “Impact toughness, hardness and shear strength of Fe and Bi added Sn-1Ag-0.5Cu lead-free solders,” *Microelectronics Reliability*, vol. 63, pp. 224–230, Aug. 2016, doi: 10.1016/J.MICROREL.2016.05.004.

[10] M. H. Hon, T. C. Chang, and M. C. Wang, “Phase transformation and morphology of the intermetallic compounds formed at the Sn-9Zn-3.5Ag/Cu interface in aging,” *J Alloys Compd*, vol. 458, no. 1–2, pp. 189–199, Jun. 2008, doi: 10.1016/J.JALLCOM.2007.04.004.

[11] H. L. Lai and J. G. Duh, “Lead-free Sn-Ag and Sn-Ag-Bi solder powders prepared by mechanical alloying,” *J Electron Mater*, vol. 32, no. 4, pp. 215–220, 2003, doi: 10.1007/S11664-003-0212-1/METRICS.

[12] L. Yang, Y. Zhang, J. Dai, Y. Jing, J. Ge, and N. Zhang, “Microstructure, interfacial IMC and mechanical properties of Sn-0.7Cu-xAl (x=0-0.075) lead-free solder alloy,” *Mater Des*, vol. 67, pp. 209–216, Feb. 2015, doi: 10.1016/j.matdes.2014.11.036.

[13] A. M. Erer and S. Oguz, “Wetting characteristic of Sn-(3-x)Ag-0.5Cu-xBi quaternary solder alloy systems,” *Soldering and Surface Mount Technology*, vol. 32, no. 1, pp. 19–23, Jan. 2020, doi: 10.1108/SSMT-08-2018-0028/FULL/XML.

[14] A. K. Gain and L. Zhang, “Harsh service environment effects on the microstructure and mechanical properties of Sn–Ag–Cu-1 wt% nano-Al solder alloy,” *Journal of Materials Science: Materials in Electronics*, vol. 27, no. 11, pp. 11273–11283, Nov. 2016, doi: 10.1007/s10854-016-5250-6.

[15] A. M. Erer, S. Oguz, and Y. Türen, “Influence of bismuth (Bi) addition on wetting characteristics of Sn-3Ag-0.5Cu solder alloy on Cu substrate,” *Engineering Science and Technology, an International Journal*, vol. 21, no. 6, pp. 1159–1163, Dec. 2018, doi: 10.1016/J.JESTCH.2018.10.002.

Impact Of Aluminum Addition On The Melting Point And Wettability Of The Sn-2Ag-0.5Cu-1 in Solder Alloy System

Masoud Giyathaddin Obaid[1*], Ahmet Mustafa Erer[2]
[1]*Faculty of science, Physics Department, Karabük University, Türkiye*

* Corresponding author e-mail address: masoudobaid34@gmail.com

ORCID Numbers: 0000-0002-6878-2108 (Masoud Giyathaddin.Obaid), 0000-0003-4358-4010 (Ahmet Mustafa.Erer)

***Abstract* -** This study explored at how adding aluminum affected the melting point and wettability of (96.5-X)Sn-2Ag-0.5Cu-1In-(x)AL quinary lead-free solder alloys with (x = 0.3,0.5,0.7,0.8,0.9 in wt%). Sessile drop technique was used to determine the contact angles of solder alloys on Cu substrate at specific temperatures (275^0C,300^0C, 325^0C). By using a differential scanning calorimeter (DSC), it was revealed that SAC205-1In-0.3Al Pb-free solder alloy exhibits lower melting temperatures than SAC205-1In-0.5Al, SAC205-1In-0.7Al, SAC205-1In-0.8Al, and SAC205-1In-0.9Al alloys. The wettability of SAC205-1In-0.3Al was found to be the best. At 325 °C on a Cu substrate, the SAC205-1In-0.3Al contact angle was lowest at 37.61°. The production cost of (96.5-x)Sn-2Ag-0.5Cu-1In-(x)Al produced solder alloys will be reduced by Sn-Al optimization (x = 0.3%,0.5%,0.7%,0.8%, and 0.9 wt. %). The results of wetting tests show that the addition of 0.3,0.5,0.7, 0.8, and 0.9 in Wt.% Al improves the wetting properties of the Sn-2Ag-0.5Cu-1In. The lowest wetting angle ($^0\theta$) was obtained as 34,66° for Sn-2Ag-0.5Cu-1In-0.8 Al alloy at a temperature of 325 °C.

Keywords – *Contact angle, Wettability, Melting temperature, sessile drop technique*

INTRODUCTION

In the recent period, many lead-free alloys have appeared, such as Sn-Ag, Sn-Cu, Sn-Zn, and others. Research has advanced to propose Sn-Ag-Cu alloy to replace the traditional solder Sn-Pb, as this alloy has good properties such as good reliability, excellent creep resistance, and thermal fatigue [1,2]. The characteristics of lead-free solder alloys are enhanced using two alternative methods. The first is the addition of elements to the SAC alloy, such as Ga, which improves the wetting properties and improves the performance of the alloy as a whole. The second method is the addition of metal, ceramic, and polymer nanoparticles or particles to obtain different SAC solder properties. Depending on the type and size of the added particles [3]. The researchers are also adding a fourth element to the SAC alloy to reduce the SAC melting temperature. According to the results, adding a little quantity of Ti can successfully refine the microstructure while also slightly lowering the melting temperature and melting range of the SAC solder alloy [4]. Wetness is defined by the ability of the molten solder to spread on its substrate during the reflow process [5]. Moser et al. [6] verified that the addition of In to SAC alloy affected the wettability, giving good wet diffusion connections on the surface of the substrate. There is an imperfection in the usage of SAC since its melting point, which ranges between 217 ^{0}C and 219 ^{0}C, is higher than that of the Sn-Pb alloy, which is 183 ^{0}C [7], as well as the high silver content causing an increase in the cost [8]. Therefore, several studies were conducted to try to reduce silver from lead-free alloys (SAC) in order to improve the properties [9], and make sure that the mechanical properties improved as a result of reducing silver [10]. Accordingly, a fourth element was added to obtain desirable properties for SAC in order to reduce the melting point and welding cost and increase reliability thermal mechanical properties [3]. This addition has attracted researchers, especially the addition of aluminum as nanoparticles or minor alloying element [11-17]. Amagai [11] noticed that adding 0.05% of aluminum as nanoparticles that had no effect on the interfacial IMC, and a small number of works were conducted to know the effect of adding aluminum on the mechanical and interfacial properties. Also, some studies confirmed that the addition of aluminum to Sn-Ag (SA) solder had an effect on Al_2Cu IMC and ambiguous Al-Cu IMC of bulk aluminum copper with a copper substrate [13, 14, 16]. The contact angle values indicate the degree of wettability, if the contact angle (ϴ) is between 0^0 and 30^0 , then it means there is a very good wetting and if the contact angle is between 40^0 and 55^0 then wetting is good.[17]. This study investigates the impacts of Aluminum addition on the wettability of the Pb-free solder alloy Sn- 2Ag- 0.5Cu-1In , to produce quinary lead-free solder alloy (96.5-x)Sn–2Ag-0.5Cu-1In–(x)Al, where x = 0.3, 0.5, 0.7, 0.8, and 0.9 wt%. Then studying the performance of the new alloy and its's physical properties microstructure, melting temperature, and intermetallic regions of alloy using X-ray diffraction (XRD), X-ray fluorescence (XRF), scanning electron microscope, energy-dispersive X-ray spectroscopy (SEM + EDX), and differential scanning calorimeter (DSC).

MATERIALS AND METHOD

In this study, Lead-free solder alloys SAC205-1In-xAl, as well as the oxygen-free environment were selected for the solder and Cu substrate, respectively. The produced quinary lead-free solder alloys ((96.5-x)Sn-Ag-Cu-1In-(x)Al) where (x=0.3%, 0.5%,0.7%,0.8%,0.9%) was subjected to X-RAY fluorescence(XRF) analysis with the help of the "RIGAKU ZSX Primus II" device in the KBU MARGEM Laboratory. The accuracy of the metal ratios in the alloy in % by weight has been obtained. Table 1 provides a list of the chemical combinations of the investigated lead-free solder alloys. A Casio-Pro Ex-F1,600 FPS model camera was used to capture images of the drops at intervals of 5, 10, 15, 30, 60, 90, 120, 150, 300, and 600 seconds. Currently, 99.85% pure electrolytic copper substrate was utilized to test the quinary lead-free solder alloy's wetting characteristics SAC205-1In-0.3Al, SAC205-1In-0.5Al, SAC205-1In-0.7Al, SAC205-1In-0.8Al, and SAC205-1In-0.9Al. The Sessile drop method was utilized to conduct wetting experiments. This method involved dropping SAC205-1In-xAl, quinary lead-free solder alloys onto a Cu substrate at different temperatures of 275, 300, and 325°C as shown in table 2. In order to quantify the contact angles for each drops from the right and left sides, images were imported into the CorelDRAW Graphics Suite 2022 x-64 software. These procedures were repeated for each temperature, and as a result, average angle values were computed and replacement diagrams were created using the EXCEL.EXE program. The DSC. analysis was performed on specimens with a maximum weight of 30 mg and at a temperature range of 40–300 °C to determine the melting temperatures of alloys (5 min.).

Table 1. XRF analysis results of Sn-Ag-Cu-In-xAl a quinary lead-free solder alloy that shows chemical composition of Pb-free solder alloys (wt. %).

Pb-free alloys	**Sn**	**Ag**	**Cu**	**In**	**Al**
96,2Sn-2Ag-0,5Cu-1In-0,3Al	96,2668	1,9713	0,4528	0,9993	0,3
96Sn-2Ag-0,5Cu-1In-0,5Al	95,4494	2,1554	0,49	0,997	0,4843
95,8Sn-2Ag-0,5Cu-1In-0,7Al	95,7915	1,9395	0,4872	1,024	0,7289

95,7Sn-2Ag-0,5Cu-1Ini-0,8Al	95,6977	2,0048	0,4195	1,0928	0,8078
95,6Sn-2Ag-0,5Cu-1In-0,9Al	95,6414	2,0532	0,4835	1,0632	0,9112

Table 2. List of The Sessile drop technique experiments that are conducted at different temperature for each quinary lead-free solder alloys formed by the addition of Al to SAC205-1In.

(x) Al (wt%)	**Temperature (^{0}C)**	**Lead-free solder alloys (96.5-x)Sn-2Ag-0.5Cu-1In-(x)Al**	**Number of experiments**
0.3	275	96.2Sn-2Ag-0.5Cu-1In-0.3Al	3
	300		3
	325		3
0.5	275	96Sn-2Ag-0.5Cu-1In-0.5Al	3
	300		3
	325		3
0.7	275	95.8Sn-2Ag-0.5Cu-1In-0.7Al	3
	300		3
	325		3
0.8	275	95.7Sn-2Ag-0.5Cu-1In-0.8Al	3
	300		3
	325		3
0.9	275	95.6Sn-2Ag-0.5Cu-1In-0.9Al	3
	300		3
	325		3
Total number of experiments			45

RESULTS AND DISCUSSION

The relationship between the contact angle, temperature, and time is depicted in Fig. 1. Lead-free solder alloys SAC205-1In-0.3Al, SAC205-1In-0.5Al, SAC205-1In-0.7Al, SAC205-1In-0.8Al, and SAC205-1In-0.9Al have contact angles that fluctuate over time rather than decreasing abruptly with temperature. For about the first thirty seconds at each temperature, the lead-free solder alloys displayed a significant reduction in contact angle. The degree of wettability is shown by the contact angle measurements. [18]. The lowest average contact angles for SAC-In-0.3Al solder alloy was 47.84^0 at temperature 275 ^{0}C, 42.10^0 at temperature 300 ^{0}C, and 39.88^0 at temperature 325 ^{0}C, for SAC-In-0.5Al solder alloy was 47.48^0 at temperature 275 ^{0}C, 46.27^0 at temperature 300 ^{0}C, and 40.12^0 at temperature 325 ^{0}C, for SAC-In-0.7Al solder alloy was 61.54^0 at temperature 275 ^{0}C, 50.78^0 at temperature 300 ^{0}C, and 48.32^0 at temperature 325 ^{0}C, for SAC-In-0.8Al solder alloy was 50.26^0 at temperature 275 ^{0}C, 47.17^0 at temperature 300 ^{0}C, and 37.95^0 at temperature 325 ^{0}C, and for SAC-In-0.9Al solder alloy was 50.02^0 at temperature 275 ^{0}C, 45.71^0 at temperature 300 ^{0}C, and 41.82^0 at temperature 325 ^{0}C.

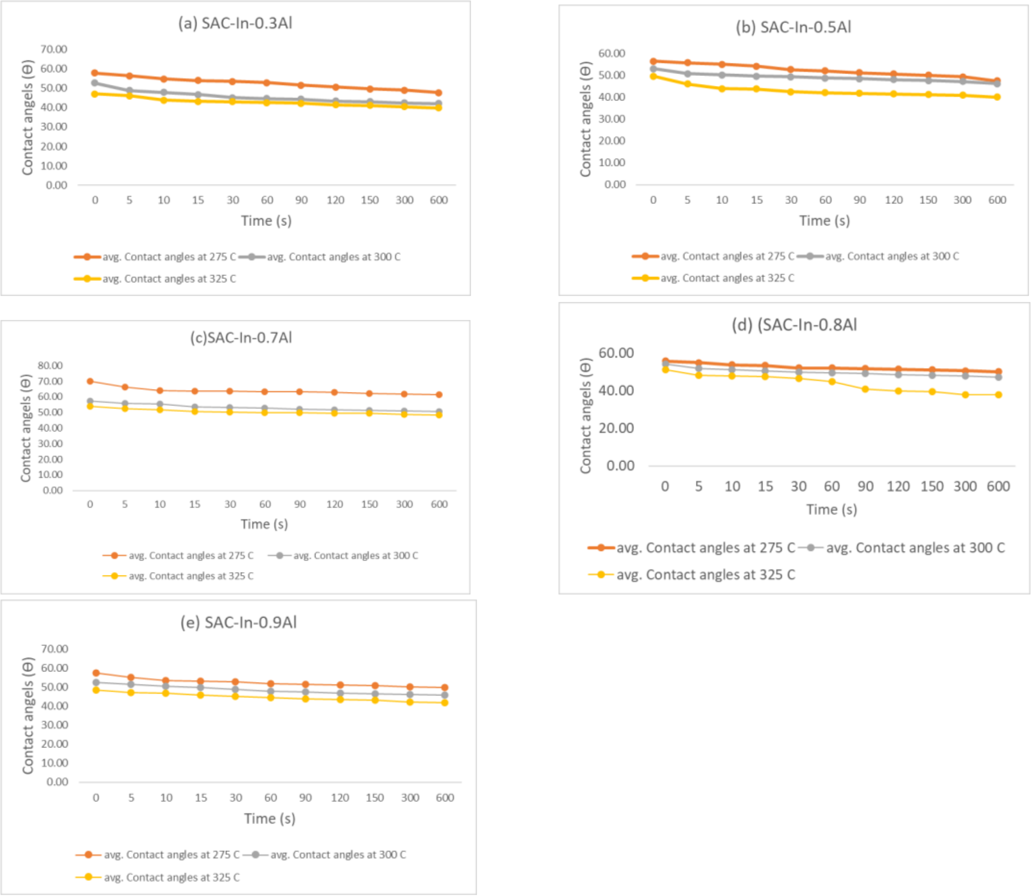

Fig.1 The average contact angle of (a) SAC205-1In-0.3Al, (b) SAC205-1In-0.5Al, (c) SAC205-1In-0.7Al, (d) SAC205-1In-0.8Al, and (e) SAC205-1In-0.9Al alloys on Cu substrate at different temperatures 275°C, 300°C, and 325°C.

The melting points of the solder alloys SAC205-1In-xAl where (x=0.3,0.5,0.7,0.8, and 0.9) were determined by DSC analysis to be 214.3, 219.7, 219.3, 219.1, and 220.5, respectively as shown in fig.2. DSC testing for solder alloys ((96.5-x)Sn-2Ag-0.5Cu-1In-xAl) were conducted in MARGEM laboratories at Karabuk University. SAC-1In solder alloy was reported to have a 217.7°C melting point [19]. As compared to SAC-1In and SAC305 (217.7 and 219.1°C, respectively), the melting temperature of a quinary lead-free solder alloy (SAC-1In-0.3Al) is lower, and the melting temperatures of other quinary lead-free solder alloys are near to those of SAC-1In. As a result, the wettability of the lead-free solder alloy SAC205-1In-0.3Al is higher to that of the solder alloys SAC205-1In-0.5Al, SAC205-1In-0.7Al, SAC205-1In-0.8Al, and SAC205-1In-0.9Al.

CONCLUSION

Using the sessile drop method in an atmosphere of argon, the influence of melting temperature on contact angle of lead-free solder alloys SAC205-1In-0.3Al, SAC205-1In-0.5Al, SAC205-1In-0.7Al, SAC205-1In-0.8Al, and SAC205-1In-0.9Al was studied. According to the experimental findings, equilibrium contact angles (Ɵ) dropped proportionately as temperature increased. The lead-free solder alloy SAC205-1In-0.3Al had the lowest contact angle and melting temperatures, which were measured as 37.61° and 214.3°C, respectively.

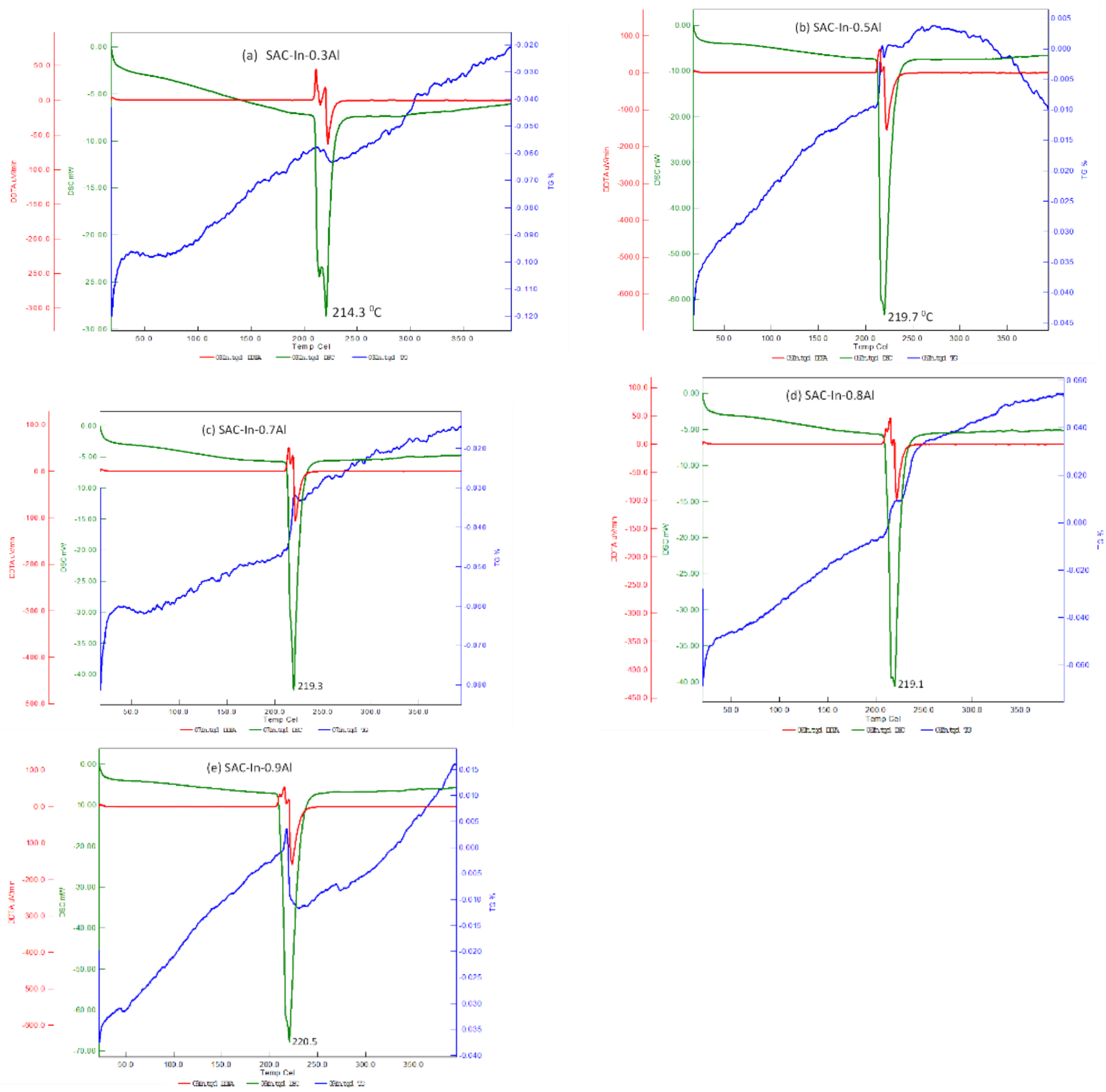

Figure 2 depicts the results of the DSC test of the alloys (a) SAC 205-1In-0.3Al, (b) SAC 205-1In-0.5Al, (c) SAC 205-1In-0.7Al, (d) SAC 205-1In-0.8Al, and (e) SAC 205-1In-0.9Al.

ACKNOWLEDGEMENT

This project has been supported by KBUBAP-21-KP-091.

REFERENCES

[1] S. Xu, A. H. Habib, A. D. Pickel, and M. E. McHenry, (2015), “Magnetic nanoparticle-based solder composites for electronic packaging applications,” *Progress in Materials Science*, vol. 67, pp. 95–160.

[2] A. A. El-Daly and A. M. El-Taher, (2013), “Evolution of thermal property and creep resistance of Ni and Zn-doped Sn-2.0Ag- 0.5Cu lead-free solders,” *Materials & Design*, vol. 51, pp. 789–796.

[3] Sun, L. and Zhang, L. (2014), “Properties and microstructure of Sn-Ag-Cu-X lead-free solder joints in electronic packing”, Advances in Materials Science and Engineering, Vol. 2015, Article ID 639028 , pp. 1-16.

[4] Chuang, C. L., Tsao, L. C., Lin, H. K., & Feng, L. P. (2012). Effects of small amount of active Ti element additions on microstructure and property of Sn3. 5Ag0. 5Cu solder. Materials Science and Engineering: A, 558, 478-484.

[5] S. K. Ghosh, A. S. M. A. Haseeb, and A. Afifi, (2013), “Effects of metallic nanoparticle doped flux on interfacial intermetallic compounds between Sn-3.0Ag-0.5Cu and copper substrate,” in *Proceedings of the IEEE 15th Electronics Packaging Technology Conference (EPTC ’13)*, pp. 21–26, Singapore.

[6] Z. Moser, P. Sebo, W. Gąsior, P. Svec, and J. Pstru´s, (2009), “Effect of indium on wettability of Sn–Ag–Cu solders. Experiment vs. modeling, Part I,” *Calphad*, vol. 33, no. 1, pp. 63–68.

[7] Illyefalvi-Vitéz, Z., Pinkola, J., Harsányi, G., Dominkovics, C., Illés, B. and Tersztyánszky, L. (2005), “Present status of transition to Pb-free soldering”, 28th International Spring Seminar on Electronics Technology: Meeting the Challenges of Electronics Technology Progress, 2005, pp. 88-93.

[8] Cheng, S., Huang, C.-M. and Pecht, M. (2017), “A review of lead-free solders for electronics applications”, Microelectronics Reliability, Vol. 75, pp. 77-95.

[9] Amagai, M., Toyoda, Y. and Tajima, T. (2003), “High solder joint reliability with lead free solders”, Presented at Proceedings of the 53rd Electronic Components and Technology Conference, 2003, pp. 317-322.

[10] Terashima, S., Kariya, Y., Hosoi, T. and Tanaka, M. (2003), “Effect of silver content on thermal fatigue life of Sn-xAg-0.5Cu flip-chip interconnects”, Journal of Electronic Materials, Vol. 32 No. 12, pp. 1527-1533.

[11] Amagai, M.A. (2008), study of nanoparticles in Sn–Ag based lead free solders. *Microelectron. Reliab.*, *48*, 1–16.

[12] Gain, A.K.; Chan, Y.C. (2012)**,**The influence of a small amount of Al and Ni nano-particles on the microstructure, kinetics and hardness of Sn-Ag-Cu solder on OSP-Cu pads. *Intermetallics*, *29*, 48–55.

[13] Xia, Y.H.; Jee, J.K.; Yu, J.; Lee, T.Y. (2008), Effect of aluminum concentration on the interfacial reactions of Sn-3.0Ag-xAl solders with copper and ENIG metallizations. *J. Electron. Mater. 37*, 1858–1862.

[14] Li, J.F.; Agyakwa, P.A.; Johnson, C.M. (2012), Effect of trace Al on growth rates of intermetallic compound layers between Sn-based solders and Cu substrate. *J. Alloys Compd. 545*, 70–79.

[15] Kantarcıo˘glu, A.; Kalay, Y.E. (2014), Effects of Al and Fe additions on microstructure and mechanical properties of SnAgCu eutectic lead-free solders. *Mat. Sci. Eng. A 593*, 79–84.

[16] Kotadia, H.R.; Panneerselvam, A.; Mokhtari, O.; Green, M.A.; Mannan, S.H. (2012), Massive spalling of Cu-Zn and Cu-Al intermetallic compounds at the interface between solders and Cu substrate during liquid state reaction. *J. Appl. Phys. 111*, 074902–074906.

[17] Moser, Z., Gąsior, W., Pstruś, J., & Dębski, A. (2008). Wettability studies of Pb-free soldering materials. *International Journal of Thermophysics*, *29*(6), 1974-1986.

[18] Erer, A. M., Candan, E., Güven, M. H., Turen, Y., “Measurement and prediction of contact angles of Pb-free SnAg solder alloys on Cu substrate”, Eur. Phys. J. Appl. Phys., 54(1), 1-4, (2011).

[19] Uyanik, O., Erer, A. M., & Türen, Y. Effect of Indium on Wettability of Sn-2Ag-0, 5Cu-1In Quaternary Solder Alloy on Cu Substrate. *El-Cezeri*, *6*(1), 1-7.

Optimizing Photovoltaic Model Parameters with an Improved Artificial Jellyfish Search Algorithm

Ramadan Ahmed Ali Agoub[1*], Aybaba Hançerlioğulları[2]

[1]*Department of Computer Engineering, Kastamonu University, Kastamonu, Türkiye,*
[2]*Department of Physics, Faculty of Science, Kastamonu University, Kastamonu, Türkiye*

* *Corresponding author:* ramadan_agoub@yahoo.com

ORCID Numbers: *0000-0001-9125-330X ([1*]Ramadan Ahmed Ali agoub), 0000-0000-1700-8480 ([2]Aybaba Hançerlioğulları*)

***Abstract* -** Photovoltaic (PV) systems are used to convert solar energy into electrical energy. The optimization of photovoltaic (PV) systems relies on the development of an accurate model of the parameter values for the solar/PV generating units. This work proposes a modified artificial jellyfish search optimizer (MJSO) with a novel premature convergence strategy (PCS) to define effectively the unknown parameters of PV systems. The PCS works on preserving the diversity among the members of the population while accelerating the convergence toward the best solution based on two motions: (i) moving the current solution between two particles selected randomly from the population, and (ii) searching for better solutions between the best-so-far one and a random one from the population. To confirm its efficacy, the proposed method is validated on three different PV technologies and is being compared with some of the latest competitive computational frameworks. İn this study, develops a novel meta-heuristic algorithm that is inspired by the behavior of jellyfish in the ocean and is called artificial Jellyfish Search (JS) optimizer. Applying new optimization methods such as the mermaid algorithm to increase the efficiency of photovoltaic (PV) systems

***Keywords* -** *Optimizer, PV sytems, Machine Learning, Artifical Jellyfish Algorithm, Solar Energy*

INTRODUCTION

The numerical simulations and results confirm the dominance of the proposed algorithm in terms of the accuracy of the final results and convergence rate. In addition, to assess the performance of the proposed approach under different operation conditions for the solar cells, two additional PV modules (multi-crystalline and thin-film) are investigated, and the demonstrated scenarios highlight the utility of the proposed MJSO-based methodology. Photovoltaic (PV) systems are used to convert solar energy into electrical energy. The importance of PV systems is considered as a main driving issue by scientists and companies for the advancement of energy compatibility and price reduction. In addition, manufacturing companies need to ensure maximum electricity production from PV power plants. Energy production from PV power systems strongly depends on weather conditions, solar radiation and temperature. In addition, these systems will inevitably suffer destruction along with the possible occurrence of electrical errors. Effective modeling of PV cells is necessary and important for controlling and predicting the performance of solar systems in different working conditions. However, modeling and parameter evaluation of PV cells is a very challenging task. The non-linear and scattered dimensions of meteorological statics etc. make it difficult to identify cell limits. Until now, several models were developed based on the physical process and related variables of PV cells.

ARTIFICIAL JELLYFISH SEARCH ALGORITHM

The simulation of the search behavior of jellyfish involves their following the ocean current, their motions inside a jellyfish swarm active and passive motion, a time control mechanism for switching among these movements, and their convergences into jellyfish bloom [1]. The new algorithm is successfully tested on benchmark functions and optimization problems. In a swarm, there are two types of motions: type A (passive motion) and type B (active motion). In the beginning, when the jellyfish swarm has just been shaped, most of jellyfish show passive motion. As time passes on, they increasingly show active motion. In passive motion, jellyfish move around their original locations. Consequently, each jellyfish updates its location by [1-5].

$$Xi(t + 1) = Xi(t) + \gamma s * \text{rand}(0, 1) * (UB - LB)$$

where X_i is a vector that contains the logistic chaotic values of the ith jellyfish, X_0 is an initial vector of jellyfish 0, generated randomly between 0 and 1. This vector is the start point that is relied on for generating the logistic chaotic values for the remainder of the jellyfish, UB and LB represent the upper and lower bounds of the search space, respectively. $\gamma s > 0$ represents the motion coefficient, associated with the motion length around locations of jellyfish. In this paper, $\gamma s = 0.1$.

To simulate the active motion (type B), we will randomly select a jellyfish (Jfj) different to the jellyfish of interest (Jfi). Consequently, to determine the direction of motion, a vector from Jfi to the Jfj is utilized to define the direction of motion. When the amount of food founded at the position of Jfj is greater than the amount at the position of Jfi , Jfi moves in the direction of Jfj . In contrast, if the available amount of food to Jfj is lesser than the available amount to Jfi , Jfi moves directly in opposite direction of Jfj . Thus, each jellyfish in a swarm moves directly to the better trend to find food. The motion direction and the updated location of a jellyfish are simulated by (55) and (56), respectively. This movement represents an effective way to exploit the search space. In Figure-1 show that of Jellyfish artificial intelligence algorithm [1-5].

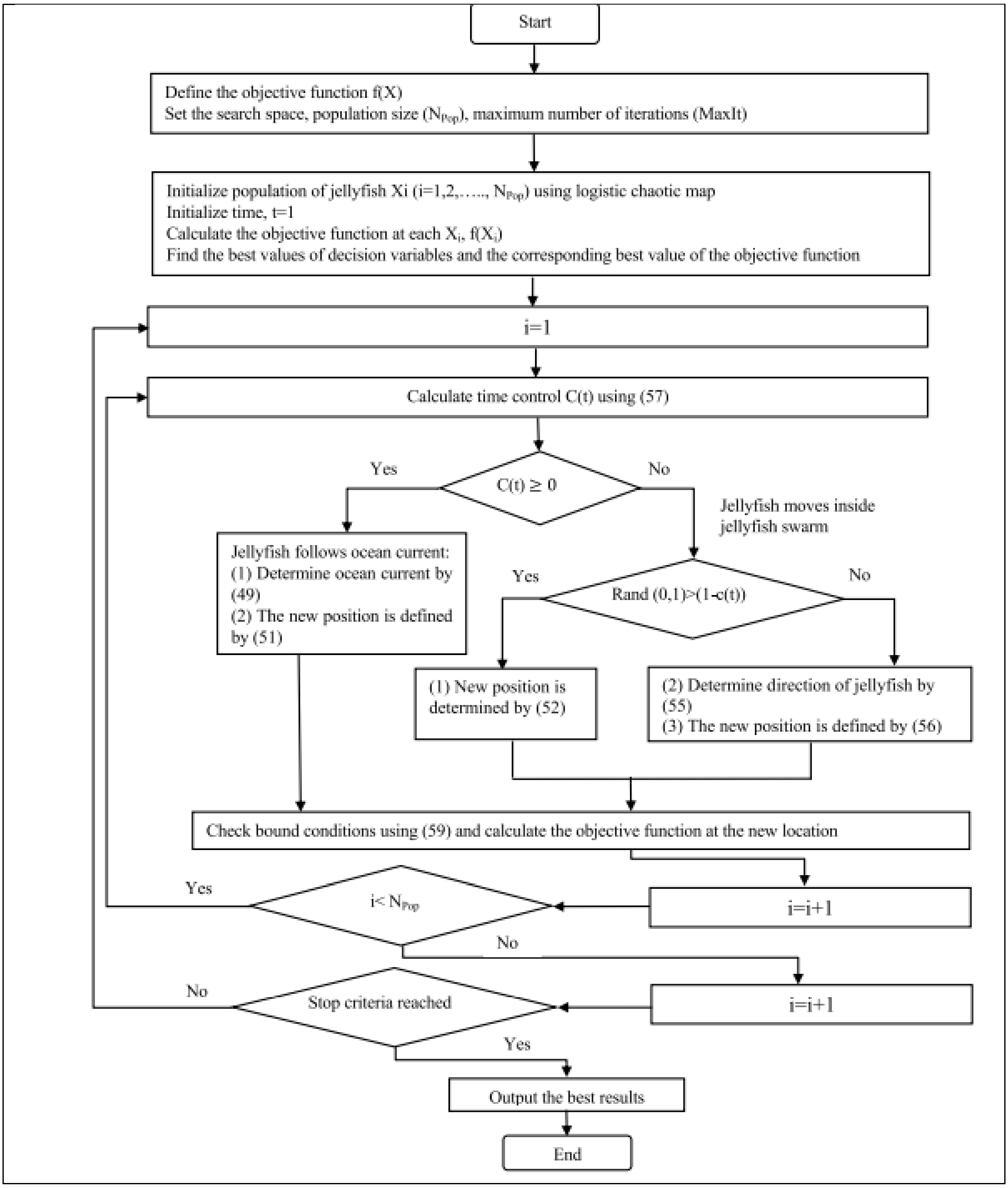

Figure.1 *Jellyfish artificial intelligence algorithm* [1]

OPTIMIZING PV/T SOLAR CELL SYTEMS

Solar Photovoltaic (PV) systems are one of the most promising renewable energy sources that convert solar energy into electrical energy in an environmentally friendly way. However, these systems have low efficiency and high relative costs. To overcome these disadvantages, a grid-connected PV system is needed to meet the load requirement. Solar cells cannot convert most of the solar radiation coming to their surface into efficient energy, and the temperature in the cells increases and a decrease in electrical efficiency is observed. Therefore, the PV cell temperature can be lowered naturally or by cooling with a forced refrigerant. Creating a hybrid system by using photovoltaic panels together with thermal systems is a solution for increasing efficiency. It is also well known that using a hybrid system reduces the need to use an external source of electrical energy. As a result of the literature review, many studies have been carried out to remove excess heat from the system by using gas and liquid fluids. Photovoltaic cells experience a decrease in efficiency with an increase in temperature due to increased resistance. PV/T systems can be designed to remove heat from the PV cells, thereby cooling the cells and increasing their efficiency by lowering the resistance. The result is a cold-running PV panel with higher efficiency and longer lifespan, and the production of hot fluids that can be used for residential, commercial or industrial applications. For monocrystalline (c-Si) and polycrystalline (pc-Si) silicon solar cells, the efficiency decreases by about 0.45% for every degree increase in temperature. For amorphous-silicone (a-Si) cells, the effect is less, with an increase in temperature of about 0.25% depending on the module design. This undesirable effect can be partially avoided by proper heat extraction with fluid circulation [6-7].

MATERIAL AND METHODS

An efficient optimization approach is needed to obtain the best value of unknown parameters in photovoltaic systems. In this work, the parameters of the single diode model (SDM) such as (IP, ISD, a, Rs, Rsh) are considered as a decision variable or a member of the mermaid algorithm Figure-2 shown that.

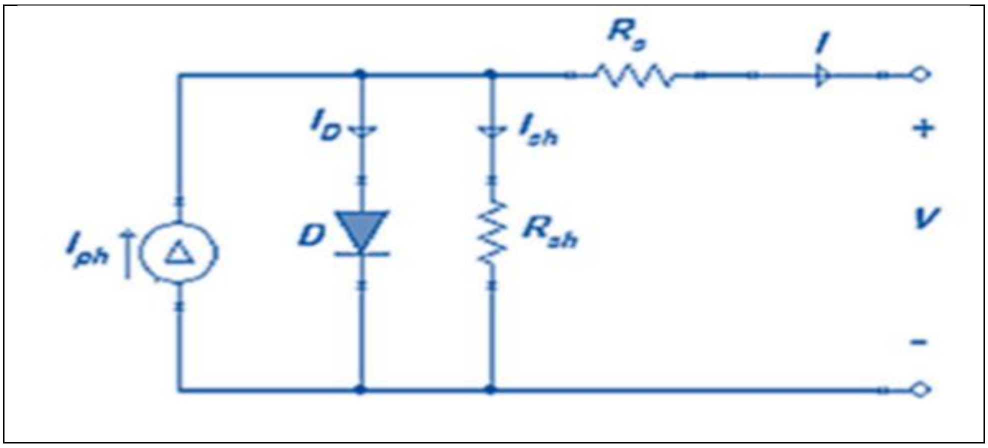

Figure 2. Equivalent circit of the single diode model (SDM)

CONCLUSION

Photovoltaic/Thermal (PV/T) systems provide hot fluid (usually water) production as well as electrical energy production. In addition, since overheating of PV systems is prevented, electricity generation performance is increased. In this study, a new aggregation model based on the efficiency and energy performance of PV/T systems was developed using the developed artificial Jellyfish Search Algorithm, and all simulation calculations were calculated with MatLap programming. The proposed system is a system based on modern group intelligence methods, and it is certain that algorithms such as jellyfish are more accurate than methods such as genetic and particle algorithms. The disadvantage of the proposed method is the high uncertainty of meta-heuristic algorithms and pseudo-random process to find optimal solutions [8-10]. As result, Our research which is all the simulation show that optimizing solar panels to increase power generation, presenting an optimization method in solar cells with mermaid algorithm and single diode model parameters with mermaid algorithm.

REFERENCES

[1] A. Jäger-Waldau, “Snapshot of photovoltaic, February 2020,” Energies, vol. 13, no. 4, p. 930, 2020.

[2] M. F. N. Khan, “A novel probabilistic generation model for grid connected PV based distributed generation,” J. Eng. Res., vol. 8, no. 1, 2020.

[3] M. S. Rawat and S. Vadhera, “A comprehensive review on impact of wind and solar photovoltaic energy sources on voltage stability of power grid,” J. Eng. Res., vol. 7, no. 4, 2019.

[4] M. A. Özçelik and A. S. Yilmaz, “Improving the performance of MPPT in PV systems by modified Perturb-and-Observe algorithm,” J. Eng. Res., vol. 3, no. 3, pp. 1–20, 2015.

[5] K. Abdul Mawjood, S. S. Refaat, and W. G. Morsi, “Detection and prediction of faults in photovoltaic arrays: A review,” in 2018 IEEE 12th International Conference on Compatibility, Power Electronics and Power Engineering (CPE-POWERENG 2018), 2018, pp. 1–8.

[6] M. K. Alam, F. Khan, J. Johnson, and J. Flicker, “A comprehensive review of catastrophic faults in PV arrays: types, detection, and mitigation techniques,” IEEE J. Photovoltaics, vol. 5, no. 3, pp. 982–997, 2015.

[7] A. Mellit, G. M. Tina, and S. A. Kalogirou, “Fault detection and diagnosis methods for photovoltaic systems: A review,” Renew. Sustain. Energy Rev., vol. 91, pp. 1–17, 2018.

[8] I. M. Karmacharya and R. Gokaraju, “Fault location in ungrounded photovoltaic system using wavelets and ANN,” IEEE Trans. Power Deliv., vol. 33, no. 2, pp. 549–559, 2017.

[9] W. Fenz, S. Thumfart, R. Yatchak, H. Roitner, and B. Hofer, “Detection of arc faults in PV systems using compressed sensing,” IEEE J. Photovoltaics, vol. 10, no. 2, pp. 676–684, 2020.

[10] S. Lu, B. T. Phung, and D. Zhang, “A comprehensive review on DC arc faults and their diagnosis methods in photovoltaic systems,” Renew. Sustain. Energy Rev., vol. 89, pp. 88–98, 2018.

6th Pak – Türk International Conference on Emerging Technologies in the field of Sciences and Engineering, May 4 – 6, 2023, Karabük University, Karabük, Türkiye

Investigation of Production Cross-Sections of ^{73}Se Radioisotope Via Proton Induced ReactionChannels

Sevki Senturk[1*], Tuncay Bayram[1] and Anes Hayder[1]

[1]*Department of Physics, Faculty of Science, Karadeniz Technical University*
* Corresponding author e-mail address: sevkisenturk61@gmail.com
ORCID Numbers: 0000-0001-8355-1307 (Sevki SENTURK), 0000-0003-3704-0818 (Tuncay BAYRAM), 0000-0001-
8166-1385 (Anes HAYDER)

Abstract—Todays, many radioisotopes are used for diagnosis and treatment in nuclear medicine. In line with the development of technology and the increasing need, studies on radioisotopes that are used and have the potential to be used in this field are still up-to-date. In this study, possible production mechanisms of ^{73}Se radio isotope, which can be used in positron emission tomography (PET), were investigated. Within the framework of the TALYS nuclear reaction calculation code, generation cross sections, reaction efficiencies and total activation values up to 60 MeV beam energy values were calculated and their compatibility with the data in the literature was examined.

Keywords— *Selenium-73, proton induced reactions, cross-section, reaction yield.*

INTRODUCTION

Many radioisotopes are used for diagnosis and treatment of diseases in the field of medicine [1]. Radioisotopes are used in nuclear medicine in various imaging devices such as Positron Emission Tomography (PET) and Single Photon Emission Tomography (SPECT). ^{73}Se is a radioisotope suitable for use in Positron Emission Tomography (PET), one of the nuclear medicine applications, due to its positron decay and 7.15 h half-life.

Radioisotopes are produced in three different ways: from nuclear reactor, linear accelerator (cyclotron) and nuclear generators. In nuclear reactors, radioisotopes produced by fission have a relatively long half-life and high purity rates. Since some of the nuclei obtained are rich in neutrons,they are used for more therapeutic purposes in nuclear medicine by beta decay, and some are used for imaging purposes by gamma decay [2]. In cyclotron, radioisotope production occurs as a result ofthe charged particles being accelerated in a magnetic field and sent to the target nucleus. Radioisotopes from the cyclotron are deficient in neutrons, so they decay by electron capture (EC) orbeta ($^{+}\beta$) decay [3]. Generators allow a short half-life radionuclide to be immediately separated froma longer half-life one for immediate use. It is very advantageous in terms of providing fast, regular use and low cost [4]. In 2004, Amjad et al. examined ^{75}As(p,3n)^{73}Se and ^{75}As(d,4n)^{73}Se reaction channels in the 0-70 MeV energy range and compared with ALICE, EMPIRE, and TALYS nuclear reaction codes for the consistency of experimental data. By normalizing the data they obtained, they determined the best cross-section values as 295 mb at 36 MeV and 203 mb at 41 MeV, respectively [5]. In another study,Fabbender et al. employed 1 µA beam current for the ^{nat}Br(p,x)^{73}Se reaction channel, and they obtained the optimal values in the 42-62 MeV range by comparing with ALICE nuclear code calculations [6]. In 2004, Rowshanfarzad et al. compered the measured ^{73}As(p,3n)^{73}Se reaction channel in 30 IBA accelerators with the nuclear calculation codes of ALICE and SRIM, which took measurements up to 30 MeV energy at 5 µA beam current. They determined the best efficiency value as 5.3 mCi/µA [7]. In this study, we have investigated the possible production mechanisms of ^{73}Se, which can be used in nuclear medicine applications. This study aims to determine the appropriate reaction channels for the use of ^{73}Se radioisotope in nuclear medicine and to provide preliminary information in experimental studies for radioisotope production by calculating the relevant optimal values. In thiscontext ^{75}As(p,3n)^{73}Se and ^{74}Se(p,d)^{73}Se reaction channels have been investigated within the framework of the TALYS 1.9 nuclear reaction code. Production cross-sections, reaction yield, and total activation values calculated up to 60 MeV energies for these reaction channels were compared with the available data in the literature.

MATERIALS AND METHODS

In this study, we investigated some possible production mechanisms of ^{73}Se using the nuclear reaction code TALYS. TALYS nuclear reaction calculation code allows us to evaluate the interaction between particles and nuclei such as protons and neutrons in the energy range of 1 keV- 200 MeV, and to evaluate between experimental and theoretical data [8]. TALYS nuclear reaction calculation code includes several different nuclear reaction models that provide a better understanding of nuclear reactions mechanisms. In the Constant Temperature Fermi Gas Model (CTFGM), the excitation energy is divided into two different parts where the constant temperature law is applied in the low energy region from 0 MeV to the matching energy EM, and fermi gas law is applied in the high energy region above EM [9]. Back Shifted Fermi Gas Model (BSFGM) was developed to evaluate the coupling energy as a modifiable parameter in the low energy region [10]. Generalised Superfluid Model (GSM) is a model developed to characterize the phase transitions from low energy region to the high energy region, where it behaves superfluid [11]. ^{75}As(p,3n)^{73}Se and ^{74}Se(p,d)^{73}Se reaction channels have been investigated using CTFGM, BSFG and GSM models of Level Density Model up to 60 MeV energy level within the framework of TALYS nuclear reaction calculation code.

RESULTS AND DISCUSSION

In this study, we have calculated the production cross-sections, reaction yield, and total activation values up to 60 MeV beam energy value for ^{75}As(p,3n)^{73}Se and ^{74}Se(p,d)^{73}Se reaction channels via TALYS 1.95 nuclear reaction calculation code. The calculated production cross-sections for the reaction channels are shown in Figures 1 and 2, respectively.

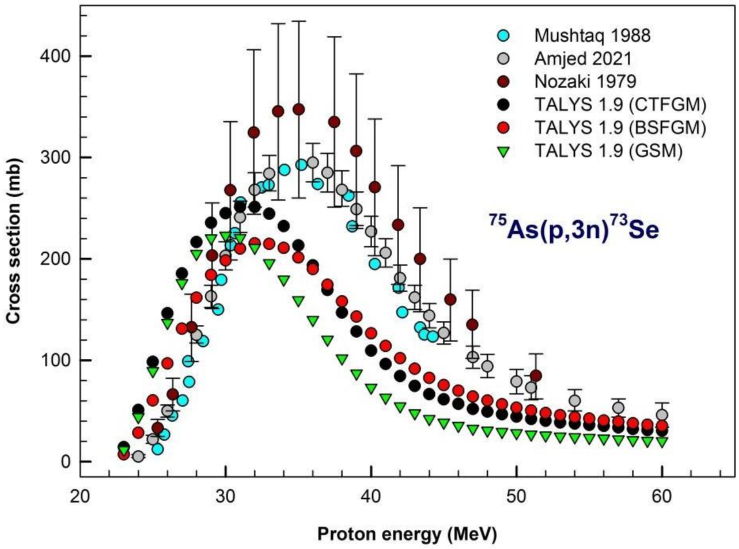

Fig. 1. Cross-section for the ^{75}As(p,3n)^{73}Se nuclear reaction.

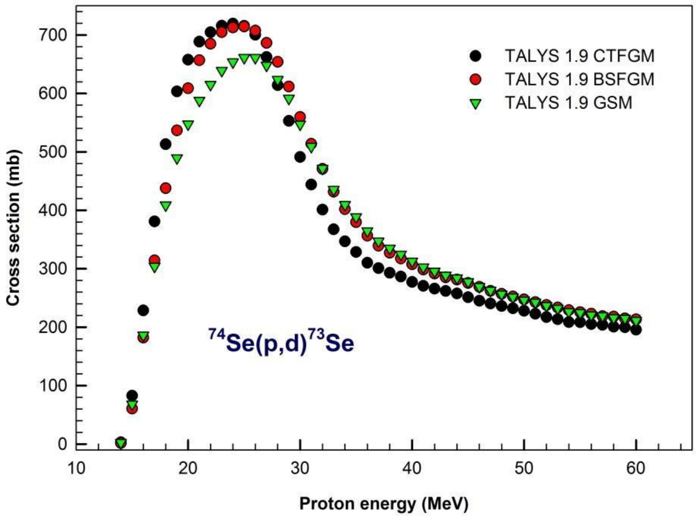

Fig. 2. Cross-section for the ^{73}Se(p,d)^{73}Se nuclear reaction.

In Fig 1, the calculated data peaked in the lower energy range, and considering this situation, it seen that it is generally in agreement with the experimental data [5, 12, 13]. The best model for ^{73}Se production by ^{75}As(p,3n)^{73}Se reaction channel has been determined as CTFGM. The maximum cross-section value obtained according to the best model has been calculated as 251.19 mb at 31 MeV. In Fig. 2, the calculated cross-section values for the ^{74}Se(p,d)^{73}Se reaction are given. In Fig.2, it seen that the obtained values peak in the range 20-30 MeV, and the best production cross-section value is also obtained from CTFGM. The maximum cross-section value obtained according to the best model has been calculated as 719.382 mb at 24 MeV. Fig. 3 and 4 show the reaction yield values for the ^{75}As(p,3n)^{73}Se and ^{74}Se(p,d)^{73}Se reaction channels. In this study, a current value of 1 mA has been used for the existing reaction channels. The reaction yield values obtained were calculated as 1.39 and 155.92 GBq/mAh, respectively. In Addition, total activation values have been calculated as seen in Fig. 5 and 6. Maximum total activity values for existing reaction channels are 129.7 and 14523.2 GBq, respectively.

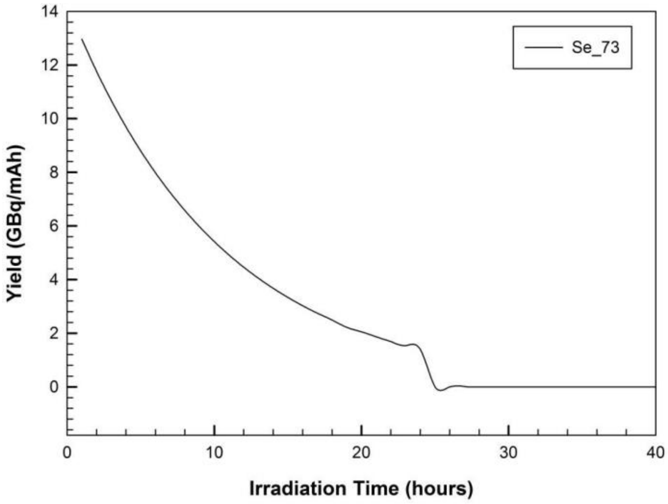

Fig. 3. Reaction yields of ^{75}As(p,3n)^{73}Se reactions.

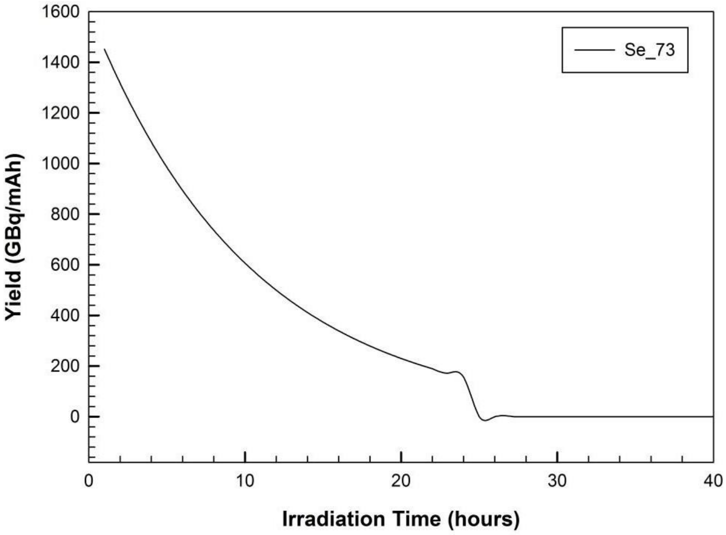

Fig. 4. Reaction yields of $^{74}Se(p,d)^{73}Se$ reactions.

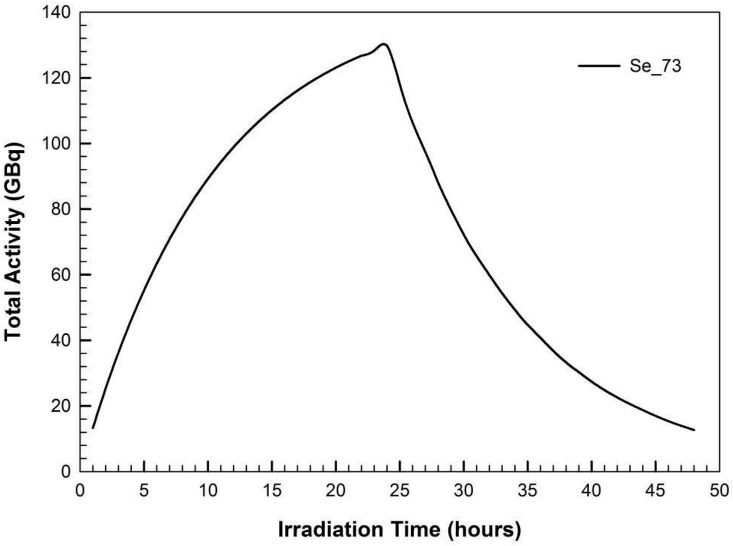

Fig. 5. Total activity of $^{75}As(p,3n)^{73}Se$ nuclear reaction.

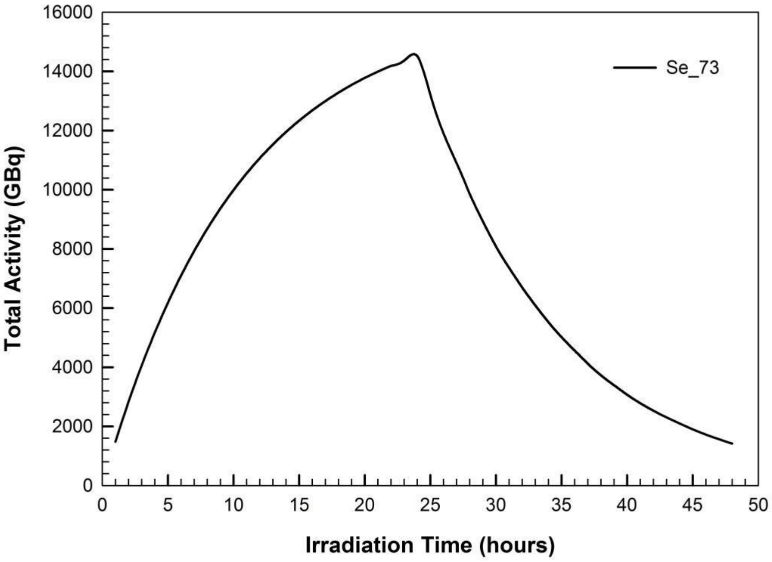

Fig. 6. Total activity of $^{74}Se(p,d)^{73}Se$ nuclear reaction.

CONCLUSION

The aim of this study is to examine the reaction mechanism of the ^{73}Se radioisotope, which has the potential to be used in nuclear medicine, at low energy levels. In this context, some possible reaction channels of ^{75}As(p,3n)^{73}Se and ^{74}Se(p,d)^{73}Se for ^{73}Se production were investigated within the framework of the TALYS 1.95 nuclear reaction code. It has been seen that GSM calculations were lower than other model calculations, and CTFGM and BSFGM were more compatible with experimental data. Maximum production cross-section values were obtained from CTFGM. In addition, reaction yield and total activation values during the irradiation time for 1 mA beam currentare also calculated and presented.

REFERENCES

[1] E. Gündoğdu et al., ‘Nükleer Tıpta Görüntüleme ve Tedavide Kullanılan Radyofarmasötikler’, *J. Lit. Pharm.*, 7(1), pp. 24–34, 2018.

[2] K. P. Willowson, ‘Production of radionuclides for clinical nuclear medicine’, *Europen Journal of Physics*, 40, 043001, 9, 2019.

[3] M. A. Synowiecki et al., ‘Production of novel diagnostic radionuclides in small medical cyclotrons’ *EJNMMI Radiopharmacy and Chemistry*, 3, 3, 2018.

[4] I. Hoffman, ‘Medical isotope production, research reactors and their contribution to the global xenon background’ *Journal of Radioanalytical and Nuclear Chemistry*, 318, 165-173, 2018.

[5] Amjed N., Aslam M. N., Hussain M., "Evaluation of nuclear reaction cross section data of proton and deuteron induced reaction on ^{75}As, with particular emphasis on the production of ^{73}Se" *Radiochim. Acta.*, vol. 190 no. 7, 525-537, 2021.

[6] Fabbender M., et al., ‘The ^{nat}Br(p,x)^{73,75}Se nuclear processes a convenient route for the production of radioselenium tracers relevant to amino acid labelling’, *Applied Radiation and Isotopes*, vol. 54, pp. 95-913, 2021.

[7] Rowshanfarzad P., et al., ‘simultaneous production and quality control of ^{73}Se and ^{75}Se radioisotopes in a 30 MeV cyclotron’, *Iran J. Radiat. Res.*, vol. 2, no. 1, pp. 1-7, Mar. 2004.

[8] Koning A., Hilaire S., Goriely S., ‘TALYS 1.95 a nuclear reaction program user manual’, 2019.

[9] Ignatyuk A.V., Istekov K.K., Smirenkin G.N., ‘The role of collective effects in the systemactics of nuclear level densities”, *Yad. Fiz.*, 29, 875, 1979.

[10] Dilg W., et al., ‘Level density parameters for the back shifted fermi gas model in the mass range 40<A<250’, *Nucl. Phys.*, vol. 217, no. 2, 1973.

[11] Baba H., ‘A shell model nuclear level density, *Nucl. Phys.*, 159, 625, 1970. 270–278, 2006.

[12] Mustaq A., Qaim S.M., Stöcklin G., "production of ^{73}Se via (p,3n) and (d,4n) reactions on arsenic", *Appl. Radiat. Isot.*, vol. 39, pp. 1085-1091, 1988.

[13] Nozaki T., Itoh Y., Ogawa K., ‘Yield of ^{73}Se for various reactions and its chemical processing’, *Int. J. Appl. Radiat. Isot.*, vol. 30, pp. 595-599, 1979.

Comparative Structural and Thermal Analysis of Aluminium Alloys Piston using FEA

MW Mustafa[1*], Haider Ali[1,2], Saeed Hassan[1], Muhammad Azeem[1,3] and Muhammad Yasir[1]

[1]Department of Mechanical Engineering, University of Wah, Wah Cantt, Pakistan
[2]Department of Computer Science and Engineering, School of Inter-disciplinary Engineering and Sciences, National University of Sciences & Technology, Islamabad, Pakistan
[3]Department of Mechanical Engineering, University of Engineering and Technology, Taxila, Pakistan

* Corresponding author e-mail address: muhammadwaqas.mustafa@wecuw.edu.pk

Abstract**—**Piston is an integral part of the engine as it receives and transfer power produced from combustion. Stresses produced in piston when subjected to pressure and temperature may lead to permanent deformation of piston. Therefore, lightweight and restraining stress Aluminium (Al) Alloys were preferred for piston. In this study the comparative analysis of 3x materials namely: Al-A4032, Al-GHY-1250 and Al-A390-T5 were carried out using Finite Element Analysis (FEA) technique. Static structural and steady-state thermal analysis were carried out to analyze stress distribution, total deformation, total heat flux and temperature distribution in different sections of the piston owing to pressure and thermal fluctuations. Al-GHY-1250 was superior in terms of total deformation with a percentage of 1.58% as well as in terms of stress distribution while it succeeds **Al-**A390-T5 in terms of total heat flux with 1.56×10^{-3}%.

Keywords**—***Engine-Piston, Aluminium Alloys, FEA, ANSYS*

INTRODUCTION

Piston, a most critical part of an internal combustion engine as it transfers the combustion power to the crankshaft of the engine. Piston has to sustain tremendous pressure and heat. This emphasizes the need of giving careful thought to the expected behaviour of the material under extreme circumstances throughout the design process. Piston materials are selected based on their durability, density, thermal expansion and wear characteristics. P.Carvalheira and P.Goncalves [1] compared Al-A390-T5 and Ductile Iron 65-45-12 for XC20i's engine using Finite Element Analysis (FEA). The design requirements, thermal expansion, thermal conductivity and mechanical strength played a significant role in determining the most suitable material. Al-A390-T5 was selected as of low inertial forces and increased volumetric efficiency. A.R. Bhagat et al. [2] investigated the thermal stress distribution using FEA to predict critical regions and higher stress of Al Alloy, Steel Alloy pistons. Moreover, stress distribution on the top of piston was reduced as a result of optimization. Cheekoti Benkata Rajam et al. [3] analyzed stress distribution and gas pressure at various piston locations using FEA. Von-Misses stress and deflection were increased up to 16 percent as a result of optimized design. Vivek Zolekar and Dr. L.N.Wankhade [4] used CATIA-V5, HyperMesh, RADIOSS for designing, topology optimization and FEA to study mechanical and thermal stress distributions of the piston's top surface.

S.Srikanth Reddy and Dr. B.Sudheer Prem Kumar [5] investigated thermal characteristics of uncoated diesel piston of Aluminium Silicon Alloy. Zirconium coated AlSi Alloy was compared using FEA in order to predict and enhance thermal stress distribution. Deepthi Kaza and T.Suresh Prakash [6] examined the pros and cons of Ductile Iron 65-45-12 and Al-A390-T5 for engine pistons using FEA. Al-A390-T5 was selected as of higher thermal expansion and conductivity with lower mechanical strength and 66% reduced weight as compared to Ductile Iron 65-45-12. Isam Jasim Jaber and Ajeet Kumar Rai [7] analyzed Al-A4032, AlSi4340 Alloy Steel, Ti-6Al-4V were taken as piston material. Silicon Nitride crown piston is better to tolerate high structural and thermal analysis than the other using FEA. Kashyap Vyas and Milan Pandya [8] used Finite Element Method (FEM) to analyze and predict thermal and stress distribution of AlGHS1300 for design optimization within permissible temperature and stress range. B.A.Devan, and G.Ravindra Reddy [9] compared AlSi, Al-MgSi, AlSiC-10 and AlSiC-12 using FEA for thermal distribution. AlSiC was selected as of reduced total heat flux. The maximum heat flux reduces by increase in composition of carbides in AlSiC Alloy. Sheikh Naim Sheikh Yusuf et al. [10] investigated Al-A2618 and Al-GHY-1250 using FEA for thermal distribution that indicates greater stress on the top of piston and a prominent reason of fatigue failure. Mr. Jadhav Vishal et al. [11] analyzed Al-A4032 and Al-GHY-1250 using FEM for thermal analysis for single cylinder petrol engine. Lower total deformation was observed in Al-GHY-1250 at various pressure conditions as compared to Al-A4032. Mr. Jadhav Vishal et al. [12] observed same results for Al-A4032 and G7Al-A2618 using FEA structural and thermal analysis. K. Sathish Kumar [13] used FEA to comparatively study Al Alloy and SiC Reinforced ZrB2 material for pistons. It was evident that stress for all materials was within the permissible limits of the respectable materials. From modal analysis it was observed that piston with Al Alloy was having less geometric stiffness while the piston with SiC Reinforced ZrB2 material had more geometric stiffness. So, SiC Reinforced ZrB2 was best choice for piston manufacturing. Bhavani Shankar Kalluri and SK Hidayatulla Sharief [14] used FEA to analyze structural and thermal distributions of Al-A2024, Al-A8090 and Ti Alloy pistons. Max. total heat flux were observed in rings and pistons of Al Alloy while Ti Alloy piston shows lowest heat flux along the edges whereas stress intensity was equivalent. P.Viswabharathy et al. [15] investigated Al Alloy and Stainless Steel using HyperMesh, RADIOSS for designing, topology optimization and FEA to study thermal stress distributions of the pistons. Pathipati Vasu et al. [16] studied Al-SiC Graphite, Al-A7075, Al-A4032, Al-A6082 and Al-GHY-1250 using FEM. It was analyzed that Al-SiC Graphite piston had least equivalent stress as compared to other materials. From strain analysis, it was evident that near piston pin area maximum strain was observed for all materials. Yao et al. [17] analyzed thermal properties using FEA for PYSZ(ZrO2-8%Y2O3), NiCoCrAlY and Al-Alloy. At the piston crown, the highest temperature was observed, and maximum temperature of Thermal Barrier Coatings (TBCs) occurred at the throat of the piston combustion chamber which was same as of conventional pistons and its better. Akhil Reddy Anugu et al. [18] used FEA to analyze Steel, Cast Iron and Al Alloy for automobile piston. Stress, deformation and strain values were low for Steel as compared to the others. Arka Roychoudhury et al. [19] analyzed mechanical properties of Al-7Si and TiSiCN coating using FEA. It was observed that thin coated layer of TiSiCN Alloy had a noticeable impact on improving the lifetime of engine piston as compared to uncoated flat head engine piston. From the literature it was evident that to investigate and identify the best suitable piston based on its mechanical properties for internal combustion engine under mechanical and thermal loads was a primary concern. Al-A390–T5 was dominantly used till 2014 later on Al-A4032 and Al-GHY-1250 were dominantly used before shifting to coated materials. Therefore, Finite Element Model of Al Alloy piston for internal combustion engine was developed to compare Al Alloys pistons based on mechanical properties using FEA. Al-A390–T5, Al-A4032 and Al-GHY-1250 were considered for comparative study.

TABLE 1. LITERATURE MATRIX

Year	**Author Name**	**FEA**		**Material/s**
		Structural	**Thermal**	
2006	P. Carvalheira, P. gonçalves [1]	✓	✓	Al-A390–T5, Ductile Iron 65-45-12
2012	A.R. Bhagat et al. [2]	✓	✓	Al Alloy, Steel Alloy
2013	Cheekoti Venkata Rajam et al. [3]	✓	X	_
2013	Vivek Zolekar, Dr. L.N. Wankhade [4]	✓	X	Al Alloy
2013	S. Srikanth Reddy, Dr. B. Sudheer Prem Kumar [5]	X	✓	Al Alloy, Zirconium (Zr)
2014	Deepthi Kaza, T.Suresh Prakash [6]	✓	✓	Al-A390-T5, Ductile Iron 65-45-12
2014	Isam Jasim Jaber, Ajeet Kumar Rai [7]	✓	✓	Al-A4032, AISI4340 Alloy Steel, Ti-6Al-4V
2014	Kashyap Vyas, Milan Pandya [8]	✓	✓	AlGHS1300
2015	B.A.Devan, G.Ravindra Reddy [9]	X	✓	AlSi, Al-MgSi, AlSiC-10, AlSiC-12

2015	Sheikh Naim Sheikh Yusuf et al. [10]	X	✓	Al-A2618, Al-GHY-1250
2016	Mr. Jadhav Vishal et al. [11]	X	✓	Al-A4032, Al-GHY-1250
2016	Mr. Jadhav Vishal et al. [12]	✓	✓	Al-A4032, G7Al A2618
2016	K. Sathish Kumar [13]	✓	✓	Al Alloy, SiC Reinforced ZrB2
2017	Bhavani Shankar Kalluri, SK Hidayatulla Sharief [14]	✓	✓	Al Alloy 2024, Al-A8090, Ti Alloy
2017	P.Viswabharathy et al. [15]	X	✓	Al Alloy, Stainless Steel
2018	Pathipati Vasu et al. [16]	✓	✓	Al-SiC Graphite, Al-A7075, Al-A4032, Al-A6082, Al-GHY-1250
2018	Yao et al. [17]	X	✓	PYSZ(ZrO2-8%Y2O3), NiCoCrAlY, Al Alloy
2021	Akhil Reddy Anugu et al. [18]	✓	✓	Steel, Cast Iron, Al Alloy
2021	Arka Roychoudhury et al. [19]	✓	X	PistonAl-7Si, TiSiCN Coating

CONSIDERATIONS FOR PISTON

Certain factors must be considered while designing engine pistons. Ideally, a piston would have:

- Extreme durability to bear the intense stress.
- Large enough bearing surface to forestall premature failure.
- Minimum weight to withstand the inertial forces.
- Effective oil sealing in the cylinder.
- High speed reciprocation without noise.
- To resist deformation due to heat or mechanical force.
- The piston pin has enough support.

METHODOLOGY

Geometric modelling of engine piston was done using CAD software named as SOLIDWORKS. Afterwards, step file was exported for ANSYS software for material allocation and FEM in order to carry out structural and thermal analysis of Al Alloys pistons for comparative study as shown in fig.1.

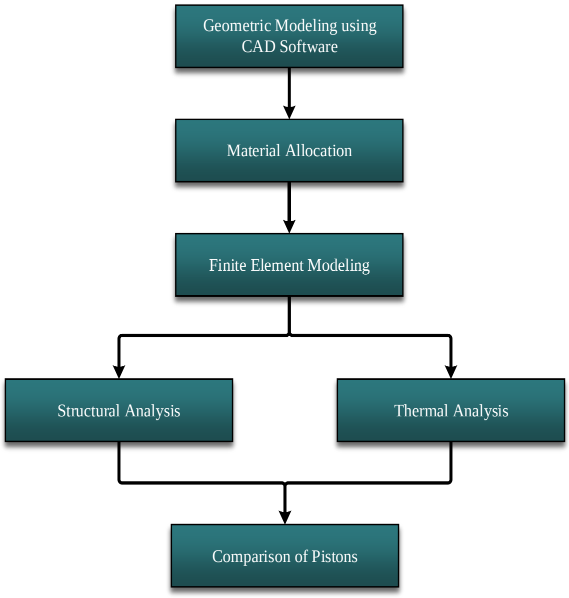

Figure 1. Methodology

J. Geometric Modelling

Design specification for Al Alloy piston was given in table II whereas its 2D drawing and 3D model was given in fig.2 in which comprehensive details of piston are prominent for visualization.

TABLE 2. DESIGN SPECIFICATIONS OF PISTON

Sr. No.	**Parameters**	**Dimension**
1	Length of Piston (L)	57 mm
2	Bore Dia. (D)	90 mm
3	Thickness of Piston Head (t_H)	8 mm
4	Radial Thickness of Ring (t_1)	1 mm
5	Axial Thickness of Ring (t_2)	2 mm
6	Width of Top Land (b_1)	10 mm
7	Width of Other Ring Bands (b_2)	3 mm
8	Mass of Piston (m)	166.36 grams

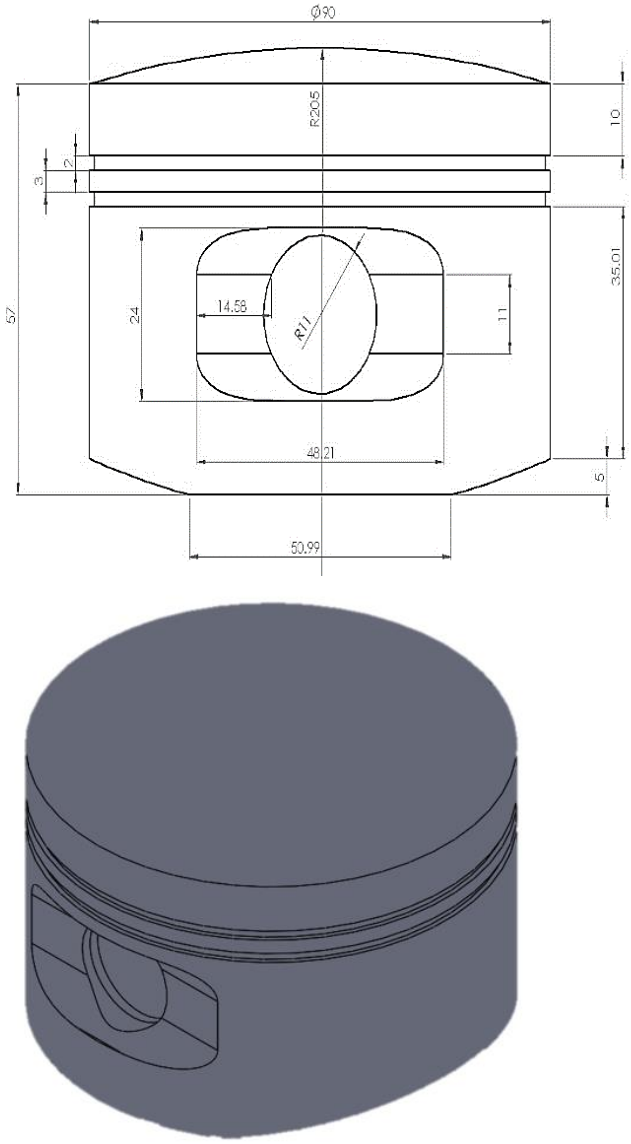

Figure 2. Geometric Modelling

K. Meshing

Step file was imported in ANSYS for tetrahedral mesh generation considering aspect ratio as given in table III. A detailed view of engine piston under study was given in fig.3.

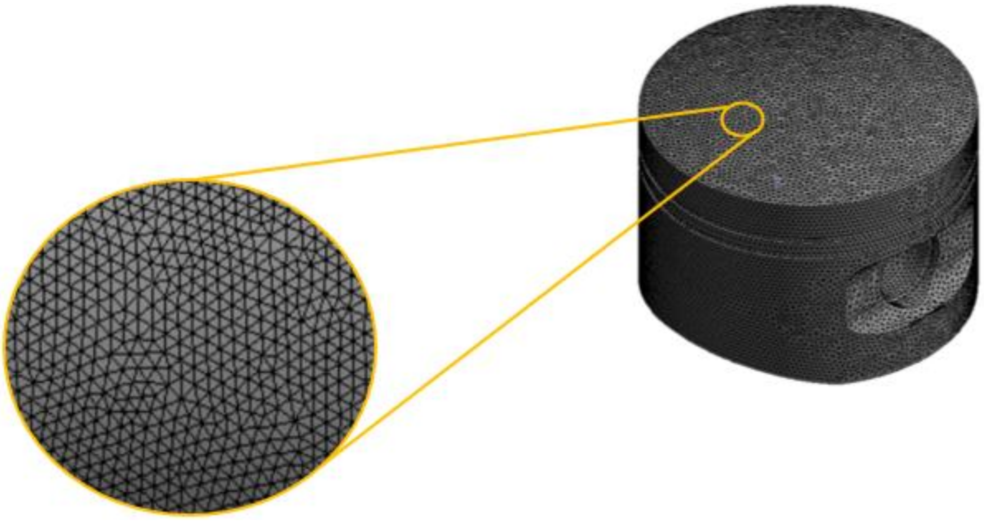

Figure 3. Finite Element Modeling of Piston (Meshing)

TABLE 3. MESH DETAILS

Element Type	Tetrahedral
No. of Elements	137054
Aspect Ratio	1.3

L. *Material and Boundary Conditions*

In table IV a comprehensive detail regarding structural and thermal properties of Al Alloy piston materials is given as used in FEA.

TABLE 4. PROPERTIES OF AL-A390-T5, AL-A4032 AND AL-GHY-1250

Material	**Al-A390-T5**	**Al-A4032**	**Al-GHY-1250**
Structural Properties			
Poisson's Ratio	0.33	0.33	0.3
Young's Modulus (GPa)	81.2	79	83
Density (kg/m^3)	2730	2680	2880
Bulk Modulus (GPa)	79.61	77.45	69.17
Shear Modulus (GPa)	30.53	29.7	31.92
Yield Strength (MPa)	240	315	1190
Ultimate Strength (MPa)	280	380	1250
Thermal Properties			
Co-efficient of Thermal Expansion (1/ºC)	1.80 x 10^-5	1.94 x 10^-5	2.00 x 10^-5
Thermal Conductivity (W/mK)	134	155	135
Reference Temperature (ºC)	22	22	22

Moreover, engine piston was subjected to a gas pressure of 9MPa to analyze the Equivalent (Von-Misses) Stress, Total Heat Flux and Total Deformation of pistons comparatively. The region around the piston was considered frictionless. Force was applied on the top of piston surface wheras fixed pin support was considered where gudgeon pin was fixed as given in fig.4.

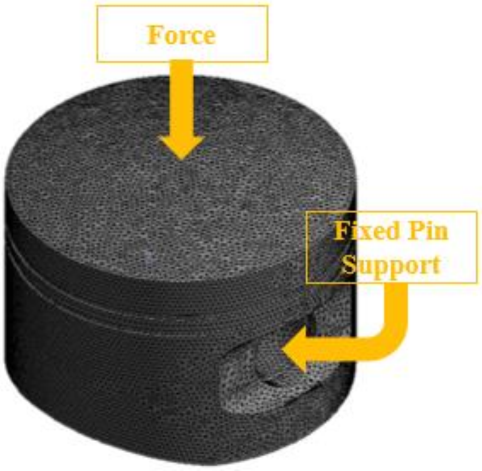

Figure 4. Boundary Conditions

RESULTS AND DISCUSSIONS

Results using FEA of Al Alloy pistons were given for comparative visualization in fig.5,6 and 7. Whereas, result comparison was given in table V.

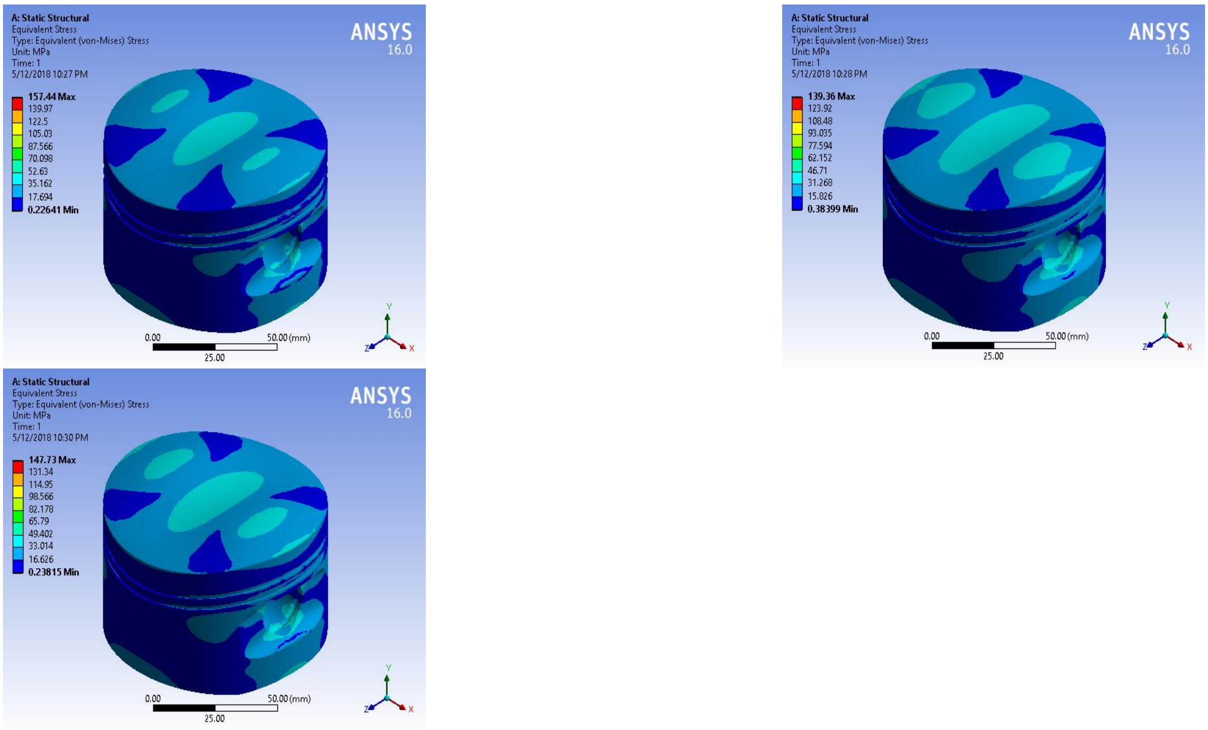

Figure 5. Equivalent (Von-Misses) Stress of Piston (a) Al-A390-T5 (b) Al-A4032 (c) Al-GHY-1250

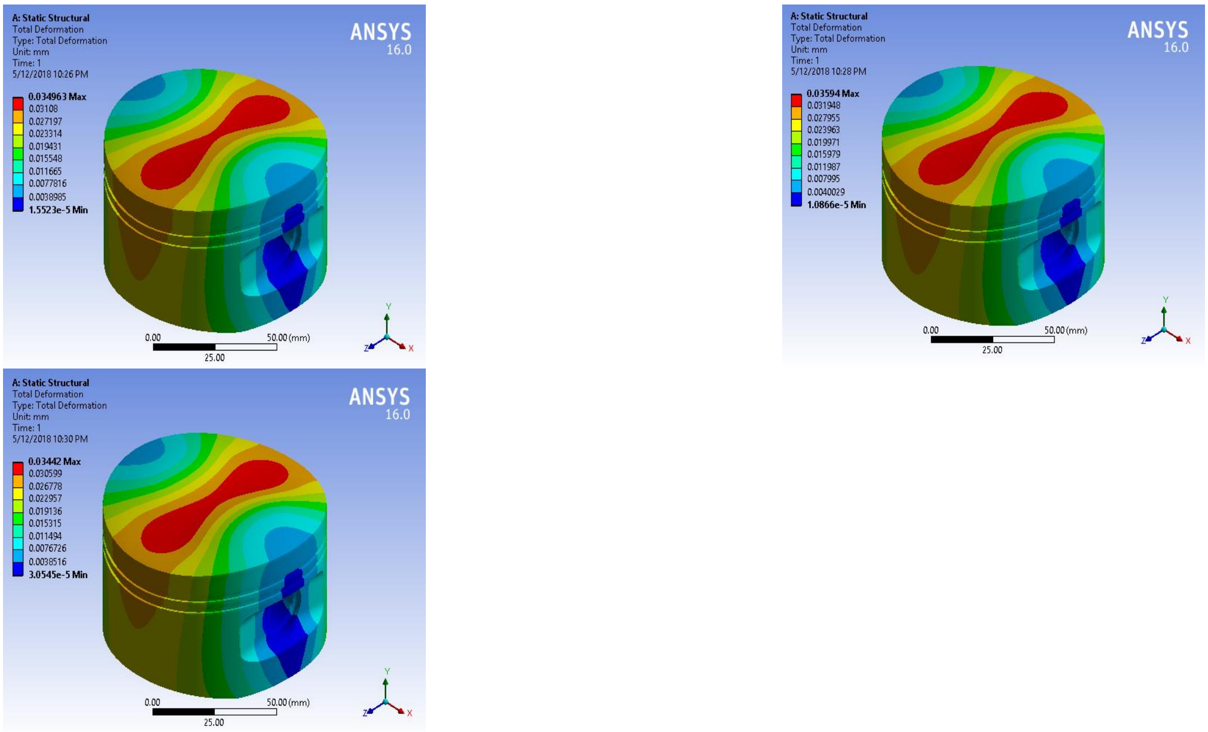

Figure 6. Total Deformation of Piston (a) Al-A390-T5 (b) Al-A4032 (c) Al-GHY-1250

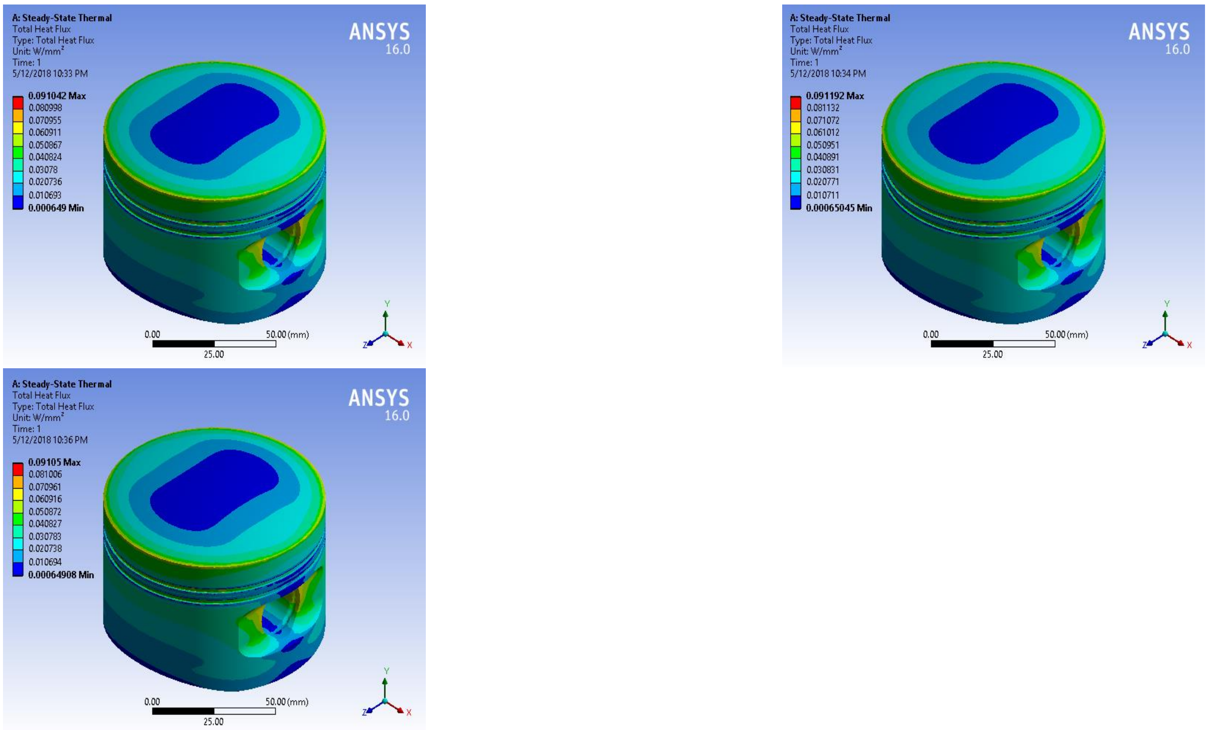

Figure 7. Total Heat Flux of Piston (a) Al-A390-T5 (b) Al-A4032 (c) Al-GHY-1250

TABLE 5. RESULTS COMPARISON OF (A) AL-A390-T5 (B) AL-A4032 (C) AL-GHY-1250

Sr. No.	**Parameters**	**Al-A390-T5**	**Al-A4032**	**Al-GHY-1250**
1	Equivalent (Von-Mises) Stress	157.44 MPa	139.36 MPa	147.73 MPa
2	Total Deformation	0.034963 mm	0.03594 mm	0.03442 mm
3	Total Heat Flux	0.091042 W/mm^2	0.091192 W/mm^2	0.09105 W/mm^2

Minimum Equivalent (Von-Misses) Stress was observed far from the centre, fixed pin support and fixed pin support axis as shown in fig.5. Moreover, minimum deformation was observed at the centre of the piston top surface whereas maximum deformation far from the centre in all analysis as given in fig.6 that is justifiable considering the boundary and load condition used in current study as given fig.4.
From the comparative study, it was observed that maximum Equivalent (Von-Misses) Stress was produced in Al-A390-T5 whereas minimum was observed in the case of Al-A4032. Minimum Total Deformation was observed for Al-GHY-1250 while maximum was observed for Al-A4032. Maximum Total Heat Flux was noticed for Al-A4032 whereas minimum for Al-A390-T5. Al-A390-T5 will be more prone to failure at high pressure because of its lower yield and ultimate strength as compared to the other two as it reached 65.6% of its yield strength owing to load conditions used in current study whereas Al-A4032 and Al-GHY-1250 reached 44.24% and 12.41% respectively. Al-GHY-1250 lead because of higher yield strength as compared to the other two Al Alloys to sustain higher pressure and load conditions. Al-GHY-1250 leads in terms of Lowest Total Deformation with a percentage of 1.58% whereas Al-A390-T5 succeeds and Al-4032 lags. Al-A4032 leads in terms of highest Total Heat Flux wit a percentage of 1.56x10^-3% whereas Al-GHY-1250 succeeds and Al-A390-T5 lags. It was evident that Al-GHY-1250 will be more sustainable as compared to Al-A390-T5 and Al-A4032 considering structural and thermal properties for higher pressure and load conditions for pistons. Thereby more practical material for developing an engine piston and its use pave the way for the creation, improvement and optimization of high-power engine/s.

REFERENCES

[1] P. Carvalheira and P. Goncalves, “FEA of Two Engine Pistons Made of Aluminium Cast Alloy A390 and Ductile Iron 65-45-12 under Service Conditions”, 5th International Conference on Mechanics and Materials in Design, 2006, Ref: A0319.0006.
[2] A.R. Bhagat, Y.M. Jibhakate and Kedar Chimote, “Thermal Analysis and Optimization of I.C. Engine Piston Using Finite Element Method”, Gas 2.1, 2012, pp. 6207-6216.
[3] Cheekoti Venkata Rajam, Venkata Krishna Murthy and Maddali VS Murali Krishna, “Design Analysis and Optimization of Piston using CATIA and ANSYS”, International Journal of Innovative Research in Engineering & Science, vol. 1(2), 2013, pp. 41-51, ISSN: 2319-5665.
[4] Vivek Zolekar and Dr. L.N. Wankhade, “Finite Element Analysis and Optimization of I.C. Engine Piston Using RADIOSS and OptiStruct”, Altair Technology Conference, India, 2013.
[5] S. Srikanth Reddy and Dr. B. Sudheer Prem Kumar, “Thermal Analysis and Optimization of I.C. Engine Piston Using Finite Element Method”, International Journal of Innovative Research in Science, Engineering and Technology, vol. 2(12), 2013, pp. 7834-7843, ISSN: 2319-8753.
[6] Deepthi Kaza, T. Suresh Prakash, “Investigation of Two Engine Pistons by FEA”, International Journal of Research, vol. 1(2), 2014, pp. 1217-1221, ISSN: 2348-6848.
[7] Isam Jasim Jaber and Ajeet Kumar Rai, “Design and Analysis of I.C. Engine Piston and Piston-Ring Using Catia and ANSYS Software”, International Journal of Mechanical Engineering and Technology, vol. 5(2), 2014, pp. 64-73, ISSN: 0976-6359.
[8] Kashyap Vyas and Milan Pandya, “Static Structural and Thermal Analysis of Aluminium Alloy Piston for Design Optimization Using FEA”, International Journal for Scientific Research & Development, vol. 2(3), 2014, pp. 671-675, ISSN: 2321-0613.
[9] B.A. Devan and G. Ravindra Reddy, “Thermal analysis of Aluminium alloy Piston”, International Journal of Emerging Trends in Engineering Research, vol. 3(6), 2015, pp. 511-515, ISSN: 2347-3983.
[10] Sheikh Naim Sheikh Yusuf, Nikhil D. Raut, Nitin D. Bhusale and Abhijeet A. Sirnaik, “Finite Element Analysis and Optimization of Piston using CAE Tools”, International Journal of Mechanical and Production Engineering, vol. 3(3), 2015, pp. 76-79, ISSN: 2320-2092.
[11] Mr. Jadhav Vishal, Dr. R.K. Jain and Mr. Yogendra S. Chauhan, “Stress Analysis of IC Engine Piston for Different Material and Pressure Load Using FEA”, International Journal of Engineering Sciences & Research Technology, vol. 5(7), 2016, pp. 340-350, ISSN: 2277-9655.
[12] Mr. Jadhav Vishal, Dr. R.K. Jain and Mr. Yogendra S.Chauhan, “Design and Analysis of Aluminium Alloy Piston Using CAE Tools”, International Journal of Engineering Sciences & Research Technology, vol. 5(7), 2016, pp. 332-339, ISSN: 2277-9655.
[13] K. Sathish Kumar, "Design and analysis of I.C. engine piston and piston-ring on composite material using Creo and ANSYS software." Journal of Engineering and Science, vol. 1(1), 2016, pp. 39-51.

[14] Bhavani Shankar Kalluri and SK Hidayatulla Sharief, “Simulation and Analysis of Thermo Mechanical coupling Load and Mechanical Dynamic Load for a Piston”, International Journal & Magazine of Engineering, Technology, Management and Research, vol. 4(6), 2017, pp. 60-70, ISSN: 2348-4845.

[15] P. Viswabharathy, N. Jeyakumar, P. Kannan and A. Vairamuthu, “Design and Analysis of Piston in Internal Combustion Engine Using ANSYS”, International Journal of Emerging Technologies in Engineering Research, vol. 5(3), 2017, pp. 62-70, ISSN: 2454-6410.

[16] Pathipati Vasu, Dr.M.Sri Rama Murthy, P.S. Amarnadh and S.V.Gopal Krishna, "Design and Analysis of IC Engine Piston with Different Materials." International Journal of Research, vol. 5(7), 2018, ISSN: 2348-6848.

[17] Zhimin Yao and Zuoqin Qian, "Thermal analysis of nano ceramic coated piston used in natural gas engine." Journal of Alloys and Compounds, 2018, pp. 441-450.

[18] Akhil Reddy Anugu, N. Vishnu Tej Reddy and D. Venkateswarlu, "Theoritical modelling and finite element analysis of automobile piston." Materials Today: Proceedings 45, 2021, pp. 1799-1803.

[19] Arka Roychoudhury, Ayan Banerjee, Prakash Chandra Mishra and Fuad Khoshnaw, "An FEA material strength modelling of a coated engine piston." Materials Today: Proceedings 44, 2021, pp. 1320-1325.

A Hybrid Machine Learning Techniques with Deep Neural Network Model for Colon Cancer Diagnosis

[1,2*]Amna Ali A. MOHAMED, [3]Aybaba HANÇERLİOĞULLARI

[1]Department of Computer Engineering, Kastamonu University, Kastamonu, Türkiye
[2]Tripoli University, Tripoli, Libya
[3]Department of Physics, Faculty of Science, Kastamonu University, Kastamonu, Türkiye

* Corresponding author: amnaalkmati@gmail.com

ORCID Numbers: 0000-0001-8344-6937 ([1]Amna Ali A. Mohamed) 0000-0000-1700-8480 ([2]Aybaba Hançerlioğulları)

***Abstract* -** Colon cancer detection is a great significant task in medical diagnosis. the detection of colorectal cancer in an early stage can significantly facilitate clinicians' decision-making and reduce mortality. The accurate detection results help to explore symptomatic treatment promptly; this can be achieved by using automatic systems with histopathological images. The combination of convolutional neural networks and supervised machine learning methods are used to achieve better classification results than using individual pre-trained deep networks. Therefore, this study is aimed to get a high performance and accuracy of CNN combined them with supervised machine learning methods. Support Vector Machine (SVM), decision tree (DT) and k-nearest neighbour (KNN) as the classification of colon cancer to get the best accuracy.

Keywords: *Colon Disease Diagnose, CNN, Machine Learning, SVM, Decision Tree, K-Nearest Neighbour.*

INTRODUCTION

Colon disease diagnosis is usually done by image processing methods, and careful learning is needed to analyze these images. The image denoising in the image pre-processing steps can reduce the features effectiveness and the classifier methods can make a mistake and the results will not be good. Also in image processing some filters cannot give us the optimum results because of losing the features. In this work, an attempt has been made to combine machine learning skills such as learning in the neural network with learning and training in humans to reveal the areas of colon disease. In the first, the convolutional neural network with SqueezeNet is used to extract the features from the colon disease images. Finally, the machine learning, support vector machine (SVM), decision tree (DT), and k-nearest neighbor (KNN) methods are used to the classification step [1-10].

ARTIFICIAL NEURAL NETWORK

A subset of artificial intelligence known as an artificial neural network (ANN) is capable of learning intricate nonlinear patterns from a set of data. Parallel computing units called ANNs have recently emerged as effective classification tools. They were first inspired by the concept of modeling mathematics and engineering to simulate the decision-making and parallel processing capabilities of the human brain. Even though ANNs still share many of the same fundamental traits as the human brain, they function much differently than biological neural networks today in terms of how they make decisions. Two primary criteria can be used to classify various ANN types [11]. The network's encoding—or, more specifically, how it stores knowledge gleaned from the data—is the first requirement. ANNs are divided into supervised and unsupervised categories using this metric. The second criterion is how the networks are decoded, or how the network handles new data after learning something from the previous input. Using this criterion, feedforward and feedback ANNs are distinguished.

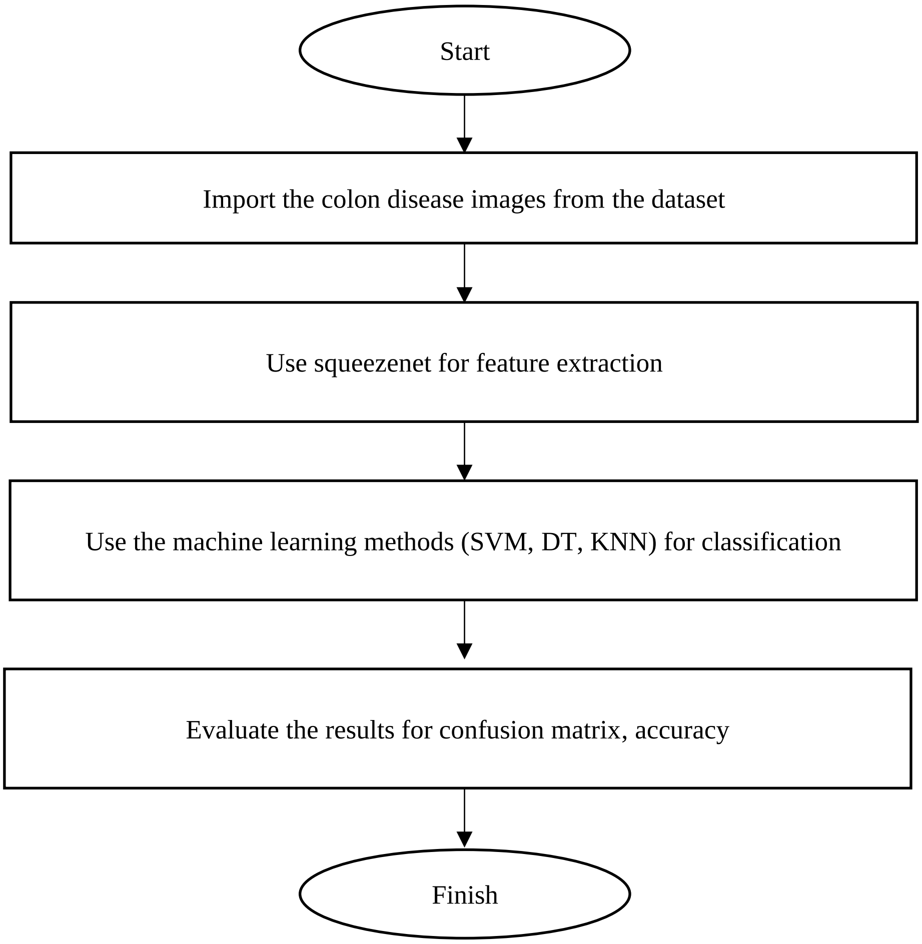

Figure 4. Flowchart of the proposed method for colon disease classification

RESULTS AND DISCUSSION

a) Dataset

In this paper, the famous dataset entitled “Lung and Colon Cancer Histopathological Images”, obtained from the open-access dataset library will be used. The dataset was obtained from: (https://www.kaggle.com/datasets/andrewmvd/lung-and-colon-cancer-histopathological-images)

This dataset contains 25,000 histopathological images with 5 classes. All images are 768 x 768 pixels in size and are in JPEG file format. In this paper, the last two datasets will use, Colon adenocarcinoma and the Colon benign tissue. These datasets depend on the colon histopathological images. In this paper, a total of 10,000 images will be used. 5000 images for cancer and 5000 images for non-cancer images. Visual examples of six histopathological images from the used dataset (where colon_n_refers to normal image and colon_ca_refers to an image with colon cancer).

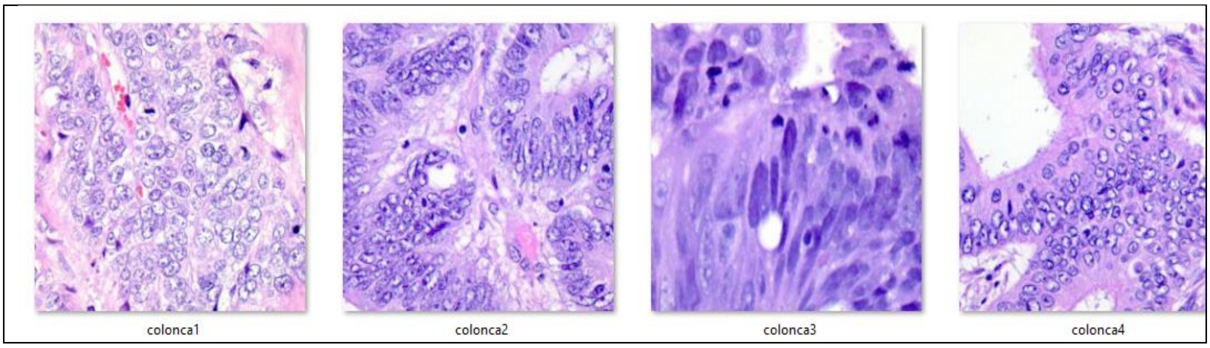

Figure 5. Some samples images from the dataset

To evaluate our results, we will use the most used measurements like Accuracy which based on confusion matrix is shown in Table 1.

Table 2: Confusion matrix

		Actual Values	
		Positive (1)	Negative (0)
Predicted Values	Positive (1)	TP	FP
	Negative (0)	FN	TN

Support vector machines, decision trees and k-nearest neighbour have been utilized in this study to categorize colon illnesses. The suggested approach has been applied to squeezenet combined with these supervised machine learning methods as the classification of colon cancer to get the best accuracy.

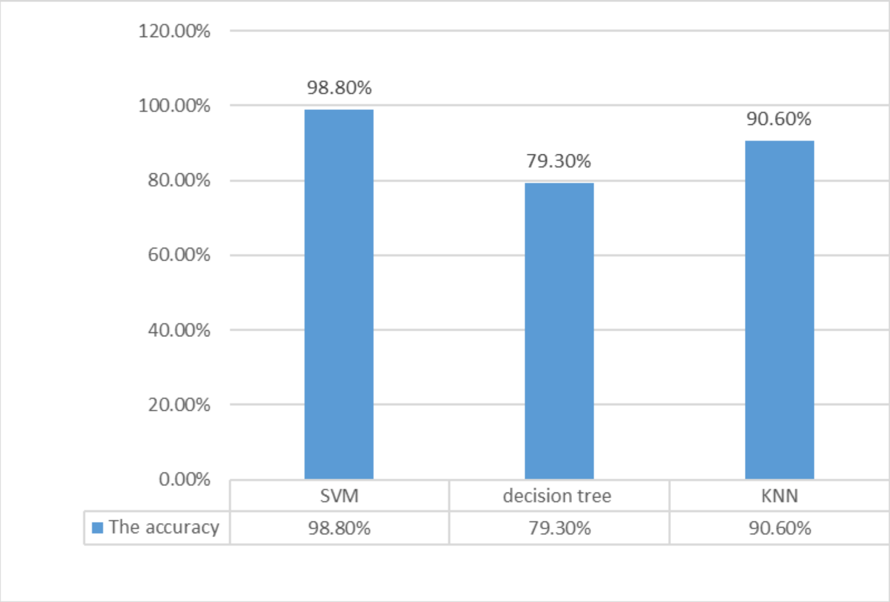

Figure 6. Mean of the accuracy index of SVM, decision tree and KNN methods based on squeezenet

The Analysis and evaluation reveal that the SqueezeNet combined by SVM approach performs quite well in terms of classification of image accuracy as it has been shown in the figure 3. In this experiment, the SVM based on SqueezeNet's accuracy is 98.80%. When the Decision-tree' experiment resulted average is 79.30% while the KNN method achieve 90.60% accuracy based on our CNN method.

CONCLUSION

In this study, a free-access database set was used for our necessary data. Using Matlab-2022a program for simulation, using different methods to reach a good accuracy in this work, we have combined machine learning based on the neural network. The machine learning algorithms SVM, decision tree and KNN have been applied to detect a colon cancer with a high accuracy. The best performance is obtained from SVM machine learning method based on the SqueezeNet pertaining neural network for colon cancer classification.

REFERENCES

[1] D. Bazazeh and R. Shubair, "Comparative study of machine learning algorithms for breast cancer detection and diagnosis," in *2016 5th International Conference on Electronic Devices, Systems and Applications (ICEDSA)*, 2016, pp. 1–4.

[2] J. Alam, S. Alam, and A. Hossan, "Multi-stage lung cancer detection and prediction using multi-class svm classifie," in *2018 International Conference on Computer, Communication, Chemical, Material and Electronic Engineering (IC4ME2)*, 2018, pp. 1–4.

[3] Y. J. Tan, K. S. Sim, and F. F. Ting, "Breast cancer detection using convolutional neural networks for mammogram imaging system," in *2017 International Conference on Robotics, Automation and Sciences (ICORAS)*, 2017, pp. 1–5.

[4] A. M. Godkhindi and R. M. Gowda, "Automated detection of polyps in CT colonography images using deep learning algorithms in colon cancer diagnosis," in *2017 International Conference on Energy, Communication, Data Analytics and Soft Computing (ICECDS)*, 2017, pp. 1722–1728.

[5] T.-C. Chiang, Y.-S. Huang, R.-T. Chen, C.-S. Huang, and R.-F. Chang, "Tumor detection in automated breast ultrasound using 3-D CNN and prioritized candidate aggregation," *IEEE Trans. Med. Imaging*, vol. 38, no. 1, pp. 240–249, 2018.

[6] S. J. Leavesley *et al.*, "Hyperspectral imaging fluorescence excitation scanning for colon cancer detection," *J. Biomed. Opt.*, vol. 21, no. 10, p. 104003, 2016.

[7] S. Rathore, M. Hussain, A. Ali, and A. Khan, "A recent survey on colon cancer detection techniques," *IEEE/ACM Trans. Comput. Biol. Bioinforma.*, vol. 10, no. 3, pp. 545–563, 2013.

[8] G. Lu, L. V Halig, D. Wang, X. Qin, Z. G. Chen, and B. Fei, "Spectral-spatial classification for noninvasive cancer detection using hyperspectral imaging," *J. Biomed. Opt.*, vol. 19, no. 10, p. 106004, 2014.

[9] R. Pike, G. Lu, D. Wang, Z. G. Chen, and B. Fei, "A minimum spanning forest-based method for noninvasive cancer detection with hyperspectral imaging," *IEEE Trans. Biomed. Eng.*, vol. 63, no. 3, pp. 653–663, 2015.

[10] A. Gopi and C. S. Reshmi, "A noninvasive cancer detection using hyperspectral images," in *2017 International Conference on Wireless Communications, Signal Processing and Networking (WiSPNET)*, 2017, pp. 2051–2055.

[11] B. Kosko, "Unsupervised learning in noise," *IEEE Trans. Neural Networks*, vol. 1, no. 1, pp. 44–57, 1990.

Techno-Economic Evaluation of Bio-Ethylene Production from Zea-Mays (Biorefinery as a sustainable solution for the utilization of waste)

Kashaf Tehreem, Usman Asghar *, Shehar Bano, Fazeel Ahmad, Waqas Ahmed Khan, Abdullah Niaz, Sami Jabbar
Department of Chemical Engineering, Wah Engineering College, University of Wah, Quaid Avenue Wah Cantt., Pakistan
*Corresponding author: Usman Asghar (usman.asghar@wecuw.edu.pk)

ORCID Numbers: 0009-0000-5344-413X (Kashaf Tehreem), 0009-0002-0590-7130 (Usman Asghar), 0009-0005-1715-609X (Shehar Bano), 0000-0002-3981-0866 (Fazeel Ahmad), 0009-0006-4011-5648 (Waqas Ahmad Khan), 0009-0000-8412-8500 (Abdullah Niaz), 0009-0003-5625-0754 (Sami Jabbar)

Abstract - The nonrenewable nature of fossil fuels and their connection to the buildup of greenhouse gases in the atmosphere have been recognized for a long time. As a result, renewable methods have been developed that utilize both non-biomass sources like wind, solar, geothermal, and hydroelectric power, and biomass sources that can be directly combusted or converted into value-added products using various thermochemical processes or using microorganisms. This combination of microorganisms and biomass has paved the way for the creation of a bioeconomy, enabling the commercial production of biofuels, biochemicals, and other miscellaneous materials. This study focuses on the production of bio-ethylene from Zea Mays (a waste biomass of corn). Ethylene is a key feedstock for various downstream chemical products like PET, ethylene oxide etc. It is responsible for the production of about half of all plastics produced globally (a fast-growing industry all over the world). Annually, over 140 million tons of ethylene are produced, and demand for it is expected to rise, particularly in developing economies. With its resemblance to ethylene in terms of chemical makeup, bio-ethylene can also be used to make plastics and other downstream products with the current machinery and production capacity. This study provides techno-economic analysis for the production of bio-ethylene from Zea Mays (corn stover). The production of bio-ethylene from biomass-based pathways involves two primary steps: fermentation to produce bioethanol from biomass, followed by the catalytic dehydration of bioethanol to bio-ethylene. This research work discusses all the technical aspects with the economic evaluation of the production process. All indicators of economic analysis (Net Present Worth, IRR etc.) shows the Bio-Ethylene from Zea Mays is economically viable (27.8% rate of return) to produce value added product (bio-ethylene) with least environmental implications.

Keywords: *Biorefinery, Zea Mays, Green house gases (GHG), bio-ethylene, fermentation, Economic evaluation, Profitability analysis, Discounted cash flow, Net present worth Rate of Return, Depreciation.*

INTRODUCTION

The first of the alkenes is ethylene, often known as ethene ($CH_2=CH_2$). It is a colorless gas that normally boils around -103.7 °C and is only moderately soluble in alcohol and water. Due to its high activity, this substance reacts readily when combined with various chemical reagents [1]. Ethylene due to its simple molecular formula and composition serves as the basic raw material for Plastic and Polymer industry [2]. Ethylene is the important feed stock used in the production of various valuable products like plastics, PET bottles, PVC pipes, ethylene glycol etc. Almost 60% of Ethylene is used in Polyethylene manufacturing [3]. Currently, Ethylene is being produced from the cracking of fossil fuel based raw materials like Naphtha, Natural gas, shale gas etc. As we know, fossil fuels are depleting day by day and their prices are on the rise which is causing ethylene to get more expensive and eventually effecting the polymer industry. The production of plastics from non-renewable feedstock is of great interest nowadays. The use of biomass for production of useful products contribute to greenhouse gas depletion [4]. In this project, we have designed a complete process for the sustainable production of Ethylene (also known as Bio-Ethylene due to its production from biomass) from a cheap waste material, i.e., Corn stover (Zea Mays) which is the remaining of the corn crop. Farmer used to get rid of this waste (corn stover) by land filling or by burning it. This action involves the serious environmental impacts (emission of GHG from its burning is major impact). Our project is a value addition project (converting waste into valuable product) which contains following Commercial advantages over the existing process:

i Reducing Environmental Hazards

ii Raw material is inexpensive which will obviously drastically affect the selling.

iii Price of Ethylene. The low-price Ethylene will give the boost to the polymer industry of Pakistan (as ethylene is feed stock for polymer industry)

iv This process is sustainable in term Ethylene production because the conventional production involves the fossil fuel based raw material which depleting day by day.

v This process is the first step towards bio-refinery in Pakistan.

a. Process Description:

The process comprises of four sections:

- Pretreatment of Corn Stover
- Saccharification and Fermentation
- Purification of Ethanol
- Catalytic dehydration of Ethanol to Ethylene

The physical and chemical processing of raw materials is the first phase. Corn stover is then ground to a thickness of 0.2 mm. To release hemicellulose sugars and break down biomass, maize stover is first processed with diluted sulfuric acid in the pretreatment and conditioning unit. Ammonia is then added to the pretreated slurry to alter its acidity to be acceptable for enzymatic hydrolysis [2]. The subsequent step involves sending the hydrolysate to an enzymatic hydrolysis and fermentation unit, where a cellulase enzyme is utilized for the enzymatic hydrolysis process. The cellulose and xylose in the hydrolyzed slurry are then fermented to create bioethanol [5]. Using glucose as the main carbon source, an enzyme manufacturing unit on-site produces the necessary cellulase enzyme. The produced beer is then divided into bioethanol, water, and residual solids in a production recovery section using distillation and solid-liquid separation [1]. A wastewater treatment unit collects and treats wastewater streams produced during the synthesis of bioethanol using anaerobic and aerobic digestion. To form HP steam, which is utilized to produce electricity and meet the demand for process heat, solids and biogas from the product recovery unit and wastewater treatment unit are burned. Bioethanol made from maize stover is first dehydrated to produce ethylene, water, and other byproducts in the ethylene manufacturing process. The dehydration reactor effluent is then pressurized and quenched. In an ethylene purification unit, the effluent is finally divided into ethylene, water, and other components [6].

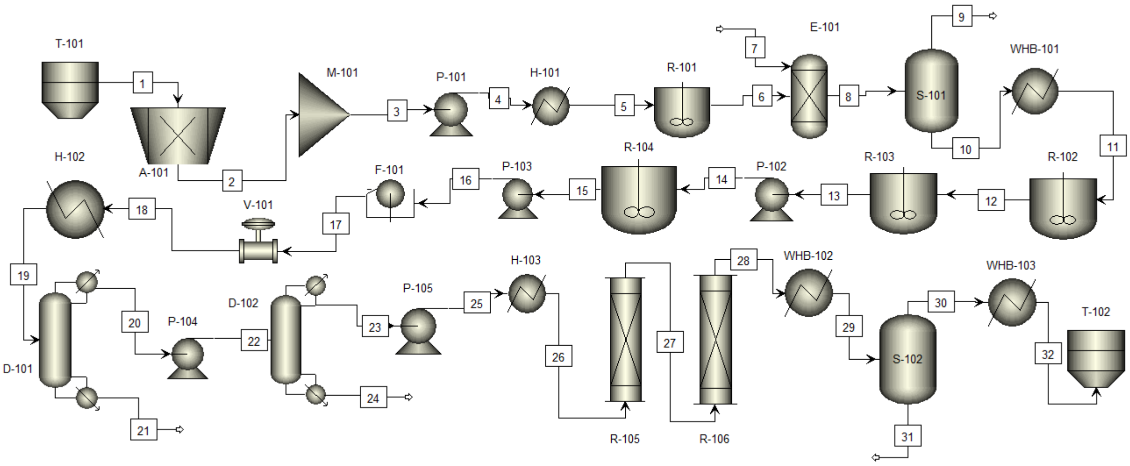

Figure 1. Process Flow Diagram for Production of Bio-Ethylene from Zea-Mays

2. Economic Analysis

Economic analysis is the crucial step in any design. Comparable to other industrial or financial initiatives, a good project should ensure a quick return on the investment and strong profitability over the anticipated lifetime. Cost estimation is a specified subject and a profession [7]. The design engineer, however, needs to be able to make quick, rough, cost estimates to decide between alternative designs and for project evaluation. Chemical plants are built to make a profit, and an estimate of the investment required, and the cost of production are needed before the profitability of a project can be assessed. In this project numerous components that frame the capital cost of a plant and the components of the operating costs are considered, and the methods used for cost estimation are evaluated.

a. Assumptions:

- 3000 tons/day of Bio-Ethylene
- Plant is 100% equity financed
- Plant initiates operation in 5-8 years
- Plant life is 20 years
- Plant availability is 330 days/year
- Zero salvage value for general plant
- MACRS depreciation method is used

b. Total Capital Investment:

Total Capital investment comprises of fixed and working capital investment. Fixed capital is the total cost of the plant ready for start-up. It is the cost paid to the contractors.

It includes the cost of:

- Design, and other engineering and construction supervision.
- All items of equipment and their installation.
- All piping, instrumentation, and control systems. Buildings and structures. Auxiliary facilities, such as utilities, land and civil engineering work.

Working capital is the additional investment needed, over and above the fixed capital, to start the plant up and operate it to the point when income is earned. It includes the cost of:

- Start-up.
- Initial catalyst charges.
- Raw materials and intermediates in the process.
- Finished product inventories.

i. Purchased Equipment Cost

Table 1. Purchased Equipment Cost

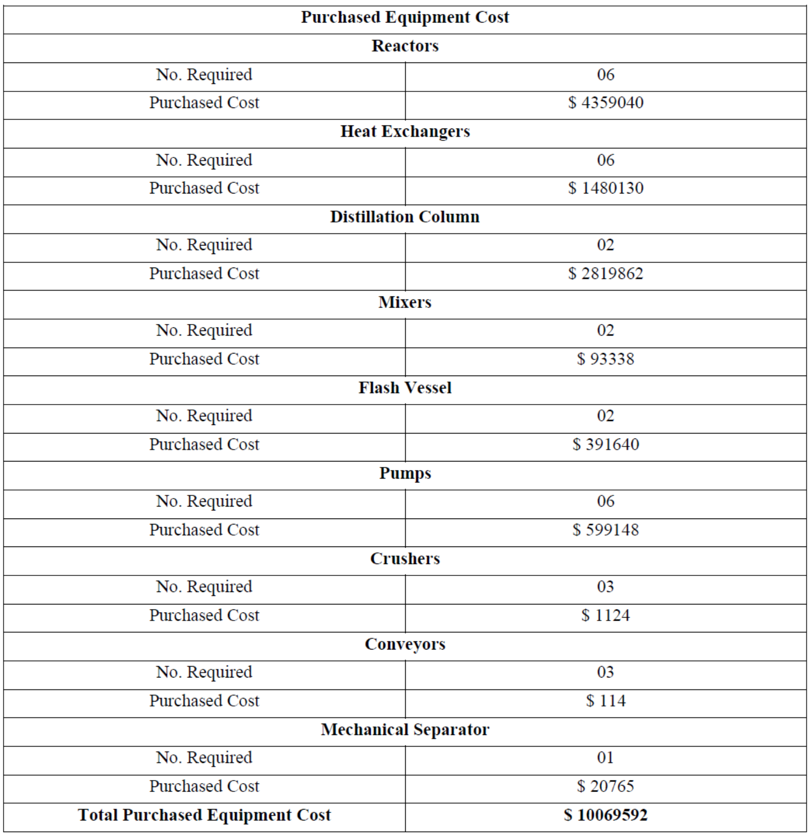

Purchased Equipment Cost	
Reactors	
No. Required	06
Purchased Cost	$ 4359040
Heat Exchangers	
No. Required	06
Purchased Cost	$ 1480130
Distillation Column	
No. Required	02
Purchased Cost	$ 2819862
Mixers	
No. Required	02
Purchased Cost	$ 93338
Flash Vessel	
No. Required	02
Purchased Cost	$ 391640
Pumps	
No. Required	06
Purchased Cost	$ 599148
Crushers	
No. Required	03
Purchased Cost	$ 1124
Conveyors	
No. Required	03
Purchased Cost	$ 114
Mechanical Separator	
No. Required	01
Purchased Cost	$ 20765
Total Purchased Equipment Cost	**$ 10069592**

ii. Direct Cost

Table 2. Direct Cost of Plant

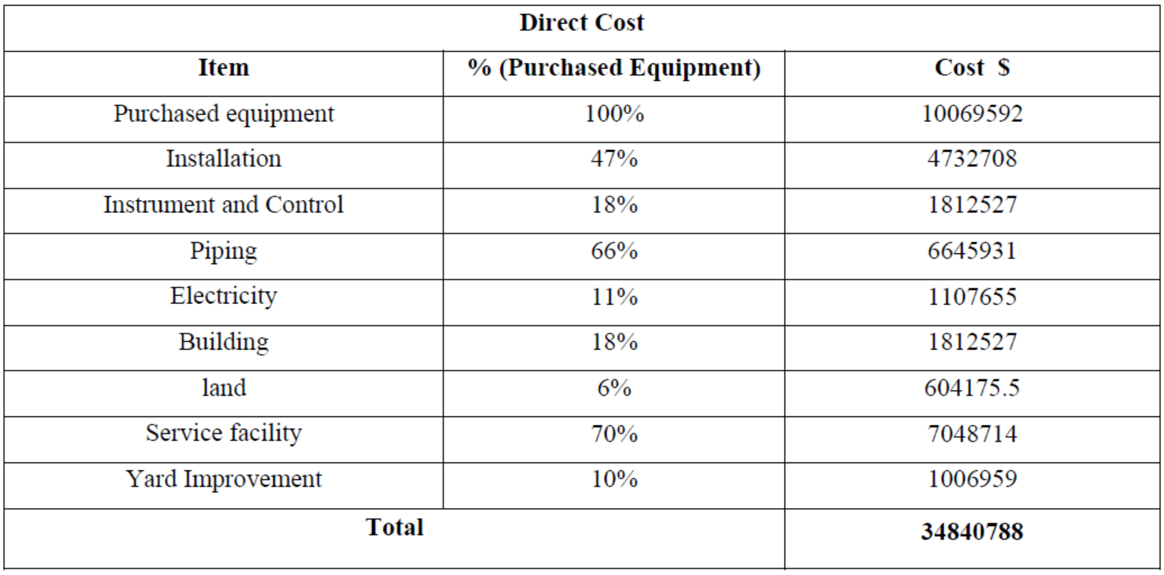

Direct Cost		
Item	**% (Purchased Equipment)**	**Cost $**
Purchased equipment	100%	10069592
Installation	47%	4732708
Instrument and Control	18%	1812527
Piping	66%	6645931
Electricity	11%	1107655
Building	18%	1812527
land	6%	604175.5
Service facility	70%	7048714
Yard Improvement	10%	1006959
Total		**34840788**

iii. Indirect Cost

Table 3. Indirect Cost of Plant

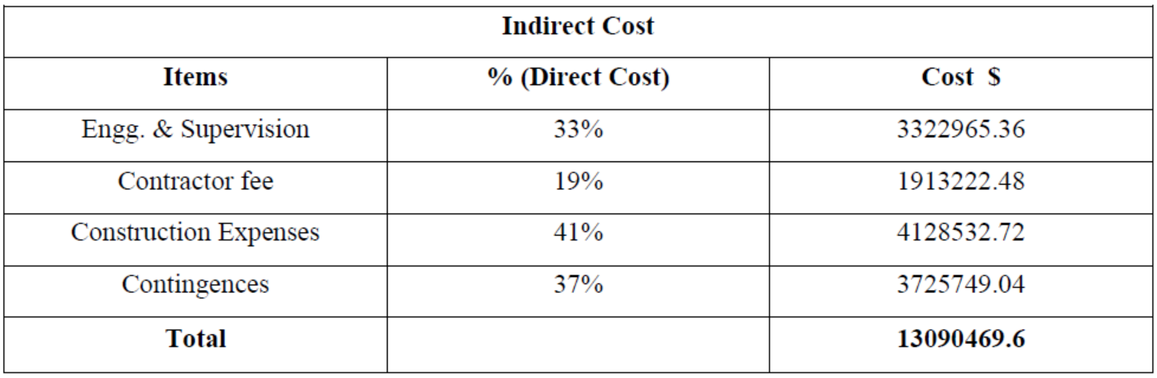

Indirect Cost		
Items	**% (Direct Cost)**	**Cost $**
Engg. & Supervision	33%	3322965.36
Contractor fee	19%	1913222.48
Construction Expenses	41%	4128532.72
Contingences	37%	3725749.04
Total		**13090469.6**

Fixed capital = direct cost + indirect Cost
Fixed capital = $47931258
Working capital investment = 15% of fixed capital investment
Working capital investment = $7189688
Total capital investment = Fixed capital investment + Working capital investment
Total capital investment = $ 55120946

An estimate of the operating costs, the cost of producing the product, is needed to judge the viability of a project, and to make choices between possible alternative processing schemes. These costs can be estimated from the flow-sheet, which gives the raw material and service requirements, and the capital cost estimate.

The cost of producing a chemical product will include the items listed below. They are divided into two groups.

c. Operating Cost

1. Variable operating costs: costs that are dependent on the amount of product produced.
2. Fixed operating costs: costs that do not vary with production rate. These are the bills that have to be paid whatever the quantity produced.

d. Total Production Cost

i. Variable Cost

Raw Material Cost

Flow rate of corn stover = 562120 kg/hr
For 330 days = 4451990400 kg/year
Price of corn stover per kg = \$0.0585/kg
Total price of corn stover = \$260441438/year

Catalyst Cost

Price of catalyst (Al_2O_3) = \$1.2/kg
Weight of catalyst = 1760 kg
Price of catalyst = \$2112/year

Miscellaneous Material

Maintenance cost = 7% of FCI Maintenance cost = \$ 335518
Miscellaneous Material = 10% of maintenance cost
Miscellaneous Material = \$ 33551

Steam Cost

Price of steam in 2022 = \$0.014/kg
Total steam required = 432000 kg/hr
For 330 days = 3421440000 kg/year
Total price of steam per year = \$ 47900160/year

Cooling water

Cooling Water price = \$0.00001/kg
Cooling Water Required = 6538000 kg/hr
Cooling water required = 51780960000 kg/year
Total price of cooling water = \$517809/year
Variable cost = raw material cost + miscellaneous cost + utilities cost
Variable cost = \$ 305502483/year

ii. Fixed Cost:

Table 4. Fixed Operating Cost for Processing Plant

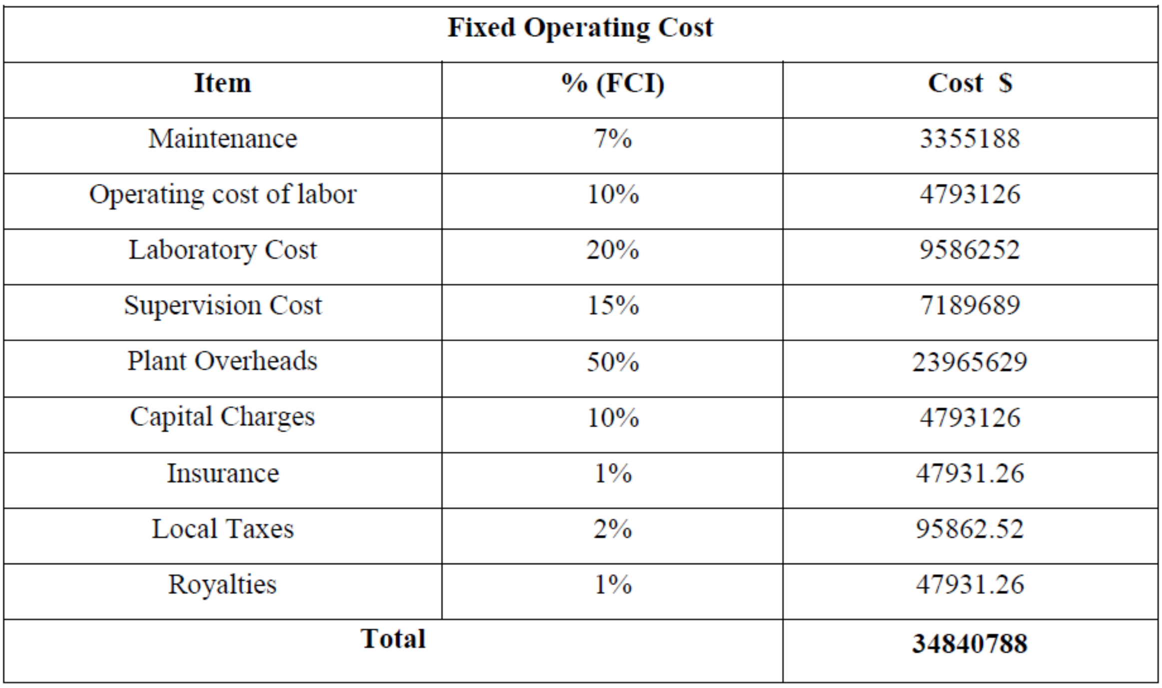

Fixed Operating Cost		
Item	**% (FCI)**	**Cost $**
Maintenance	7%	3355188
Operating cost of labor	10%	4793126
Laboratory Cost	20%	9586252
Supervision Cost	15%	7189689
Plant Overheads	50%	23965629
Capital Charges	10%	4793126
Insurance	1%	47931.26
Local Taxes	2%	95862.52
Royalties	1%	47931.26
Total		**34840788**

iii. Direct Production Cost

Direct Production Cost = variable cost + fixed cost
Direct Production Cost = \$ 305502483 + \$ 34840788
Direct Production Cost = \$ 340343271

iv. Overhead Charges:

30% of direct production cost
Overhead charges = (0.3)(340343271)=
$ 102102981
Total production cost = Direct Production Cost + Overhead Charges
Total production cost = $442446252/year
Total production rate = 990000000kg/year
Production cost ($/kg) = Total production cost / Total production rate
Production cost ($/kg) = $ 0.47/kg

e. Profitability Analysis:

Total Income
Selling Price = $600/ton
Total Production per year = 990000 ton/year
Total Income = $594000000/year
Gross Profit
Gross Profit = Total Income - Total Production Cost
= $ 594000000 /year – $442446252/year
= $151553748/year
Depreciation:
Machinery and equipment = 20% of FCI
= $ 9586251
Building = 4% of Building cost
= $ 1812527
Total Depreciation = Machinery and equipment + Building
= $ 11398778
Profit before Taxation:
Net Profit before Taxation = Gross profit – Depreciation
= $ 151553748 /year - $ 11398778/year
= $ 140154970/year
Net Profit after Taxation:
Net Profit after Taxation = (1-0.40)* Profit before taxation
= $ 15335449/year
Rate of Return
Rate of Return
= Net ProfitTotal Capital Investment × 100
= 27.8 %
Pay Back Period
= 1Rate of Return
= 3.5 years

f. Economic Feasibility Analysis:

i. Discounted Cash Flow:

Total Capital Cost = CFC + CL +CWC
CFC = Fixed Capital
CL = Land Cost
CWC = Working Capital
Annual Expense = Cost of manufacturing
COM=0.304FCI+2.73COL+1.23(CUT+CRM)
COL = Cost of Labor
CUT = Utilities Cost
CRM = Raw Material Cost

ii. Net Present Worth:

The The future profitability of an investment, project, or business is assessed using net present value. The NPV of an investment is essentially the total discounted to present value of all future cash flows during the investment's lifetime[8].

iii. Cash Flow:

Cash flows include all money produced or spent for the benefit of the investment, such as interest and loan repayments as well as capital outlays. The cash flow for each period comprises both inflows for profits, revenues, and dividends as well as outflows for costs[9].

iv. Internal Rate of Return:

An internal rate of return computation is used in capital planning to determine whether projects or investments are worthy of funding and to rank them. The discount rate at which the net present value (NPV) is zero is known as the IRR. (when time-adjusted future cash flows equal the initial investment). An indicator of actual investment performance is the annual rate of return, or IRR[6].

Table 5. Cumulative Cash Flow Analysis

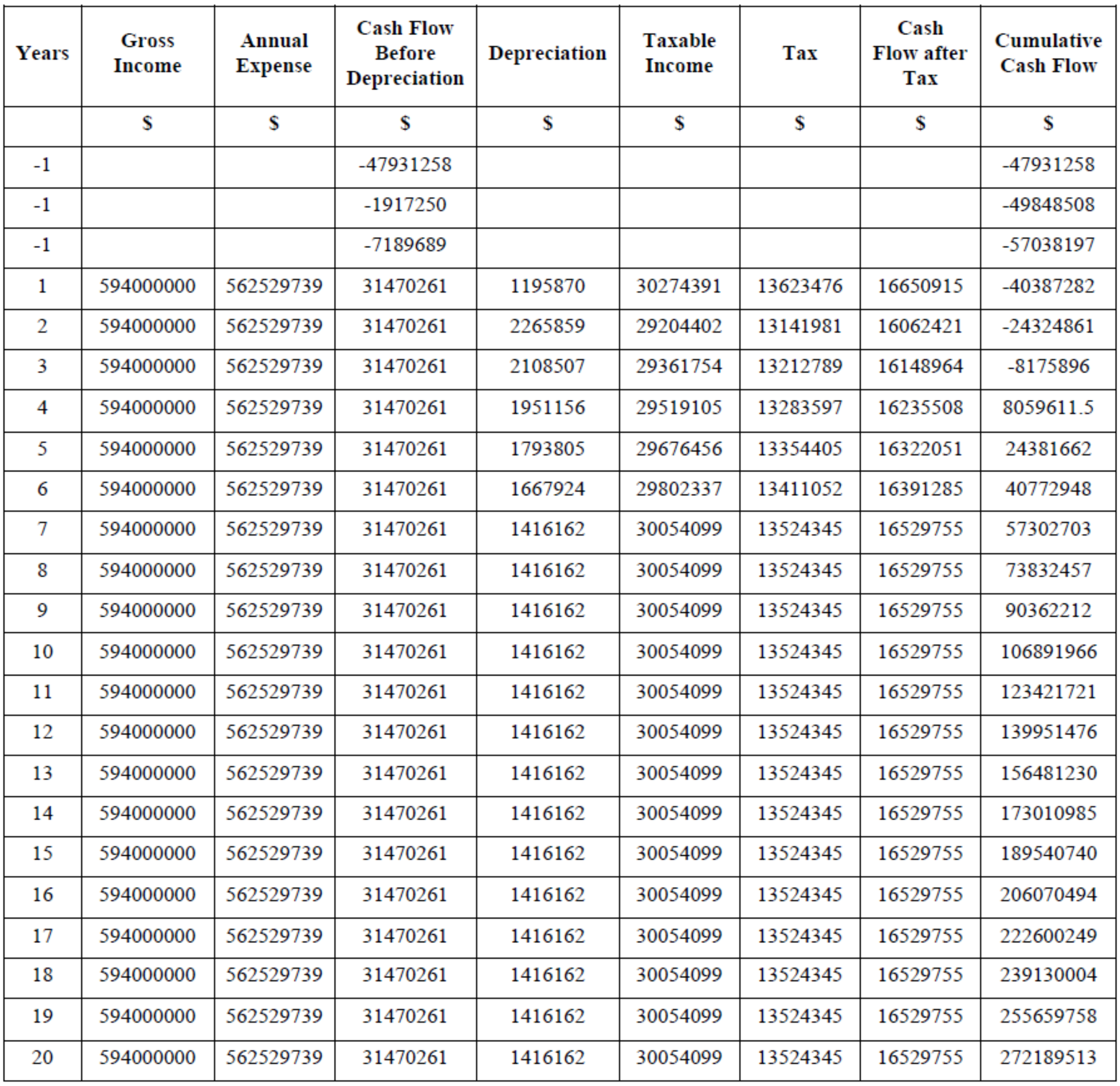

Years	Gross Income	Annual Expense	Cash Flow Before Depreciation	Depreciation	Taxable Income	Tax	Cash Flow after Tax	Cumulative Cash Flow
	$	$	$	$	$	$	$	$
-1			-47931258					-47931258
-1			-1917250					-49848508
-1			-7189689					-57038197
1	594000000	562529739	31470261	1195870	30274391	13623476	16650915	-40387282
2	594000000	562529739	31470261	2265859	29204402	13141981	16062421	-24324861
3	594000000	562529739	31470261	2108507	29361754	13212789	16148964	-8175896
4	594000000	562529739	31470261	1951156	29519105	13283597	16235508	8059611.5
5	594000000	562529739	31470261	1793805	29676456	13354405	16322051	24381662
6	594000000	562529739	31470261	1667924	29802337	13411052	16391285	40772948
7	594000000	562529739	31470261	1416162	30054099	13524345	16529755	57302703
8	594000000	562529739	31470261	1416162	30054099	13524345	16529755	73832457
9	594000000	562529739	31470261	1416162	30054099	13524345	16529755	90362212
10	594000000	562529739	31470261	1416162	30054099	13524345	16529755	106891966
11	594000000	562529739	31470261	1416162	30054099	13524345	16529755	123421721
12	594000000	562529739	31470261	1416162	30054099	13524345	16529755	139951476
13	594000000	562529739	31470261	1416162	30054099	13524345	16529755	156481230
14	594000000	562529739	31470261	1416162	30054099	13524345	16529755	173010985
15	594000000	562529739	31470261	1416162	30054099	13524345	16529755	189540740
16	594000000	562529739	31470261	1416162	30054099	13524345	16529755	206070494
17	594000000	562529739	31470261	1416162	30054099	13524345	16529755	222600249
18	594000000	562529739	31470261	1416162	30054099	13524345	16529755	239130004
19	594000000	562529739	31470261	1416162	30054099	13524345	16529755	255659758
20	594000000	562529739	31470261	1416162	30054099	13524345	16529755	272189513

v. Cumulative Cash Flow Diagram:

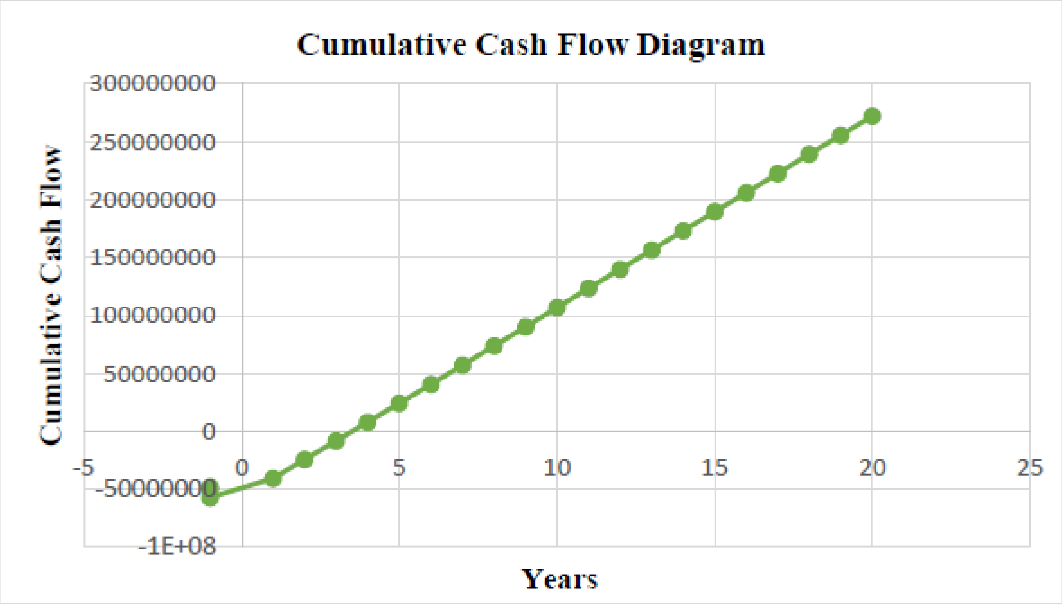

Figure 2: Cumulative Cash Flow Diagram for Breakeven Analysis

Minimum Acceptable Rate of Return (MAAR) = 15%
Internal Rate of Return = i %
$NPW=net\ profit(1+i)ni(1+i)n-TCI=0$
By hit and trial method
IRR = 31%
NPW = \$11984107
IRR > MAAR
31% > 15%

CONCLUSION

It is concluded from this research work that Bio-ethylene production from Zea Mays is a technically feasible and sustainable project as it produces ethylene from the waste biomass (Zea Mays, i.e., Corn Stover) and this waste biomass is being disposed-off in Pakistan as land fillings, by burning of this waste to get energy (this is causing severe environmental fall outs in Pakistan). The process conditions (like suitable temperature, pressure etc.) are developed during this work to make it a technically viable process. Zea Mays being a waste biomass is inexpensive and due to its large-scale cultivation in Pakistan, it is abundantly available. Biorefinery projects are much needed for the developing economies like Pakistan to produce expensive products from inexpensive raw material (waste biomass). The economic analysis of this project also confirmed the technical & economic feasibility of this biorefinery project. All indicators of economic sustainability are positive and endorse the viability of this project. 27% Rate of return makes this project is financially attractive for the investors and the IRR is 31% which quite higher than other minimum acceptable rate of return, actually this much IRR makes this project to stand out as compared to any alternative investment options. Moreover, there are very few environmental hazards associated with this project, which can be controlled by proper waste management. Another aspect of this research work is that we can also produce bioethanol from the same biomass waste (Zea Mays) which is a biofuel.

REFERENCES

[1] S. Amornraksa, I. Subsaipin, L. Simasatitkul, and S. Assabumrungrat, ‘Systematic design of separation process for bioethanol production from corn stover’, *BMC Chem. Eng.*, vol. 2, no. 1, p. 10, Dec. 2020, doi: 10.1186/s42480-020-00033-1.
[2] M. Yang, X. Tian, and F. You, ‘Manufacturing Ethylene from Wet Shale Gas and Biomass: Comparative Technoeconomic Analysis and Environmental Life Cycle Assessment’, *Ind. Eng. Chem. Res.*, vol. 57, no. 17, pp. 5980–5998, May 2018, doi: 10.1021/acs.iecr.7b03731.

[3] ‘I13IR_Bioethy_MB_Jan2013_final_GSOK (2).pdf’.
[4] P. Haro, P. Ollero, and F. Trippe, ‘Technoeconomic assessment of potential processes for bio-ethylene production’, *Fuel Process. Technol.*, vol. 114, pp. 35–48, Oct. 2013, doi: 10.1016/j.fuproc.2013.03.024.
[5] P. P. Van Uytvanck, B. Hallmark, G. Haire, P. J. Marshall, and J. S. Dennis, ‘Impact of Biomass on Industry: Using Ethylene Derived from Bioethanol within the Polyester Value Chain’, *ACS Sustain. Chem. Eng.*, vol. 2, no. 5, pp. 1098–1105, May 2014, doi: 10.1021/sc5000804.
[6] D. Humbird *et al.*, ‘Process Design and Economics for Biochemical Conversion of Lignocellulosic Biomass to Ethanol: Dilute-Acid Pretreatment and Enzymatic Hydrolysis of Corn Stover’, NREL/TP-5100-47764, 1013269, Mar. 2011. doi: 10.2172/1013269.
[7] ‘Chemical_Process_Design.pdf’.
[8] J. N. Markham *et al.*, ‘Techno-economic analysis of a conceptual biofuel production process from bioethylene produced by photosynthetic recombinant cyanobacteria’, *Green Chem.*, vol. 18, no. 23, pp. 6266–6281, 2016, doi: 10.1039/C6GC01083K.
[9] J. McKechnie, M. Pourbafrani, B. A. Saville, and H. L. MacLean, ‘Exploring impacts of process technology development and regional factors on life cycle greenhouse gas emissions of corn stover ethanol’, *Renew. Energy*, vol. 76, pp. 726–734, Apr. 2015, doi: 10.1016/j.renene.2014.11.088.

Structural and Electronic Characterization of m-Fluoroaniline and m-Iodoaniline: A Density Functional Theory Study

Yavuz EKİNCİOĞLU [1*] and Abdullah KEPCEOĞLU [2,3]
[1] Bayburt University, Department of Opticianry, 69000, Bayburt, Türkiye
[2] Koç University, Department of Molecular Biology and Genetics, 34450, İstanbul, Türkiye
[3] Koç University Surface Science and Technology Center (KUYTAM), Rumelifeneri, Istanbul, 34450, Türkiye

* Corresponding author e-mail address: yekincioglu@bayburt.edu.tr

ORCID Numbers: 0000-0002-8610-1245 (Yavuz EKİNCİOĞLU), 0000-0002-4743-5517 (Abdullah KEPCEOĞLU)

Abstract - This study aimed to investigate the electronic and structural characteristics of m-fluoroaniline (MFA) and m-iodoaniline (MIA). Density functional theory (DFT) and CAM-B3LYP/LanL2DZ methods were employed to determine various properties such as the highest occupied molecular orbital (HOMO) and lowest unoccupied molecular orbital (LUMO) energy levels, chemical reactivity descriptors, nonlinear optical properties, Mulliken population analysis, molecular electrostatic potential map, thermodynamic properties, and UV-Vis spectral analysis. In addition, the research explored the vertical and adiabatic ionization energy parameters of these molecules by constructing singly charged cation radicals using the same level theory. The obtained results were compared with experimental data from the literature.

Keywords — *DFT, Molecular properties, HOMO, LUMO, NLO, UV-Vis, Adiabatic Ionization, Vertical Ionization*

I. INTRODUCTION

Aromatic amines, especially aniline, are crucial in biology and materials science due to their numerous technological uses [1, 2]. Aniline serves as a precursor for creating dye and sensitizer molecules, enabling the production of non-linear optical molecules [3-5]. Aniline represents the molecular model for aromatic amines, with its structure known in the gas phase by microwave spectroscopy and in the solid state by X-ray crystallography [6-9]. The structural and electronic properties of aniline were analyzed through semiempirical and ab initio calculations [10-14]. The presence of a substituent atom in aniline changes the charge distribution in the molecule, thereby altering its structural and electronic characteristics [15]. Aniline can form three isomeric configurations: ortho, meta, and para isomers. Ortho and para isomers have been studied theoretically and experimentally as a substitute for different atoms in the literature [16-21]. However, information on the structural and electrical properties of substitute anilines, specifically MFA (MFA) and MIA (MIA) compounds, is scarce. Therefore, future experimental research will greatly benefit from these findings. In this study, we use theoretical calculations to demonstrate the differences in the structural and electrical properties of substituted anilines.

II. MATERIAL AND METHODS

The conformer analysis of *MFA* and *MIA* was carried out by the Spartan 08 package program [22] using Merck molecular force field (MMFF) in the molecular mechanic method. then, the ground state geometries of each isomer were optimized in the gas phase using the Coulomb-attenuating method-functional hybrid Becke three-parameter Lee–Yang–Parr exchange-correlation functional (CAM-B3LYP) and the LanL2DZ basis set with the Gaussian09 program. Also, adiabatic ionization parameters were calculated by optimizing the most stable molecular conformational geometry and the same molecular geometry as the neutrals were used to calculate the vertical ionization parameters.

III. RESULTS AND DISCUSSION

A. Geometrical Structure Analysis

The optimized structure along with numbering of the atoms of *MFA* and *MIA* compounds obtained from the B3LYP/LANL2DZ method is show in Fig 1. The optimized structural selected bond lengths, bond angles and dihedral angles of these compounds are presented in Table II. The energy and dipole moments values of these compounds are also displayed in Table I. As indicated in table I, *MFA* has the lowest energy value of the compounds, hence it is the most stable of these compounds. In the aniline ring, our calculations of C1-C3, C1-C4, and C6-C3 bond lengths are calculated at 1.41082 1.41412, and 1.38906 Å for *MFA*. In additionally these bond lengths for ***MIA*** have calculated 1.41247, 1.41164, and 1.39669 respectively. each two compounds have approximately the same values among C-C bond lengths. But, C-X (X=F, I) bond lengths for fluorine and iodine atoms attached to the aniline ring were obtained as 1.39681, and 2.12926 Å respectively. As shown in Table II, the computed bond angles and dihedral angles values for both compounds are almost the same.

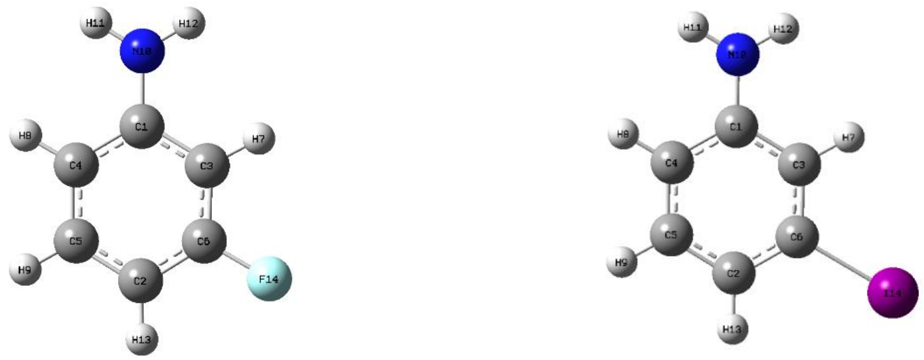

MFA ***MIA***

Fig. 1. Lowest energy structure of ***MFA*** and ***MIA*** compounds

Table I. Energy and dipole moment values of ***MFA*** and ***MIA*** compounds

Compounds	**Energy (Hartree)**	**Dipole Moment (Debye)**	**Point Group**
MFA	-386.625110	3.706085	C1
MIA	-298.151130	3.244160	C1

Table II. The Bond Lenghts (Å), Bond Angles (°) and Dihedral Angles (°) of ***MFA*** and ***MIA*** compounds

Parameters	***Compounds***	
	MFA	***MIA***
Bond Lenghts (Å)		
N10-C1	1.38881	1.39006
C1-C3	1.41082	1.41247
C1-C4	1.41412	1.41164
C6-F14	**1.39681**	-
C6-I14	-	**2.12926**
C6-C3	1.38906	1.39669
C6-C2	1.39160	1.40004
Bond Angles (°)		
N10-C1-C3	120.38226	120.29603
N10-C1-C4	120.65442	120.71257
C1-C3-C6	118.44227	119.72753
C3-C6-F14	**117.4919**	**-**
C3-C6-I14	**-**	**118.99267**
F14-C6-C2	**118.39351**	**-**
I14-C6-C2	**-**	**119.24641**
C6-C2-C5	116.74355	118.09567
Dihedral Angles (°)		
N10-C1-C3-C6	179.99892	-179.99905

N10-C1-C4-C5	179.99113	-179.99961
F14-C6-C3-C1	**-179.98357**	**-**
I14-C6-C3-C1		**-179.99814**
F14-C6-C2-C5	**179.97602**	-
I14-C6-C2-C5	-	**179.99713**

B. FMO and Chemical Reactivity Descriptors

The highest occupied molecular orbital (HOMO) and the lowest unoccupied molecular orbital (LUMO) play important roles in determining the electronic, electric, and optical characteristics of molecules [23]. The LUMO functions as an electron acceptor and so describes the compounds' susceptibility to attack by nucleophiles [24]. The HOMO functions as an electron donor and so characterizes the compounds' susceptibility to assault by electrophiles. The HOMO-LUMO gap energy is the energy difference between HOMO and LUMO energies. The compositions' chemical reactivity and kinematic stability can be investigated with the help of the HOMO-LUMO gap energy. The softer the compound, the smaller the HOMO-LUMO gap energy value, and the harder, less reactive, and less stable the compound, the greater the HOMO-LUMO gap energy value [25, 26]. As seen in Fig. 2, the colors red and green are represented in positive and negative phases, respectively. According to the HOMO-LUMO energy gap values, the most soft, reactive, and stable chemical is MIA.

MFA	***MIA***
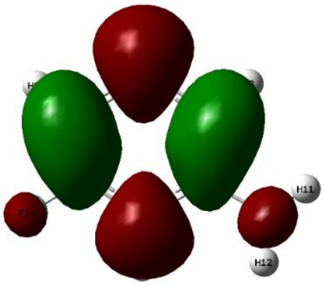	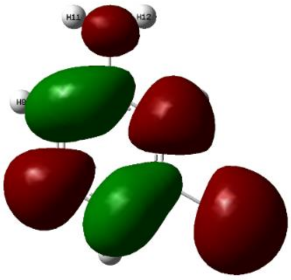
$\mathbf{E_{LUMO} = -4.60\ eV}$	$\mathbf{E_{LUMO} = -4.57\ eV}$
⇧	⇧
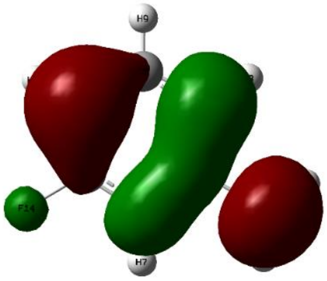	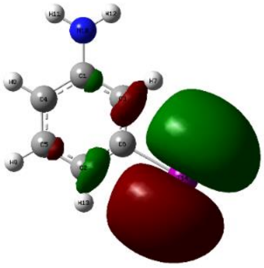
$\mathbf{E_{HOMO} = -8.71\ eV}$	$\mathbf{E_{HOMO} = -5.35\ eV}$

Fig. 2. HOMO-LUMO Plot of ***MFA*** and ***MIA*** compounds

The global chemical reactivity descriptors are defined by the Koopman's theorem [27]. the ionization potential (I) and electron affinity (A) values can be calculated through HOMO and LUMO orbitals energies using the equations $\mathrm{I} = -\mathbf{E_{HOMO}}$ and $A = -\mathbf{E_{LUMO}}$. İn additionally, chemical potential (μ), global hardness (η), global softness (S), electrophilicity index (ω) and the electronegativity (χ) are expressed by the following equations. . These quantum chemical parameters were calculated using equation 1-5 [28]. The hardness corresponds to the gap between $\mathbf{E_{HOMO}}$ and $\mathbf{E_{HOMO}}$ $\mathbf{E_{LUMO}}$energies and is indicator the stability and reactivity of compounds. The softness describes the capacity of an atom or a group of atoms to accept electrons. The obtainde values of global reactivity descriptors were presented in table III.

$$\mu = -\frac{(I+A)}{2} \qquad \text{Equation 1}$$

$$\eta = \frac{(I-A)}{2} \qquad \text{Equation 2}$$

$$S = \frac{1}{\eta} \qquad \text{Equation 3}$$

$$\omega = \frac{\mu^2}{2\eta} \qquad \text{Equation 4}$$

$$\chi = \frac{(I+A)}{2} \qquad \text{Equation 5}$$

Table III. Chemical reactivity descriptors of ***MFA*** and ***MIA*** compounds

Compounds	**E_{gap} (eV)**	**I (eV)**	**A (eV)**	**μ (eV)**	**η (eV)**	**S (eV)**	**ω (eV)**	**χ (eV)**
MFA	4.11	8.71	4.60	-6.65	2.05	0.24	10.78	6.65
MIA	0.78	5.35	4.57	-4.96	0.39	1.28	31.54	4.96

C. Nonlinear Optical (NLO) Properties

Nonlinear Optical (NLO) Properties is most important properties for optical modulation, optical switching, optical logic, and optical memory in the areas of telecommunications, optical interconnections, and signal processing [29-31]. The dipole moments (μ), the polarizabilities (α), and the first-order hyperpolarizabilities (β) of compounds have calculated using the finite-field approach. The obtained values were presented in table IV. The μ, (α), and β values using the x, y, z components are calculated using follows equations.

$$\mu_{tot} = \left(\mu_x + \mu_y + \mu_z\right)^{1/2} \qquad \text{Equation 6}$$

$$\alpha_{tot} = \frac{1}{3}\left(\alpha_{xx} + \alpha_{yy} + \alpha_{zz}\right) \qquad \text{Equation 7}$$

$$\beta_{tot} = \left(\beta_x^2 + \beta_y^2 + \beta_z^2\right)^{1/2} \qquad \text{Equation 8}$$

were β_x, β_y and β_z are defined to be

$$\beta_x = \left(\beta_{xxx} + \beta_{xyy} + \beta_{xzz}\right) \qquad \text{Equation 9}$$

$$\beta_y = \left(\beta_{yyy} + \beta_{yzz} + \beta_{yxx}\right) \qquad \text{Equation 10}$$

$$\beta_z = \left(\beta_{zzz} + \beta_{zxx} + \beta_{zyy}\right) \qquad \text{Equation 11}$$

Total first hyper polarizability from Gaussian 09 output is given in Equation 12.

$$\beta_{tot} = \left[\left(\beta_{xxx} + \beta_{xyy} + \beta_{xzz}\right)^2 + \left(\beta_{yyy} + \beta_{yzz} + \beta_{yxx}\right)^2 + \left(\beta_{zzz} + \beta_{zxx} + \beta_{zyy}\right)^2\right]^{1/2} \qquad \text{Equation 12}$$

The dipole moment is one of the most important results for electronic properties due to the distribution of charges on atoms in a compound and used to study the intermolecular interactions. The intermolecular interactions are stronger when the dipole moment is higher. A molecule's reaction to an applied electric field is characterized by its polarizability and first hyper polarizability. The calculated β_{tot} and α_{tot} values in table IV were converted into electrostatic units (esu) (1 a.u. = 8.6393×10^{-33} esu) and (1 a.u. = 0.1482×10^{-24} esu), respectively [27, 28]. For MFA and MIA molecules, the computed dipole moment is 3.7061 D and 3.2442 D, respectively. As a result, MFA has a greater estimated dipole moment than MIA. Polarizability values for MFA and MIA compounds were determined to be 9.584 x10^{-24} esu and 12.505 x 10^{-24} esu respectively. Also, both the MFA and MIA compounds' first-order hyperpolarizabilities were calculated to be 2369.14 x 10^{-33} esu and 2465.26 x 10^{-33} esu respectively. Urea is one of the model molecules used to investigate the NLO properties of compounds {Dixon, 1994 #42}. It is frequently used as a benchmark for comparison.

Polarizability and first-order hyperpolarizabilities values for urea are found to be 3.8312 x10^{-24}esu and 0.1947 × x 10^{-30} esu, respectively. Polarizability values for MFA and MIA molecules are roughly 2.5 and 3 times larger than urea, respectively. Furthermore, the first-order hyperpolarizabilities found for MFA and MIA compounds are roughly 12 and 12, 5 times larger than the magnitude of urea, respectively.

Table IV. NLO values of ***MFA*** and ***MIA*** compounds

Parameters	***MFA***	***MIA***
Dipole moment (Debye)		
μ_x	3.6862	3.0614
μ_y	0.3834	-1.0735
μ_z	0.0003	0.0000
μ_{tot}	3.7061	3.2442
Polarizability (a.u)		
α_{xx}	88.08	134.61
α_{yy}	76.82	87.98
α_{zz}	29.10	30.54
α_{tot} **(a.u)**	64.673	84.380
α_{tot} **(esu)**	9.584 x10^{-24}	12.505 x 10^{-24}
Hyperpolarizability (a.u)		
β_{xxx}	-153.81	45.21
β_{xxy}	196.46	139.04
β_{xyy}	-24.19	-139.23
β_{yyy}	1.34	127.60
β_{xxz}	-0.041	0.0002
β_{xyz}	0.024	-0.0009
β_{yyz}	-0.0051	-0.0011
β_{xzz}	-6.032	32.24
β_{yzz}	5.490	11.93
β_{zzz}	-0.012	-0.0027
β_{tot} **(a.u)**	274.229	285.354
β_{tot} **(esu)**	2369.14 x 10^{-33}	2465.26 10^{-33}

D. Mulliken Populations

The Mulliken atomic charges calculations were carried out the determination of electron population of each atom in compounds. Atomic charges have an impact on a variety of molecular characteristics, including the dipole moment, electrical parameters, polarizability, and refraction [32]. It is essential to comprehend these charges. All hydrogen atoms have positive charges, as seen in figure 3. In general, the carbon atoms in the ring have positive charges, however the C6 MIA has a negative charge and the MFA has a positive charge. Each of the two compounds' nitrogen atoms carries a negative charge. İodine and fluorine substituted atoms have positive and negative charges, respectively.

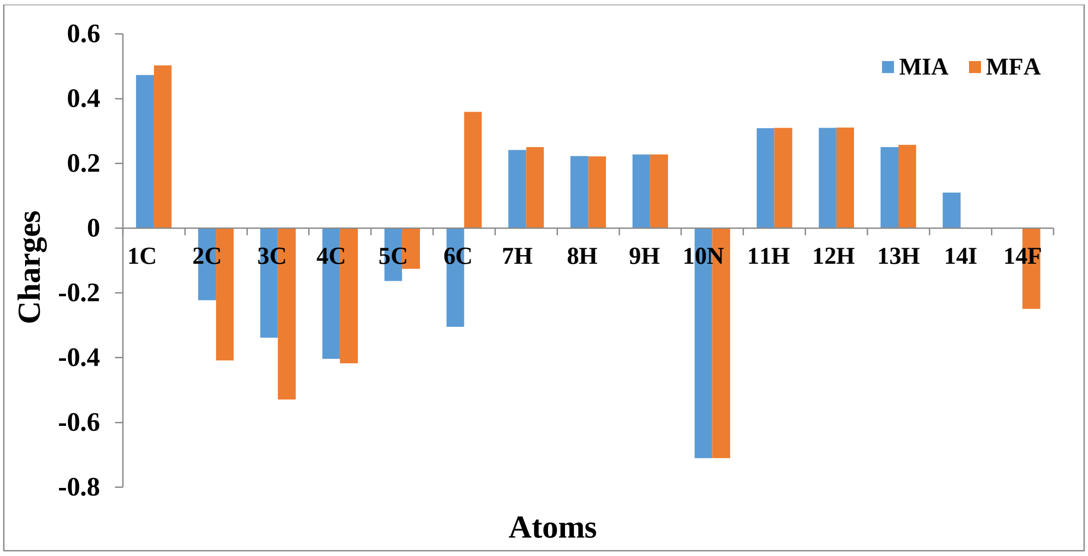

Fig. 3. Mulliken populations of ***MFA*** and ***MIA*** compounds

E. Molecular Electrostatic Potential Map

The molecular electrostatic potential maps are one of the key computation techniques used to examine the distribution of electron densities over the compounds. It is very beneficial for predicting a compound's reactivity to nucleophilic and electrophilic assaults. Intermolecular interaction types can be inferred thanks to MEPs [28, 33]. The MEP maps of the substances produced on the density surface are shown in Figure 4. These maps' red and yellow colors indicate areas that are more electron-rich (electrophilic reactivity), while their blue color indicate areas that are more electron-poor (nucleophilic reactivity). For MFA, the electrophilic and nucleophilic regions are primarily located on the fluorine atom and close to the nitrogen atom, respectively. The electrophilic region for MIA is localized on all compounds. Additionally, the color codes of these MEP maps are in the range between **-5.465×x10^{-2} a.u — 5.465 ×x10^{-2} a.u** and **-4.736×x10 a.u — 4.736 ×x10 a.u** MFA and MIA respectively.

-5.465×x10^{-2} a.u — 5.465 ×x10^{-2} a.u	**-4.736×x10 a.u — 4.736 ×x10 a.u**
MFA	***MIA***

Fig. 4. Molecular electrostatic potential of ***MFA*** and ***MIA*** compounds

F. Thermodynamic Properties

Table V shows the thermodynamic properties of MFA and MIA compounds in the gas phase, including thermal, heat capacity, entropy, zero-point vibrational energy, sum of electronic and zero-point energies, sum of electronic and thermal free energies, and rotational constants. We discovered that the heat capacity, entropy, and zero-point vibrational energy were acquired in the sequence MIA > MFA. The thermal, sum of electronic and zero-point energies, and sum of electronic and thermal free energies have been calculated in the following order: MFA > MIA. These findings can be used to conduct experiments on the chemical reactions of MFA and MIA [34].

Table V. Thermodynamic properties for *MFA* and *MIA* compounds

Parameters	***MFA***	***MIA***
Total energy (thermal), E total (kcal. Mol^{-1})		
TOTAL	73.758	72.841
Electronic	0.000	0.000
Translational	0.889	0.889
Rotational	0.889	0.889
Vibrational	71.980	71.064
Heat capacity at const. volume, C v (cal. Mol^{-1} K^{-1})		
TOTAL	25.886	27.346
Electronic	0.000	0.000
Translational	2.981	2.981
Rotational	2.981	2.981
Vibrational	19.925	21.384
Entropy, S (cal. Mol^{-1} K^{-1})		
TOTAL	79.837	87.365
Electronic	0.000	0.000
Translational	40.030	42.054
Rotational	28.126	30.281
Vibrational	11.680	15.030
Zero-point vibrational energy, E 0 (kcal mol^{-1})	69.65156	68.27284
Sum of electronic and zero-point energies (Hartree/Particle)	-386.514113	-298.042330
Sum of electronic and thermal free energies (Hartree/Particle)	-386.507570	-298.035050
Rotational constants (GHz)		
A	3.30655	3.23079
B	1.75968	0.56568
C	1.18983	0.48139

G. TD-DFT Results: UV-Vis Spectra and Ionization Energies

Figure 5 depicts the calculated UV-Vis spectra of the neutral m-fluoroaniline and m-iodoaniline isomers using time-dependent density functional theory (TD-DFT). The spectra demonstrate strong absorption bands at around 190 nm and weaker absorption bands at around 210 nm. The major contributions to the electronic transitions of the m-fluoroaniline and m-iodoaniline isomers are presented in Tables 6 and 7, respectively. Specifically, the first excited state of the m-fluoroaniline isomer arises from the transition of the highest occupied molecular orbital (HOMO) to the lowest unoccupied molecular orbital (LUMO), while the most intense transition in the m-iodoaniline isomer results from the combined transitions of H-1 to LUMO and H-1 to L+1. These findings offer valuable insights into the electronic structure and bonding of the isomers and can facilitate the interpretation of their spectroscopic properties.

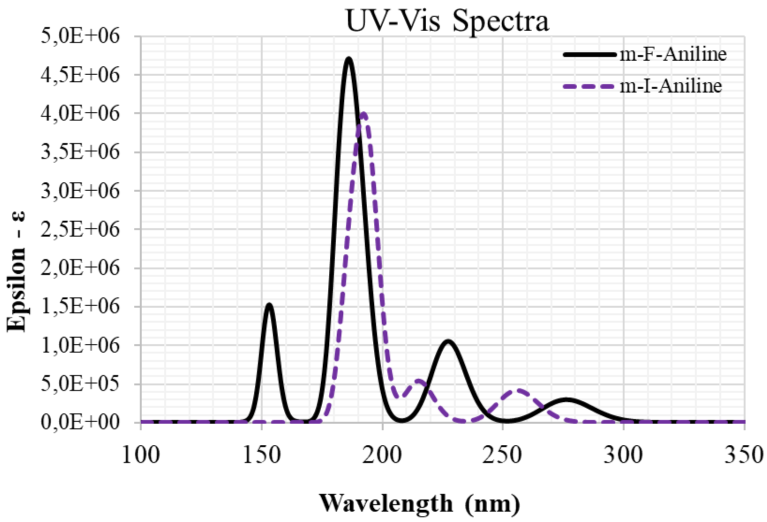

Fig. 5. Calculated UV-Vis spectra of the titled molecules (GaussSum program was used to plot spectra)

The Table VI. shows the energy values and dipole moments for different isomers of m-fluoroaniline and m-iodoaniline. For m-fluoroaniline, there are slight differences in the relative energy values between the Adiabatic Ionization (AI) and Vertical Ionization (VI) processes, indicating that the VI process requires more energy to ionize the molecule. For m-iodoaniline, there is only an AI process, and the relative energy values are consistent across different units. The dipole moment values for the isomers indicate that m-iodoaniline is more polar than m-fluoroaniline. These numerical values can provide valuable information about the properties and behavior of these molecules.

Table VI. Molecular energies (relative to its neutrals) and dipole moments of the molecules (AI: Adiabatic Ionization, VI: Vertical Ionization)

Isomers	Energy (Hartree)	Relative Energy (Hartree)	Relative Energy (kcal/mol)	Relative Energy (cm^{-1})	Relative Energy (eV)	Dipole Moment (D)
m-fluoroaniline (AI)	-386,337	0,288	756,115	180,716	7,837	6,370
m-fluoroaniline (VI)	-386,332	0,293	184,066	64376,696	7,982	6,555
m-iodoaniline (AI)	-297,866	0,286	179,217	62680,632	7,772	10,953
m-iodoaniline (VI)	-297,866	0,286	179,217	62680,632	7,772	10,953

The Table VII. shows that the first excited state (State 1) corresponds to a transition from HOMO to LUMO, which accounts for 79% of the transition. State 2 corresponds to a transition from HOMO to L+1, which accounts for 86% of the transition. The contributions of HOMO to L+2 and L+3 are the major contributors to State 3, with a total percentage of 97%. State 4 involves a combination of transitions from H-1 to LUMO and HOMO to L+2, accounting for 79% of the transition. State 5 corresponds to a transition from HOMO to L+4, which accounts for 87% of the transition.

States 6, 8, and 7 correspond to transitions from H-1 to LUMO and H-1 to L+1, HOMO to L+5 and L+6, and HOMO to L+5 and L+6, respectively, with different percentages of contribution. State 9 involves transitions from H-1 to L+2 and L+3, accounting for 83% of the transition, while State 10 involves transitions from H-1 to L, H-1 to L+2, and H to L+2 with different contributions. Overall, the table provides valuable information on the excited states and electronic transitions of the m-fluoroaniline isomer.

Table VII. TD-DFT results for the excited states of the neutral m-fluoroaniline isomer (f is the oscillator strength)

Excited State	ΔE (nm)	f	Major Contributions to the Transitions (percentage)
1	261.603141774	0.0003	HOMO→LUMO (79%)
2	255.737697267	0.0671	HOMO→L+1 (86%)
3	243.421276578	0.0001	HOMO→L+2 (11%), HOMO→L+3 (86%)
4	228.138580599	0.0005	H-1→LUMO (18%), HOMO→L+2 (61%)
5	214.903355714	0.0871	HOMO→L+4 (87%)
6	193.664781337	0.538	H-1→LUMO (14%), H-1→L+1 (75%)
7	187.658649309	0.0003	HOMO→L+5 (69%), HOMO→L+6 (21%)
8	186.532155341	0.2944	HOMO→L+5 (24%), HOMO→L+6 (71%)
9	184.272688513	0.0001	H-1→L+2 (10%), H-1→L+3 (83%)
10	168.761747468	0.0	H-1→L (31%), H-1→L+2 (22%), H→L+2 (12%)

The major contributions to the transitions are identified by the orbitals involved in the transitions. H-1 and L+1 represent the highest occupied molecular orbital (HOMO) and lowest unoccupied molecular orbital (LUMO), respectively, while L+2, L+3, and L+4 represent the second, third, and fourth lowest unoccupied molecular orbitals, respectively.

The Table VIII. shows that the most intense transition occurs at a wavelength of 179.46 nm with an oscillator strength of 0.3649 and is dominated by the H-1 to LUMO transition (45%) and H-1 to L+1 transition (31%). Additionally, the table shows that the contributions of higher energy transitions (such as those involving L+2, L+3, and L+4) are relatively small.

Table VIII. TD-DFT results for the excited states of the neutral m-iodoaniline isomer (f is the oscillator strength)

Excited State	ΔE (nm)	f	Major Contributions to the Transitions (percentage)
1	247.211917557	0.048	H-1->L+1 (14%), HOMO->LUMO (83%)
2	209.397387286	0.1709	H-1->LUMO (16%), HOMO->L+1 (80%)
3	179.458361817	0.3649	H-1->LUMO (45%), H-1->L+1 (31%), HOMO->L+1 (12%)
4	174.21095282	0.57	H-1->LUMO (35%), H-1->L+1 (48%)
5	167.993432533	0.0	HOMO->L+2 (95%)
6	156.965859387	0.0014	HOMO->L+3 (94%)
7	147.7920075	0.2448	H-2->LUMO (91%)
8	145.709475863	0.0028	HOMO->L+4 (71%)
9	144.97683935	0.0014	H-3->LUMO (86%)
10	141.761025626	0.0031	H-1->L+3 (78%), HOMO->L+4 (11%)

These results provide valuable information about the electronic properties and behavior of the m-iodoaniline isomer, which can be useful for understanding its reactivity and potential applications in various fields.

IV. CONCLUSION

In this study, we performed detailed investigations on MFA and MIA molecules using quantum chemical calculations. The structural, electronic, and UV-Vis analyses of the title compounds were calculated by the DFT/CAMB3LYP/LanL2DZ method. Our results show that substituents attached to the benzene ring of aniline produce both structural and electronic distortions, with the HOMO-LUMO gap values being one of the most significant effects. Additionally, the polarizability values for MFA and MIA molecules are roughly 2.5 and 3 times larger than urea, respectively. The first order hyperpolarizabilities found for MFA and MIA compounds are roughly 12 and 12.5 times larger than the magnitude of urea, respectively. According to Mulliken population analysis, all hydrogen atoms have positive charges, while the carbon atoms in the ring generally have positive charges. However, C6 MIA has a negative charge, and MFA has a positive charge. In summary, the UV-Vis spectra of the m-fluoroaniline and m-iodoaniline isomers were calculated using TD-DFT, with strong absorption bands observed at around 190 nm and weaker absorption bands at around 210 nm. The major electronic transitions and excited states of the isomers were identified, providing insights into their electronic structure and bonding. Additionally, energy values and dipole moments were determined for the isomers, offering further information about their properties and behavior. These findings can be useful for interpreting the spectroscopic properties of the isomers and understanding their potential applications in various fields.

ACKNOWLEDGMENTS

This work was supported by the Scientific and Technical Research Council of Turkey (TUBITAK) under Grant No. 118C476 and Grant No. 122F301. However, the entire responsibility of the publication belongs to the authors of the publication. The financial support received from TÜBİTAK does not mean that the content of the publication is approved in a scientific sense by TÜBİTAK.

REFERENCES

[1] H. S. Nalwa, “Handbook of organic conductive molecules and polymers,” Wiley, 1997.
[2] M. E. Vaschetto, B. A. Retamal, and A. P.” Monkman, Density functional studies of aniline and substituted anilines,” Journal of Molecular Structure: THEOCHEM, 468(3), pp. 209-221 1999.
[3] N. E. Agbor, J. P. Cresswell, M. C. Petty, and A. P. Monkman, "An optical gas sensor based on polyaniline Langmuir-Blodgett films," Sensors and Actuators B: Chemical, 41(1-3), pp. 137-1411997.
[4] J. O. Morley, "Nonlinear optical properties of organic molecules. 19. Calculations of the structure, electronic properties, and hyperpolarizabilities of phenylsydnones," The Journal of Physical Chemistry, 99(7), pp. 1923-1927, 1995.
[5] P. Naik, I. M. Abdellah, M. Abdel-Shakour, R. Su, K. S. Keremane, A. El-Shafei, A., and A. V. Adhikari, "Improvement in performance of N3 sensitized DSSCs with structurally simple aniline based organic co-sensitizers," Solar Energy, 174, pp. 999-1007, 2018.
[6] Y. Wang, S. Saebø, and C. U. Pittman Jr, "The structure of aniline by ab initio studies," Journal of Molecular Structure: THEOCHEM, 281(2-3), pp. 91-98, 1993.
[7] D. G. Lister, and J. K. Tyler, "Non-planarity of the aniline molecule," Chemical Communications (London), (6), pp. 152-153, 1966.
[8] D. G. Lister, J. K. Tyler, J. H. Høg, and N. W. Larsen, "The microwave spectrum, structure and dipole moment of aniline," Journal of Molecular Structure, 23(2), pp. 253-264, 1974.
[9] M. A. K. O. T. O. Fukuyo, K. Hirotsu, and T. Higuchi, "The structure of aniline at 252 K," Acta Crystallographica Section B: Structural Crystallography and Crystal Chemistry, 38(2), p. 640-643,1982.
[10] W. J. Hehre, L. Radom, and J. A. Pople, "Molecular orbital theory of the electronic structure of organic compounds. XII. Conformations, stabilities, and charge distributions in monosubstituted benzenes," Journal of the American Chemical Society, 94(5), pp. 1496-1504, 1972.
[11] W. J. Parr, and R. E. Wasyushen, "A MINDO/3 study of the planarity of the amino-fragment in some para-substituted anilines," Journal of Molecular Structure, 38, pp. 272-276, 1977
[12] A. D. Gorse, and M. Pesquer, "A theoretical study of aniline and some derivatives in their ground states," Journal of Molecular Structure: THEOCHEM, 281(1), pp. 21-32, 1993.
[13] F. M. Moghaddam, R. Pourkaveh, and A. Karimi, "Oxidative heck reaction as a tool for para-selective olefination of aniline: a DFT supported mechanism," The Journal of Organic Chemistry, 82(19), pp. 10635-10640, 2017.
[14] M. Kurt, M. Yurdakul, and Ş. E. N. A. Y. Yurdakul, "Molecular structure and vibrational spectra of 3-chloro-4-methyl aniline by density functional theory and ab initio Hartree-Fock calculations," Journal of Molecular Structure: THEOCHEM, 711(1-3), pp. 25-32, 2004.
[15] M. E. Vaschetto, and B. A. Retamal, "Retamal, Substituents effect on the electronic properties of aniline and oligoanilines," The Journal of Physical Chemistry A, 101(37), pp. 6945-6950, 1997.
[16] R. Errabelli, Z. Zheng, and A. B. Attygalle, "Formation of Protonated ortho-Quinonimide from ortho-Iodoaniline in the Gas Phase by a Molecular-oxygen-mediated, ortho-Isomer-specific

Fragmentation Mechanism," Journal of the American Society for Mass Spectrometry, 31(4), pp. 864-872, 2020.

[17] R. L. Hand, and R. F. Nelson, "The Anodic Decomposition Pathways of Ortho-and Meta-substituted Anilines," Journal of the Electrochemical Society, 125(7), pp. 1059, 1978.

[18] C. Tian, Q. Wang, X. Wang, G. An, and G. Li, "Visible-Light Mediated ortho-Trifluoromethylation of Aniline Derivatives," The Journal of Organic Chemistry, 84(21), pp. 14241-14247, 2019.

[19] M. Oyama, and K. Kirihara, "Spectroscopic investigation of oxidation products of ortho-or meta-substituted aniline derivatives in acetonitrile using an electron-transfer stopped-flow method," Electrochimica acta, 49(22-23), pp. 3801-3806, 2004.

[20] S. V. Kessar, P. Singh, K. N. Singh, P. V. Bharatam, A. K. Sharma, S. Lata, and A. Kaur, "A Study of BF3-Promoted ortho Lithiation of Anilines and DFT Calculations on the Role of Fluorine–Lithium Interactions," Angewandte Chemie, 120(25), pp. 4781-4784, 2008.

[21] S. Rahman, M. A. Rub, S. Mahbub, M. T. R. Joy, S. Rana, and M. A. Hoque, "Spectroscopic and DFT studies of the charge transfer complexation of iodine with aniline and its derivatives in carbon tetrachloride medium," Journal of Molecular Liquids, 351, pp. 118667, 2022.

[22] Y. Shao, L. F. Molnar, Y. Jung, J. Kussmann, C. Ochsenfeld, S. T. Brown, and M. Head-Gordon, "Advances in methods and algorithms in a modern quantum chemistry program package," Physical Chemistry Chemical Physics,. 8(27), pp. 3172-3191,2006.

[23] I. Fleming, "Molecular orbitals and organic chemical reactions," John Wiley & Sons, 2011.

[24] M. Karelson, V. S. Lobanov, and A. R. Katritzky, "Quantum-chemical descriptors in QSAR/QSPR studies," Chemical reviews, 96(3), pp. 1027-1044, 1996.

[25] N. R. Sheela, S. Muthu, and S. Sampathkrishnan, "Molecular orbital studies (hardness, chemical potential and electrophilicity), vibrational investigation and theoretical NBO analysis of 4-4′-(1H-1, 2, 4-triazol-1-yl methylene) dibenzonitrile based on abinitio and DFT methods," pectrochimica Acta Part A: Molecular and Biomolecular Spectroscopy, 120, pp. 237-251, 2014.

[26] M. Miar, A. Shiroudi, K. Pourshamsian, A. R. Oliaey, and F. Hatamjafari, "Theoretical investigations on the HOMO–LUMO gap and global reactivity descriptor studies, natural bond orbital, and nucleus-independent chemical shifts analyses of 3-phenylbenzo [d] thiazole-2 (3 H)-imine and its para-substituted derivatives: Solvent and substituent effects," ournal of Chemical Research, 45(1-2), pp. 147-158, 2021.

[27] T. Koopmans, "The classification of wave functions and eigen-values to the single electrons of an atom," Physica, 1(1), pp. 104-113, 1934.

[28] Y. Ekincioğlu, H. Ş. Kılıç, and Ö. Dereli, "DFT Study of Conformational Analysis, Molecular Structure and Properties of para-, meta-and ortho 4-Methoxyphenyl Piperazine Isomers," Brazilian Journal of Physics, 51(4), pp. 958-968, 2021.

[29] C. Andraud, T. Brotin, C. Garcia, F. Pelle, P. Goldner, B. Bigot, and A. Collet, "Theoretical and experimental investigations of the nonlinear optical properties of vanillin, polyenovanillin, and bisvanillin derivatives," Journal of the American Chemical Society, 116(5), pp. 2094-2102, 1994.

[30] J. Wu, J. Luo, and A. K. Y. Jen, "High-performance organic second-and third-order nonlinear optical materials for ultrafast information processing," Journal of Materials Chemistry C, 8(43), pp. 15009-15026, 2020.

[31] S. Suresh, and D. Arivuoli, "Nanomaterials for nonlinear optical (NLO) applications: a review," Rev. Adv. Mater. Sci, 30(3), pp. 243-253, 2012.

[32] F. De Proft, C. Van Alsenoy, A. Peeters, W. Langenaeker, and P. Geerlings, "Atomic charges, dipole moments, and Fukui functions using the Hirshfeld partitioning of the electron density," Journal of computational chemistry, 23(12), pp. 1198-1209, 2002.

[33] P. Sjoberg, P. and Politzer, "Use of the electrostatic potential at the molecular surface to interpret and predict nucleophilic processes," Journal of Physical Chemistry, 94(10), pp. 3959-3961, 1990.

[34] M. A. Lillo-Ródenas, D. Cazorla-Amorós, and A. Linares-Solano, "Understanding chemical reactions between carbons and NaOH and KOH: an insight into the chemical activation mechanism," Carbon, 41(2), pp. 267-275, 2003.

6th Pak – Türk International Conference on Emerging Technologies in the field of Sciences and Engineering, May 4 – 6, 2023, Karabük University, Karabük, Türkiye

Analysis of Analytical Approximate Solutions of Relaxation Oscillation Differential Equation of Fractional Order

Aamra Urooj[1*], Muhammad Yaqub Khan[2] and Qazi Mehmood Ul Hassan[1]

[1]*Department of Mathematics, University of Wah, Wahcantt*
[2]*Department of Mathematics, Riphah International University, Islamabad*

* Corresponding author e-mail address: uw-22s-math-phd-001@student.uow.edu.pk

ORCID Numbers: 0000-0003-4622-3966 (Aamra1.Urooj1), 0000-0000-0000-0000 (Muhammad Yaqub2.Khan2), 0000-0002-6602-3868 (Qazi Mehmood1.Ul Hassan1)

Abstract— Fractional calculus has gained a considerable amount of interest and attraction by authors and researchers in field of physics and engineering as it is useful in fabricating various physical phenomenon of massive significance. Relaxation oscillation is one of the most fundamentals and notice worthy phenomenon in physics and engineering that can be dealt mathematically by a differential equation of fractional order. Generating solution and explicating the results of associated FDE is crucial. This article unfolds the mathematical approach to this physical phenomenon and figure out the different analytical techniques for finding its solution. Homotopy Analysis Method and Adomian Decomposition Method are implemented, and the solution is compared with the exact one. Moreover, the results are plotted by utilizing maple software to perceive the performance of the solutions developed by the aforementioned techniques. The plots are helpful in investigating the effectiveness and reliability of methods.

Keywords — *Relaxation Oscillation, Fractional Differential Equation, Adomian Decomposition Method, Homotopy Analysis Method, Laplace Transform method*

INTRODUCTION

Fractional differential equations are of great use in mathematical modelling of various physical [1], engineering phenomena [2] and various phenomena in psychology, rheology, viscoelasticity, and fluid dynamics. Most of the physical phenomena are simply governed by differential equations of first and second order. When the fractional differential of order α is introduced where either α lies in (0, 1) or in the interval (1, 2), the phenomenon is referred as fractional phenomenon. For instance, slow relaxation and oscillations of an oscillator can be efficiently modelled by Fractional Differential equation known as Fractional Relaxation Oscillation Equation (FROE). The investigation of FROE provides us the relation between stress and strain of viscoelastic material. As the applications for FROE continue to expand, finding a solution to FROE is becoming into a hot topic. As it involves special functions such as Mittag-Leffler functions, which are rather challenging to calculate, its analytical solution is tough to calculate explicitly. In the collected works, innumerable powerful and efficient approaches are suggested to obtain the analytical solution to FDEs. Recently, Zhang Man, Xiao Zhong Yang and Yanhua Cao applied block by block method for numerical investigation of FROE [3]. M-Izadi [4] studied the simulating FROE Using a computational algorithm. Chanchlani Lata [5] dealt the FROE with Elzaki Transform method. This article helps to analyse the effectiveness and accuracy of various analytical techniques for finding the solution of FROE. FROE is of remarkable significance in mathematical approach to viscoelastic phenomenon known as relaxation oscillation phenomenon. The relaxation oscillation equation is an initial value problem related to relaxation and oscillation phenomenon. Relaxation oscillation comprises of two alternating processes taking place on different time scales. It comprises of long period relaxation alternating with short period oscillation. This process is modelled mathematically by fractional differential equation[6-7] and is investigated by different methods such as Homotopic technique[8], G. Adomian decomposition method (ADM)[9] and Laplace transform method [10]. This article provides an analytical solution for the FROE in the form of Mittage-Leffler function. Homotopy analysis method is an analytic method for finding solutions to fractional differential equation in the form of series while Adomian decomposition method is semi analytic method for finding solution to FDEs in the form of infinite convergent series. The Laplace transform method (LTM) utilizes the Laplace transform operator and is mainly dependent upon Laplace transform of the Mittage Leffler function of two parameters represented as $E_{\alpha,\beta}(z)$. Article is organized in the four sections. Section 1 includes introduction, Section 2 includes some preliminaries, Section 3 involves implementation of different techniques for finding the solution and Section 4 includes results and discussion. A relaxation oscillator is built on the principle of working of structure which comes back to its equilibrium spot after disturbance. The relaxation equation in standard form is written as

$$f'(t) + \beta f(t) = g(t),\ \beta \in R$$

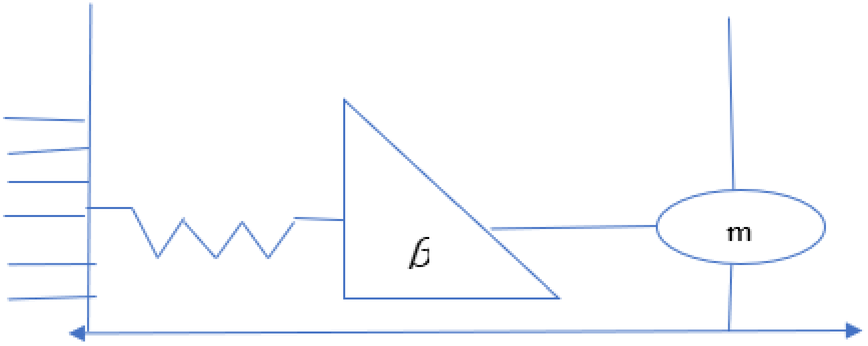

Fig. 1.Maxwell Viscoelastic Model

$\beta = E\,\eta$ is a constant. "E" is Modulus of Elasticity while η is coefficient of viscosity. For an oscillatory system, that is oscillating against the external force

$$f''(t) + Af(t) = g(t)$$

$A = \omega^2_0$ with ω_0 denotes the frequency of oscillating system and coefficient of damping is supposed to be zero. When deliberate relaxation and damped oscillation occurs, derivative of fractional order appears in the relaxation and oscillation models. Fractional relaxation-oscillation equation can be written as

$$\mathcal{D}^{\alpha} f(t) + Af(t) = g(t), t > 0, \alpha \in (0,2) \setminus \{1\}$$

$$D^{\alpha}f(t) + Af(t) = g(t) \qquad (1)$$

Together with the initial condition

$$f^{j}(0) = b_j \qquad (2)$$

Equations (6-7) constitute the fractional relaxation oscillation equation.

RESULTS AND DISCUSSION

Solution of FROE by ADM

$$f(t) = \int_0^t (t\text{-}\tau)^{\alpha\text{-}1} E_{\alpha,\alpha}(\text{-}A(t\text{-}\tau)^{\alpha})\, g(\tau)d\tau + b_0 D^{\alpha\text{-}1}(\tau)^{\alpha\text{-}1} E_{\alpha,\alpha}(\text{-}A(\tau)^{\alpha})d\tau$$

By HAM, solution of FROE is

$$f(t) = E_{\alpha,\alpha}(\text{-}At^{\alpha}) + \int_0^t G^*(t\text{-}\tau)g(\tau)d\tau \text{-}(A\text{-}1)\int_0^t G^*(t\text{-}\tau)g(\tau)d\tau + \cdots$$

While, by LTM

$$f(t) = \int_0^t (t-\tau)^{\alpha-1}E_{\alpha,\alpha}(-A(t-\tau)^{\alpha})g(\tau)d\tau + \sum_{n=1}^{k} b_n t^{\alpha-n}E_{\alpha,\alpha-n+1}(-At^{\alpha})$$

Solution of FROE obtained by the ADM, HAM and LT method is presented below graphically.

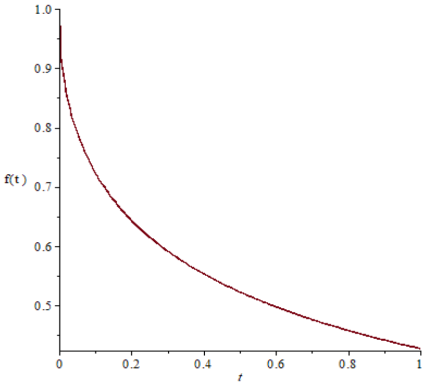

Fig.2. Solution of FROE by ADM

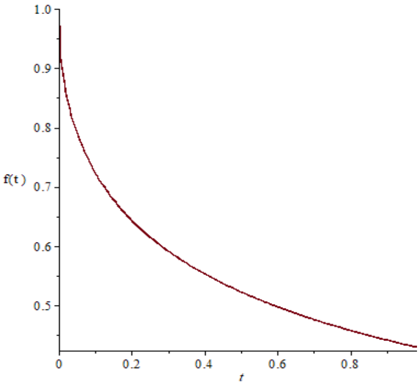

Fig.3. Solution of FROE by HAM

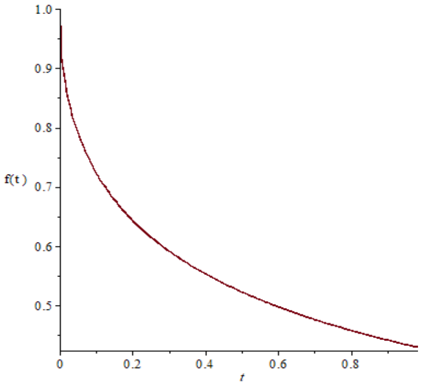

Fig.4. Solution of FROE by LTM

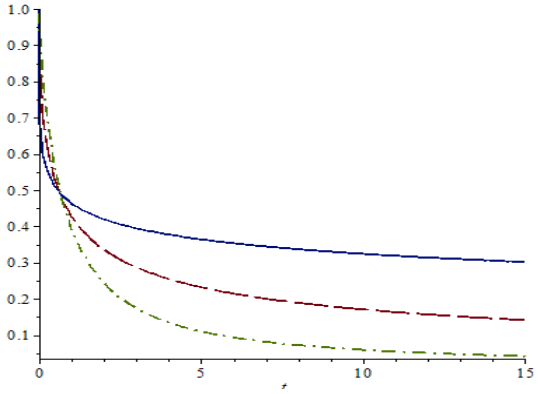

Fig.5. Solution of FROE for different values of alpha

The above figure shows the solution of relaxation oscillation equation for different values of alpha. For relaxation oscillation equation FDE all impulsive-response solutions exhibit the algebraic decay as n approaches infinity. HAM is useful for solving linear and nonlinear FDEs in the sense that this method provides solution in the form of convergent series. Also, it provides great freedom to make choice about initial guesstimate and linear operator. By changing the convergence control parameter in HAM, we are able to regulate the region and rate of convergence. While, ADM provides great freedom of selecting linear operators and this technique is valuable in computing solution of FDEs in the form of series that is rapidly convergent. Adomian Decomposition technique can be directly applied to linear, nonlinear, homogeneous, non-homogeneous differential equations as well as integral equations whose coefficients are either variables or constants. ADM starts with a computational work and there is no need to assume additionally.

CONCLUSION

The objective of this article was to analyze the effectiveness of different mathematical techniques for solving Relaxation oscillation equation. This objective is achieved by applying the three useful and effective methods that are ADM, HAM and Laplace method. All the three methods successfully solved both types of equations and accurate results are obtained. The solutions evaluated by ADM and HAM are in the form of series of infinite terms. Although all methods generate solutions close to each other, but the advantage of Laplace transform method over other two methods is that it is relatively easy and gives exact solution.

REFERENCES

[1] I. Podlubny, "An introduction to fractional derivatives, fractional differential equations, to methods of their solution and some of their applications," *Mathematics in science and engineering*, vol. 198, p. xxiv+ 340, 1999.
[2] Y. Sun, Z. Zeng, and J. Song, "Existence and uniqueness for the boundary value problems of nonlinear fractional differential equation," *Applied Mathematics*, vol. 8, pp. 312-323, 2017.
[3] M. Zhang, X. Yang, and Y. Cao, "Numerical analysis of block-by-block method for a class of fractional relaxation-oscillation equations," *Applied Numerical Mathematics*, vol. 176, pp. 38-55, 2022.
[4] M. Izadi, "A computational algorithm for simulating fractional order relaxation–oscillation equation," *SeMA Journal*, vol. 79, pp. 647-661, 2022.
[5] L. Chanchlani, "Fractional Relaxation-oscillation Model with Elzaki Decomposition Method," *AIJR Abstracts*, p. 54, 2022.
[6] R. Gorenflo and F. Mainardi, "Fractional relaxation of distributed order," in *Complexus Mundi: Emergent Patterns in Nature*, ed: World Scientific, 2006, pp. 33-42.
[7] F. Mainardi, A. Mura, R. Gorenflo, and M. Stojanović, "The two forms of fractional relaxation of distributed order," *Journal of Vibration and Control*, vol. 13, pp. 1249-1268, 2007.
[8] S.-J. Liao, "An approximate solution technique not depending on small parameters: a special example," *International Journal of Non-Linear Mechanics*, vol. 30, pp. 371-380, 1995.
[9] N. T. Shawagfeh, "Analytical approximate solutions for nonlinear fractional differential equations," *Applied Mathematics and Computation*, vol. 131, pp. 517-529, 2002.
[10] M. T. Holm, "The Laplace transform in discrete fractional calculus," *Computers & Mathematics with Applications*, vol. 62, pp. 1591-1601, 2011.

Design And Development of Voice and Gesture Controlled Smart Wheelchair Using Dc Motors for Specially Abled Persons

Anas Ibrar*, Hifza Azam, Shukaib Malik, Rana Nabeel Ahmad

University of Wah, Wah Engineering College, Wah, Pakistan

* Corresponding author e-mail address: anas.ibrar@wecuw.edu.pk

Abstract - Physically challenged persons those who are suffering from different physical disabilities face many challenging problems in their day-to-day life for commutating from one place to another and even sometimes they need other person to change their place. There are 144 million disable people who use a wheelchair in 32 developed countries, accounting for 1.82 percent of the global population. A sector of physically challenged people finds it very difficult to use traditional wheelchairs. There have been many significant efforts over the past few years to develop smart wheelchair platforms that could enable the person for its ease of operation without any difficulty. Researchers have been working on computer-controlled chairs which utilize sensors and quick control algorithms to minimize the level of human intervention. This research is based on a design that aids the voice activation system for physically disabled people by incorporating manual operation. Arduino microcontroller and voice recognition have been used to support the movement of the wheelchair. The wheelchair does not respond to an incorrect speech command. Depending on the direction given through voice and gesture wheelchair will be able to move in four different directions i.e., forward, backward, left, right. The Arduino controls the wheelchair directions The prototype is designed in such a way that it can be used independently and efficiently with less effort. It saves time, reduces cost and energy of the users.

***Keywords* —** *Especially Able, Smart, Wheelchair, Voice Control, Gesture Control*

INTRODUCTION

Whether it be a physical constraint, a specific development, or social collaboration, insufficiency includes at least one of these elements. The various types of disabilities include hearing loss, vision loss, physical impairment, speech impairment, and mental incapacity. These persons with disabilities deal with a variety of problems on a daily basis. Since they are unable to move like other individuals, people view them as being heavy. 15% of the global population is hampered by physical failure, according to those obstacles. Many years ago, individuals began to think about wheelchairs as a way to simplify their lives. Nevertheless, as everything is changing in a controlled manner, the evolution of wheelchairs is also changing. People used a self-moving wheelchair right away [1]. The electric wheelchair had already been invented by then, in 1890, but there have since been several problems with them. Alterations to increase adaptability and comfort for vulnerable groups of people. Our main goal is to provide those who are physically unable with the chance to develop. This is a sobering reality for them, and occasionally they must deal with this calumnious situation in their daily lives. Aside from the 15% of people who are debilitated, 3% of people are disabled in some way. People with disabilities in their hands as well as their spinal cord cannot use standard wheelchairs. In this way, the voice control system will assist them and eliminate any problems they may have with wheelchair control. Between 10% and 16% of the country's population in Bangladesh is thought to be disabled. 2011 is the evaluation year that there are more than millions of people with disabilities in Asia, including about 101,585 in Bangladesh, who usually go without the benefits of social improvement From an Asian perspective, it will also make various disabilities possible for people and work to reduce costs. Two basic types of wheelchairs are available for the disabled; one is operated physically using our bodies, and the other is operated in a similar manner using an engine. However, when using these wheelchairs, several people groups have difficulties. The risk of client weakness and upper-extremity injury is increased when manual wheelchairs are taken into account because of their severe mechanical decline. Due to their disability, people frequently face a variety of problems that they do not need to deal with [2].

RELEVANT WORK

In 2020, AKM Bahalul Haque et. Al proposed a voice and gesture Controlled Wheel Chair with Obstacle Detection power by solar. The majority of the time, people with disabilities are ignored. To continue, they now require human assistance 24 hours a day. To travel from one location to another as needed, they require a wheelchair. In contrast to another ongoing human interaction, it would be considerably simpler if the wheelchair they need for their job was automated and under their direct control. In this study, a design that takes into account these factors were suggested. Voice commands and hand gestures operated the wheelchair. Solar power was utilized in the system to increase its energy efficiency. Accordingly, the battery successfully rejuvenated while moving across the entire area. Additionally suitable for obstacle recognition is this smart wheelchair. [3]

In 2017, S.H.Shete et.al cooperated on design of Solar Powered Touch Screen Wheel chair. Our daily lives depend heavily on the sun. This essay examined how solar energy can be utilized to power a wheelchair, reducing the effort required from the disabled individual. For people with physical disabilities, a wheelchair is a basic necessity. There must be an outside person or somebody who is willing to exert significant effort in order to maneuver the wheelchair. Their study focused on using an Android mobile application on a smart Android phone to control a wheelchair system. It is advised to use the wheelchair control system in conjunction with an Android application on a mobile device. This project makes use of a microcontroller circuit, sensors Arduino kit and DC motors to make the wheelchair move and identify obstacles in its path [4]. Neela Madheswari et.al worked on solar powered wheelchair for physically challenged persons with Voice Controller in 2017. A smart system controlled by any smartphone for automatic motion made possible by this paper and can be economically assembled into any existing wheelchair. The primary idea at play is a smartphone with an Android operating system, Bluetooth wireless technology and a 3-axis accelerometer. By disseminating the application, they created, the goal of this method can be expanded to additional smartphone devices operating on Android. System's microprocessor, the PIC16F877, controls the DC motor that powers the wheelchair's linear motion as well as the wheelchair's multiple dc motor directions in the major second section of our system architecture. The wheelchair's front wheels are turned by the DC motor, which is controlled by a pair of dc rear wheels [5]. In 2019, Varsha Pathak1worked on Android based Automated Smart Wheel Chair, - Their idea focuses primarily on using an application on a smart Android phone to handle a wheelchair system. It is advised to use the wheelchair system using an android application on a smart mobile device and system. A wheelchair may be operated using the technology by utilizing an Android device. The goal of this initiative is to make it easier for elderly persons who have trouble moving about and disabled or handicapped people to move around. As a result of this design, the exceptional people will be able to live a life with less reliance on other people. A new method of interacting between people and tools or machines may be possible with the help of Android technology. Thus, using Android technology, their issue can be resolved.to control the movement of a wheelchair [4]. Sasikala in 2020 worked on Wi-Fi Communication based Human Machine Interface (HMI) Wheelchair for Disabled Person The people who are really put to the test have difficulty walking because of a sickness, injury, or disability. With a wheelchair, you can go around without relying on your abilities to be outgoing and make money. Through the Android mobile device, the person speaks, and the voice command is then translated into material. This product is finally delivered to the small controller. A Bluetooth module controls the development of this structure with the assistance of servo engines, The suggested agenda includes servo-powered wheelchairs that are battery-operated. Additionally, the current framework should be extended to include the existing joystick-based framework [6]. Dr. Emna Baklouti presented work on Self-directed wheelchair guidance with Real time Hindrance Detection Using 3D Sensor in 2017 In order to avoid collisions and safeguard the rider, autonomous wheelchairs working in dynamic environments must assess their surroundings and real time alteration of the control signal. In this study, paper offer a reliable, straightforward, and real-time self-governing navigation module that moves a wheelchair in the direction of a predetermined objective while also having the ability to avoid hindrances in a 3D dynamic environment. They employ a fuzzy logic controller to instruct the mobile robot to go toward the objective (FLC). They used the Xbox 360 Kinect to give an accurate map of the area for obstacle avoidance. The obstacle evasion control Deformable Virtual Zone receives the created map as input (DVZ). Results from simulations and actual experiments are provided to demonstrate the viability and effectiveness of the suggested control system [7]. In 2020, Tan Kian Hou et.al presented work on Arduino Based Voice Controlled Wheelchair prototype to help those with both limb limitations, utilizing a manual wheelchair that is easily available on the market everywhere. The speech recognition module's voice commands are processed by an Arduino controller, which also manages motorized mobility of wheelchair. The prototype design also included an optional joystick command and a Bluetooth module to do away with unsightly wires. The wheelchair proved quite successful at understanding voice instructions in Chinese, English and Malay. The prototype's overall price was kept low to make it accessible [8]. Aayushi B Thakur, Dr. Shubhangi D C worked on Design and Development of Smart Solar Based Wheelchair Using Voice Recognition and Head Gesture Control System in 2020 System introduce a solar-powered wheelchair in this paper, together with a 3-axis accelerometer (ADXL335) controlled gesture, a Bluetooth module setup for voice recognition, and an ATmega microcontroller. The entire device was set up using an Arduino board and a few mathematical techniques. The movements can be distinguished from any type of physical movement picked up by an individual's accelerometer, and the voice recognition worked using an Android application and a Bluetooth module. prototype only need to issue a few commands to Android device in order for the voice to be recognized and the necessary action to be taken as a result. Voice and gesture recognition can be explained as a process or method that describes how computers can read body language and builds a connection between the human and computer worlds [9]. Jigmee et.al worked on Wheelchair based on Head Gesture movement for Quadriplegic Patients in 2018. For the purpose of assisting paraplegic patients with movement, paper presents a Robotic Wheelchair that can be controlled using a head motion. A DC stepper motor, Raspberry Pi, a relay, gyroscope, ultrasonic sensors, accelerometer are all part of the Robotic Wheelchair. Head's movement are picked up by MPU 6050 sensor and a signal is sent to the Pi controller. After analyzing the signal controller allows the movement of wheelchair for navigation. Navigational data is used by ultrasonic sensors to assist in avoiding hindrances. The wheelchair is created in a way that is economical, but still guarantees the users' security, adaptability, and mobility [10]. Gaurav Kumar Soni1, Vidhata Poddar2, Yogita Sahu3, Pratima Suryawanshi4 in 2017 proposed work on AVR Microcontroller Based Wheel Chair Direction Control using Hand Gesture Recognition. The proposed task involves designing and creating a wheelchair that uses hand gestures and a gesture control system. People who are unable to walk due to a physical condition, an injury, or another impairment use wheelchairs. The potential for developing hand gesture-based wheelchairs or smart wheelchairs is vast, according to recent developments. The wheelchair in the current article is gesture-based and uses an accelerometer sensor to control the wheelchair's direction. This study proposes a hand-gesture controlled user interface model and highlights usability, application, and technological developments. We describe a highly helpful integrated solution to actual detection. The glove hand gesture-based data technology, which uses an accelerometer sensor to track hand movements to control a wheelchair, is widely utilized. This study suggested control mechanism for wheelchair by a small 3-axis wireless system, low voltage supply and low-cost system using AVR microcontroller [11]. Dr. V. Balambica., Alex Anto., Dr M Achudhan., Vishwa Deepak, Mohammed Juzer, Tamil Selvan in 2021 presented work on Automatic Wheelchair for Physically Disabled People controlled by PID Sensor. Proposed wheelchair operates on the straightforward idea of SENSOR. The wheelchair is controlled using hand obstruction by using a PID SENSOR, resulting in reflected infrared light falling on the sensor which will give the received information to Arduino board in order to give a signal to the motor in order to move the wheelchair in the desired direction as per the person's wishes. Additionally, we have PID sensors fitted for left, right, and reverse directions. As a result, the wheelchair begins to move when the infrared sensor module receives a signal from an object (in this case, a hand or finger) that is blocking the infrared beam from reaching the IR receiver. Moreover, for halting the wheelchair Simply place an object, such as a hand, above the PID sensor to prevent infrared rays from being detected by the IR receiver. This will prevent the IR receiver from signaling the wheelchair's motors to advance any further and will cause the wheelchair to come to a stop. Therefore, this proposed wheelchair's design enables auto-control by applying infrared sensors and circuitry based on an Arduino Uno microcontroller. This concept aims to assist those who are physically challenged and live in poverty and cannot afford to purchase an expensive, fully motorized wheelchair. A standard wheelchair with DC motors powers the entire setup, which also includes an Arduino Uno, beeper, switch, motor driver modules, and batteries [12]. In 2022 Shwetha V., Gayathri P. presented work on voice-controlled wheelchair to assist people with physical limitations, a voice-controlled wheelchair built on the ANFIS platform was developed and put into use. The sufferer can operate the electrical wheelchair by speaking commands. Using a variety of test commands and perturbations, the implemented wheelchair prototype system's functionality and overall performance were evaluated. The simulator and prototype model findings show that the ANFIS-based controller used in conjunction with online sensor signals can increase wheelchair performance and improve quality of life for people with physical incapacities. The implemented prototype offers a number of advantages, including affordability, position tracking, and safety. It features sensors that can identify both static and moving objects, as well as any slick roads. a feed-forward neural network having multiple layer structure of (7-25-10-5) was implemented for classification to identify the voice of each speaker using appropriate training and testing datasets [13]. Susan Shore in 2017 presented work on the long-term influence of wheelchair delivery on the lives of people with incapacities to have a favorable continuous impact on income and employment in less resourced parts of the world, despite fluctuations in distance travelled into the community and overall health status over time. These findings should be confirmed by additional research, which should also look at the causes of varied fluctuation. This study supports the value of long-term monitoring of wheelchair distribution-related outcomes in low-resource settings [14]. In 2017 Sadaphal Avinash et.al proposed Self-control Solar Operated Wheelchair To provide an economical motion vehicle for the physically disabled, a wheelchair powered on solar is invented with the inherent materials like casters, PMDC motor, steel bars. The wheelchair is driven by the 12V rechargeable battery. The speed is restricted to 3km/hr for safety and to avoid shuddering of the solar frame. And by using the toggle jack which has the capacity of lifting load of 100kg, the seat adjustment is done [15].

General Idea

The concept behind this research is the creation of five voice and gesture commands that can be utilized to control the wheelchair. The goal of this work is to create an accurate, intelligent system that can recognize when words are spoken in English and respond to voice commands with the greatest performance possible.

The following commands will be used:

- Forward
- Backward
- Stop
- Left
- Right.

Voice controlled mode:

We have vocal control over the wheelchair. Forward, Stop, Left, Right, and Back are the five vocal commands that can be recognized by the speech recognition software operating on a Module as being issued by a specific user. Following speech processing, the mobile platform receives the required motion commands over an RF link. Additionally, it offers a wide range of other facilities for using the wheelchair. The micro controller takes input from the RF receiver, checks its database, and executes operations like move forward, which causes the motors to go forward, and move backward,

Gesture controlled mode:

Instead of using the old buttons, we can control our wheelchairs with hand gestures. You simply need to carry a little transmitting gadget with an acceleration meter in your palm. This will give the Wheelchair the proper instructions so that it can carry out our requests. The transmitting device includes an Arduino Nano, an mpu6050 and RF transmitter module. The encoded data is received by a slave RF module at the receiving end. Our relays will subsequently be operated in accordance with the instructions after this data has been evaluated by a micro controller.

Hardware Components

The hardware components of proposed system are *12v Battery (80-100amp), Arduino Nano,* Arduino Uno, *Relays,* PCB, Voltage Regulators, *Mpu6050 Sensor, Bluetooth Module HC 05, Resistors,* Jumper Wires, *RF module*

Block Diagram:

block diagram of hardware is displayed in the following figure 1.1.

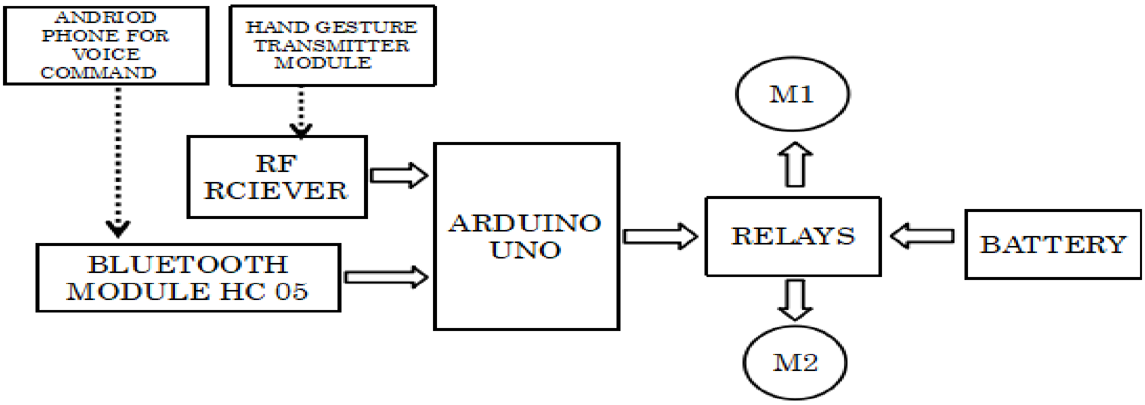

FIGURE 1.1 : BLOCK DIAGRAM OF HARDWARE

Through the figure, we can see that at very beginning it will check if hand gesture is on or not. If yes, then accelerometer will create a numerical value according to movement of hand and send it to Arduino Nano. Arduino Nano will create a command and transfer it to master Bluetooth module. Master Bluetooth module will send the received data to slave Bluetooth module and then to Arduino Uno. Arduino Uno will send signal to motor drivers and motor drivers will move the wheel. If hand gesture is not on then it will wait for a voice command. Voice command is transferred through an android app and received by Bluetooth module and signal will be sent to Arduino Uno and it will control motor drivers.

Working Principle:

This wheelchair has two special features for different types of abled people who can use gesture control and the voice recognition method for the movement of the wheelchair. In addition to the movement in case of emergency or any obstacle found in front of the wheelchair, the wheelchair can immediately stop moving. Moreover, the methods of the individual features are split into several parts in detail.

Gesture mode:

Gesture control uses an accelerometer, it is an electromechanical gadget used to quantify speeding up powers. An accelerator resembles a primary circuit for some bigger electronic gadgets. The capacitance accelerometer detects changes in capacitance between microstructures situated in the gadget. If an accelerative power moves one of these structures, the capacitance will change, and the accelerometer will interpret that capacitance to voltage for elucidation. After the conversion analog to digital converter over the Arduino, the signals are passed to the DC motor. DC motors themselves are extremely basic; any fundamental DC Motor will have two leads that can be legitimately joined to a battery or power supply of adequate limit. The side of the engine that is associated with the positive of the power source will figure out what direction the engine rotates.

Voice Control:

Voice controller is fundamental point to control the wheelchair through the human voice. This venture is for the most part utilized for physically tested individuals who are subject to a wheelchair and particularly those people who control utilize their hands to drag their wheelchair because of some incapacity. In this framework, we have utilized the voice acknowledgment module to perceive the voice of the client for controlling the bearing of the wheelchair. The progression of utilized in this venture is to utilize voice in order to this task can likewise fill in android application. The accepting circuit is available at the switchboard. The direction was set in the Arduino board. The android app can be constrained by giving voice directions.

METHODOLOGY

- At very beginning it will check if hand gesture is on or not.
- If yes, then accelerometer will create a numerical value according to movement of hand and send it to Arduino nano.
- Arduino nano will create a command and transfer it to RF transmitter module.
- RF transmitter module will send the received data to RF receiver and then to Arduino uno.
- Arduino uno will send signal to relays and relays will operate the wheel.

- If hand gesture is not on then it will wait for a voice command.

FIGURE 1.2: FLOW CHART

The flow chart explains the working of wheelchair as first of all system will check if gesture mode is on or not if not then it will move towards voice mode and accept the respective commands and execute them and it will also check obstacle if obstacle is detected then wheel chair will stop moving and wait for command if obstacle is not detected it will accept the command from android phone and move in that direction if gesture mode is on system will move towards the gesture mode and receive commands from hand gesture module it will again check for the distance and then move in required direction

Hardware implementation:

FIGURE 1.3: back view of wheel chair

FIGURE 1.4: side view of wheelchair

RESULTS

The independence of those who are physically handicapped is a social requirement. The usage of wheelchairs enables the mobility of those with physical disabilities. Physically challenged individuals utilized manual wheelchairs at first. However, electrically powered wheelchairs are becoming more and more common in society. The project's objective was to create a voice- and gesture-controlled wheelchair for people with disabilities. The technology was tested for the motion of the wheel chair utilizing voice and gesture after the design and construction of the wheelchair with the corresponding interface circuits. Modern concepts were used to implement the suggested design. Following the development of the wheelchair's smoothly equipped design, this would be adopted for individuals with disabilities. The prototype will initially wait for the turning on gesture mode in the absence of a gesture, speech mode will automatically switch on.

Discussion about Cases

Voice Mode:

The speech recognition module will accept a voice command from an Android phone and respond with the desired signal, which is represented as a voice command, while also recognizing the user's input. Forward, left, right, left forward, right forward, and stop are the six user instructions. The motor control direction for each command will vary and be adjusted separately.

Left:

if the voice command is left, the left wheel will be set to reverse, and right wheel will be set as forward.

Right:

if the voice command is right, the left wheel will set to forward, and right wheel will set as backward.

Forward:

if the voice command is forward, both left and right wheel will set to forward.

Left Forward:

if the voice command is left forward then the left wheel will be set to reverse, and right wheel will be set as forward and after some delay both wheels will stop and then both left and right wheel will set to forward.

Right Forward:

if the voice command is the left wheel will set to forward, and right wheel will set as backward. after some delay both wheels will stop and then both left and right wheel will set to forward.

Stop:

if the voice command is stop then both wheels will stop.

Gesture Mode:

In gesture mode the system will accept command from gesture module and detect what is user input there are five-user commands forward, backward, left, right and stop.

Forward:

if the voice command is forward, both left and right wheel will set to forward.

Left:

if the voice command is left, the left wheel will be set to reverse, and right wheel will be set as forward.

Right:

if the voice command is right, the left wheel will set to forward, and right wheel will set as **Backward.**
Stop:
if the voice command is stop then both wheels will stop.
Applications
Used in Hospital's
Health care centers
Old age homes
Physically handicapped individuals in industries.

CONCLUSION

The wheelchair will be a unique combination of several features at a time. These features will help in making the physically disabled person more independent It will be powered with 12v DC battery and will operate in dual modes.

ACKNOWLEDGMENT

We are thankful to Allah Almighty for successful completion of our project. Our special thanks to our supervisor for giving her supervision. We are also grateful to teachers who gave her precious time and guiding us in research completion and all faculty members who helped us with their advice and comments. We are also grateful to our parents for their prayers that helped us throughout our project. We are thankful to the administration of Electrical Department for allowing us to use the lab equipment as per requirement.

REFERENCES

[1] Pipkin, J. (2018). *U.Va. Team's Solar-Powered Wheelchair Wins World Cerebral Palsy Day Competition*. [online] UVA Today. Available at: https://news.virginia.edu/content/uva-teams-solar-powered-wheelchairwins-world-cerebral-palsy-day-competition.
[2] Wu, J., Zhang, D. and Pan, G. (2019). *Gesture Recognition with a 3-D Accelerometer*. [online] https://www.researchgate.net. Available at: https://www.researchgate.net/publication/221601229_Gesture_Recognition_with_a_3-D_Accelerometer
[3] Ilyas Malik, M., Bashir, T. and Farooq Khan, M. (2019). [online] Ijcsmc.com. Available https://www.ijcsmc.com/docs/papers/June2017/V6I6201776.pdf
[4] Joshi, K., Ranjan, R. and Sravya, E. (2019). *Design of Voice-Controlled Smart Wheelchair for Physically Challenged Persons: Proceedings of IEMIS 2018, Volume 3*. https://www.researchgate.net.
[5] YATNALLI, M., M., M. and M., M. (2019). *GUESTURE BASED WHEEL CHAIR CONTROL USING KINECT CAMERA*. [online] Kscst.iisc.ernet.in. Available at: http://www.kscst.iisc.ernet.in/spp/40_series/SPP40S/02_Exhibition_Project s/163_40S_BE_2158.pdf [Accessed 25 Aug. 2019].
[6] Balderas, D. and Rojas, M. (2016). Human Movement Control. *Automation and Control Trends*. [online] Available at: https://www.intechopen.com/books/automation-and-control-trends/humanmovement-control
[7] Pipkin, J. (2018). *U.Va. Team's Solar-Powered Wheelchair Wins World Cerebral Palsy Day Competition*. [online] UVA Today. Available at: https://news.virginia.edu/content/uva-teams-solar-powered-wheelchairwins-world-cerebral-palsy-day-competition.
[8] How to Mechatronics (2019). *Arduino and MPU6050 Accelerometer and Gyroscope Tutorial – How to Mechatronics*. [online]
[9] How to Mechatronics. Available at: https://howtomechatronics.com/tutorials/arduino/arduino-and-mpu6050accelerometer-and-gyroscope-tutorial/
[10] Richardson, L. (2018). *How do solar panels work?* [online] Solar News. Available at: https://news.energysage.com/solar-panels-work/.
[11] Benne de Bakker (2019). *How to use SHARP IR Distance Sensor with Arduino (GP2Y0A710K0F)*. [online] Makerguides.com. Available at: https://www.makerguides.com/sharp-gp2y0a710k0f-ir-distance-sensorarduino-tutorial/

[12] Instructible. (2019). *Voice Activated Arduino (Bluetooth + Android)*. [online] Available at: https://www.instructables.com/id/Voice-ActivatedArduino-Bluetooth-Android/ [Accessed 24 Nov. 2019].
[13] Fritzing.org. (2016). *Fritzing*. [online] Available at: https://fritzing.org/home/ [Accessed 24 Nov. 2019].

The Role of Ion Properties in Reflectron System Design for Time-of-Flight Mass Spectrometry: A SIMION Simulation-Based Investigation

Abdullah Kepceoğlu[1,2*]

[1] *Department of Molecular Biology and Genetics, Faculty of Science, Koc University, Istanbul, Türkiye*
[2] *Koç University Surface Science and Technology Center (KUYTAM), Rumelifeneri, Istanbul, 34450, Turkey*

* Corresponding author e-mail address: abdullahkepceoglu@gmail.com, akepceoglu@ku.edu.tr
ORCID Number: 0000-0002-4743-5517 (Abdullah.Kepceoğlu)

Abstract**—** This study aimed to investigate the impact of multiple ions and the reflector parameters on the mass resolution of a reflectron time-of-flight mass spectrometry (ReTOF-MS) system. The charged particle optics simulation software, SIMION, was utilized to simulate ion behavior within the reflectron and electro-optics sections of the system, while optimizing the system design by altering the geometrical parameters of the electrodes and reflectron. Specifically, the effect of ion parameters, such as ion energy (IE), birth position (BP), statistical distribution (SD), and mass (m), on the mass resolution (R) of the system was evaluated. In addition, the influence of various reflectron parameters, including reflectron geometry, electrode position and shape, and applied voltages, was investigated. The simulations encompassed a broad range of ion and reflectron parameters, offering insights into the effects of these parameters on the system's mass resolution. The findings emphasize the necessity of optimizing the reflectron and electro-optics design of a time-of-flight mass spectrometry system.

Keywords **—** *mass spectrometry, reflectron, charged particle optics, simulation, ion properties, resolution, ion trajectories.*

INTRODUCTION

Reflectron time-of-flight mass spectrometry (ReTOF-MS) is a widely used analytical tool for identifying and characterizing complex molecules [1]. ReTOF-MS has numerous applications in fields such as materials science, chemistry, and biology, where it is used to identify and quantify analytes with high sensitivity and accuracy. The performance of ReTOF-MS systems is highly dependent on various ion and reflectron parameters, including ion energy, birth position, statistical distribution, and mass, as well as reflectron geometry, electrode position and shape, and applied voltages [2]. To achieve optimal performance, it is essential to carefully consider and optimize these parameters. The charged particle optics simulation software, SIMION, provides a powerful tool for simulating ion behavior and optimizing the design of ReTOF-MS systems. Through simulations, it is possible to evaluate the impact of various ion and reflectron parameters on the mass resolution of the system, and to identify the optimal parameter values for a given application. In this study, we use SIMION to investigate the impact of multiple ion and reflectron parameters on the mass resolution of a ReTOF-MS system. Our goal is to provide insights into the optimization of ReTOF-MS systems for various applications, with a focus on improving the mass resolution of the system. Specifically, we evaluate the effect of ion energy, birth position, statistical distribution, and mass, as well as reflectron geometry, electrode position and shape, and applied voltages on the mass resolution of the system. Our simulations encompass a broad range of ion and reflectron parameters, providing insights into the effects of these parameters on the system's mass resolution. Ultimately, our study aims to contribute to the development of optimized ReTOF-MS systems for a range of practical applications.

RESULTS AND DISCUSSION

In this part a mass spectrometer consists of a single stage ion acceleration region, a reflectron and a detector is designed to investigate the effects of the various parameters on the resolution of the mass spectrometer. A TOF-MS system and subsystems can be seen in Fig. 1.

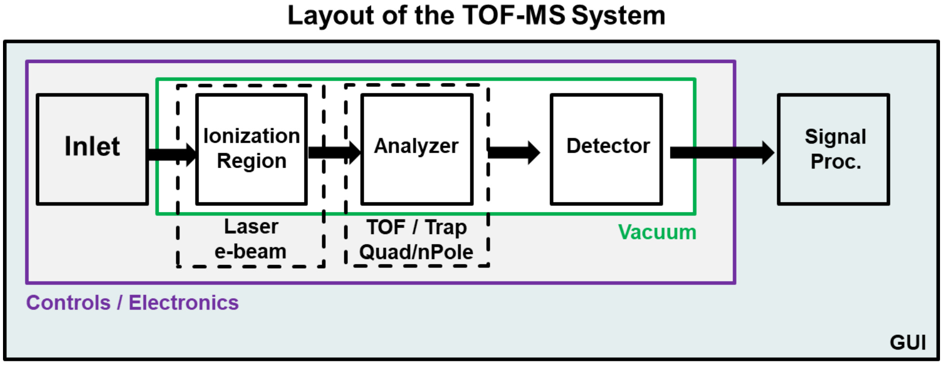

(a)

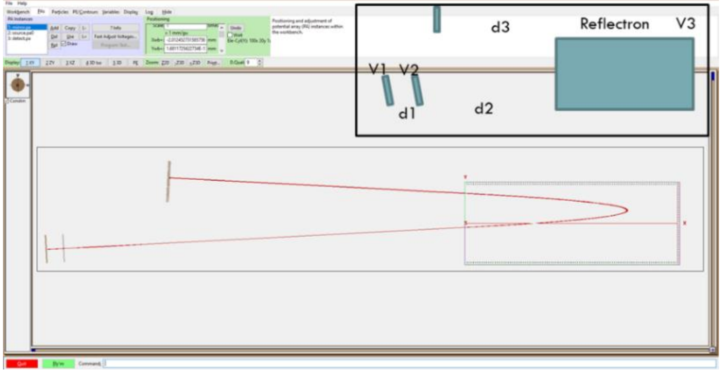

(b)

Fig. 1. Sub systems of a mass spectrometer (a) SIMION Example of a reflectron system and the variables defined in the inset (b).

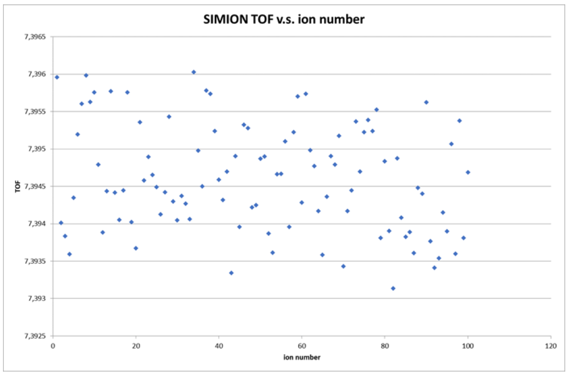

V1 (V)	V2 (V)	V3 (V)	Mean TOF (us)	FWHM	Resolution
5000	0	5000	7,394599	0,001681	2198,869
4500	0	5000	7,384808	0,00075	4921,21
4500	0	5000	7,385675	0,000584	6326,97
4250	0	5000	7,388101	0,000293	12589,35
4000	0	5000	7,398148	0,00022	16847,97
3875	0	5000	7,406132	0,000483	7664,031
3750	0	5000	7,416304	0,000783	4733,779
3500	0	5000	7,444333	0,001439	2587,265
3000	0	5000	7,538719	0,002706	1392,829

Fig. 2. Pusher plate (V1) potential dependent time-of-flight (TOF) (left) and corresponding calculated spectrometer resolution (right).

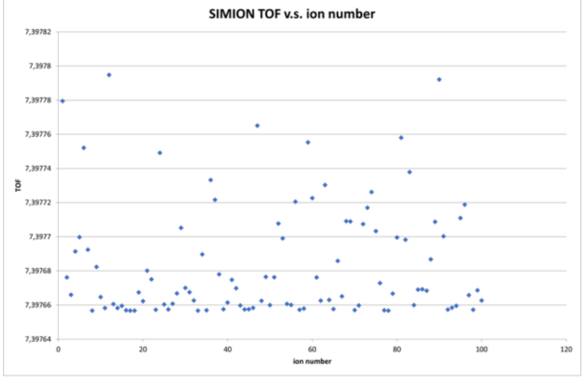

V1 (V)	V2 (V)	V3 (V)	Birth Position (x, y)	Mean TOF (us)	FWHM	Resolution
4000	0	5000	-192,-12	7,402000782	0,001921291	1926,309431
4000	0	5000	-192.1,-12	7,400455823	0,001483241	2494,690136
4000	0	5000	-192.2,-12	7,399092542	0,001081548	3420,602091
4000	0	5000	-192.3,-12	7,398399551	0,000690762	5355,2414
4000	0	5000	-192.4,-12	7,397870048	0,000346222	10683,71385
4000	0	5000	-192.45,-12	7,39774642	0,000233041	15872,17695
4000	0	5000	-192.475,-12	7,397703304	0,000122999	30072,31742
4000	0	5000	-192.5,-12	7,397684079	7,88803E-05	46891,85797
4000	0	5000	-192.55,-12	7,39771329	0,000160043	23111,68053

Fig. 3. Ion birth position dependent time-of-flight (TOF) distribution (left) and corresponding calculated spectrometer resolution (right) for the fixed electrode potential.

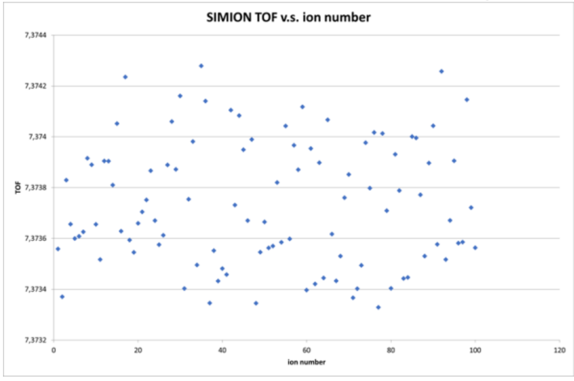

V1 (V)	V2 (V)	V3 (V)	Kinetic Energy (eV)	Mean TOF (us)	FWHM	Resolution
4000	0	5000	0	7,398484579	7,20592E-05	51336,1198
4000	0	5000	0.01	7,398230072	6,27699E-05	58931,33993
4000	0	5000	0.1	7,397684079	7,88803E-05	46891,85797
4000	0	5000	0.5	7,396695737	8,05205E-05	45930,5275
4000	0	5000	1	7,397689437	9,06955E-05	40783,09316
4000	0	5000	5	7,392828294	7,38709E-05	50038,86406
4000	0	5000	10	7,390489122	8,90218E-05	41509,44728
4000	0	5000	50	7,380738214	0,000299679	12314,41699
4000	0	5000	100	7,37373513	0,000574023	6422,857058

Fig. 4. Ion kinetic energy dependent time-of-flight (TOF) distribution (left) and corresponding calculated spectrometer resolution (right) for the fixed electrode potential and ion birth position (-192.5,-12).

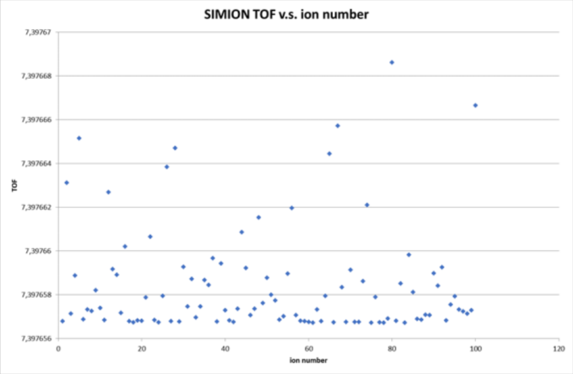

V1 (V)	V2 (V)	V3 (V)	Statistic	Mean TOF (us)	FWHM	Resolution
4000	0	5000	Gaussinan 3D dist 0.01 Stdev	7,397659	7,90539E-06	467886,8
4000	0	5000	0.02 Stdev	7,397664	2,73456E-05	135262,4
4000	0	5000	0.03 Stdev	7,397672	5,69326E-05	64968,74
4000	0	5000	0.04 Stdev	7,397685	8,52626E-05	43381,78
4000	0	5000	0.05 Stdev	7,397688	0,0001071	34536,22
4000	0	5000	0.1 Stdev	7,397776	0,000352235	10501,19
4000	0	5000	Spehere filled Radius 0.01	7,397684079	7,88803E-05	46891,85797
4000	0	5000	Radius 0.05	7,3977	0,000142384	25978,05
4000	0	5000	Radius 0.1	7,389011	0,002135412	1730,114

Fig. 5. Ion statistics dependent time-of-flight (TOF) distribution (left) and corresponding calculated spectrometer resolution (right) for the fixed electrode potential, ion birth position (-192.5,-12) and ion kinetic energy (0.1eV).

The investigation was conducted by simulating the behavior of ions in the mass spectrometer system using SIMION version 8.2.0.11. We first examined the pusher plate potential dependent resolution of the system (Fig. 1) and found that the resolution was strongly dependent on the potential applied to the pusher plate electrode. In Fig. 2, we present the pusher plate potential dependent time-of-flight (TOF) and corresponding calculated spectrometer resolution. The highest resolution value was obtained for a pusher plate potential of 4000V.
Next, we investigated the ion birth position dependent resolution of the system for a fixed electrode potential (V1=4000V, V2=0V, and V3=5000V) (Fig. 3). We found that the resolution was highly dependent on the ion birth position, with the highest resolution obtained for an ion birth position of (x=-192.5mm, y=-12mm, and z=0), with a value of around 47000. After identifying the optimal ion birth position, we investigated the ion kinetic energy dependent resolution of the system (Fig. 4). We found that the resolution was highly dependent on the ion kinetic energy, with the highest resolution obtained at an ion kinetic energy of 0.1eV for the fixed electrode potential and ion birth position (-192.5,-12).

Finally, we investigated the ion statistics dependent resolution of the system (Fig. 5). We found that the resolution was strongly dependent on the ion statistics, with the highest resolution obtained at a statistical weight of 1 for the fixed electrode potential, ion birth position (-192.5,-12), and ion kinetic energy (0.1eV). Overall, our investigation demonstrates the importance of carefully controlling the pusher plate potential and ion parameters, such as birth position, kinetic energy, and statistics, in achieving high resolution in a mass spectrometer system. Our findings provide important insights for the design and optimization of mass spectrometer systems for various applications in materials science, chemistry, and biology.

CONCLUSION

The simulations in this study have highlighted the importance of optimizing ion and reflectron parameters for achieving high mass resolution in a ReTOF-MS system. Our results suggest that the mass resolution of the system is highly dependent on ion energy, statistical distribution, ion birth position, reflectron geometry, and applied voltages. Furthermore, we found that a specific ion birth position can significantly affect the system's mass resolution. These findings underscore the importance of careful consideration of system design and parameter optimization for achieving high mass resolution in ReTOF-MS. Future studies may focus on further optimization of the system design for specific applications in fields such as materials science, chemistry, and biology.

ACKNOWLEDGEMENT

This work was supported by the Scientific and Technical Research Council of Turkey (TUBITAK) under Grant No. 118C476 and Grant No. 122F301. However, the entire responsibility of the publication belongs to the authors of the publication. The financial support received from TÜBİTAK does not mean that the content of the publication is approved in a scientific sense by TÜBİTAK. The author wishes to acknowledge the late Dr. Mehmet Taşer for his insightful discussions and guidance during this research. His passing is a great loss to our field, and we are grateful for the opportunity to have known and learned from him.

REFERENCES

[1] Jones, B. M., & Kaiser, R. I. (2013). Application of reflectron time-of-flight mass spectroscopy in the analysis of astrophysically relevant ices exposed to ionization radiation: Methane (CH4) and D4-methane (CD4) as a case study. The Journal of Physical Chemistry Letters, 4(11), 1965-1971.

[2] Chien, B. M., Michael, S. M., & Lubman, D. M. (1994). The design and performance of an ion trap storage—reflectron time-of-flight mass spectrometer. International Journal of Mass Spectrometry and Ion Processes, 131, 149-179.

The Collimator Optimization for ^{133}Xe and ^{201}Tl Isotopes on the Simulation SPECT Imaging Model

Anes Hayder[1*], Tuncay Bayram[2] and Sevki Senturk[3]

[123]*Department of Physics, Faculty of Science, Karadeniz Technical University*

* Corresponding author e-mail address: anes.m.s.q@gmail.com
ORCID Numbers: 0000-0001-8166-1385 (Anes Hayder), 0000-0003-3704-0818 (Tuncay Bayram),
0000 0001 8355 1307 (Sevki Senturk)

Abstract— Since the performance of the gamma camera is significantly influenced by the geometrical design of collimators, geometrical collimator optimization is crucial for creating high-quality images. In this study, optimizations for the parallel hole collimator have been considered by regarding Low Energy General Purpose (LEGP) collimator for the ^{133}Xe isotope and the Medium Energy General Purpose (MEGP) collimator for the ^{201}TI isotope. The Monte Carlo simulation platform (GATE) was used for researching the effect of hole lengths for the two types of hexagonal parallel hole collimators (LEGP and MEGP) on the spatial resolution and the sensitivity of the Single-Photon Emission Computed Tomography (SPECT). The optimal hole lengths for the considered collimators were predicted by the trade-off between the spatial resolution and the sensitivity. The results of this work are found to be consistent with previous studies' results.

Keywords— SPECT, Collimator, Monte Carlo Simulation, GATE.

INTRODUCTION

In nuclear imaging applications, radionuclides with half-lives of a couple of hours to several days, and gamma energies of 30 keV to 300 keV are commonly used. Both the ^{133}Xe and ^{201}TI isotopes have physical properties that make them good for use in SPECT imaging systems [1]. The ^{133}Xe isotope, which has a half-life of 2 h and a gamma energy of 81 keV, is used in lungs image and pulmonary function scanning, while the ^{201}TI isotope, which has a half-life of 73 h and a gamma energy of 167 keV, is used in the diagnosis of several heart diseases and tumor diagnosis [2]. In SPECT, the images of the organs are produced through the detection of the emitting gamma rays from the patient's body at different angles [3]. Generally, the nuclear imaging device's performance is limited by many parameters, some of which regard components of the imaging instruments, and others related to the observer's performance. The collimator is an essential part of the SPECT, placed in front of the detector to orient gamma radiation toward the crystal and restrict the passage of undesired gamma rays. According to the radioactive energy utilized in a SPECT scan, the parallel hole collimator categories are generally low-energy collimator, medium-energy collimator, and high-energy collimator [4]. Some performance parameter such as sensitivity and spatial resolution effectively limited by the collimator design and geometry of collimator holes (hole shape, hole diameter, and hole length). Consequently, the balance between sensitivity and spatial resolution in the collimator selection plays a curial role in image quality [5,6]. Usually, Monte Carlo simulation platforms are employed to modify and improve the image quality of gamma cameras. One of these platforms that are widely used in gamma camera modelling is the GATE [7]. It is built on the versatile simulation toolkit Geant4, and as a result, it encompasses all of the features of Geant4. It comprised of several hundred C++ classes. The Geant4's application for tomography emission (GATE) provides high accuracy in nuclear imaging applications [8,9]. In this study, the GATE platform is used to optimize the Low Energy General Purpose (LEGP) collimator for the ^{133}Xe isotope and the Medium Energy General Purpose (MEGP) collimator for the ^{201}TI isotope for the SPECT simulation model.

MATERIALS AND METHODS

In this work, the standard SPECT simulation model is utilized, for finding the optimal collimators ^{133}Xe and ^{201}TI isotopes. The spatial resolution and sensitivity of the simulation model are estimated, using the LEGP collimator for ^{133}Xe isotope and the MEGP collimator for ^{201}TI isotope. Fig. 1 shows the hexagonal parallel hole-collimator modelled with GATE simulation platform. Collimators with various hole-lengths are used to evaluate the two imaging protocols at multiple distances from a point source positioned in the centre of a cylinder phantom with a diameter and length of 10 cm and 20 cm, respectively. The characteristics of the simulation detector model are presented in (Table 1).

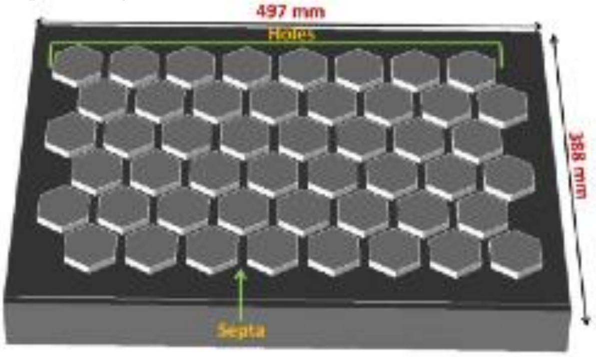

Fig. 1. Schematic diagram of hexagonal parallel hole-collimator.

TABLE I. Detector Properties Of Standard Spect Simulation

Detector		
FOV	500 (mm) × 395 (mm)	
Crystal		
Dimensions	497 (mm) × 388 (mm)	
Thickness	9.5 (mm)	
Type	NaI	
Photo-Multitube		
Dimensions	497 (mm) × 388 (mm)	
Thickness	25 (mm)	
Collimator	**LEGP**	**MEGP**
Dimensions	497 (mm) × 388 (mm)	
Hole shape	Hexagonal	Hexagonal
Hole length	31 (mm) - 40 (mm)	55 (mm) - 64 (mm)
Hole diameter	1.9 (mm)	3 (mm)
Septa thickness	0.2 (mm)	10.5 (mm)
Material	lead	lead

Point Spread Function (PSF) method was used to estimate the spatial resolution of the simulation SPECT model [10, 11] , using LEGP and MEGP collimators at various hole lengths (31 mm to 40 mm) and (55 mm to 64 mm), respectively. The full-width half maximum (FWHM) of both point sources are evaluated by (PSF) method via the following:

$$\mathrm{FWHM} = \sqrt{2\log 2} \times \sigma \qquad (1)$$

where σ is the standard deviation for the Gaussian distribution [12]. The ratio of the number of gamma-ray photons detected by the SPECT system to the total activity of the used source is defined as sensitivity [13]. The acquisition of point sources (^{133}Xe and ^{201}TI) with an activity of 0.02 mCi placed in the air-filled phantom for 20 seconds was used to determine the spatial resolution and sensitivity of the simulation system.

RESULTS AND DISCUSSION

The imaging performance of the SPECT standard simulation model was evaluated, by simulating the LEGP collimator for the ^{133}Xe isotope and MEGP collimator for the ^{201}TI isotope. Collimators with various hole lengths (31 mm to 40 mm) of LEGP and (55 mm to 64 mm) of MEGP were utilized to estimate the imaging protocols (FWHM and sensitivity). Each hole-length was used at 8 different distances, which are 10 cm, 12 cm, 14 cm, 16 cm, 18 cm, 20 cm, 22 cm, and 24 cm. The spatial resolution (FWHM) and sensitivity to the simulation model at different distances from the ^{133}Xe a point source based on various hole-lengths with the LEGP-collimator is shown in Fig. 2. Furthermore, the same performance parameter (FWHM and sensitivity) to the simulation model with MEGP collimator based on various hole-lengths at different distances from ^{201}TI is shown in Fig. 3. As indicated in these two figures; the FWHM deteriorates as source-to-collimator distance increases, while the sensitivity is almost unaffected by the variation of these distances. At source-to-collimator distance increases, FWHM degradation results from increasing the spread angle of gamma rays that spread the radiation profile. Due to the influences of the ratio of the number of collimator holes to the source distance from the collimator surface, the sensitivity rate is unaffected [14]. In other words, the detector's capacity to distinguish between two points on the imaging object is not the same in all movement regions depending on the object-to-detector distance. This means the acquisition time for object imaging at short distances is decreasing [12].

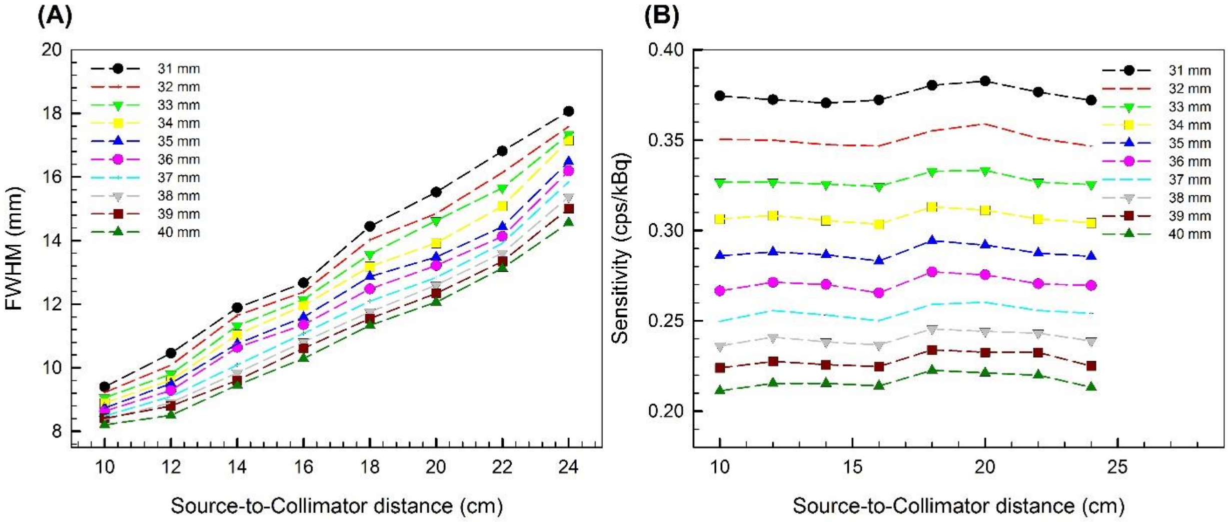

Fig. 2. The (A) FWHM and (B) Sensitivity of standard SPECT simulation model using LEGP-collimator for ^{133}Xe isotope as a function of hole-lengths at various source-to-collimator distances.

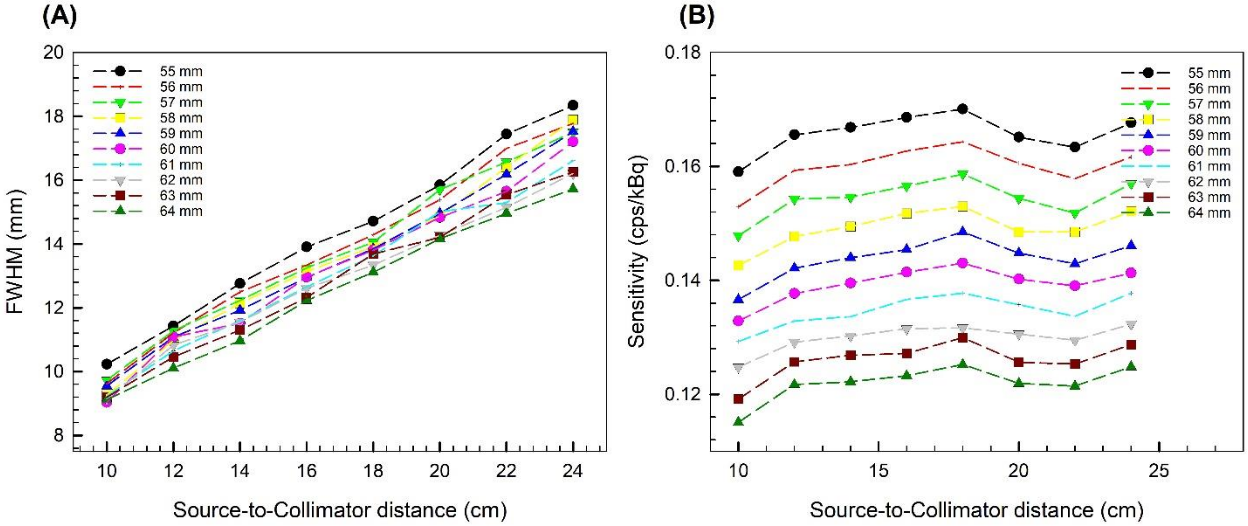

Fig. 3. The (A) FWHM and (B) Sensitivity of standard SPECT simulation model using MEGP-collimator for ^{201}TI isotope as a function of hole-lengths at various source-to-collimator distances.

Fig. 4 and Fig. 5 illustrated both the sensitivity and FWHM to the SPECT simulation model at different hole-lengths based on various distances from the point sources ^{133}Xe with LEGP, and ^{201}TI with MEGP sequentially. The linear variation in the FWHM values utilizing the LEGP-collimator for the ^{133}Xe isotope and the MEGP-collimator for the ^{201}TI isotope is 8.20-18.06 mm and 9.04-18.34 mm, respectively. The fluctuations in the values of FWHM using the MEGP-collimator for the ^{201}TI isotope were noted; these fluctuations result from multi scattering events in medium-energy photons. In contrast, the degradation of the sensitivity values with increasing hole-lengths of collimators (LEGP and MEGP) was noted. As a result, the FWHM enhancement and sensitivity degradation caused by increasing the hole-lengths of the LEGP and MEGP collimators are shown in Fig. 4 and Fig. 5. This enhancement at FWHM and degradation in sensitivity return to increase absorption of scattering gamma rays by the collimator as hole-lengths increase [15, 14].

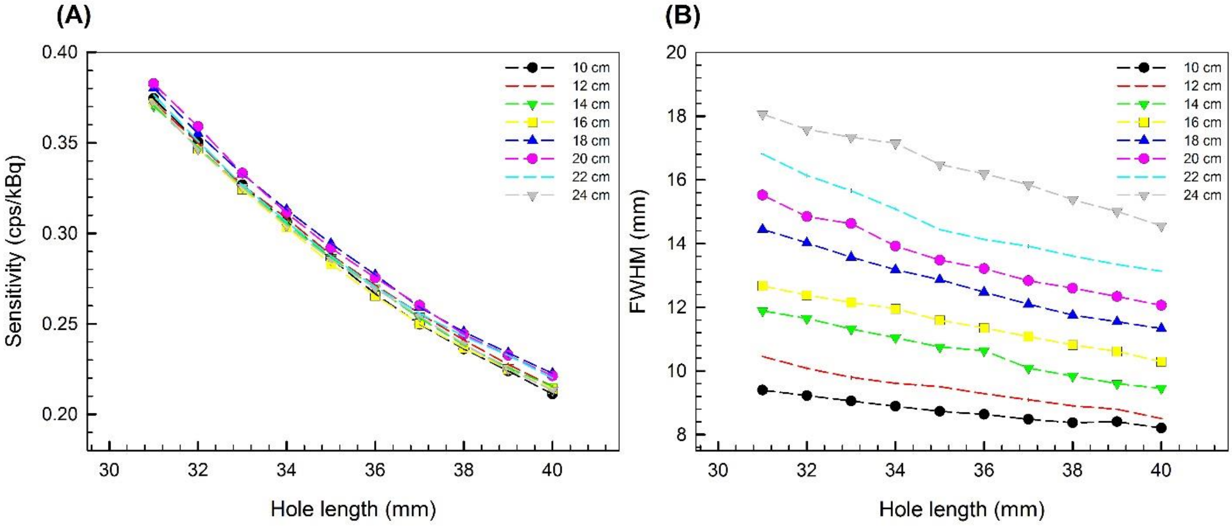

Fig. 4. The (A) Sensitivity and (B) FWHM of standard SPECT simulation model using LEGP-collimator for ^{133}Xe isotope as a function of hole-lengths at various source-to-collimator distances.

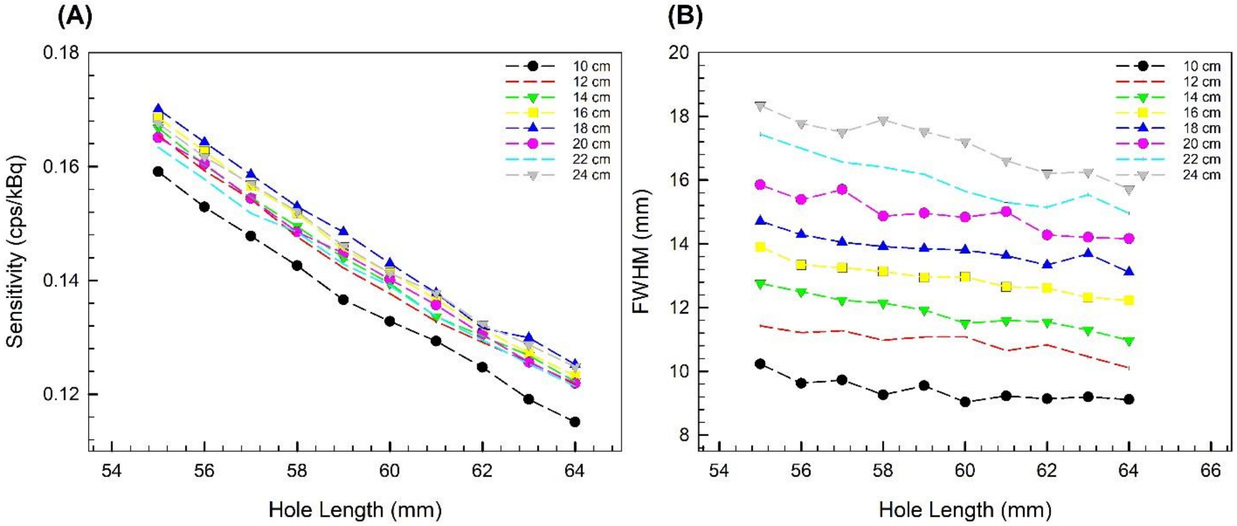

Fig. 5. The (A) Sensitivity and (B) FWHM of standard SPECT simulation model using MEGP-collimator for ^{201}TI isotope as a function of hole-lengths at various source-to-collimator distances.

Fig. 6 and Fig. 7 show the trade-off between FWHM and sensitivity for the simulation model based on the optimal hole lengths for the LEGP and MEGP collimators at all source-to-collimator distances. The collapse in the values of FWHM and the improvement in sensitivity values with an increase in the collimator’s hole-lengths are observed in the mentioned figures.

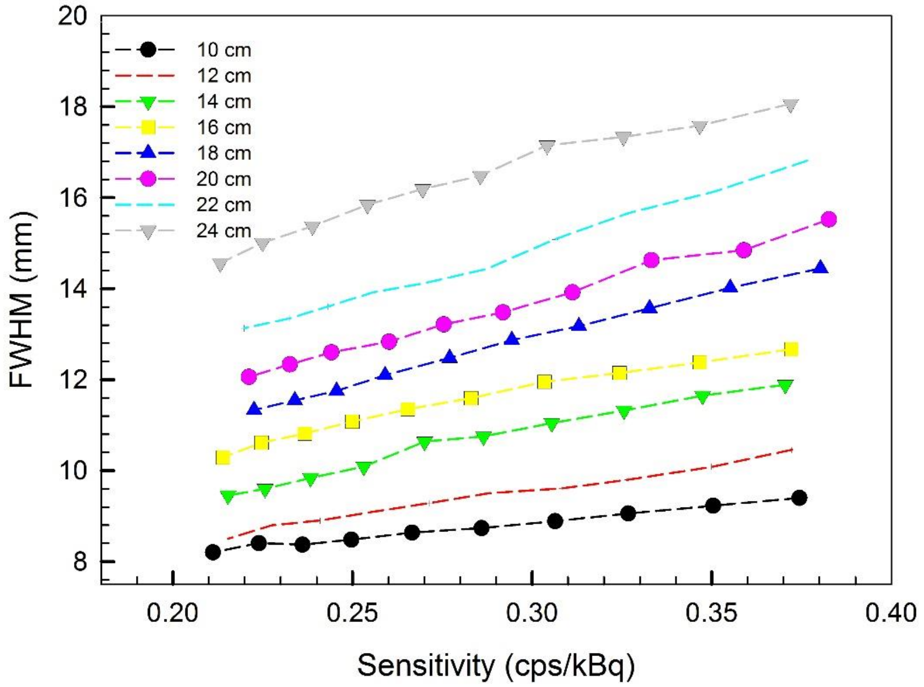

Fig. 6. The trad-off between FWHM and Sensitivity of Standard SPECT simulation model using LEGP-collimator for ^{133}Xe isotope.

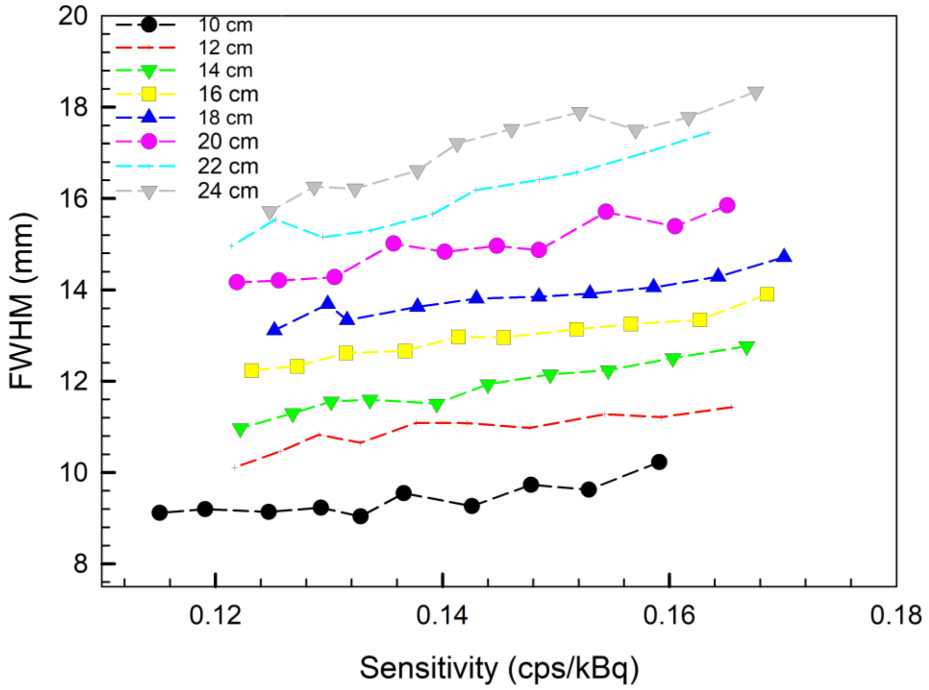

Fig. 7. The trad-off between FWHM and Sensitivity of Standard SPECT simulation model using MEGP-collimator for ^{201}TI isotope.

CONCLUSION

The geometry design of parallel hole collimators has a considerable influence on the quality of the image on the standard SPECT simulated model. A comparison is done for the performance of parallel-hole collimators with different hole lengths at various distances from point isotope source based on sensitivity and spatial resolution. As the collimator hole lengths increase, spatial-resolution improves while sensitivity decreases. Based on the results that have been found in previous nucle ar imaging device simulation studies, the trade-offs between spatial resolution and sensitivity are the same as our study results. It is possible to fabricate a collimator with excellent characteristics and enhance manufacturing precision by simulating a collimator of the desired dimension.

REFERENCES

[1] G. Kramer-Marek and J. Capala, ‘The role of nuclear medicine in modern therapy of cancer’, *Tumor Biology*, vol. 33, pp. 629–640, 2012.

[2] H. Demir, ‘Thallium-201 Imaging’, in *Encyclopedia of Metalloproteins*, New York, NY: Springer New York, 2013, pp. 2203–2212.

[3] N. Fuin, A. Bousse, S. Pedemonte, S. Arridge, S. Ourselin and B. Hutton, "Collimator design in SPECT, an optimisation tool," *IEEE Nuclear Science Symposuim & Medical Imaging Conference*, Knoxville, TN, USA, 2010, pp. 3149-3154.

[4] K. Van Audenhaege, R. Van Holen, S. Vandenberghe, C. Vanhove, S. D. Metzler, and S. C. Moore, ‘Review of SPECT collimator selection, optimization, and fabrication for clinical and preclinical imaging’, *Med Phys*, vol. 42, no. 8, pp. 4796–4813, Aug. 2015.

[5] M. Holstensson, M. Partridge, S. E. Buckley, and G. D. Flux, ‘The effect of energy and source location on gamma camera intrinsic and extrinsic spatial resolution: an experimental and Monte Carlo study’, *Phys Med Biol*, vol. 55, no. 6, pp. 1735–1751, Mar. 2010.

[6] F. Kharfi, ‘Principles and Applications of Nuclear Medical Imaging: A Survey on Recent Developments’, Imaging and Radioanalytical Techniques in Interdisciplinary Research - Fundamentals and Cutting Edge Applications. InTech, Mar. 13, 2013.

[7] G. Santin *et al.*, ‘GATE: a Geant4-based simulation platform for PET and SPECT integrating movement and time management’, *IEEE Transactions on Nuclear Science*, vol. 50, no. 5, pp. 1516–1521, 2003.

[8] J. Apostolakis and D. H. Wright, ‘An Overview of the Geant4 Toolkit’, *AIP Conference Proceedings*, vol. 896, no. 1, pp. 1–10, 2007.

[9] J. Allison *et al.*, ‘Geant4 developments and applications’, *IEEE Transactions on Nuclear Science*, vol. 53, no. 1, pp. 270–278, 2006.

[10] G.J. Royle, N.E. Royle, R. Pani, R.D. Speller, "Design of high resolution collimators for small gamma cameras", *1995 IEEE Nuclear Science Symposium and Medical Imaging Conference Record*, vol.3, pp.1584-1586 vol.3, 1995.

[11] S. C. Moore, K. Kouris, and I. Cullum, ‘Collimator design for single photon emission tomography’, *Eur J Nucl Med*, vol. 19, no. 2, pp. 138–150, 1992.

[12] NEMA Standards Publication NU 1-2018: Performance Measurements of Gamma Cameras. National Electrical Manufacturers Association, 2019.

[13] P. Taherparvar and A. Sadremomtaz, ‘Development of GATE Monte Carlo simulation for a CsI pixelated gamma camera dedicated to high resolution animal SPECT’, *Australas Phys Eng Sci Med*, vol. 41, no. 1, pp. 31–39, Dec. 2017.

[14] N. Shaikh, J. N. Warrier, and S. Bhattacharya, ‘Dimensional Comparison of Parallel-Hole type Collimator’, 2016.

Electrospun biotin- and streptavidin-coated quartz crystal microbalance surfaces: characterization and mass sensing performance using OpenQCM

Erhan Ermek[1,5], Esra Ayan[2], Nurettin Tokay[2], Hasan DeMirci[2,3], Abdullah Kepceoğlu[2,4*]

[1] *Department of Molecular Biology and Genetics, Faculty of Science, Koc University, Istanbul, Türkiye*
[2] *Department of Molecular Biology and Genetics, Faculty of Science, Koc University, Istanbul, Türkiye*
[3]*Stanford PULSE Institute, SLAC National Laboratory, Menlo Park, CA, USA*
[4] *Koc University Surface Science and Technology Center (KUYTAM), Rumelifeneri, Istanbul, Türkiye*
[5]*ME Research and Technologies (MERT Electronics), Sarıyer, Istanbul, Türkiye*

* Corresponding author e-mail address: abdullahkepceoglu@gmail.com, akepceoglu@ku.edu.tr

ORCID Numbers: 0009-0007-3660-4702 (Erhan Ermek), 0000-0001-7906-4426 (Esra Ayan), 0000-0003-4934-4173 (Nurettin Tokay), 0000-0002-9135-5397 (Hasan DeMirci), 0000-0002-4743-5517 (Abdullah Kepceoğlu)

Abstract - In this study, a quartz crystal microbalance (QCM) sensor surface was coated with biotin and/or streptavidin using the electrospinning method. The coated surfaces were analyzed using the Raman spectroscopy method. QCM measurements were carried out using the OpenQCM platform. The results indicate that the electrospinning method can be used to coat QCM surfaces with biotin and/or streptavidin and that the coated surfaces exhibit distinct morphological and spectroscopic properties. The QCM measurements showed that the coated surfaces are highly sensitive to changes in mass, indicating their potential for use in biosensing applications. Overall, this study provides new insights into the use of QCM sensors coated with biotin and/or streptavidin for biological sensing and detection applications.

Keywords — *Quartz crystal microbalance (QCM), Biotin, Streptavidin, Electrospinning, Surface coating, Raman spectroscopy, Biosensing*

INTRODUCTION

Streptavidin, a protein capable of binding to biotin, exhibits a homotetrameric structure consisting of 126 amino acid residues in each identical monomer. Its secondary structure is characterized by the formation of an anti-parallel eight-stranded β-barrel tertiary structure [1]. The Trp120 residue in each monomer is responsible for connecting the monomer to its adjacent subunits, resulting in the formation of functional dimers within the tetramer. While the precise function of streptavidin remains unclear, previous research suggests its involvement in microbial defence mechanisms. The strong non-covalent bond between biotin and streptavidin has attracted significant attention in various scientific fields, owing to its exceptional specificity and high affinity, estimated to be in the femtomolar range ($K_d = 10^{-13}$ - 10^{-15} M). This affinity is approximately an order of magnitude greater than that observed in well-known antigen-antibody interactions. The unique binding affinity displayed by the streptavidin-biotin complex possesses remarkable characteristics. Regions of the protein involved in interactions with other proteins or targets typically exhibit high flexibility and plasticity. Moreover, these regions tend to be located on the exposed surface of the protein. An essential segment of streptavidin, known as the apo-state streptavidin loop (L3/4; residues 45–52), plays a crucial role in biotin interaction and governs the binding process [2]. Streptavidin, biotin and Streptavidin-Biotin complex structures are presented in Fig. 1. Quartz crystal microbalance (QCM) sensors offer precise analysis of environmental changes, achieving high resolution at levels around ng/cm^2. They are particularly useful for accurately monitoring humidity [3], as well as detecting and analyzing atmospheric pollutants or organic chemicals [4].

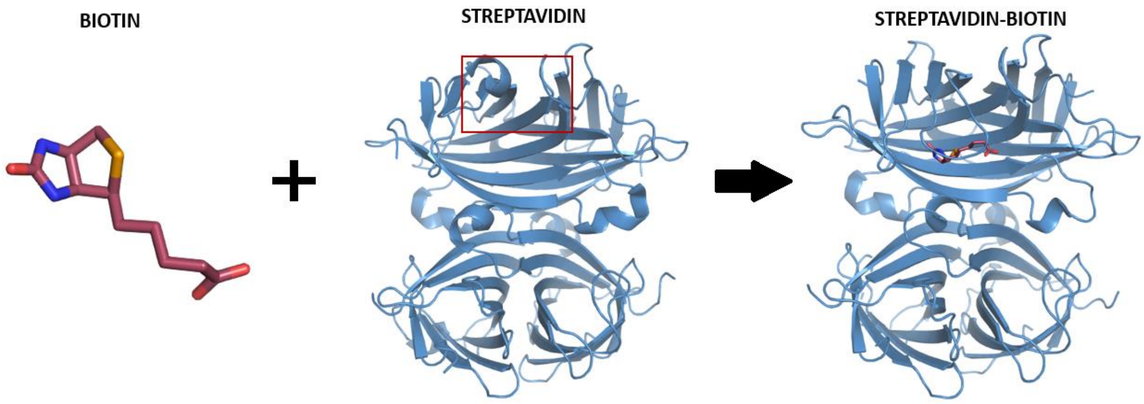

Fig. 1. Biotin and Streptavidin molecules with Streptavidin-Biotin complex [2]

MATERIALS AND METHODS

QCM measurements were conducted utilizing a custom-designed OpenQCM setup (Fig. 2., lower panel). Quartz crystal frequency measurements were performed using a PC. The measurements were carried out at the fundamental frequency, and a simultaneous collection of dissipation data was accomplished. Data acquisition was facilitated through the utilization of open-source OpenQCM software and Teensy firmware. The lab-made system was augmented with the integration of the Teensy microcontroller as the hardware component. Fig. 2 illustrates phase and amplitude data obtained from the fundamental mode of a 10 MHz QCM (Quartz Crystal Microbalance) driven in an open-loop configuration. The quartz crystals utilized in the experiments were 5 mm in size (Raltron 18pf-HC49U) and incorporated electronic circuit elements with silver electrodes of a specific diameter. Q-values were measured at a temperature of approximately 20K employing the available system, yielding resonance frequencies of 9996348.043 Hz (stdev = 54.319).

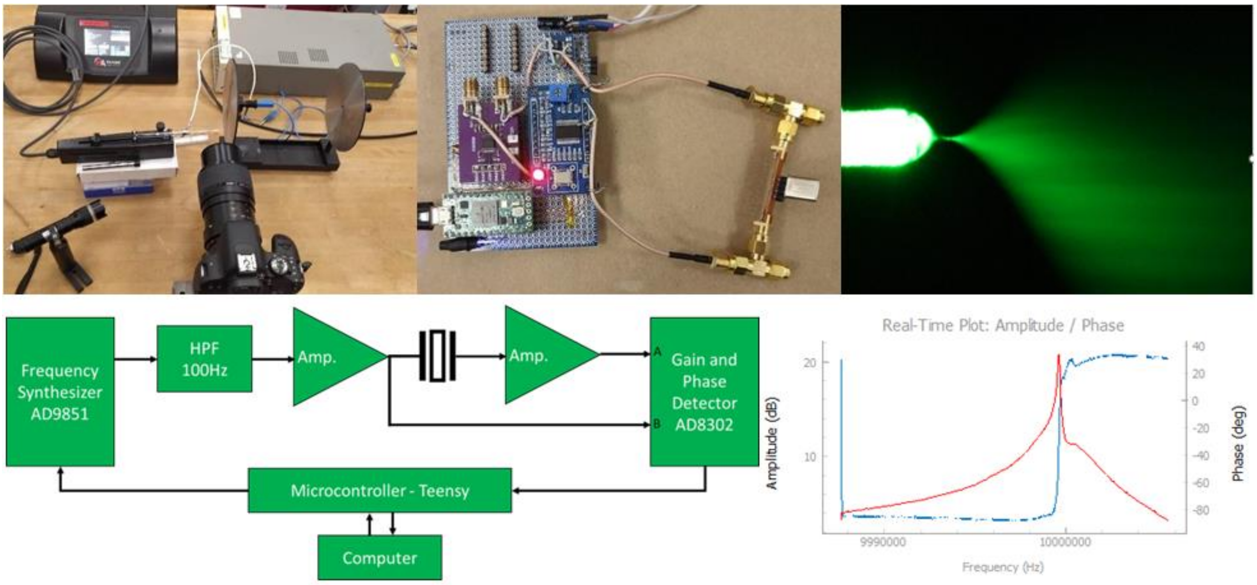

Fig. 2. Electrospinning setup, OpenQCM measurement setup and electrosprayed sample (up) and block diagram of the QCM setup and real-time measurement (down)

Samples of biotin at concentrations of 5 mg/mL, 0.5 mg/mL, and 0.05 mg/mL were prepared, along with streptavidin samples at concentrations of 1.5 mg/mL, 0.5 mg/mL, and 0.05 mg/mL. The prepared biotin and streptavidin samples were loaded into a 500 µL Hamilton syringe (Model No. 80830; Hamilton Company, NV). Fluid flow was controlled using a syringe pump (Harvard PHD ULTRA, Syringe Pump Infuse/Withdraw Programmable), while a positive high voltage (SRS PS350, Sunnyvale, CA) was applied to the syringe tip. The QCM sensor, acting as a collector, was grounded to initiate the electrospraying process.

RESULTS AND DISCUSSIONS

We have conducted an investigation into the correlation between the distance from the syringe tip to the collector (measured using a QCM sensor) and the electrospraying current. The purpose was to ascertain the impact of distance on the stability of the electrospraying process, which exhibited an inverse proportional relationship (Fig. 3.). Biotin samples were meticulously dispensed using a flow rate of 2 µL/min, employing an accelerating potential of 5 kV, and maintaining a syringe tip-to-ground electrode distance of 5-8 cm. The samples were subjected to QCM measurements, which were carried out for a duration of 10 seconds (Fig. 4.). The experimental results clearly demonstrate that the deposition of biotin samples induces a frequency decrease of approximately 10 Hz on the resonance frequency. Remarkably, the anticipated frequency pattern identified in the biotin samples did not manifest in the case of streptavidin. Rather, a substantial decline in frequency within the 150 to 200 Hz range was recorded, alongside an anomalous value in one sample and a frequency reduction of approximately 10 Hz in another sample, diverging from the results of the remaining three measurements. These inconsistencies may potentially arise from experimental inaccuracies. Nevertheless, when the process was conducted utilizing an equivalent sample flow rate, a more pronounced decrease in frequency was observed, which can be attributed to the molecular weight of streptavidin.

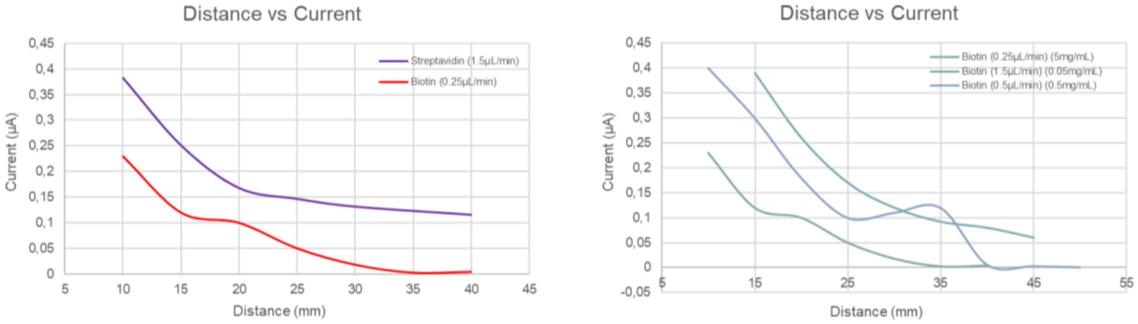

Fig. 3. Syringe tip and collector electrode distance dependant current plots

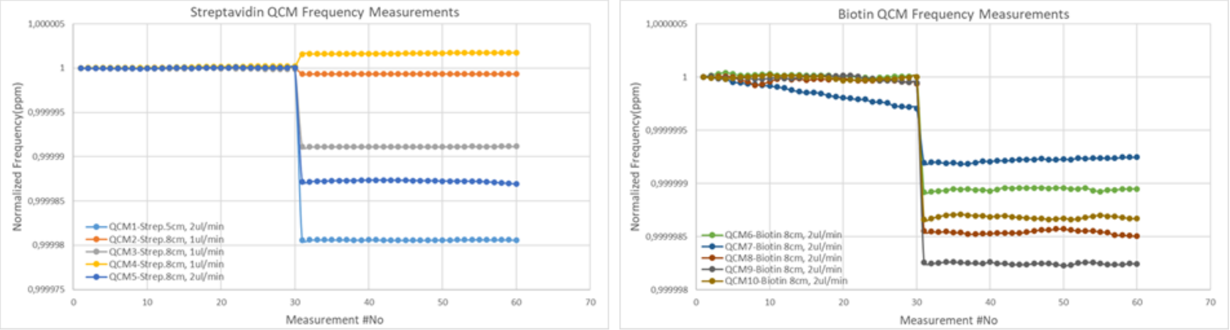

Fig. 4. Resonance frequency shifts of the streptavidin and biotin electrosprayed QCM sensors

Additionally, we have performed Raman microscopy measurements to evaluate the surfaces of the QCM sensors coated with biosamples and gain a deeper understanding of the observed variations. We utilized a 532 nm laser excitation with a power of 0.56 mW and a Leica 20× objective to capture Raman spectra of the QCM sensors. The spectra were acquired from two sides: the (black) quartz side and the (red) silver-coated side, as shown in Fig. 5. Furthermore, we presented Raman spectra of biotin-coated QCM sensors (with black representing the pure biotin sample) in Fig. 6, and streptavidin-coated QCM sensors (with black representing the quartz part) in Fig. 7.

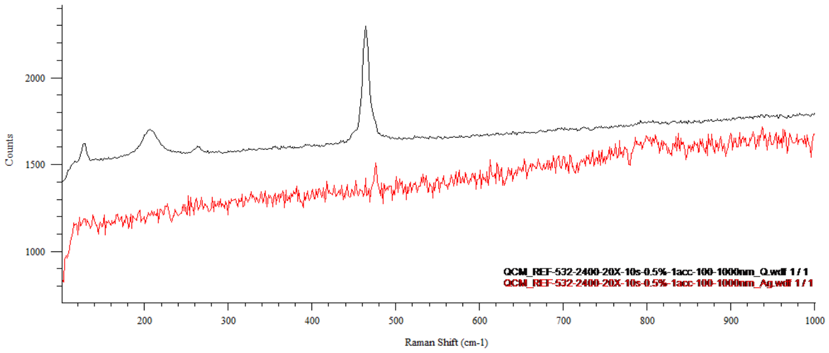

Fig. 5. Raman spectra of the QCM (black) quartz side, (red) silver-coated side

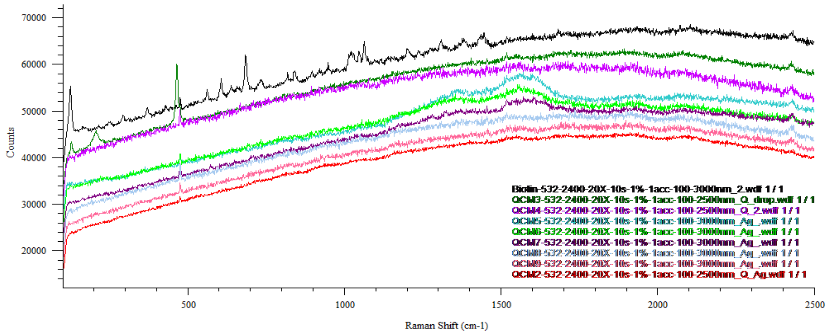

Fig. 6. Raman spectra of the biotin-coated QCM sensors (black is the pure biotin sample)

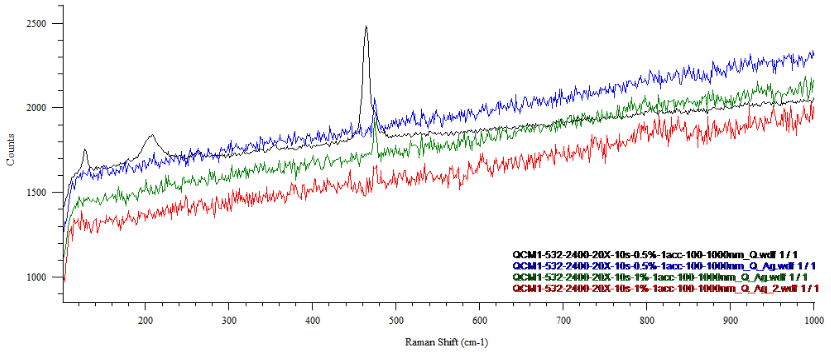

Fig. 7. Raman spectra of the Streptavidin-coated QCM sensors (black is the quartz part)

ACKNOWLEDGEMENT

This work was supported by the Scientific and Technical Research Council of Turkey (TUBITAK) under Grant No. 118C476 and Grant No. 122F301. However, the entire responsibility of the publication belongs to the authors of the publication. The financial support received from TÜBİTAK does not mean that the content of the publication is approved in a scientific sense by TÜBİTAK. The authors acknowledge ME Research and Technologies (MERT Electronics) for providing the QCM sensors and OpenQCM hardware.

REFERENCES

[1] Hendrickson, W. A., Pähler, A., Smith, J. L., Satow, Y., Merritt, E. A., & Phizackerley, R. P. (1989). Crystal structure of core streptavidin determined from multiwavelength anomalous diffraction of synchrotron radiation. Proceedings of the National Academy of Sciences, 86(7), 2190-2194.

[2] Ayan, E., Yuksel, B., Destan, E., Ertem, F. B., Yildirim, G., Eren, M., & DeMirci, H. (2022). Cooperative allostery and structural dynamics of streptavidin at cryogenic and ambient temperature. Communications Biology, 5(1), 73.

[3] Yu, X., Chen, X., Yu, X., Chen, X., & Ding, X. (2021). A quartz crystal microbalance (QCM) humidity sensor based on a pencil-drawn method with high quality factor. IEEE Transactions on Electron Devices, 68(10), 5149-5154.

[4] Fauzi, F., Rianjanu, A., Santoso, I., & Triyana, K. (2021). Gas and humidity sensing with quartz crystal microbalance (QCM) coated with graphene-based materials–A mini review. Sensors and Actuators A: Physical, 330, 112837.

6th Pak – Türk International Conference on Emerging Technologies in the field of Sciences and Engineering, May 4 – 6, 2023, Karabük University, Karabük, Türkiye

Numerical Modeling for Stresses Analysis in Single Lap Joints for Aerospace Applications

Muhammad Azeem[1,2], Saeed Hassan [1*], Moin Khan[1], MW Mustafa and Shahid Iqbal[1]

[1] *Department of Mechanical Engineering, University of Wah, Wah Cantt, Pakistan*
[2] *Department of Mechanical Engineering, University of Engineering and Technology, Taxila, Pakistan*

* Corresponding author e-mail address: saeed.hassan@wecuw.edu.pk

***Abstract*—**Over the last few decades industry was shifting towards composite material applications in aerospace industry. Light weight materials were preferred as of good strength to weight ratio thereby enhancing system efficiency. This study presents a numerical modelling procedure and stress analysis of single lap joint between metal (AA 6061-T6) and composite (carbon/epoxy laminate) whereas stainless steel 304 was used as a rivet material. Joint was modelled with three different joining techniques namely: adhesive, hybrid and riveted joining. ABAQUS/Standard cohesive zone model (CZM) tool was used for simulating adhesive and hybrid joints while simple finite element analysis (FEA) tool was used for simulating riveted joint under tensile loading. Fracture toughness (GIIC) was determined using analytical expression, with the help of tensile load. The results were evaluated in terms of Von Mises stress, shear stress, and normal stress in X, Y & Z directions. It was observed that adhesive joint shows much lower stresses as compared to hybrid and riveted joint because of equal distribution of the load along the whole surface.

Keywords* — *Lap Joint, Composite, FEA, ABAQUS

INTRODUCTION

Because of their strength and light weight, fiber metal laminated materials (FMLs) are frequently utilized in the automotive, civil infrastructure, and aerospace industries. Depending on the applications, many fiber kinds are included into FMLs. For instance, carbon fiber is employed in applications that demand high tensile and compressive stiffness and good fatigue strength. However, glass fiber is utilized because of its excellent tensile strength, water and fire resistance, and ability to withstand adverse conditions. Since Kevlar absorbs impact energy, it is utilized as a shock absorber [1]. In place of traditional connecting methods (bolts and rivets), novel joining techniques (adhesive or hybrid) are now being developed for FMLs [2]. To simulate the aforementioned innovative joining procedures, a special tool called the cohesive zone model (CZM) (triangular, exponential, or trapezoidal method) is used [3-6]. In the current work, we compare traditional and contemporary joining methods, such as riveting, adhesive, and hybrid joints that use single lap joints to withstand Von-Misses, shear, and normal loads. We also evaluated the stress concentration area.

LITERATURE REVIEW

The adhesively bonded single lap joints (SLJs) in Sheet Molding Compounds (SMC) were investigated by Mazumdar and Mallick [1] under static and fatigue response. The performance of the joint was examined in relation to overlap length, adhesive its thickness, preparation of the surface, test speed, and water exposure. The findings led to the conclusion that the overlap length and adhesive thickness are the only factors that affect the ratio of stress to static strength. Additionally, it was discovered that the static and fatigue failure loads were unaffected by the 214-hour submersion in water, and that fatigue strength is roughly 50–54% of static strength.

Composite material joints can be divided into three categories: mechanically fastened joints, adhesively bonded joints, and hybrid joints (which combine both mechanical and rivet fastening). Hybrid joints are typically used in the automotive and aerospace industries to link sheet metal and composite materials. Hybrid joints have enhanced tensile and fatigue strength compared to basic adhesives or simple bolted joints [2].

In recent years, numerous industry sectors, including the automotive, aerospace, and transportation industries, have become more interested in hybridization joints, which combine an adhesive layer with a typical mechanical joint. This is because they outperformed mechanical joints or bonded joints in terms of preferred achievement. In this study, the researcher looked at how adhesive strength and rivet strength responded when combined. The exclusive facial properties of hybrid joints—the adhesive compares to the stress distribution, regardless of bolts discovering intermittent stress distribution—lead to the refined characteristics of hybrid joints. The author came at the conclusion that loads may be shared between glue and bolts if the adhesive modulus was too low. The author further determined that while bolts would carry the maximum stress in the event that the adhesive failed, this would still contribute to a secure procedure [3].

Experimental fatigue testing on composite adhesively bonded step joints were performed by Tenchev and Falzon [4]. They demonstrated how the static strength and fatigue life of the composite were dramatically lowered by this sort of adhesive junction, which is often used in repairs.

Under various environmental circumstances, Zhang et al. [5] investigated the fatigue behaviour of an adhesively bonded pultruded glass fiber reinforced plastic (GFRP) DLJ. A fiber tear in the GFRP laminates was the predominant mode of failure in this instance. In the presence of excessive humidity, the mechanism of failure changed from cohesive to interfacial (adhesive/composite interface). Test temperature and humidity both had an impact on the joints' fatigue lifetime and fracture behaviour.

The author explored double-lap joints under tensile loading for unidirectional and quasi-isotropic composite adherends utilizing moiré interferometry in an experimental setting, a finite element approach numerically, and an analytical one-dimensional closed-form solution. Other than the fringe waviness caused by the three-dimensional free-edge phenomenon in the quasi-isotropic composite joint, the displacement fields for adhesive and hybrid joints were obtained in an improved concession from both analysis, such as after experimentation as well as finite element analysis appropriately [6].

There aren't many studies of double lap hybrid joints in the literature, and there aren't many full-field experimental results. In the current study, the failure loads and failure modes of composite to aluminum dual lap hybrid joints were examined. Adhesive-only and adhesive and rivet combinations are the joining possibilities. Finite Element Analysis is used to examine these two types of joints and compare the results to experimental data. Another experimental comparison between this strategy and Wen-Yen Chuang et al. was also conducted [7]. F. Moroni et al. [8] investigated traditional joining methods and adhesive bonding. In comparing the advantages of using hybrid welded/bonded, riveted/bonded, or clinch-bonded joints to simple adhesive, spot-welded, riveted, or clinched joints, the author discovered that the contribution of adhesive bonding is more apparent in hybrid-fastener joints than in weld bonded joints, with a significant improvement of the mechanical performances relative to simple fastened joints.

In this study, A. Graner Solana et al. [9] a series for load levels in continuous amplitude fatigue testing of single lap joints (SLJs) to gather experimental data suggested by the author and the related fatigue damage model. The creation of an elastoplastic damage model is able to forecast the patterns of rear face strain observed in experiments as well as the fatigue life under various fatigue loads. It was being run in the FEA code of ABAQUS and used for user-defined subletting to locate the failure, which resulted in a reduction in adhesive young's modulus and yield stress.

The titanium flanges on the Turbine Exhaust Duct (TED) of the Vinci-engine for the Ariane five rocket were adhered to a carbon fiber composite material. The findings of equivalent experimental tensile tests were compared to the analysis of FE-models of the tensile test specimens (SLJ and DLJ) in this study. According to the study, if an appropriate joint design is adopted, the local stress concentrations caused by the applied thermal and structural loads on the adhesive surface are not high enough to harm the joint [10]. Jen and Ko [11] discussed their research about the impact of adhesive dimensions on the fatigue strength of adhesively bonded Al SLJs. Their experimental findings showed that, with the exception of specimens with an adhesive thickness of 0.5 mm, the fatigue resistance dropped as the overlap length rose. They came to the conclusion that the interfacial peeling stress was the primary cause of the fatigue failure of the SLJs through finite element analysis (FEA). Using FEA, Ngoc and Paroissien [12] investigated adhesively and hybrid ally bolted/bonded SLJs. Geometrical and material nonlinearities were taken into account when conducting two- and three-dimensional investigations. It was determined that hybrid bolted/bonded joints outlast bolted joints in terms of fatigue life. Press-fitted or drive-fitted joints perform better in terms of fatigue when combined with adhesive. A few academics have looked into the outcome of this combination. The static and endurance performance of steel/Al component mixed hybrid joints was examined by Croccolo et al. [13]. In terms of its release force, the press-fitted joint's performance improved with the introduction of glue. Similar to cantilever beams, the researcher looked into the mechanical characteristics of SLJs in this work. Through the use of finite element analysis, stress distributions for a number of typical attributes have been produced in the adhesive layer. The author came to the conclusion that the Poisson's ratios and Young's modulus had a significant impact on the distribution of stress in the beams [14].

In this study [15], the investigation into the modal characteristics of single lap joints and cyclic vibration peel loading was carried out. Steel-aluminum SLJ specimens were used for vibration fatigue tests, followed by measurements of the modal response. The author developed a Finite Element model to analyse the impact of Young's modulus and adhesive layer contact area on the modal frequencies of SLJ structures. By conducting experiments, the author came to the conclusion that a decrease in modal frequency was seen when the adhesive contact area and Youngs modulus were both decreased.

Three different joining methods for SLJs—adhesive joining, mechanical fastening, and hybrid joining—were compared by Yogesh and Arunkumar [16]. The hybrid joint performs better than other types of joints when compared using tensile testing to assess joint strength and failure modes. Adhesive bonding was shown to be appropriate for acrylic type adhesive and for rubber type adhesive.

Due to their reduced weight, greater stiffness, and improved fatigue qualities, composite materials have seen a sharp growth in application over the past couple of decades, particularly in the aerospace industry. The design of fiber metal laminated materials (FML) assemblies typically involves the interaction of metallic elements (AA 6061 T6) and composite materials (carbon fiber), and these interfaces frequently turn out to be the weakest parts of the constructions. Due to the tensile and fatigue properties of double lap joint design, this research has concentrated on comparing various joining strategies of composites with metals. Simple adhesive joints, hybrid joints (adhesive + rivets), and joints with adhesive pins embedded in metal plates were created and tested for this purpose. Additionally, these joints' finite element modelling and subsequent experimental validation are part of the research. The hybrid joint, which combines glue and fasteners, demonstrated greater strength in the results; nevertheless, the unique notion of using sticky pins was unsuccessful [17].

TABLE IX. LITERATURE MATRIX

LITERATURE MATRIX						
Reference No.	Type of Joints		Type of loading			Adhesive / Hybrid Joint
	Single Lap Joint	Double lap Joint	Static Loading	Fatigue Loading		
				Experimentally	FEA	
[1] S. K. Mazumdar and P. K. Mallick	✓		✓	✓		Adhesive Joint
[2] Makqto Imanaka et al.	✓		✓	✓		Hybrid Joint
[3] G. Kelly	✓			✓		Hybrid Joint
[4] R. T. Tenchev and B. G. Falzon	✓			✓		Adhesive Joint
[5] Y. Zhang et al.		✓		Investigated Stiffness degradation		Adhesive Joint
[6] M.Y. Tsai and J. Morton		✓		Investigated Stress distribution		Adhesive Joint
[7] Wen-Yen Chuang,Jia-LinTsai		✓	✓	✓		Adhesive Joint
[8] F. Moroni et al.	✓			✓	FEA	Hybrid Joint
[9] A. Graner Solana et al.	✓			✓	FEA	Adhesive Joint
[10] Fredrik Fors	✓		✓	✓	FEA	Adhesive Joint
[11] Y.M. Jen and C.W. Ko	✓			✓	FEA	Adhesive Joint

[12] C.-T. Hoang-Ngoc and E. Paroissien	✓			✓	FEA	Adhesive Joint
[13] D. Croccolo et al.	✓		✓	✓		Adhesive Joint
[14] Xiaocong He	✓			✓	FEA	Adhesive Joint
[15] Yu Du and Lu Shi	✓			✓	FEA	Adhesive Joint
[16] T. L. Yogesh and N. Arunkumar	✓		✓			Adhesive/ Hybrid joint
[17] Khawaja et al.		✓	✓	✓	FEA	Hybrid joint

MATERIALS AND METHODS

In the present day, fiber metal laminates (FMLs) are replacing conventional materials in the construction of large, heavy structures like bridges, aircraft, wind turbine blades, etc. Their excellent strength to weight ratio has significantly expanded their uses, for example in the case of the Boeing 767, which is also made utilizing FMLs. Its main metal body is built of alloys, and its composite-material wings are linked to it utilizing a variety of joints (adhesive, rivets, and hybrid).

In this study, we used a computer simulation to test the performance of a carbon fiber-reinforced aluminum alloy (CARALL) under normal, shear, and Von Misses stresses. Models for the specimens were created using published data [2]. In figure 1, geometry with dimensions displayed.

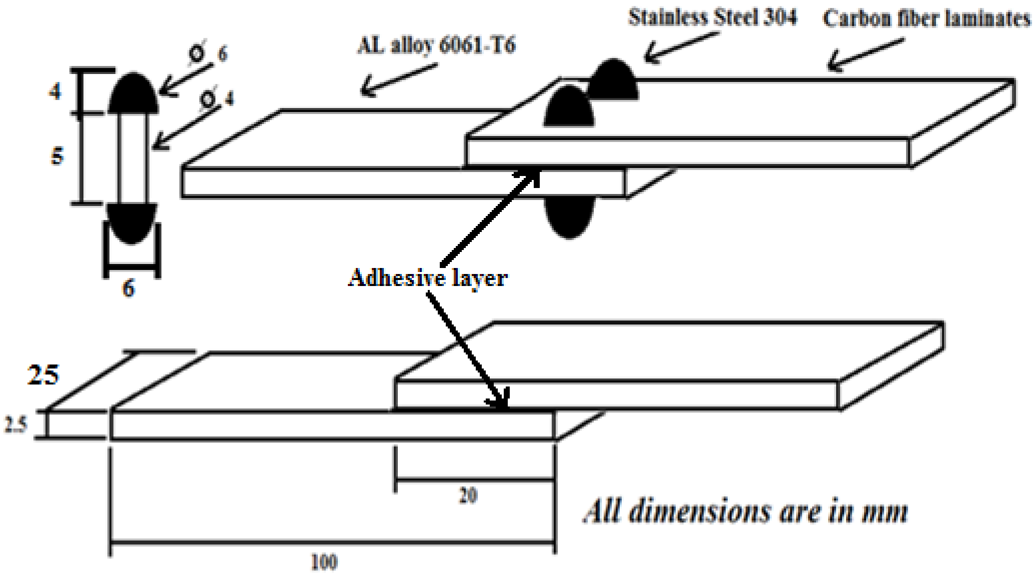

Fig. 1. Joints design with dimensions

The basis metal for this model was aluminum alloy 6061-T6. It is common to utilize this alloy in construction. Carbon fiber laminates are used to simulate the other overlapped part. It is frequently employed in the structure of aircraft wings. Three different types of joints were used: epoxy araldite LY 5052 as resin for adhesive joints, Aradur 5052 [7] as a hardener for rivet joints, and hybrid joints that combine rivet and adhesive joints. Table 1 provides the material qualities.

TABLE X. MATERIAL PROPERTIES

Material	**Density** (Kg/m^3)	**Young's Modulus** (GPa)	**Poisson's ratio**
Aluminum 6061-T6	2700	68.9	0.33
CFRP	1800	230	0.35
Stainless steel 304	8000	197	0.29

ANALYTICAL CALCULATIONS

Calculating G_{IIC}:

The $\mathbf{G_{IIC}}$ value is calculated using the following formulation [8].

$$G_{IIC} = \frac{F_{max}^{\;2}(E_s t_s + 3E_0 t_0)}{3E_0 t_0 w^2 (E_s t_s + E_0 t_0)} \qquad (1)$$

Where;

G_{IIC} = Fracture energy

F_{max} = Maximum bearing force in Newton

E_o = Young’s Modulus of overlap part (Carbon/epoxy)

E_s = Young’s Modulus of base metal (Aluminum)

W= width of the specimen

t_o = Thickness of overlap part

t_s = Thickness of base metal

According to published data; we know the maximum bearing force is 5000 N, width of specimen is 25 mm, t_o and t_s are 2.5 mm, E_s is 68.9×10^9 Pa and E_o is 230×10^9 Pa. Substituting these values in equation1 gives energy release rate as

G_{IIC} = 72 J/m^2

Designing criterion for rivet joints [2]:

Diameter of the rivet hole d = 2t

D = 2x2.5 = 5mm

Pitch of rivets = 2d

P = 2x5 = 10mm

Margin m = 1.5d = 1.5x5 = 7.5mm

Transverse pitch= P_t = 2d = 10mm

generation, and boundary condition definition. Then, ANSYS was used to solve the problem. The post-processor in ANSYS was used to generate the plots of the solution's results.

FINITE ELEMENT ANALYSIS

Utilizing the cohesive zone model, joints (riveted, adhesive, and hybrid) were modelled and simulated using the commercial software ABAQUS. While the opposite end of the carbon fiber was loaded with 5000 N of force in the positive "X" direction, the free end of the base metal was restricted in terms of translation and rotation. Figure 2 below displays boundary conditions and force.

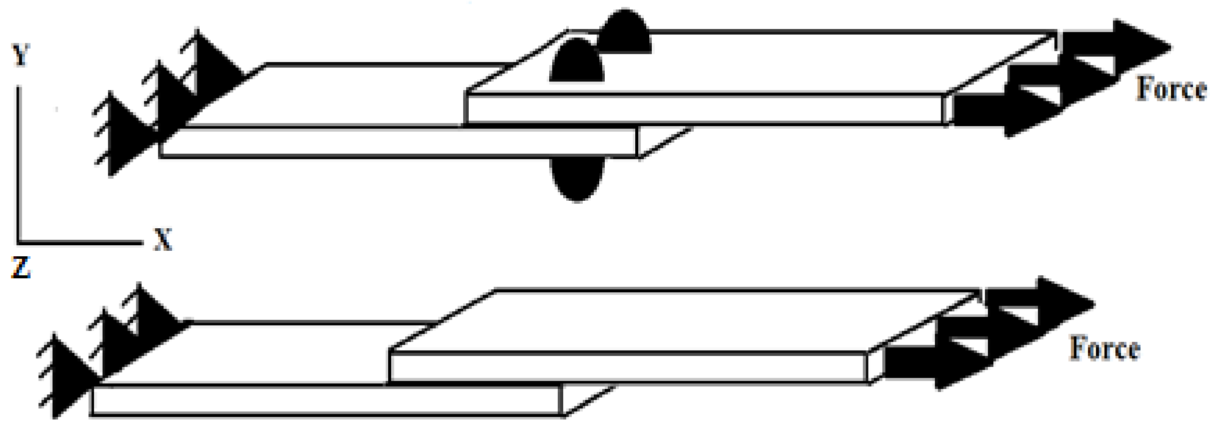

Fig. 2. Joints design with boundary and loading conditions

Description of each module with respect to joint type is briefly described in these lines.

M. *Part Module*

Geometry of all type of joints were modeled according to dimensions using 3D deformable solid. All dimensions are given in figure1. While the designing criterion of rivet is shown in analytical calculation which was taken from published data[2].

N. *Property Module*

Material properties were assigned in each part in property module. Aluminum alloy, CFRP and Stainless Steel were modeled as an isotropic material. Densities, Poisson ratio and Elastic values of these materials are given in table1. Each part of the property module received a set of material properties. As isotropic materials, aluminum alloy, CFRP, and stainless steel were modelled. Table1 lists the densities, Poisson ratio, and elastic values of these materials.

The stiffness in the normal (E/Knn), first (G1/Kss), and second directions (G2/Ktt) was assumed to represent the adhesive layer. Figure 3 depicts the graphic representation of adhesive behaviour, while Table 2 provides its values. Maximum stress damage was used to assign damage attributes, which were then converted into damage for traction separation law. Sub-options were used to assign the GIIC value during damage evolution. Equation 1 of the analytical computation used to derive this number is a numerical formula. Utilizing damage stabilization cohesive, the viscosity coefficient value was also assigned in the sub-option. Its value was 1×10^{-5} for traction separation law.

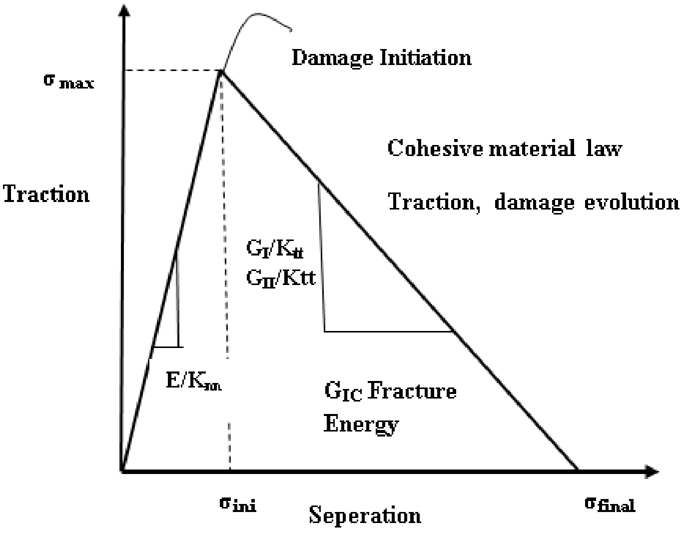

Fig. 3. Traction-separation phenomenon used in adhesives.

TABLE XI. MATERIAL PROPERTIES

E/K_{nn} (GPa)	**G_1/K_{ss}** (GPa)	**G_2/K_{tt}** (GPa)
3.44	1.27	1.27

O. *Assembly Module*

Each part was assembled according to its geometry as shown in figure-1. After assembly each geometry was shifted from local to global coordinate system and independent mesh was assigned to each part of all joint geometries.

P. *Step Module:*

Step was created for assigning load condition as recommended in figure2. According to these joint configurations, static general type load was assigned to the part with nonlinear geometry and in incremental fashion as per requirement of joint.

Q. *Interaction Module:*

Interaction module plays a vital role in these types of joints. In adhesive joint, tie constraints are applied between the surfaces of Aluminum, Carbon fiber and adhesive for simulating adhesion effect between them. Hard contact interaction was also defined between Aluminum and Carbon fiber to restrict them into their boundaries. Riveted joint surfaces were physically separated with each other so tie constrained were not assigned to them. Penalty friction formation was assigned on the surfaces of rivet, Aluminum and Carbon fiber using coefficient of friction. In hybrid joint combination of adhesive and rivet joint interactions was introduced for simulating this joint.

R. Mesh Module:

Regarding pieces, each sort of joint model was independently meshed. Aluminum and carbon fiber were meshes in riveted joints using Sweep Hex, a 3D stress element known as C3D8R in ABAQUS, and rivets were meshes in Free Tet, a 3D stress element known as C3D10 with component deletion.

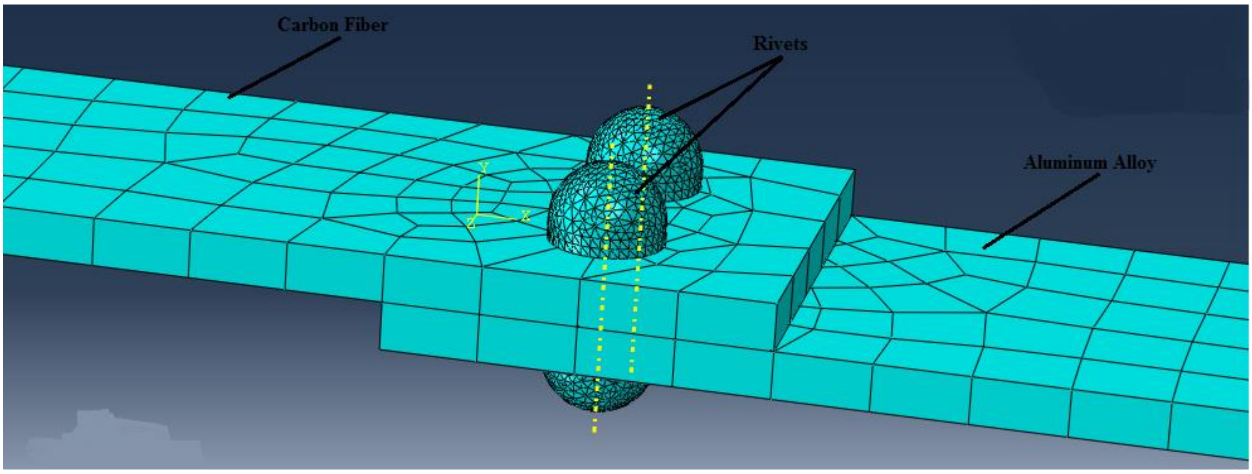

Fig. 4. Meshed assembly of riveted joint.

Aluminum and carbon fiber were meshes in the adhesive joint using Structured Hex elements of the same type as those described above, while the adhesive was meshes using Sweep Hex (where the sweep path was in the direction of the force), and the cohesive element was referred to in ABAQUS as COH3D8 through component deletion. After part meshing, edit mesh was carried out, and cohesive elements were given zero thickness, as seen in figure 5.

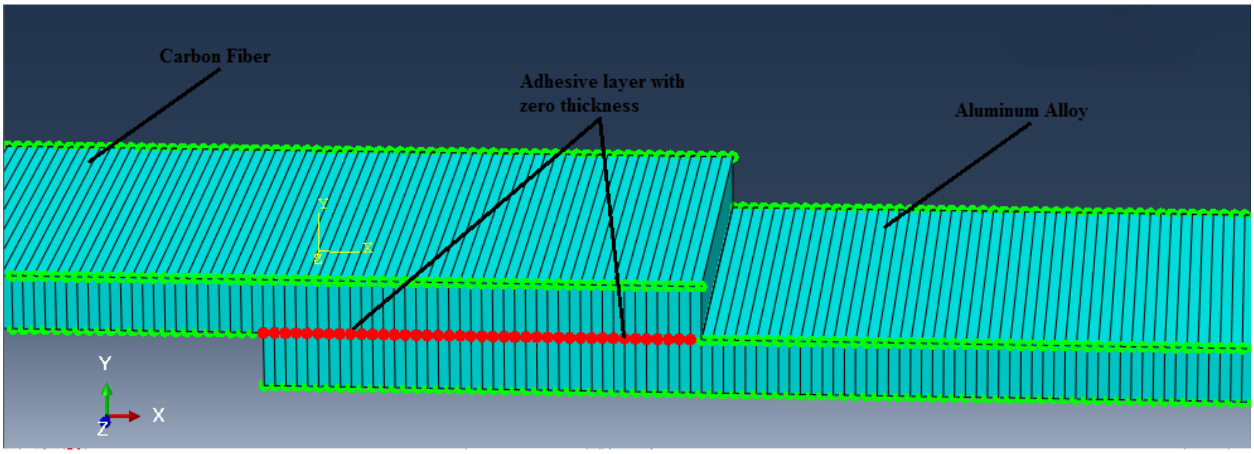

Fig. 5. Meshed assembly of adhesive joint with zero thickness of adhesive.

Sweep Hex was used to mesh the aluminum, carbon fiber, and glue in the hybrid junction. While Free Tet and rivet were mated. The remaining variables were identical to those mentioned previously. After part meshing, the mesh was edited, and cohesive elements were given a zero thickness, as seen in figure 6.

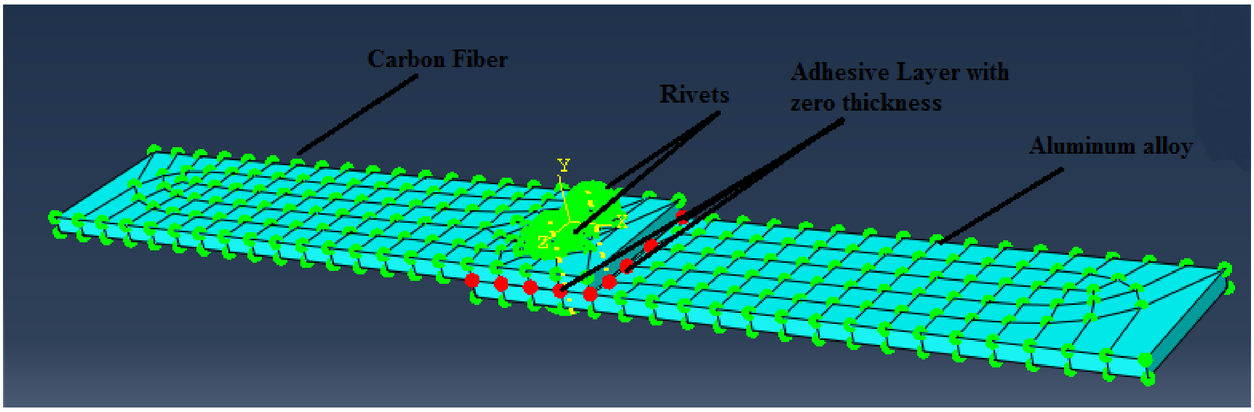

Fig. 6. Meshed assembly of hybrid joint with zero thickness of adhesive

S. Load Module:

First boundary condition was applied on left side of base metal (aluminum alloy) using initial step. This side was restricted for any type of displacement and rotation in X, Y and Z directions. Second condition was applied using first step on right side of carbon fiber and allowed its motion in only positive X-axis with 5000 N force. These boundary conditions are shown in figure2.

T. Job Module:

Job was created and submitted after setting field outputs. ABAQUS determined the concentration of Von Misses, shear and normal stresses in x, y and z directions within the bond in the form of analytical values and color combination. Results were evaluated for comparing different joint results as shown below in figure7,8,9,10 & 11 (a, b, c).

U. Visualization Module

The ratio of maximum to minimum stress and area of stress concentration was examined in this module.

RESULTS AND DISCUSSION

The normal and shear stress fields were evaluated along three different planes in adhesive and hybrid joints (P1-P3), and two different planes in riveted joint (P1&P3). These stresses were distributed across the joint thickness as shown in figure (12). A force of approximately 5kN was applied to all joints. The evolution of Von Mises, shear and normal stresses for the adhesive, hybrid and riveted joint is presented in figure no. 7, 8, 9, 10 & 11 and stress values are given in Table3. As per expectation, antisymmetric effects are related to the midplane (adhesive). Adhesive and Hybrid joints show Von Mises, shear and normal stress concentration at the interfaces adherend–adhesive (plane P2) was observed while on the other hand riveted joint shows maximum concentration on rivets.

Von Mises yielding criterion is widely used to analyze the withstanding capability of an engineering design for a given load and the critical points under certain loading condition. Shearing stress and normal stresses in the direction of tensile loading play a vital role in these types of joints because force is parallel to the surface and most of the joints fail in this mode. Stresses in Y and Z axis are not so significant because there is a little twisting which affects at the ends of the joints.

Joint efficiencies are same in all cases, The mode of failure in adhesive is in fact cohesive because a thin adhesive layer can be observed between the adherend's surfaces. Adhesive joint shows minimum stress because the force is equally distributed along the surface. In Hybrid joints, adhesive fails cohesively and rivets experience shearing failure because it shows higher stress as compared to adhesive joint but lower as compared to rivet joint. Hybrid joint distribute the stresses along the surface due to adhesive. Existence of hole/holes in the structure causes some stress concentration on rivet. Riveted joint shows maximum value of stress on a rivet because stress is mainly concentrated on it and it fails by shearing.

The probability of failure in the Riveted joints is higher than in Hybrid and Adhesive joints respectively, as can be concluded from table 3.

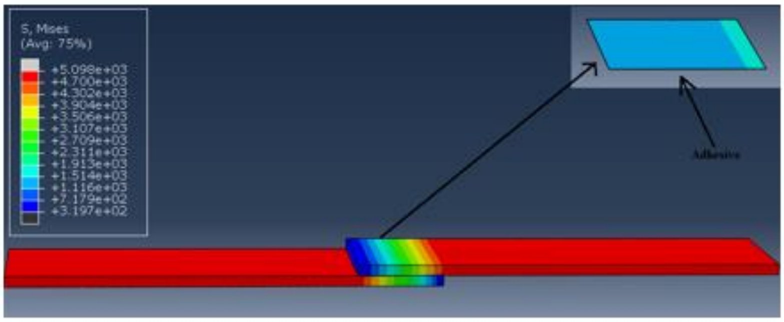

Figure 7 (a) Von Mises stresses in adhesive joint

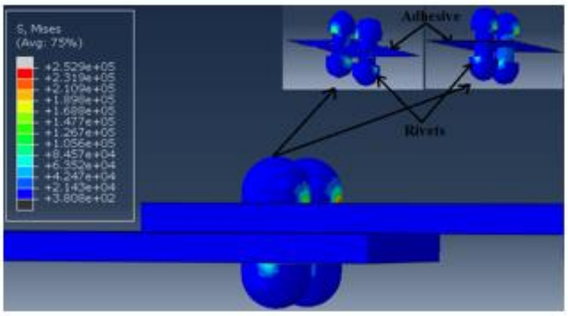

Figure 7 (b) Von Mises stresses in hybrid joint

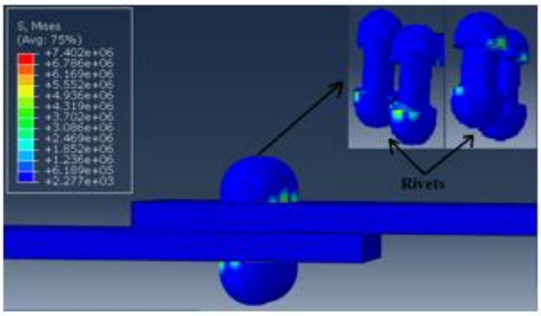

Figure 7 (c) Von Mises stresses in riveted joint

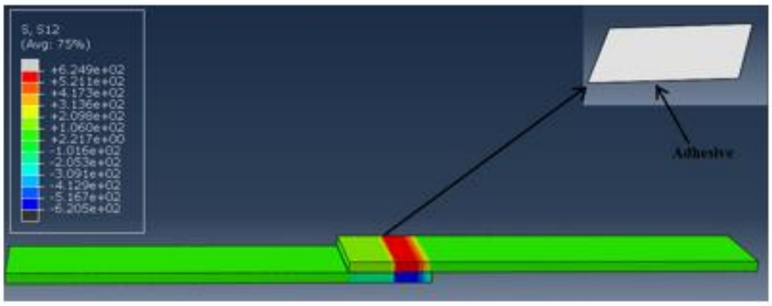

Figure 8 (a) Shear stresses in adhesive joint

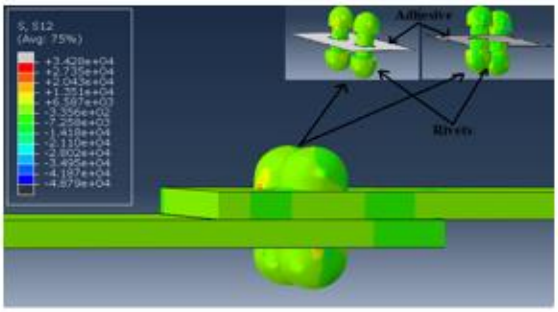

Figure 8 (b) Shear stresses in hybrid joint

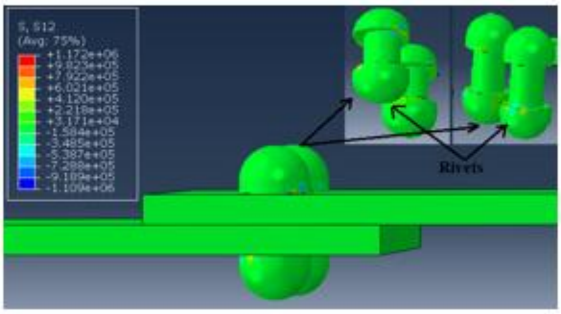

Figure 8 (c) Shear stresses in riveted joint

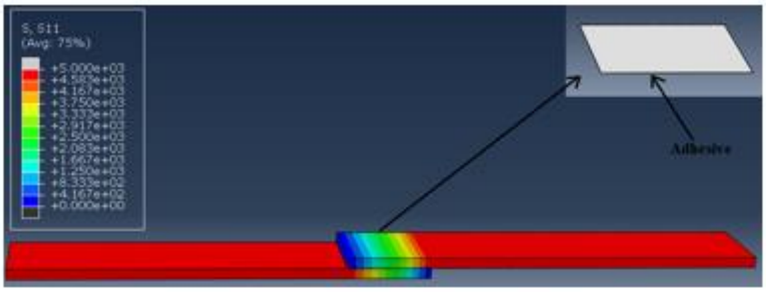

Figure 9 (a) X-axis stresses in adhesive joint

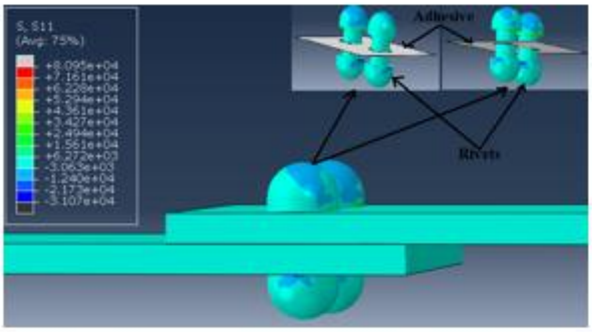

Figure 9 (b) X-axis stresses in hybrid joint

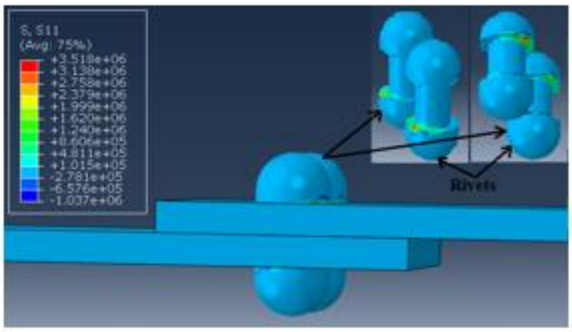

Figure 9 (c) X-axis stresses in riveted joint

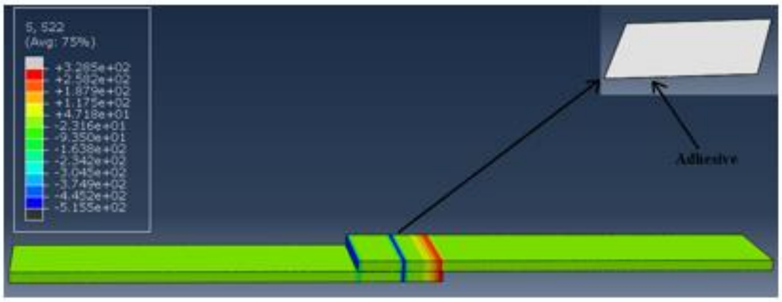

Figure 10 (a) Y-axis stresses in adhesive joint

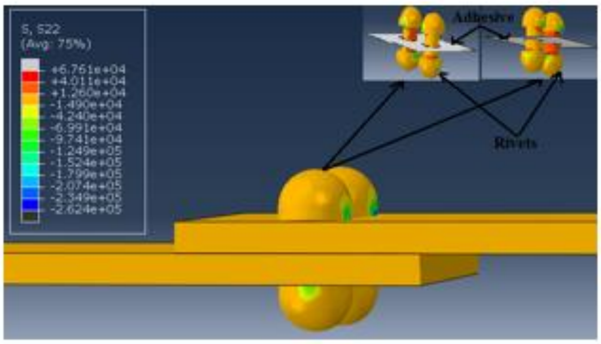

Figure 10 (b) Y-axis stresses in hybrid joint

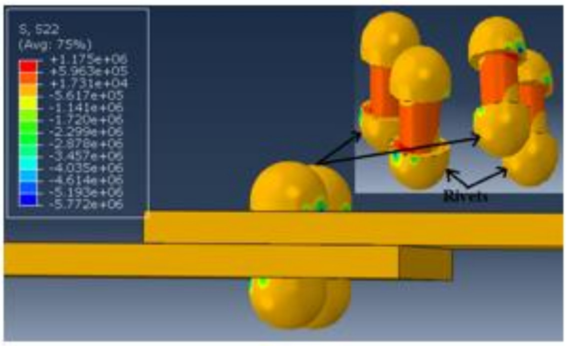

Figure 10 (c) Y-axis stresses in riveted joint

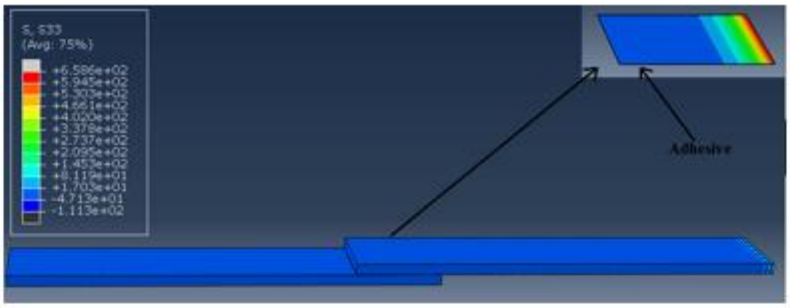

Figure 11 (a) Z-axis stresses in adhesive joint

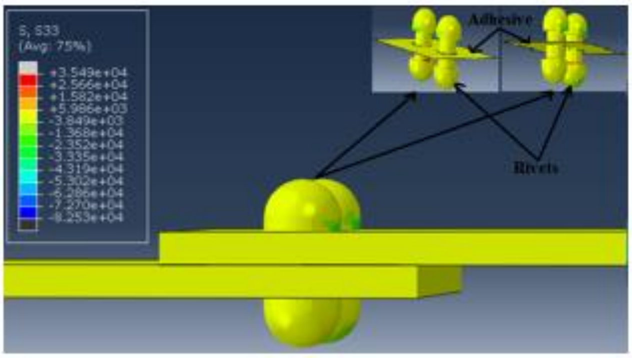

Figure 11 (b) Z-axis stresses in hybrid joint

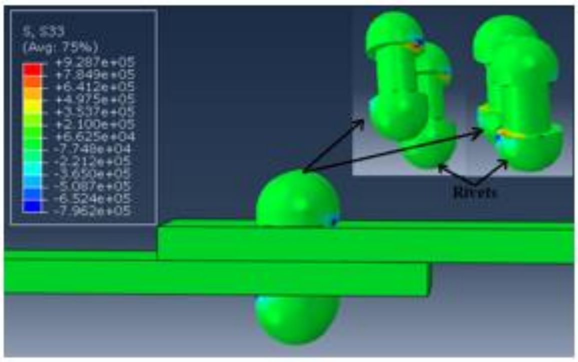

Figure 11 (c) Z-axis stresses in riveted joint

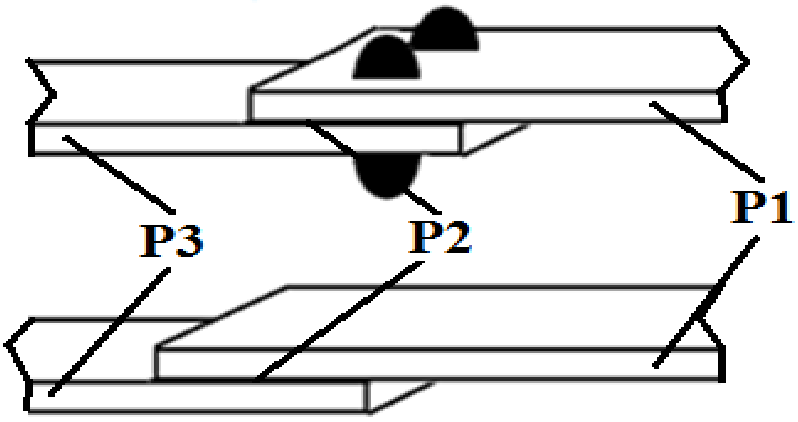

Fig. 12. Schematic Representation of planes

TABLE XII. MATERIAL PROPERTIES

Types of Joints	Von Mises Stress (N/m^2)	Shear Stress (N/m^2)	Normal stress in x direction (N/m^2)	Normal stress in y direction (N/m^2)	Normal stress in z direction (N/m^2)
Bonded	1.9x10^3	6.2x10^2	5x10^3	3.3x10^2	6.0x10^2
Hybrid	2.53x10^5	3.43x10^4	8.1x10^4	6.8 x10^4	2.6x10^4
Riveted	7.4x10^6	1.2x10^6	3.52x10^6	1.2x10^6	9.3x10^5

CONCLUSION:

In this study, a three-dimensional finite element model that takes into account interface elements in adhesive and hybrid joint joints was used to assess the stress distribution in single-lap joints. Adhesive, hybrid, and riveted joints were the three types of joints that were examined. At the interface (adhesive-adherend), in relation to the adhesive's midplane, and at the end of the overlap region, two of them

(Adhesive and Hybrid) showed noticeable stress concentration effects. Because a rivet is the only link between two adherents, a riveted joint demonstrates stress concentration on rivets.

In order to determine Von Mises stress, stress from shear, and normal stress in the X, Y, and Z directions, the tensile test was conducted. As a result of joining procedures, antisymmetric effects between adherends vanished and a worldwide trend of stresses was seen. When joining two dissimilar materials, it is crucial to take these effects into consideration because they are so significant.

The computational model (CZM) showed promising ability to identify the impacts of stress concentration in bonded lap joints. It enables the estimation of stresses at interfaces between various joints and disparate materials. Finite element analysis does not frequently experience this. The method can be used to identify the failure type (Adhesive, Cohesive, and Adherent) of bonded joints if an acceptable damage model is given.

Because the loads are evenly distributed across the joint's whole surface, bonded joints exhibit the fewest strains. Because there is a hole in the hybrid joint, there are somewhat larger stresses there than on the rivet. Due to a high stress concentration on the rivets, a riveted joint exhibits the largest magnitude of stresses.

REFERENCES

[1] S. K. Mazumdar and P. K. Mallick, [1998] “Static and fatigue behavior of adhesive joints in SMC-SMC composites”. Polymer Composites, Vol. 19(2), pp. 139–146.

[2] Makqto Imanaka, Kosuke Haraga and Tetsuya Nishikawa, [2006]. “Fatigue Strength of Adhesive/Rivet Combined Lap Joints”. The Journal of Adhesion, Vol. 49:3-4, pp: 197–209.

[3] G. Kelly, [2006] “Quasi-static strength and fatigue life of hybrid (bonded/bolted) composite single-lap joints”. Composite Structures, Vol. 72(1), pp. 119–129.

[4] R. T. Tenchev and B. G. Falzon, [2008] “An experimental and numerical study of the static and fatigue performance of a composite adhesive repair,” Key Engineering Materials, vol. 383, pp. 25–34.

[5] Y. Zhang, A. P. Vassilopoulos and T. Keller, [2009] “Environmental effects on fatigue behavior of adhesively-bonded pultruded structural joints”. Composites Science and Technology, vol. 69 (7-8), pp. 1022–1028.

[6] M.Y. Tsai and J. Morton, [2010]. “An investigation into the stresses in double-lap adhesive joints with laminated composite adherends”. International Journal of Solids and Structures, Vol. 47, pp: 3317-3325.

[7] Wen-Yen Chuang,Jia-LinTsai [2013], “Investigating the performances of step wise patched double lap joint”. International Journal of Adhesion & Adhesive, Vol.42, pp. 44-50.

[8] F. Moroni, A.Pirondi , F.Kleiner, [2010]. “Experimental Analysis and Comparison of the Strength of Simple and Hybrid Structural Joints”. International Journal of Adhesion & Adhesives, Vol. 30, pp: 367–379

[9] A. Graner Solana, A. D. Crocombe, and I. A. Ashcroft [2010]. “Fatigue life and backface strain predictions in adhesively bonded joints”. International Journal of Adhesion and Adhesives, Vol. 30, no. 1, pp. 36–42.

[10] Fredrik Fors [2010]. “Analysis of Metal to Composite Adhesive Joints in Space Applications”. MS thesis.

[11] Y.M. Jen and C.W. Ko, [2010] “Evaluation of fatigue life of adhesively bonded aluminum single-lap joints using interfacial parameters”. International Journal of Fatigue, vol. 32 (20), pp. 330–340.

[12] C.-T. Hoang-Ngoc and E. Paroissien, [2010] “Simulation of single lap bonded and hybrid (bolted/bonded) joints with flexible adhesive”. International Journal of Adhesion and Adhesives, Vol. 30(3), pp. 117–129.

[13] D. Croccolo, M. de Agostinis and N. Vincenzi, [2011] “Experimental analysis of static and fatigue strength properties in press-fitted and adhesively bonded steel-aluminium components”. Journal of Adhesion Science and Technology, vol. 25(18), pp. 2521–2538.

[14] Xiaocong He, [2012]. “Effect of Mechanical Properties of Adhesives on 46 Stress Distributions in Structural Bonded Joints”. Proceedings of the World Congress on Engineering 2010 Vol II. WCE 2010, June 30 - July 2, 2010, London, U.K.

[15] Yu Du and Lu Shi [2014]. “Effect of Vibration Fatigue on Modal Properties of Single Lap Adhesive Joints”. International Journal of Adhesion & Adhesives, Vol. 53, pp: 72–79.

[16] T. L. Yogesh and N. Arunkumar [2015]. “Failure Mode and Analysis of the Bonded/bolted Joints between a Hybrid Fibre Reinforced Polymer and Aluminium Alloy”. Journal of Advanced Materials and Processing, Vol.3 (2), pp 49-60

[17] Khawaja, A. H., Tariq, A., Khan, W. A., & Baig, Y. (2016). “A comparison of different joining options of hybrid composite joints for improved fatigue life”. The Nucleus, 53(4), 254-259.

LIST OF PARTICIPANTS

No	First Name	Last Name	Affiliation	Country	Participant
1	Abdullah	Kepçeoğlu	Koç University	Türkiye	Speaker
2	Erhan	Ermek	Koç University	Türkiye	Participant
3	Esra	Ayan	Koç University	Türkiye	Participant
4	Nurettin	Tokay	Koç University	Türkiye	Participant
5	Hasan	Demirci	Koç University /Stanford PULSE Institute	Türkiye /USA	Participant
6	Jameel-Un	Nabi	University of Wah	Pakistan	Invited Speaker
7	Ayben	Karasu Uysal	KTO Karatay University	Türkiye	Invited Speaker
8	Serkan	Akkoyun	Sivas Cumhuriyet University	Türkiye	Invited Speaker
9	Tuncay	Bayram	Karadeniz Technical University	Türkiye	Speaker
10	Zeenat	Haq	University of Wah	Pakistan	Speaker
11	Yosuf-den	Jamasali	Mindanao State University	Philippines	Speaker
12	Şeref	Turhan	Kastamonu University	Türkiye	Participant
13	Aslı	Kurnaz	Kastamonu University	Türkiye	Participant
14	Aybaba	Hançerlioğulları	Kastamonu University	Türkiye	Participant
15	Volodymyr V.	Tkach	Chernivtsi National University	Ukraine	Speaker
16	Marta V.	Kushnir	Chernivtsi National University	Ukraine	Participant
17	José I. F.	Martins	University of Porto	Portugal	Participant
18	Jarem R.	Garcia	State University of Ponta Grossa	Brazil	Participant
19	Tetiana V.	Morozova	National Transport University	Ukraine	Participant
20	Necdet	Karakoyun	Yüzüncü Yil University of Van	Türkiye	Participant
21	Petro I.	Yagodynets	Chernivtsi National University	Ukraine	Participant
22	Yana G.	Ivanushko	Bukovinian State Medical University	Ukraine	Participant
23	Serkan	Oguz	Karabük University	Türkiye	Speaker
24	Ahmet Mustafa	Erer	Karabük University	Türkiye	Participant
25	Cafer Mert	Yeşilkanat	Artvin Çoruh University	Türkiye	Participant
26	Samet	Nohutçu	Karabük University	Türkiye	Speaker
27	Hayriye Ertek	Emre	Karabük University	Türkiye	Participant
28	Ramazan	Kaçar	Karabük University	Türkiye	Participant
29	Sajjad Saeed Ali	Ali	Selçuk University	Türkiye	Speaker
30	Nejdet	Şen	Selçuk University	Türkiye	Participant
31	Israa	Zainal	University of Kirkuk	Iraq	Participant
32	Fatih	Özcan	Selçuk University	Türkiye	Participant

33	Ramadan Ahmed Ali	Agoub	Tripoli University	Libya	Speaker
34	Muhammad Waqas	Mustafa	University of Wah	Pakistan	Speaker
35	Haider	Ali	University of Wah	Pakistan	Participant
36	Saeed	Hassan	University of Wah	Pakistan	Participant
37	Muhammad	Azeem	University of Wah	Pakistan	Participant
38	Muhammad	Yasir	University of Wah	Pakistan	Participant
39	Moin	Khan	University of Wah	Pakistan	Speaker
40	Shahid	Iqbal	University of Wah	Pakistan	Participant
41	Masoud Giyathaddin	Obaid	Karabük University	Türkiye	Speaker
42	Madiha	Rashid	University of Wah	Pakistan	Speaker
43	Arifa	Bashir	University of Wah	Pakistan	Participant
44	Sania	Rauf	University of Wah	Pakistan	Participant
45	Shumaila	Naz	University of Wah	Pakistan	Participant
46	Khalid	Agayr	Polytechnic University	Morocco	Speaker
47	Rachid	Benhida	Université Côte d’Azur	France	Participant
48	Khaoula	Khaless	Polytechnic University	Morocco	Participant
49	Kashaf	Tehreem	University of Wah	Pakistan	Speaker
50	Usman	Asghar	University of Wah	Pakistan	Participant
51	Shehar	Bano	University of Wah	Pakistan	Participant
52	Ahmet	Öztürk	Karabük University	Türkiye	Speaker
53	Mücahit	Coşkun	Karabük University	Türkiye	Participant
54	Ferhat	Toprak	Karabük University	Türkiye	Participant
55	Enes	Taşoğlu	Karabük University	Türkiye	Participant
56	Onur	Canbulat	Karabük University	Türkiye	Participant
57	Fazeel	Ahmad	University of Wah	Pakistan	Speaker
58	Waqas Ahmed	Khan	University of Wah	Pakistan	Participant
59	Abdullah	Niaz	University of Wah	Pakistan	Participant
60	Sami	Jabbar	University of Wah	Pakistan	Participant
61	Javid	Shabbir	University of Wah	Pakistan	Speaker
62	Irum	Jamil	University of Wah	Pakistan	Speaker
63	Faisal	Nawaz	University of Wah	Pakistan	Participant
64	Hakan	Öcal	Bartın University	Türkiye	Speaker
65	Bushra	Shakoor	University of Wah	Pakistan	Speaker
66	Faiza	Asghar	University of Wah	Pakistan	Participant
67	Bilal	Karaduman	Istanbul Commerce University	Türkiye	Speaker
68	Vedat	Tavas	Istanbul Commerce University	Türkiye	Participant
69	Ayşe	Nallı	Karabük University	Türkiye	Participant

70	Seyran	Ibrahimov	Karabük University	Türkiye	Speaker
71	Amna Ali A.	Mohamed	Tripoli University	Libya	Speaker
72	Mehmet	Dağ	Karabük University	Türkiye	Speaker
73	Najm Abdullah Saleh	Saleh	Karabük University	Türkiye	Speaker
74	Ayesha	Bibi	University of Wah	Pakistan	Speaker
75	Kashif	Iqbal	University of Wah	Pakistan	Participant
76	Hamza	Mehfooz	University of Wah	Pakistan	Participant
77	Raja	Rehan	University of Wah	Pakistan	Participant
78	Aftab	Haider	University of Wah	Pakistan	Participant
79	Lina Majeed Hayder	Al-Haider	Baghdad University	Iraq	Speaker
80	Ramoona	Shahzad	University of Puncab	Pakistan	Participant
81	Fakeeha	Farooq	University of Puncab	Pakistan	Participant
82	Arslan	Mehmood	University of Wah	Pakistan	Participant
83	Rubba	Tahir	University of Wah	Pakistan	Participant
84	Attaullah	Sial	University of Wah	Pakistan	Speaker
85	Muhammad	Shakeel	University of Wah	Pakistan	Participant
86	Aamra	Urooj	University of Wah	Pakistan	Speaker
87	Qazi Mehmood Ul	Hassan	University of Wah	Pakistan	Participant
88	Muhammad Yaqub	Khan	University of Wah	Pakistan	Participant
89	Khurram	Shehzad Baig	University of Wah	Pakistan	Participant
90	Usman	Asghar	University of Wah	Pakistan	Participant
91	Saba	Fatima	University of Wah	Pakistan	Participant
92	Zahid	Halim	GIK Institute of Engineering Science and Technology	Pakistan	Invited Speaker
93	Fariha K.	Vardag	Quaid-i-Azam University	Pakistan	Invited Speaker
94	Abdul	Muneem	GIK Institute of Engineering Science and Technology	Pakistan	Participant
95	Mehran	Bashir	GIK Institute of Engineering Science and Technology	Pakistan	Participant
96	Marium	Awan	University of Wah	Pakistan	Participant
97	Muhammad	Idrees	University of Wah	Pakistan	Participant
98	Shumaila	Naz	University of Wah	Pakistan	Participant
99	Nihal	Büyükçizmeci	Selçuk University	Türkiye	Speaker
100	Kevser	Sözen	Selçuk University	Türkiye	Participant
101	Huseyngulu	Guliyev	National Aviation Academy	Azerbaijan	Speaker

102	Asim	Ullah	GIK Institute of Engineering Science and Technology	Pakistan	Participant
103	Ramoona	Shahzadi	University of Wah	Pakistan	Participant
104	Fakeeha	Farooq	University of Wah	Pakistan	Participant
105	Javeria	Amin	University of Wah	Pakistan	Speaker
106	Anas	Ibrar	University of Wah	Pakistan	Participant
107	Hifza	Azam	University of Wah	Pakistan	Speaker
108	Sana	Akhter	University of Wah	Pakistan	Participant
109	Nabeel	Ahmad	University of Wah	Pakistan	Participant
110	Shakaib	Malik	University of Wah	Pakistan	Participant
111	Yavuz	Ekincioğlu	Bayburt University	Türkiye	Speaker
112	Syed Waqas	Hassan	University of Wah	Pakistan	Participant
113	Arzu	Cevdetoğlu	Mosi Textile R&D Center, Izmir	Türkiye	Speaker
114	Zührenur	Göktaş	Mosi Textile R&D Center, Izmir	Türkiye	Participant
115	Abdurrahman Ahmed	Mustafa	Karabük University	Türkiye	Participant
116	Khalid Hadi Mahdi	Aal-shabeeb	Karabük University	Türkiye	Speaker
117	Mahmut	Böyükata	Kırıkkale University	Türkiye	Participant
118	Abdurahman	Büber	Kırıkkale University	Türkiye	Participant
119	Şevki	Şentürk	Karadeniz Technical University	Türkiye	Speaker
120	Anes	Hayder	Karadeniz Technical University	Türkiye	Speaker
121	Osman	Ülker	Kırıkkale University	Türkiye	Participant
122	Javad	Rahebi	İstanbul Topkapı University	Türkiye	Speaker
123	Hussein Sheet Ahmed	Ahmed	University of Telafer	Iraq	Participant
124	Murat	Yücel	Gazi University	Türkiye	Participant
125	Necla	Çakmak	Karabük University	Türkiye	Participant
126	Jalaleddin	Mohamed	Karabük University	Türkiye	Speaker
127	Alper	Köseoğlu	Karadeniz Technical University	Türkiye	Participant